# Optical Design and Experimental Development of Grazing Incidence Fixed Slit Spectrometers for High Resolution Plasma Diagnostics

Michael C. Hettrick

1996

submitted in partial fulfillment of the requirements for the degree of

*Doctor of Philosophy*

The Graduate University for Advanced Studies

Japan

# Abstract

Three new classes of reflection grating spectrometer invented by the author are reviewed. The optical designs were devised for use at grazing incidence and have the following features in common: 1) a stationary ("fixed") entrance slit, 2) a fixed exit slit or normal incidence focal surface, 3) spectral images absent of low order aberrations, 4) only simple surface shapes (plane or sphere), 5) scanning motion(s) of only a single optic and 6) a small number of optical surfaces. These capabilities are crucial for soft x-ray and extreme ultraviolet spectroscopy in astrophysics, in the diagnostics of inertially and magnetically confined plasmas and in the study of material properties such as in surface science and optical component characterization. The geometrical insight which led to each design is presented and the detailed optical properties are derived from first principles and further verified using numerical raytracing computations. Experimental results are reported to demonstrate the practical viability and significance of each spectrometer design in several fields of scientific research.

The first design class consists of a plane (or ultra-large radius) grating surface having groove spacings which vary continuously across its width and operating in converging light (a virtual object). This varied line-space (or "VLS") plane grating design originated from the constraints imposed by an extreme ultraviolet space astronomy satellite, in which a high efficiency, slitless and stigmatic spectrum was required onto a small normal incidence detector within a short physical envelope. This mission (EUVE) was successfully deployed by NASA and provided the first high resolution ($\lambda/\Delta\lambda \sim 300$) spectra of extra-solar objects in the 70-760 Angstrom region using three grating channels in the spectrograph. A high resolution array of such plane gratings is now under construction for use on a future soft x-ray astronomy mission (XMM).

Improvements to this basic plane VLS grating design resulted in a versatile laboratory instrument. The High Resolution Erect Field Spectrometer (HIREFS) provides for the scan of wavelength between fixed slits by a pure rotation of the grating, without compromise of spectral or spatial resolution. The author designed, built and calibrated fifteen such systems operating from ~ 6 Angstroms to ~ 1500 Angstroms. These spectrographs and monochromators are currently in use at ~ 10 laboratories worldwide in a variety of applications. These include diagnosis of z-pinch plasmas, extreme ultraviolet lasers and femtosecond laser-produced gas harmonics, long beam calibration of astronomical telescopes, multilayer optics characterization, non-linear material interactions, soft x-ray CCD development and x-ray atomic fine structure (XAFS). Using 10 micron slits, spectral resolving powers of 1,500 to 35,000 (depending upon the grating focal length) have been obtained combined with stigmatic image spatial resolutions of approximately 5 arcseconds in the non-dispersive direction. Soft x-ray efficiencies of ~ 5-10% are obtained for the imaging spectrometer comprised of three

reflections. Due to the plane grating surface and the minimal amount of variation in the groove spacing, the uniformity of intensity is good in the meridional direction of the output aperture.

A second class of spectrometer was conceived to enable higher throughput primarily as a monochromator. The In-Focus Monochromator (IFM) is comprised of a self-focusing VLS grating and fixed entrance and exit slits. To scan wavelength the grating is rotated, and the resulting aberrations are corrected by a small translation along its surface. Due to the varied spacing, such translation results in a change to the groove density and all its derivatives at the fixed optical axis. This provides enough degrees of freedom to entirely remove first order defocusing, make second order aberrations negligible and minimize spherical aberration. In this way, a single optical element provides in-focus spectral images at all wavelengths scanned between stationary slits. This combination of desirable properties in the IFM is possessed by no other grazing incidence monochromator. The fundamental novelty of this new condition of grating focusing may be appreciated from the fact that the surface translation would have no such effect in the case of a classical (equally-spaced) grating.

The author designed a compact model of the IFM and has built and calibrated six such systems now in use for CCD characterization, optics and detector calibration, laser-plasma diagnostics and photo-electron spectroscopy. Using 10 micron slits, resolving powers of ~ 500 are obtained in the 6-400 Angstrom region at a typical absolute efficiency of 25%. One of these six IFM systems was a stigmatic version which delivers high brightness point-like monochromatic images to a target surface in ultra-high vacuum. The system has a solid collection angle of 30 mrad x 3.4 mrad and provides maximum reflection efficiency in the extreme ultraviolet by use of rhodium coatings on the mirror surfaces.

In addition to the applications reported here, synchrotron radiation facilities have also built the above types of monochromator using the author's published inventions of a plane varied-space grating in a converging beam or a rotating and translating self-focusing varied-space grating. These facilities have variously renamed these monochromators (e.g. "VLS Monk-Gillieson", "HERMON", etc.).

The third class of spectrometer was motivated by the desire for a high energy grating monochromator which maintains a fixed aperture output beam over a broad range in scanned wavelength and does not require high accuracy for the mechanism which scans wavelength. When operated at a small graze angle (e.g. $1^{o}$), conventional rotation of a reflection grating about its central groove results in a diffracted wavelength which is very sensitive to the angle of rotation. Such rotation also produces a large change in the numerical aperture of the diffracted beam as a function of wavelength and a defocusing of the image. However, if a grating is rotated about its surface normal, then the beam geometry and focusing conditions remain essentially unchanged at grazing incidence, while the incident photon views an effectively increased groove spacing. The Surface Normal Rotation (SNR) monochromator enables, for example, the use of a simple

concave grating with equidistant grooves operating on the Rowland circle. The surface normal rotation geometry also provides for a broader curve of diffraction efficiency and thus a wider range in wavelength which can be efficiently covered by a single grating. In addition, the accuracy required of the rotation scan is extremely low, due to the cosine dependence of the wavelength upon the rotation angle. Finally, the use of equally-spaced grooves and a single optical surface minimize the variation of efficiency across the diffracted output aperture.

Theoretical calculations and soft x-ray experimental results are presented for two single-element versions of the SNR monochromator designed for application to the testing of astronomical telescopes (ASTRO-D and XMM). The first of these reports the highest photon energy (4 keV) yet obtained for a reflection grating. The second design maintains a resolving power of approximately 1,000 over the soft x-ray region from 10 to 50 Angstroms, by providing a tilt rotation of the grating simultaneous with the surface normal rotation. It is interesting to note that the SNR technique exhibits the unconventional property that the performance improves as the graze angle is reduced. Being the only known case in the history of gratings where the optical aberrations are smaller at grazing incidence than at normal incidence clearly illustrates that such a geometrical solution would not have evolved from the usual method of revising classical designs.

Recently there has been a growth in the use of increasingly sophisticated and immovable sources of soft x-ray radiation, including magnetically confined fusion plasmas, inertially confined plasmas driven by lasers or other pulsed sources and charged particle accelerators. This has been accompanied by the development of new and essentially immovable soft x-ray detectors such as streak cameras, charge-coupled devices (CCDs) and x-ray calorimeters. Adaptations of the classical Rowland circle and plane grating geometries are found inadequate to couple efficiently to such sources and detectors. Future advances in short wavelength spectroscopy must be made with equally advanced spectrometer geometries which employ stationary slits yet maintain high spectral and spatial resolutions.

The high efficiency resulting from use of a minimum number of grazing incidence reflections, the high spectral resolution provided by varied groove spacings and novel yet simple scanning motions of accurate plane or spherical optical surfaces, and the high spatial resolution enabled by stigmatic geometries, make the spectrometer systems presented in this work useful in many fields of current research. Of particular interest is the application of such new geometries to the study of the spatial and temporal inhomogeneities in plasmas. A varied line-space monochromator can provide high spectral resolution and two-dimensional spatial imaging of extended plasmas at high throughput by use of only two optical elements.

# Acknowledgments

This thesis is dedicated to the teachers of my youth, who gave me the idealistic enthusiasm to pursue a life in science, and to my children Brian, Justin and Stacie who now give me the will to continue. I owe a debt of gratitude to my parents (and in memory of my mother) and my wife who stood behind me through the years to make the present effort possible.

I thank my Japanese colleagues, Prof. Kuninori Sato, Prof. Yoshiaki Kato and Prof. Hiroshi Tsunemi for their advocacy of my work and for their advice to finally obtain this Ph.D. Prof. Sato is deserved of special appreciation for all his efforts and encouragement which made this thesis application possible.

The work presented here was done over a 16 year period beginning with a spontaneous and exciting period as a 22 year old under the sponsorship of Prof. Stuart Bowyer at the Space Sciences Laboratory in Berkeley. I am thankful for this embryonic stage and academic freedom which stimulated my career in optics.

Finally, I would like to thank my many customers in the U.S. who have always been in the market for a new spectrometer, in particular Dr. Mark Bautz of MIT. Without their scientific applications and financial support, the designs presented in this thesis would not have seen the light of day.

# Table of Contents

# 1. Introduction

## *1.1 Short Wavelength Spectroscopy*

Spectroscopy is the most powerful diagnostic tool available to understand the physics of matter at high temperature. Plasmas exhibit spectral features characteristic of the constituent elements, densities, temperatures, dynamics and fields present. In astrophysics, spectroscopy has long been a crucial technique of observation. From the first Fraunhofer lines seen in the Solar spectrum to the emission lines of stellar coronae, the absorption edges of the interstellar medium, the x-ray continua of active galactic nuclei and accreting binary systems, the extreme ultraviolet continua of hot white dwarf stars, and the Doppler shifts of distant galaxies, astronomers have gained fundamental insight into the structure and evolution of stars, galaxies and even the universe at large.

Plasma conditions such as exist in the cores of stars are now being recreated in the laboratory. Short pulse laser-produced plasmas and magnetically confined plasmas reach ionization temperatures of several keV, resulting in the emission of light at short wavelengths. For example, the soft x-ray region from 0.1 keV to 2 keV in photon energy contains the K-shell transitions of B, C, N, O, F, Ne, Na, Mg, Al, Si , and P and the L-shell transitions of Cl, A, Ti, Ca, Cr, Ni, Fe and other metals. The extreme ultraviolet region from 10 eV to 100 eV additionally contains the important K-shell transitions of H, He, Li and Be as well as multiple ionization stages of all elements. Diagnosis and control of these man-made plasmas will require the use of spectrometers designed to operate from the vacuum ultraviolet to the x-ray.

Much of this instrumentation was originally developed for astronomical observations aboard sounding rockets and satellites. For example, solid state detectors, gas proportional counters and charge-coupled devices (CCDs) provide inherent spectral resolution due to the production of electrons in numbers proportional to the incident photon energy. However, the highest resolution available with these devices is approximately 50 eV for a CCD. State of the art development of calorimeter detectors has recently produced approximately 10 eV resolution, with improvement possible in the future. However, spectral resolutions of less than 1 eV are needed to unambiguously identify the physically distinct species and conditions present in laboratory plasmas. Such high resolutions can be obtained only by dispersive spectrometers.

## *1.2 Dispersive Spectroscopy Instrumentation*

Dispersion operates on the principle of division and recombination of an incident wave. The recombination results from constructive interference between the divided

components, and therefore occurs at a wavelength-dependent (dispersed) angle from the optical surface. A *crystal*, whether natural or man-made ("multilayer") *divides the amplitude* of the incident wave through reflection of only a small fraction of the intensity at each crystal plane. The resulting Bragg condition for constructive interference allows only a single wavelength to emerge, at a diffracted angle equal to the angle of incidence. In contrast a *diffraction grating divides the wavefront* among the grooves on its surface. The emerging angle of diffraction changes continuously as a function of wavelength to maintain constructive interference (a path length change of one wavelength for light divided between adjacent grooves) and therefore can produce a simultaneous *spectrum. In short, a grating multiplexes and a crystal does not.*

The earliest diffraction gratings divided the incident wavefront by simple absorption and transmission in periodic intervals. Such amplitude transmission gratings are still in use when high efficiency is not needed. Modern transmission gratings may eliminate the absorption by providing a continuous change of transmitted phase through "blazing" or shaping of the groove form. This can provide high diffraction efficiency, but is limited in use to those wavelengths at which suitably transmitting and refractive optical materials are available.

Reflection gratings consist of grooves formed as surface modulations coated with a material which is highly reflective to the wavelength of interest. The groove shape determines the distribution of energy among the diffracted wavelength spectrum. An additional capability of reflection gratings is optical focusing provided by the curvature of the optical surface. Rowland was the first to exploit this degree of freedom, in the invention of a concave grating spectrometer requiring only this single reflection[1].

In the text which follows, the term "spectrometer" or "spectroscopic instrument" refers to any instrument capable of discriminating wavelength. The more specific term "monochromator" refers to a spectrometer in which only a narrow spectral band of radiation passes through an exit slit, and the term "spectrograph" refers to a spectrometer which produces a simultaneous spectrum upon a spatially imaging detector.

To understand the properties and limitations of various design geometries using gratings, a discussion of the general conditions for image formation in diffractive optical systems is presented.

## *1.3 The Light Path Function for Diffraction Gratings*

The focusing property of gratings is understood on the basis of the phase path-length, **F**, traversed by rays impinging different regions of the grating aperture **G**:

$$\mathbf{F} = \mathbf{L} + m\,\mathbf{N}\,\lambda \qquad (1\text{-}1)$$

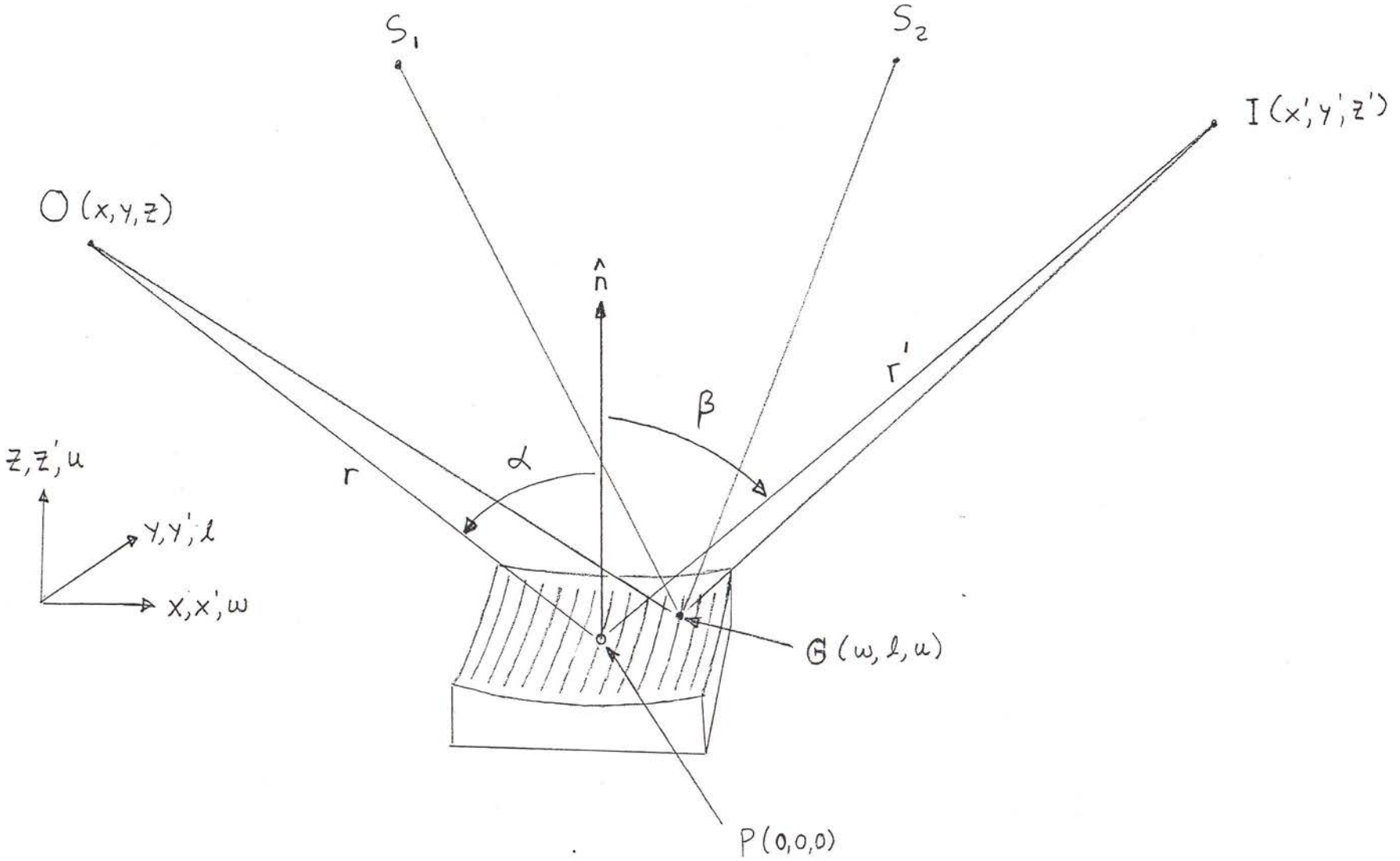


Fig. 1-1. Geometry of the light path function in Fermat analysis of diffraction gratings.

where **L** is the physical path length, m is an integer, **N** is the groove number and $\lambda$ is the wavelength of the radiation. As illustrated in Figure 1-1, $\mathbf{L} = <\mathrm{O}\mathbf{G}> + <\mathbf{G}\mathrm{I}>$ is a function of the object and image positions, O(x,y,z) and I(x',y'z') respectively, and the coordinates on the grating surface $\mathbf{G}(\omega,\ell,u)$.

Fermat's principle of least time states that constructive interference will occur at an image position for which this path-length is stationary relative to the grating aperture, or $\delta\mathbf{F}/\delta\mathbf{G} = \mathbf{0}$. Bold type denotes a function dependent upon position on the grating surface.

To facilitate analysis of the type of aberrations present, it is convenient to express these functions as power series in the grating coordinates[2]:

$$\mathbf{L} = \sum L_{ij}\, \omega^i\, \ell^j \tag{1-2}$$

In the usual case where the grating surface is a section of a sphere of radius R, and where both object and image lie within the xz plane, the series coefficients $L_{ij}$ may be written in cylindrical coordinates for the object and image positions. From Figure 1-1:

$$L_{00} = r + r' \tag{1-3}$$

$$L_{10} = \sin\alpha - \sin\beta \tag{1-4}$$

$$L_{20} = 1/2\,(\cos^2\alpha\,/r - \cos\alpha\,/R) + 1/2\,(\cos^2\beta\,/r' - \cos\beta\,/R) \tag{1-5}$$

$$L_{02} = 1/2\,(1/r - \cos\alpha\,/R) + 1/2\,(1/r' - \cos\beta\,/R) \tag{1-6}$$

$$L_{12} = -1/2\,\sin\alpha\,/r\,(1/r - \cos\alpha\,/R) + 1/2\,\sin\beta\,/r'\,(1/r' - \cos\beta\,/R) \tag{1-7}$$

$$L_{30} = -1/2\,\sin\alpha\,/r\,(\cos^2\alpha\,/r - \cos\alpha\,/R) + 1/2\,\sin\beta\,/r'\,(\cos^2\beta\,/r' - \cos\beta\,/R) \tag{1-8}$$

$$\begin{aligned} L_{40} = {} & 1/2[(\sin^2\alpha\,/r^2)(\cos^2\alpha\,/r - \cos\alpha\,/R) - 1/4(\cos^2\alpha\,/r - \cos\alpha\,/R)^2/r \\ & + 1/4(1/r - \cos\alpha\,/R)/R^2 + (\sin^2\beta\,/r'^2)(\cos^2\beta\,/r' - \cos\beta\,/R) \\ & - 1/4(\cos^2\beta\,/r' - \cos\beta\,/R)^2/r' + 1/4(1/r' - \cos\beta\,/R)/R^2] \end{aligned} \tag{1-9}$$

+ H.O.T.

where $z = r\cos\alpha$, $z' = r'\cos\beta$, $x = -r\sin\alpha$ and $x' = r'\sin\beta$. In accordance with Fermat's principle, non-zero values for the derivatives of the corresponding wavefront aberration coefficients $F_{ij}$ result in aberrant positions for the light ray relative to the intended image point I. Derivatives with respect to $\ell$ yield a *(sagittal) image height* given by

$$H = r'\,\delta\mathbf{F}/\delta\ell = r' \sum_{ij} j\, F_{ij}\, \omega^i\, \ell^{j-1} \tag{1-10}$$

and derivatives with respect to $\omega$ result in a *(meridional) spectral width* given by

$$\Delta\lambda = (d_o/m) \sum_{ij} i F_{ij} \omega^{i-1} \ell^j \qquad (1\text{-}11)$$

where $d_o$ is the groove spacing at the pole P (0,0,0).

It is useful to classify the various component terms of **F**:

$F_{00}$ = principal ray path-length.
$F_{10} = \sin\alpha - \sin\beta + m\lambda/d_o = 0$ specifies the grating equation (for the principal ray).

and the wavefront aberrations:

$F_{20}$ = defocusing.
$F_{02}$ = astigmatism .
$F_{30}$ = (meridional) coma
$F_{12}$ = astigmatic (sagittal) coma .
$F_{40}$ = spherical aberration.

## a) The Focusing Conditions of Classical Spherical and Plane Gratings

A classical grating is one consisting of straight and parallel grooves spaced by equal intervals in the xy plane (along the chord of **G**). This constraint is based on practical limitations of the mechanical motions inherent in the historical manufacture of gratings. We therefore substitute $\mathbf{N} = \omega/d_o$ in equation (1-1), which appears only in the grating equation term ($F_{10}$). With this constraint, Rowland[1] found that both defocusing and meridional coma are absent for a concave grating if the object (typically a slit), grating center, grating center of curvature and spectral image are disposed on the same circle, thus:

$$r = R \cos\alpha \qquad \text{and} \qquad r' = R \cos\beta \qquad (1\text{-}12)$$

To alter the wavelength in a Rowland circle spectrometer, at least one of the optical elements (slit, grating, slit/detector) must move along the circle, so as to change the angle of incidence or diffraction in the grating equation. While this motion requires high mechanical accuracy and results in a change in direction of the principal ray, geometries based on this classical grating have dominated the field of spectroscopic instrumentation since their inception over a century ago, due to their inherent high spectral resolution.

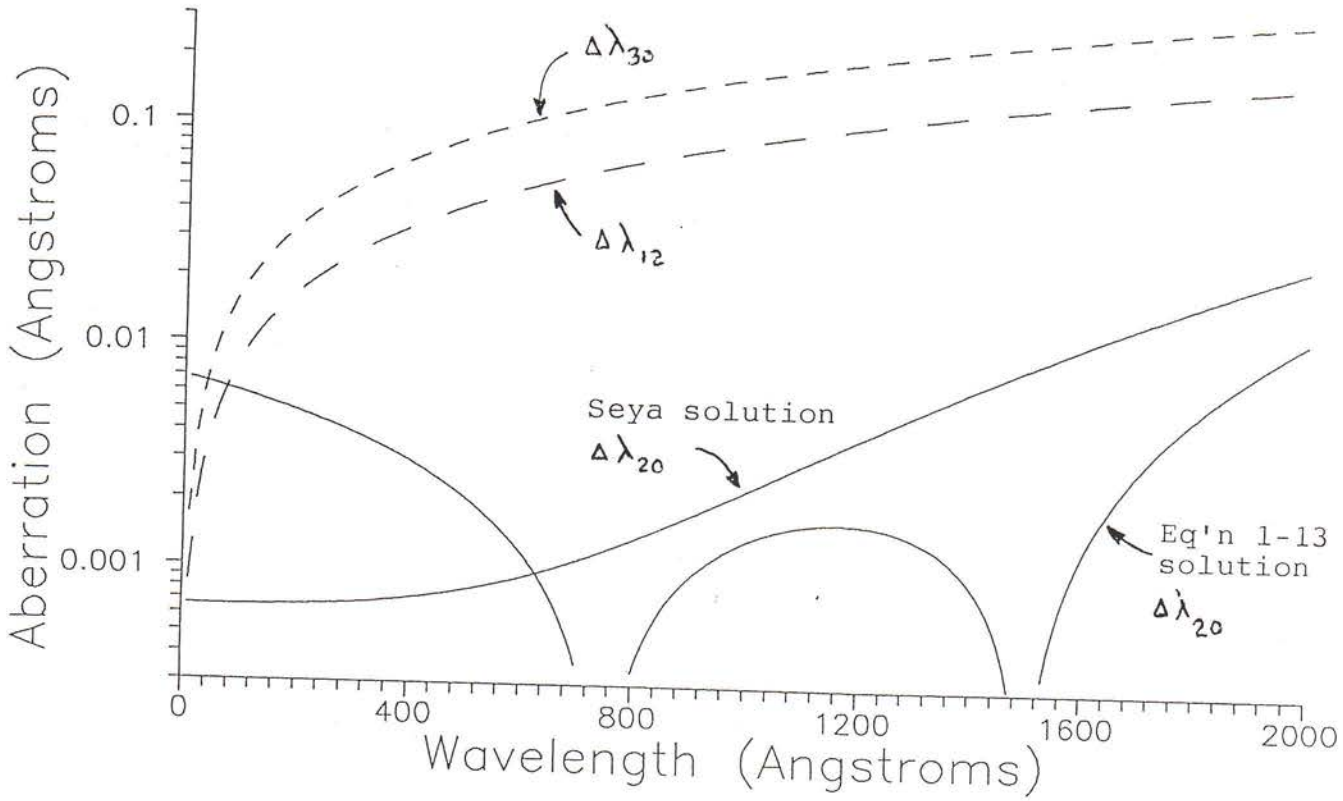


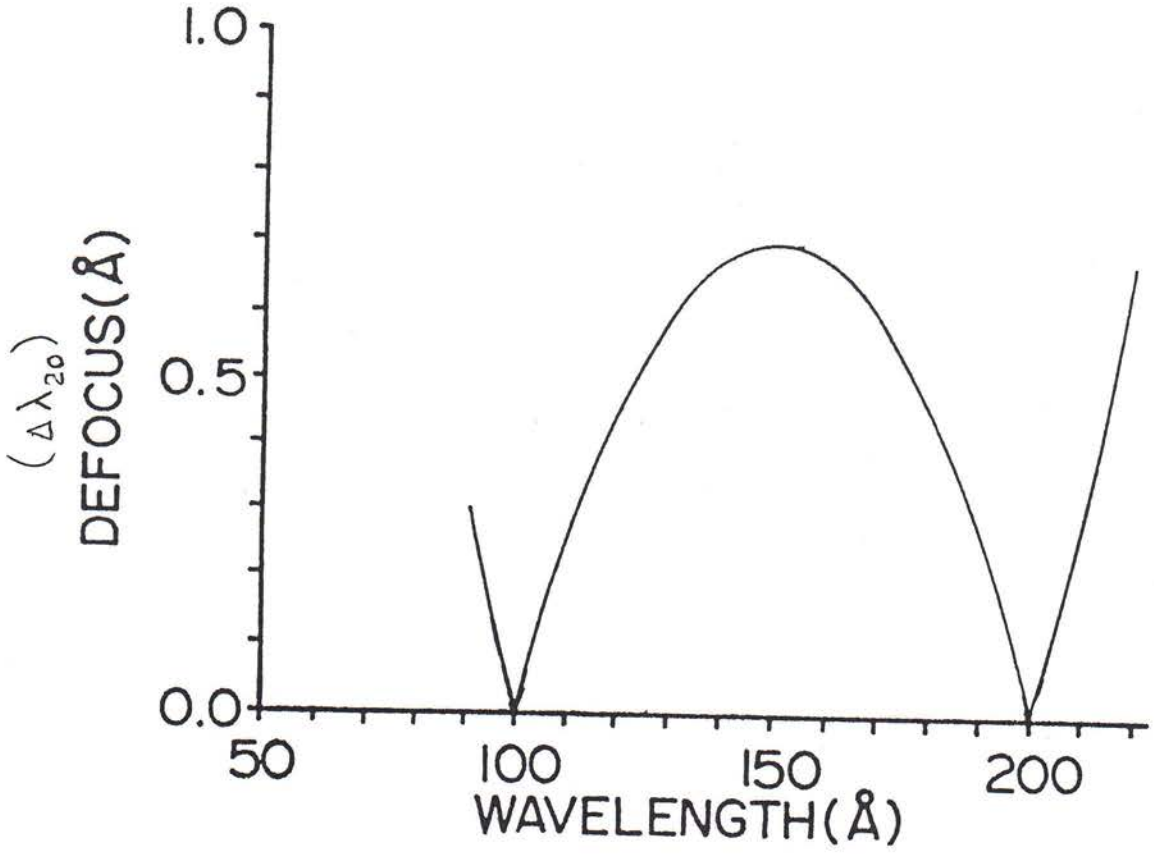


Fig. 1-2. Fermat calculated extremum spectral aberrations upon pure rotation of classical grating: a) near-normal incidence ($2\theta = 70.5^{o}$) coma $\Delta\lambda_{30}$, astigmatic coma $\Delta\lambda_{12}$, and de-focusing $\Delta\lambda_{20}$; b) grazing incidence ($2\theta = 164^{o}$) de-focusing.

In the more favorable laboratory configuration where the object, grating center and image are fixed in space, there are insufficient degrees of freedom available to simultaneously correct for even the lowest order wavefront aberrations present in equations (1-5) through (1-8). When such a concave grating purely rotates about the y-axis to change the wavelength diffracted to the image position, only the object distance, image distance and included angle ($2\theta = \alpha + \beta$) may be chosen independently in an attempt to minimize the wavefront aberrations. At normal or near-normal angles of incidence, this does allow for high resolution. For example, in the Seya monochromator[3,4] an angle of $2\theta = 70.5°$ and $r = r' = R/1.2245$ results in the removal of $F_{20}$ along with its first and second derivatives with respect to wavelength at a wavelength of zero. Figure 1-2a shows the defocusing, coma and astigmatic coma aberrations for a Seya monochromator having a 15 x 15 $mm^2$ grating aperture (30 mrad x 30 mrad), 1/d = 1200 grooves/mm and R = 500 mm. While the actual resolution may also be limited by slit widths, the geometrical aberrations allow for a spectral resolving power ($\lambda/\Delta\lambda$) of order 10,000 over most of the indicated range.

High resolution may also be obtained at two scanned wavelengths, for any $2\theta$, by forcing $F_{20} = 0$ at the two corresponding pairs of $(\alpha,\beta)$. This requires the following choice for r and r':

$$r/R = (\cos^2\beta_2\cos^2\alpha_1 - \cos^2\beta_1\cos^2\alpha_2) / [\cos^2\beta_2(\cos\alpha_1 + \cos\beta_1) - \cos^2\beta_1(\cos\alpha_2 + \cos\beta_2)] \quad (1\text{-}13)$$

$$r'/R = (\cos^2\beta_2\cos^2\alpha_1 - \cos^2\beta_1\cos^2\alpha_2) / [\cos^2\beta_1(\cos\alpha_2 + \cos\beta_2) - \cos^2\beta_2(\cos\alpha_1 + \cos\beta_1)]$$

This solution is also shown in Figure 2a, using the same input parameters of grating size, groove density, radius and included angle. However, if the included angle increases towards grazing incidence ($2\theta$ approaching $\pi$), the defocusing rises abruptly between the two correction wavelengths. For example, with input parameters of $2\theta = 164°$, R = 10 meters, 1/d = 1500 grooves/mm and a 65 mm meridional grating aperture (approximately 6 mrad), Figure 1-2b reveals that the defocus aberration is 0.7 Angstroms at a wavelength of 150 Angstroms. This is a resolving power of only approximately 200, which is insufficient for high resolution spectroscopy of plasmas. The difference between a resolving power of 10,000 at normal incidence and 200 at grazing incidence dramatically illustrates the limitations of extending normal incidence techniques to grazing incidence.

Of coarse, defocusing could be corrected by translating the grating along the bisector of the included angle, analogous to the classical normal incidence Johnson-Onaka mounting[3,5,6]. However, at grazing incidence such translation must be in a direction approximately *normal* to the incident and diffracted rays and hence causes a direct and

significant change in the beam directions. The amount of the change is typically comparable or larger than the illuminated aperture itself, requiring both the source and the detector to move as a function of wavelength.

Classical plane gratings correspond to setting R = infinity in the above equations. This results in the absence of focusing power, thus additional optics (typically mirrors) must be used. In the classical configuration, pre-collimating and post-focusing mirrors move the grating object point and image points, respectively, to infinity (r = r '= infinity)[7]. Such systems are common in the visible and ultraviolet region of the spectrum, however when used at shorter wavelengths they suffer from reduced efficiency due to the large number of reflections, and reduced resolution due to aberrations of the grazing incidence mirrors.

## b) Toroidal Gratings and Astigmatic Coma

In addition to narrow spectral widths, many spectroscopic diagnoses require imaging in the non-dispersive (sagittal) direction which lies along the length of the slit. This requires removal of the astigmatic term $F_{02}$, a condition referred to as *anastigmatism*. The more stringent condition in which both first degree aberrations (astigmatism and defocusing) are absent is referred to as *stigmatism*. The point-like spectral images produced by a stigmatic instrument are useful when the brightest irradiation is required upon a sample (e.g. photo-electron or fluorescence spectroscopy) or when the target or source must be spatially imaged. The latter requirement is particularly important in the case of plasma diagnostics.

However, from equation (1-6), the spherical grating exhibits astigmatism at all angles except the spectroscopically useless case of $\alpha = \beta = 0$. As the incidence and diffracted angles increase, the focusing power of a sphere increases in the meridional direction (resulting in shorter spectral focal lengths), but diminishes in the sagittal direction (resulting in longer sagittal focal lengths). The result is that the astigmatism of a grazing incidence spherical grating is approximately equal to the unencumbered size of the linearly expanding incident beam.

The classical solution to this problem is to provide different radii of curvature in the meridional and sagittal directions of the grating. Such toroidal surfaces allow the adjustment of focusing in the two directions. For example, if the grating surface is shaped as a section of a bicycle-tire, with major radius R and minor radius $R_S$, then equations (1-5), (1-8) and (1-9) remain unchanged to describe the meridional aberrations and equations (1-6) and (1-7) are modified by substituting $R_s$ for R. The result is that astigmatism of the bicycle-tire toroid is absent if the minor radius is[8]:

$$R_S = (\cos \alpha + \cos \beta) / (1/r + 1/r') \qquad (1\text{-}14)$$

which in combination with the Rowland circle condition becomes simply:

$$R_s / R = \cos\alpha \cos\beta \qquad (1\text{-}15)$$

Therefore, the ratio of the radii is equal to the square of the nominal graze angle. Such a small minor radius has the unfortunate effect of significantly increasing another aberration, that of astigmatic coma. From equation (1-7), this becomes[9]:

$$\Delta\lambda_{12}/\lambda = \text{T.F.} \times ( 8 f_y^2 )^{-1} \qquad (1\text{-}16)$$

where

$$\text{T.F.} = (1 - \cos^2\alpha /\cos^2\beta)/(1 - \sin\beta /\sin\alpha)$$

and where $f_y = 1/\Phi_y = r'/(\ell_{max}-\ell_{min})$ is the sagittal speed of the beam. For example, if $\alpha$ = 86° and $\beta$ = 88°, the factor T.F. = 1640. If the beam speed is 100 ($\Phi_y$ =10 mrad), then the spectral resolution is only 1 part in 50. Such large amounts of astigmatic coma have been the cause of the low spectral resolution attained with toroidal grating spectrometers. The solution to this problem is therefore another critical ingredient in the new designs which will be shown to provide high spatial resolution without sacrifice of spectral resolution at grazing incidence.

## c) Holographic Gratings

In the visible and near ultraviolet, coherent light sources (lasers) have previously been used to record interference fringes as the grooves of gratings commonly referred to as "holographic gratings"[10]. As the interference fringes in general are curved and non-equidistant, the groove density (1/**d**) becomes a function of the 2-D coordinates on the grating aperture. This degree of freedom can be used to provide phase path-length corrections to the aberration terms given above. If as illustrated in Figure 1-1, point recording sources $S_1$ and $S_2$ of wavelength $\lambda_S$ are used, then the groove number for the resulting holographic aberration-corrected grating is:

$$\mathbf{N} = [ < S_1\mathbf{G} > - < S_2\mathbf{G} > - ( < S_1P > - < S_2 P > ) ] / \lambda_S \qquad (1\text{-}17)$$

Such gratings are commercially available, and have been used to improve the spectral and spatial resolution of a number of visible and ultraviolet spectrometers. However, because the groove patterns produced are characteristic of the recording wavelength, holographic gratings manufactured using visible and near UV laser are incapable of significantly reducing aberrations of gratings operating in the extreme ultraviolet and soft x-ray regions of the spectrum. For use at such short wavelengths and in grazing

incidence geometries, it is absolutely necessary to provide additional freedom in the placement of grooves on the grating surface.

### d) Varied Line-Space Gratings

In nomenclature which has since become common, a varied line-space (VLS) grating is a design in which the groove positions are relatively unconstrained, yet possess sufficient symmetry to permit a mechanical ruling[11].

Consistent with the power series formalism adopted for the light-path function, the groove number can then be specified as a polynomial in the ruled width coordinate $w$:

$$\mathbf{N} = \Sigma_i \, N_i \, w^i \tag{1-18}$$

where $N_1$ is the groove density ($\rho_o = 1/d_o$) at the pole and where $N_i$ ( i = 2, 3, etc.) may be positive or negative values. The local groove density, projected onto the xy plane, may therefore also be represented by a polynomial in $w$:

$$1/\mathbf{d} = \Sigma_i \, \rho_{i-1} \, w^{i-1} \tag{1-19}$$

where

$$\rho_{i-1} = i \, N_i$$

Substitution of equation (1-18) into equation (1-1) enables a high level of aberration correction, through insightful choice of the ruling coefficients ($\rho_1$, $\rho_2$, $\rho_3$, etc.) to balance the path-length aberrations in particular geometries.

The above formalism provides a framework in which the new designs presented in this work can be analyzed and compared. However, because of the unconventional geometries developed, it will be necessary to extend the above formalism in subsequent discussions of particular designs. This will include the use of virtual object points ($r < 0$) in conjunction with plane gratings (R = infinity), off-plane gratings (y not equal to 0) with non-parallel grooves (**N** = function of $w$ and $\ell$), a translating grating pole (P = function of $\lambda$) and grating rotation about the z-axis (effective **N** = function of $\lambda$).

## *1.4 Grazing Incidence Reflection*

The need for grazing incidence is based upon the reflection efficiency of optical surfaces, which is given by the Fresnel coefficients[12,13]:

$$R_\sigma = [ ( a - \cos \phi )^2 + b^2 ] / [ (a + \cos \phi )^2 + b^2 ] \qquad (1\text{-}20)$$

for the intensity of the polarization component having its electric field normal to the plane of incidence, and

$$R_\pi = R_\sigma \; [ (a - \sin \phi \tan \phi)^2 + b^2 ] / [ (a + \sin \phi \tan \phi)^2 + b^2 ] \qquad (1\text{-}21)$$

for the parallel component, where

$$2a^2 = [ ( n^2 - k^2 - \sin^2\phi )^2 + 4n^2k^2 ]^{1/2} + ( n^2 - k^2 - \sin^2\phi ), \qquad (1\text{-}22)$$
$$2b^2 = [ ( n^2 - k^2 - \sin^2\phi )^2 + 4n^2k^2 ]^{1/2} - ( n^2 - k^2 - \sin^2\phi ), \qquad (1\text{-}23)$$

$\phi$ is the angle of incidence as measured from the surface normal and $n + ik$ is the complex optical index of refraction of an assumed opaque coating.

The index of refraction may be related to physical quantities as follows:

$$2 ( 1 - n ) = ( r_e N_a f_1 / \pi ) \lambda^2 \qquad (1\text{-}24)$$

$$2 k = ( r_e N_a f_2 / \pi ) \lambda^2 \qquad (1\text{-}25)$$

where $r_e$ is the classical electron radius $e^2/(m_e c^2) = 2.82 \times 10^{-13}$ cm, $N_a$ is the number density of atoms, $f_1 + if_2$ is the complex scattering factor as given by Henke[13] and $\lambda$ is the wavelength of the incident radiation.

In the limit of normal incidence ($\phi = 0$) and in the absence of absorption ($k=0$), equations (1-20) through (1-23) degenerate into the classical reflection coefficient at a dielectric interface:

$$R = ( n - 1 )^2 / ( n + 1 )^2 \qquad (1\text{-}26)$$

As the wavelength decreases, equation (1-24) indicates that the refractive index becomes smaller than and asymptotically approaches unity, resulting in:

$$R = ( n - 1 )^2 / 4 \qquad (1\text{-}27)$$

which in physical units becomes:

$$R = ( r_e N_a f_1 / 4\pi )^2 \; \lambda^4 \qquad (1\text{-}28)$$

In the limiting case of unbound electrons, Drude theory results in a real scattering factor $f_1$ equal to the atomic number Z of the atom, hence the product $N_a f_1$ is the number density of electrons in the material, $N_e$. In this case, valid when the radiation wavelength is much smaller than the plasma wavelength ($\lambda_{pl} = c/\upsilon_{pl}$), equation (1-24) becomes simply $(\lambda/\lambda_{pl})^2$, and the normal incidence reflectance is $[\lambda/(2\lambda_{pl})]^4$. Having a high electron density ($4.66 \times 10^{24}$ cm$^{-3}$) gold has a high plasma frequency and is thus one of the best reflectors over the broadband at short wavelengths. This numerically results in the approximation $R \sim 1.1 \times 10^{-10} \lambda^4$, where the wavelength is in Angstrom units. Because this equation neglects absorption features, it is valid only to within an order of magnitude, yet correctly indicates that the normal incidence reflectance drops rapidly and becomes small (<10%) below several hundred Angstroms. For example, at a wavelength of 10 Angstroms, it indicates a reflectance of order $10^{-6}$. Exact use of the Fresnel equations and the optical constants tabulated by Palik[12], including the absorption term k, results in more precise reflectance values. As plotted in Figure 1-3, these are well fit by the power law:

$$R = 1.27 \times 10^{-10} \lambda^{3.48} \tag{1-29}$$

Exhibiting a normal incidence reflectance of approximately $10^{-3}$ at 100 Angstroms and essentially immeasurable ($2 \times 10^{-7}$) at 10 Angstroms, the situation becomes hopeless.

To remedy this problem, one may exploit the fact that the refractive index of materials in the soft x-ray region is slightly less than that of the incident (vacuum) medium, that is slightly less than 1. As given by Snell's law, this results in an angle of refraction into the medium, $\phi_n = \arcsin [ ( \sin \phi ) / n ]$, which is *larger* than the angle of incidence $\phi$. Therefore, there exists a critical angle of incidence

$$\phi_{critical} = \arcsin ( n ) \tag{1-30}$$

for which the refracted wave is evanescent (propagates along the surface), resulting in a rise in the amplitude of the reflected wave. Such a discontinuity is also evident from the Fresnel coefficient (1-20), which in the case of a non-absorbing medium can be rewritten as:

$$R_\sigma = [( n^2 - \sin^2\phi )^{1/2} - \cos \phi]^2 / [( n^2 - \sin^2\phi )^{1/2} + \cos \phi ]^2$$

$$= \sin^2 ( \phi - \phi_n ) / \sin^2 ( \phi + \phi_n ) \tag{1-31}$$

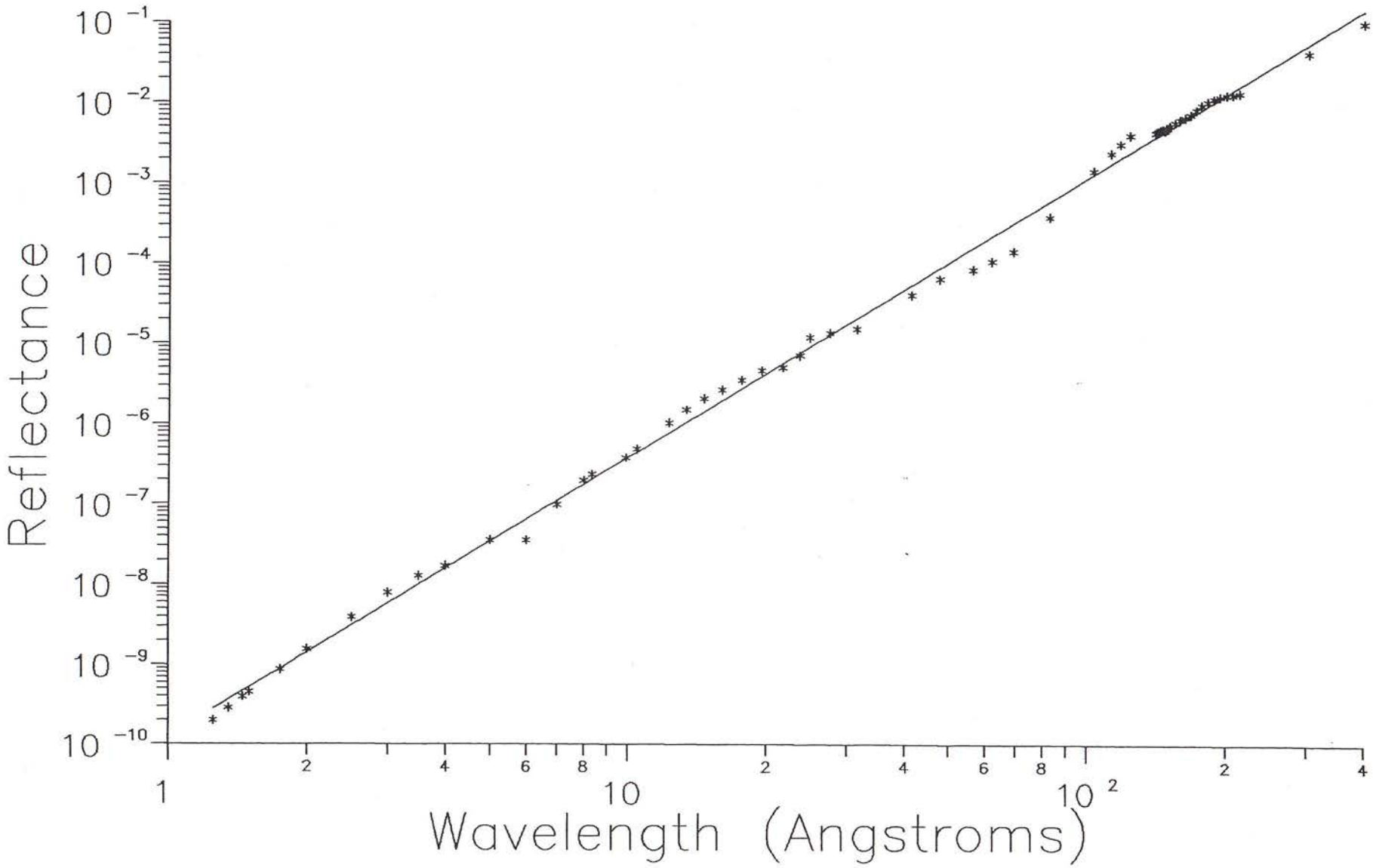


Fig. 1-3. Normal incidence reflectance of opaque gold at short wavelengths.

This ideal case would result in total external reflection (R = 1) at $\phi=\phi_{critical}$ where $\phi_n = \pi/2$.

Defining the graze angle $\gamma = \pi/2 - \phi$, equation (1-30) can be expressed in physical quantities:

$$\gamma_{critical} \sim \cos\phi \sim [\, 2\,(\,1 - n\,)\,]^{1/2} \qquad (1\text{-}32)$$

$$\sim (\, r_e N_e / \pi\,)^{1/2}\, \lambda \qquad (1\text{-}33)$$

Substituting the constants and the electron density for gold, we have

$$\gamma\ (\text{degrees}) \sim 0.37\ \lambda\ (\text{Angstroms}) \qquad (1\text{-}34)$$

Due to the presence of finite absorption, the actual reflectance is not 100% at this angle, but typically exceeds 50% within a graze angle approximately two times shallower. For example, at Al-$K_\alpha$ (8.34 Angstroms), the critical angle calculated from equation (1-34) is approximately 3.1°, and using measured values of n = 0.999085 and $k=3.1\times10^{-4}$ in the Fresnel equations results in the reflectance plot of Figure 1-4 showing a 50% reflectance at an angle of 1.9°.

To obtain accurate reflectance curves as a function of wavelength, the measured values of the complex optical constants given by Palik[12] are used with equations (1-20) through (1-24). Figure 1-5 plots the unpolarized reflectances of opaque gold at various graze angles from the x-ray to the infrared. A reflectance of 50% requires a graze angle of approximately 10° in the extreme ultraviolet and 2° in the soft x-ray. To obtain usable reflectance at Cu-K (1.54 Angstroms) in the x-ray would require a graze angle of 1/2°.

As shown in Figure 1-5, the normal incidence reflectance of gold does not approach 100% until the wavelength exceeds approximately 5000 Angstroms. Therefore coatings such as aluminum are commonly used to provide high reflectance in the ultraviolet. However, even when coated with a protective overcoating of $MgF_2$ or LiF, the normal incidence reflectance of aluminum drops rapidly below approximately 1000 Angstroms. It is in this short wavelength region where coatings with high atomic number, such as gold, are superior.

## *1.5 Prior Soft X-Ray Grating Spectrometers*

Prior to this work, begun in 1981, short wavelength grating spectrometers were based almost exclusively on classical plane and concave gratings. Astronomical spectrographs employed transmission gratings[14,15] in combination with grazing incidence telescopes, or

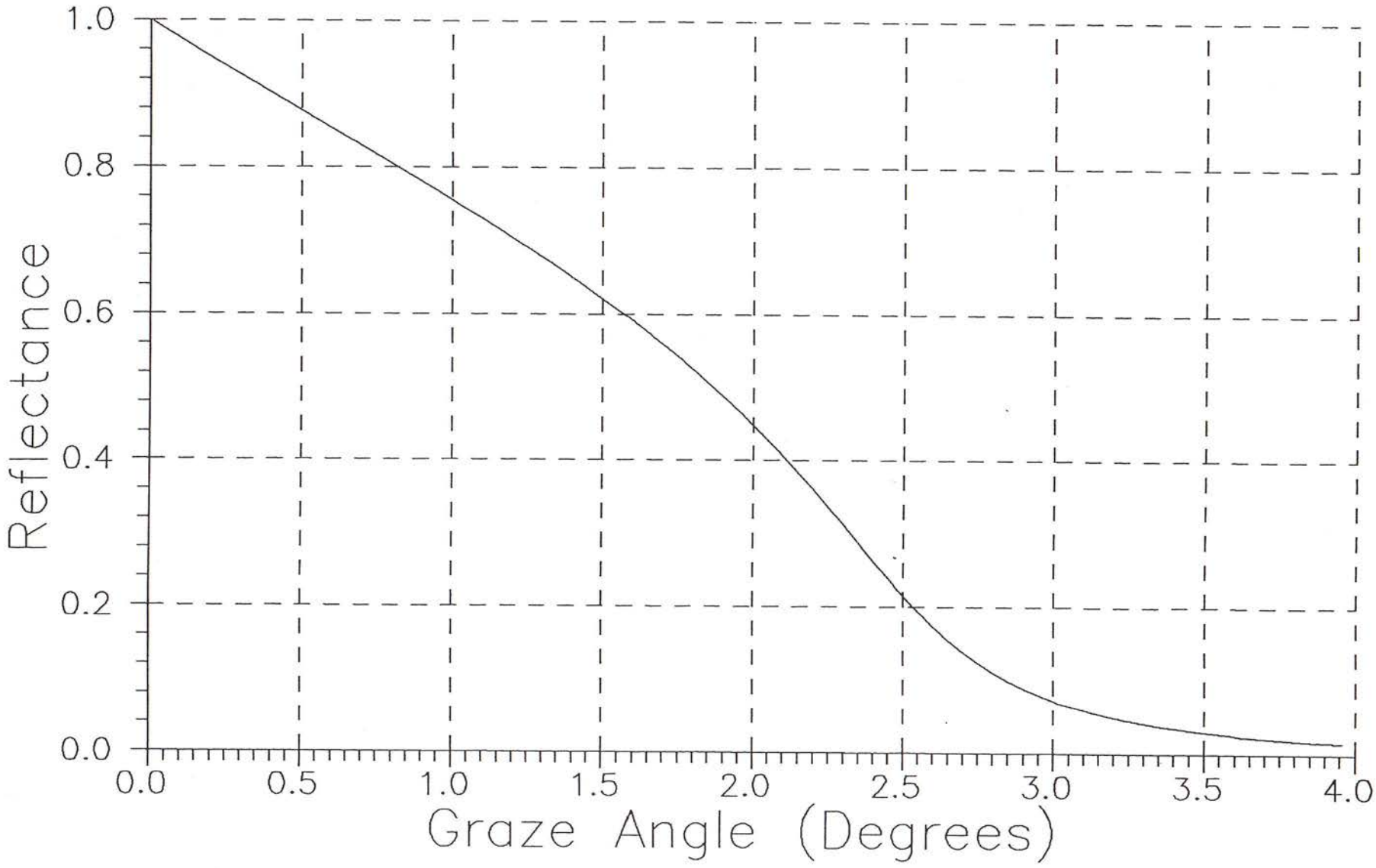


Fig. 1-4. Reflectance rise at 8.34 Å near the critical graze angle for gold.

Fig. 1-5. Unpolarized reflectance of opaque gold at graze angles from 0.5° to normal incidence and wavelengths from the infrared to the x-ray.

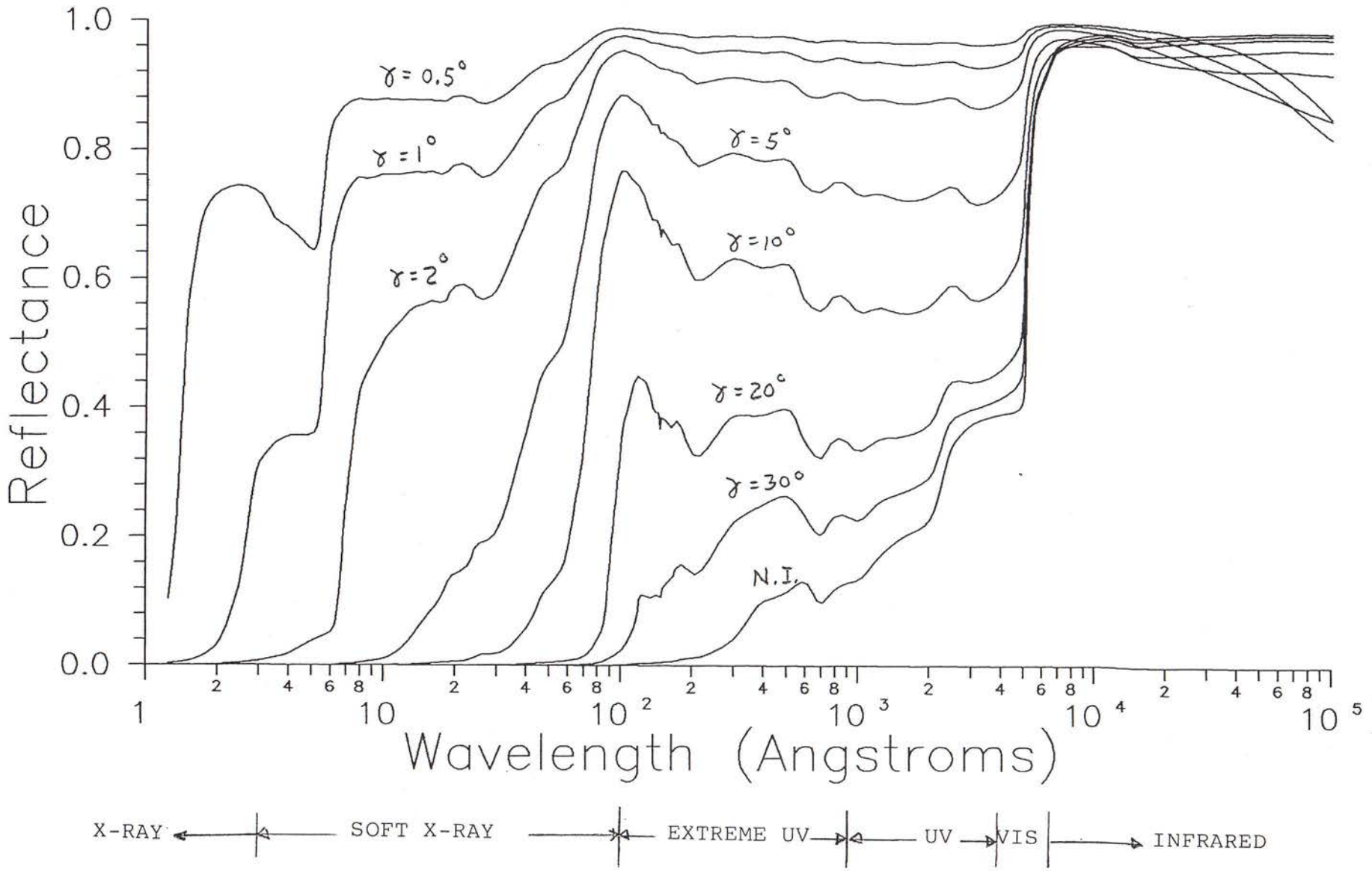

used Rowland circle gratings[16,17]. Commercial spectrometers available for high resolution use at these wavelengths were of the movable-slit Rowland circle type[18,19]. Stigmatic designs typically obtained only low spectral resolution by use of aspherical mirrors or toroidal gratings either classically ruled[8] or recorded holographically[20]. High resolution fixed slit designs required multi-reflection systems having various sophisticated mechanical motions, and were based on classical plane gratings[21-23] or classical concave gratings operating on the Rowland circle[24]. Varied spacing had just started to become available, and was first applied to reduce the aberrations of classical designs, such as the coma and astigmatism of the Seya monochromator[25]. The potential of varied spacing or other new geometries to provide high resolution at grazing incidence was in its infancy, and viewed with skepticism by the mainstream in optics instrumentation.

However, the use of increasingly sophisticated and immovable sources of radiation and detection placed and continues to place new and severe demands on the geometrical properties of the diffraction grating. In addition to the desire for high spectral, spatial and temporal resolution, there is a general requirement for both the source and detector to remain stationary as wavelength is adjusted, and for the detector to lie at a normal angle to the radiation. Furthermore, to obtain useful throughput, a soft x-ray spectrometer must minimize the absorption losses by using a small number of grazing incidence reflections.

Such small graze angles are found to severely degrade the imaging properties of optical systems designed for normal incidence illumination. For example, when the Rowland circle is used at grazing incidence, the slit(s) or detector must translate accurately over very long distances, resulting in large astigmatism and the inability to use stationary sources and detectors. In addition, the focal surface is also illuminated at a grazing angle, resulting in low detection efficiency and narrow bandpasses available with small high resolution electronic detectors.

In the past, when a particular short wavelength application arose, researchers revised such mature and familiar designs as the classical plane grating / focusing mirror and the Rowland circle, in order to provide acceptable performance at grazing incidence. Such an adaptive approach resulted in several clever yet complex optical and mechanical systems. These all require auxiliary optics to maintain high resolution in the case when stationary slits must be used. Such complications have compromised both the theoretical and practically attained performance of such grazing incidence systems.

In contrast, the approach taken in this work has been to develop reflective grating systems specifically for grazing incidence, starting with no classical design constraints. Beginning with the intuitive geometrical concept behind each design, the following sections will explain the theoretical and experimental development of these fundamentally new geometrical solutions to the problem of providing high resolution spectroscopy at grazing incidence.

*"J'ai en vue les erreurs systematiques qui produisent un changement de foyer sans alterer la nettete des images."*

Cornu, 1875.

# 2. Variable Line-Space (VLS) Plane Grating Spectrometers

## *2.1 The Extreme Ultraviolet Explorer Spectrograph*

In 1981, NASA commissioned a study[26] to investigate options for including spectroscopy to an imaging mission (The Extreme Ultraviolet Explorer, or "EUVE") designed to survey the entire sky in the largely unexplored wavelength region $\lambda \sim 100$-912 Angstroms. To perform useful science, yet have minimal impact upon the original mission, the following requirements were to be met by candidate spectrometer designs:

1) Collection of incident light using a single 40 cm diameter grazing incidence telescope.
2) Maximum length of 150 cm, including the telescope and spectrometer.
3) Simultaneous spectral coverage from 100 to 600 Angstroms.
4) $\lambda/\Delta\lambda > 100$, including the blurring due to a satellite jitter of 1 arc-minute.
5) Use of micro-channel plate detectors having 50 mm aperture and 100 micron pixels.
6) A minimum detectable flux $< \sim 5 \times 10^{-27}$ erg/cm$^2$/sec/Hz for 12 hours of observation.
7) No moving components.

These severe constraints precluded the use of any known spectrometer geometry. Transmission grating spectrographs were studied and found to have unacceptably low dispersion and low efficiency. Concave gratings were found to violate the length constraint, due to the need for an entrance slit at the focus of the telescope. In addition, the astigmatic spectral images from a concave grating at grazing incidence would contain high background from diffuse nightglow features in the earth's upper atmosphere, making the sensitivity unacceptable. An exhaustive search revealed that all existing or proposed spectrometers were incapable of simultaneously meeting all of the above requirements. This prompted the author to design a new grating spectrograph for inclusion aboard the EUVE satellite.

### a) Basic Concept and Fermat Analysis

It is well known that the grating equation derives from finding the angle to which a locally plane wave will be diffracted if adjacent grooves are to provide a constructive interference pattern at the chosen wavelength. This requires simply that the product of the groove spacing along the surface tangent times the difference in the sines of the angles of incidence and diffraction equals an integer number of wavelengths. Indeed, the grating equation can be used alone, without use of Fermat's principle, to determine the aberrations by simply determining the direction of the diffracted ray at each point on the grating surface. Such *raytracing* uses the angles of incidence and diffraction as measured relative to the **local** surface normal and the groove spacing measured along the **local** surface tangent. When expressed in this way, the local groove spacing varies across the surface of even so-called "equidistant" groove classical gratings. This is because

This is because grooves spaced equally on the chord of, for example, a concave spherical grating, are not equally-spaced along the varying slopes of the surface tangent. The *ab-initio* use of such local variations in the spacing to determine the Rowland circle or other classical object and image locations begs the question: "*Why not* ***invert*** *this procedure and, starting with desirable object and image locations, determine the required local groove spacings ?*" This results in simply an **inverted grating equation**[27]:

$$\mathbf{d}(w) = m\,\lambda_o \,/\, [\,\sin\beta(w) - \sin\alpha(w)\,] \qquad (2\text{-}1)$$

where $\lambda_o$ is any chosen value of a correction wavelength, and where the groove spacing and angles of incidence and diffraction vary across the grating aperture. In this equation, **d** is a function only of $w$, hence the grooves are assumed to be straight and parallel. The spacings **d** vary continuously (groove-to-groove) across the meridional section in order to maintain adherence to the inverse grating equation and thus constructive interference at the image. This varied line-space (VLS) grating technique allows the degree of freedom to select the focal length of the grating independent of the object distance.

Consider a plane grating surface (R = infinity) positioned in the ***converging*** beam from the EUVE telescope, as illustrated in Figure 2-1. Such a position is necessary to obey the length constraint described above. In zero order, the grating acts as a plane mirror, diverting the telescope focus without aberration to the point denoted m=0. By force of equation (2-1), all first order rays of wavelength $\lambda_o$ illuminating the grating along line AB are brought to a meridional (spectral) focus without aberration ($F_{i0} = 0$ for all i). In addition, if the distance from this focus to the grating midpoint P is set equal to the distance $r_o$ from that midpoint to the virtual object produced by the telescope, then all rays $\lambda_o$ illuminating the central groove CD have the same path-length and therefore are also brought to this point focus. In this way, astigmatism and higher order astigmatism is also removed ($F_{0j} = 0$ for all j). The only aberrations possible at $\lambda_o$ are mixed terms $F_{ij}$ where neither i nor j equals 0. The magnitudes of these wavefront coefficients are obtained by expansion[28] of the geometrically determined path-length distances per Sec. 1.3:

$$F_{12} = (\sin\beta_o - \sin\alpha_o) / (2\,r_o^2) \qquad (2\text{-}2)$$

$$F_{22} = 3\,(\sin^2\beta_o - \sin^2\alpha_o) / (4\,r_o^3) \qquad (2\text{-}3)$$

$$F_{15} = -3 / (8\,r_o^4) \qquad (2\text{-}4)$$

$$+ \text{H.O.T.}$$

Differentiating **F** to convert these wavefront aberrations into spectral aberrations using equation (1-11), we have for the dominant aberration of sagittal coma ($F_{12}$):

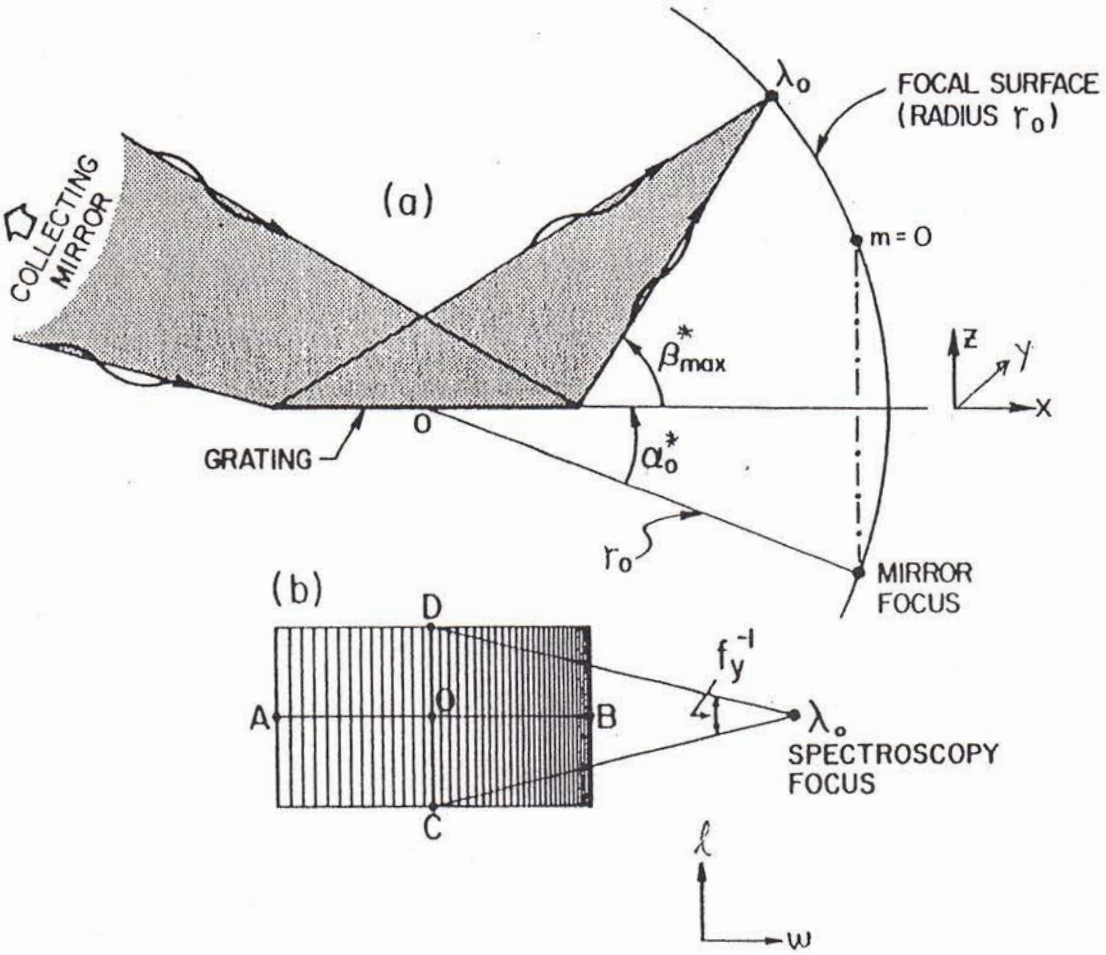


Fig. 2-1. Geometry of variable line-space plane grating spectrometer. Collecting mirror is upstream of the converging beam: (a) projection upon the dispersion plane; (b) grating plane having variably spaced straight grooves.

$$\Delta\lambda_{12} / \lambda = (8 f_y^2)^{-1} \qquad (2\text{-}5)$$

where $f_y$ is the sagittal beam speed as defined previously. Comparing the sagittal coma aberrations of equations (2-5) for the VLS plane grating and equation (1-16) for the classical toroidal grating, one finds a reduction by the factor T.F. Given the previous example of $f_y = 100$ now results in a spectral resolution of 1 part in $8 \times 10^4$, which is a factor of 1640 improvement over the 1 part in 50 obtained with the toroidal grating! This is due to the converging beam geometry of the present design, in which removal of astigmatism is provided by the upstream (telescope) optic and hence the grooves are not curved. In the case of EUVE, the fast incident beam ($f_y = 6.24$) results in an astigmatic coma of 1/310 in wavelength, from the extreme corners of the grating.

Using equation (1-10) to convert the limiting wavefront aberration to a sagittal image height, we have:

$$H = r_o (m \lambda_o / s_o) / (2 \cos\alpha_{min} f_x f_y) \qquad (2\text{-}6)$$

where $f_x$ is the incident meridional beam speed [$f_x = 1/(\cos\alpha_{min} - \cos\alpha_{max}) = 1/\Phi_x$].

Because of the plane surface, the reflected zero order image is at a distance from the grating equal to that of the telescope focus. As this results in equal focal lengths for the zero order image and the correction wavelength $\lambda_o$, it is intuitively obvious that the focal length cannot change significantly between or near these two constrained points. Therefore, the focal surface for highest spectral resolution (meridional focii) must be nearly perpendicular to the diffracted rays. This is desirable to provide high detection efficiency for devices such as the micro-channel plate, and to minimize the required detector aperture. The magnitude of the aberrations for wavelengths other than $\lambda_o$ have been determined through light-path function analysis[28] and the precise functional form of the meridional focal surface has also been determined[11,37] [Sec. d) below]. The focal surface for minimum sagittal aberrations is clearly the circle of radius $r_o$ centered on the grating pole and passing through both stigmatic correction points. The astigmatism is zero for all wavelengths imaged on this anastigmatic focal circle.

The use of straight and parallel grooves greatly facilitates the manufacture of this VLS grating, allowing the use of mechanical ruling engines. In addition, the plane grating surface provides for the lowest possible scattering and most uniform groove profile across the aperture, as there are no slope changes which could result in undesirable variations to the groove depth and shape during ruling[25] by a tool in fixed orientation.

## c) Off-Plane Version (Fan Grating)

Consider placing the virtual object at non-zero values of y, that is out of the dispersion xz-plane of Figure 2-1. To produce a path-length difference between adjacent grooves, dispersion still occurs only normal to the grooves, that is within the xz-plane. Furthermore, since there is no path-length difference and hence no dispersion in the direction along the length of a groove, there must be symmetry about this direction, resulting in the diffracted rays being dispersed onto the surface of a cone whose axis of symmetry is the diffracting groove. This three-dimensional case is therefore known as *off-plane* or *conical* diffraction, resulting in a generalized version of the grating equation[29]:

$$m\lambda/\mathbf{d} = (\sin\beta - \sin\alpha)\ \sin\gamma \qquad (2\text{-}7)$$

where $\gamma$ is the complement of the off-plane angle, and therefore is measured relative to the grating surface tangent. The half-apex angle of the dispersion cone is thus equal to $\gamma$, and the linear dispersion along the arc of this cone is obtained by simply differentiating equation (2-7) and multiplying by the focal length **r'**:

$$d\mathbf{s}/d\lambda = \mathbf{r'}\ (\Delta\beta \sin\gamma) / \Delta\lambda = m\,\mathbf{r'} / (\mathbf{d}\cos\beta) \qquad (2\text{-}8)$$

To maintain focus across the grating aperture requires that this linear dispersion is constant. If we consider the central groove CD in Figure 2-1, then the angle of diffraction ($\beta$) must be unchanged, simplifying the focusing condition to imply a constant value of **r'/d**. This ratio is intuitively correct, as it represents a constant product of the lever arm distance and the angular dispersion on the cone. The variation in **r'** is almost linear with $\ell$:

$$\mathbf{r'}/r'_o = [\ 1 + 2\,(\ \ell / r'_o)\cos\gamma_o + (\ \ell/r'_o)^2\ ]^{1/2}$$

$$\sim\ 1\ +\ (\ \ell / r'_o)\cos\gamma_o \qquad (2\text{-}9)$$

One therefore imagines that it can be well balanced by a linear variation of **d** with $\ell$, which has the geometry of straight grooves which fan-out from a "ruling focus" as illustrated in Figure 2-2a. The groove spacing for such a *fan grating*[27] can thus be written as:

$$\mathbf{d}/d_o = 1 + \ell\,/\,(\ r'_o\cos\gamma_o + \Delta RF\,/\cos\gamma_o\ ) \qquad (2\text{-}10)$$

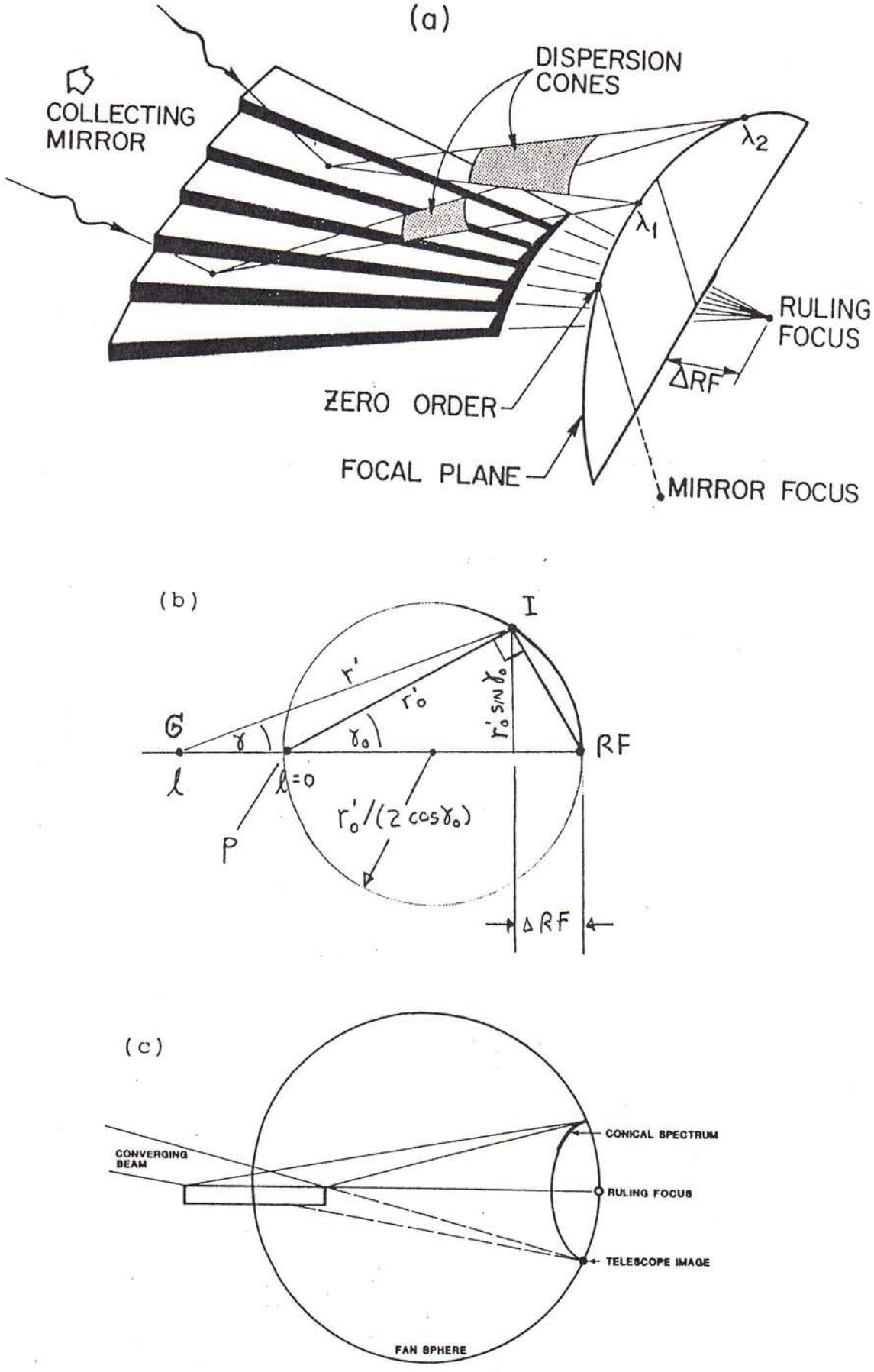


Fig. 2-2. Geometry of off-plane VLS grating ("Oriental fan"). a) perspective drawing, b) trigonometry of ruling focus placement, c) 3-D dispersion of conical diffraction.

Equating the linear coefficients of equations (2-9) and (2-10) results in a constraint for the position of the ruling focus which causes the linear dispersion to be stationary ($\delta/\delta\ell = 0$) at the grating pole:

$$\Delta RF = r'_o \tan\gamma_o \sin\gamma_o \qquad (2\text{-}11)$$

This mounting constraint has a simple geometrical interpretation. As indicated in Figure 2-2b, the grating pole, image point and ruling focus are the points of a right triangle having an apex angle $\gamma_o$ and hypotenuse $r'_o/\cos\gamma_o$. Thus these three points lie on a circle[11,28,39] whose diameter is the distance from the grating pole to the ruling focus, and the dispersed spectrum lies on a "fan sphere" at the intersection of the diffraction cone as shown in Figure 2-2c.

As in the case of the in-plane solution, this off-plane VLS grating is absent of all path-length error terms in the groove length dimension ( $F_{0j} = 0$ ), due to the fact that the central groove is everywhere equidistant from both image and virtual object. Assuming the angular separation between the grooves of the fan grating are constant, the residual wavefront aberrations are derived[28] in a manner similar to that for the in-plane grating:

$$F_{12} = ( \sin\beta_o - \sin\alpha_o ) / ( 2\, r'^2_o ) \qquad (2\text{-}12)$$

$$F_{30} = ( \sin\beta_o - \sin\alpha_o ) / ( 6\, r'^3_o ) \qquad (2\text{-}13)$$

$$F_{31} = ( \sin\beta_o - \sin\alpha_o ) / ( 2\, r'^4_o ) \qquad (2\text{-}14)$$

$$+ \text{ H.O.T.}$$

resulting in a spectral aberration:

$$\Delta\lambda / \lambda = ( 8\, f^2 )^{-1} \qquad (2\text{-}15)$$

where $$f = 1 / ( f_x^{-2} + f_y^{-2} )^{1/2} = 1/(\Phi_x^2 + \Phi_y^2)^{1/2}$$

Thus, this off-plane design has some meridional coma, which is absent in the in-plane design. This results in a spectral resolution which is also limited by the meridional speed of the incident beam. To correct for this additional aberration requires the angular spacings of the fan grooves be varied[28].

Because the focal lengths are equal at m=0 and at the first order correction wavelength, the focal surface is expected to be well approximated by the plane which is normal to the central groove of the grating, and low aberrations are expected in-between

or near these two correction points. Both light-path function and raytrace calculations were performed to substantiate and analyze these effects in greater detail[28].

## d) Linear Dispersion Considerations

The above equations, based on the inverted grating equation and direct use of the light-path function, have been confirmed through numerical raytracings on both the in-plane and off-plane gratings[27,28]. Both of these two grating designs have **plane surfaces**, are situated in the **converging beam** (a virtual object), and provide a **quasi-stigmatic** focal surface which is **erect** to the diffracted beam. Also common to both designs is that this is accomplished by a **variation in the spacings of straight grooves** (permitting mechanical ruling) across the grating surface in order that the focal length to the spectrum equals that to the aberration-free zero order image. However, the in-plane and off-plane versions of this VLS design class differ in two important respects. First, the grooves of the fan grating are not parallel, which makes it difficult to fabricate it accurately using existing ruling technology. Second, the off-plane geometry limits the net practical resolution attainable at the focal plane.

To understand this second problem, one notes that the above design analysis considered only *geometrical* aberrations of the grating itself due to errors in the light-path function. However, the resolution is also limited by the dispersive power of the grating, necessary to separate the spectral images by more than the minimum size of the image. From equation (2-8), the dispersive resolution for both off-plane and in-plane gratings can be written as:

$$\Delta\lambda_{disp} = m\,(d\cos\beta)\,\Delta x / r' \qquad (2\text{-}16)$$

where $\Delta\lambda_{disp}$ is the additional contribution to $\Delta\lambda$ due to the finite linear dispersion of the grating, and where $\Delta x$ is the size of the image in the absence of geometrical aberrations. This minimum size is not infinitesimal, due both to the finite size of the object and due to the finite size of an exit slit or detector pixel. In the case of the in-plane grating, $\beta$ is large (approaching $90^\circ$ at grazing incidence), resulting in a dispersion which is $1/\cos\beta$ higher than in the case of near normal incidence ($\beta \sim 0$). In effect, the product $(d\cos\beta)$ represents the smaller groove spacing apparent if viewed by the radiation diffracted from the grating. This is why in-plane grazing incidence soft x-ray gratings do not require extraordinarily smaller groove spacings than normal incidence visible gratings. For example, a given density grating will provide the same dispersive resolving power ($\lambda/\Delta\lambda$) at 6000 Angstroms in normal incidence and at 100 Angstroms at a $1^\circ$ graze angle ($\cos 89^\circ \sim 1/60$). Unfortunately, gratings which operate at normal incidence, or at small angles $\beta$ projected onto the dispersion plane, do not gain this enormous compensating factor. Therefore, both transmission gratings and off-plane grazing incidence gratings (where $\beta_{off\text{-}plane}$ is small in accordance with the grating equation) require groove spacings a factor of $\cos\beta_{in\text{-}plane}$ smaller in order to provide the same dispersive resolution.

A practical example is the case of EUVE, which employs micro-channel plate detectors having 100 micron pixels, and a telescope which has an angular resolution of 1 arcminute (due dominantly to assumed pointing errors on orbit). Thus, in the absence of grating-induced aberrations, the extremum width of the spectral image is:

$$\Delta x = \Delta x_{det} + (\cos\beta / \cos\alpha)\, \Delta\tau\, T \qquad (2\text{-}17)$$

where T is the effective focal length of the telescope (136 cm) and $\Delta\tau$ is its image quality in radians. The factor in the parenthesis is obtained by differentiating the grating equation to determine the grating magnification in finite order. In the case of EUVE, the effect of $\Delta\tau$ = 1 arcminute was minimized by choice of a negative spectral order for which the grating de-magnifies it approximately a factor of 2 upon diffraction to the spectral focus. Thus, the net extremum value of $\Delta x$ is approximately 0.1 mm + 0.2 mm = 0.3 mm.

To obtain a dispersive contribution less than 1/200 in wavelength at 100 Angstroms requires that $\Delta\lambda_{disp}$ be less than 0.5 Angstroms. From equation (2-16), an in-plane grating of focal length 485 mm with $\beta = 73^{o}$ then requires a groove spacing of 2800 Angstroms, which is well within the range of ruling technology (3600 g/mm).

However, an off-plane design exhibits $\cos\beta \sim \cos\alpha \sim 1$, resulting in no de-magnification of the incident beam size (equation 2-17) and no decrease in the apparent groove spacings (equation 2-16). The result is a requirement for a groove density which would be approximately 6 times higher, or 20,000 g/mm. This is the same as would be required of a normal incidence grating. Since the scatter of a grating scales as the square of the groove density, such an off-plane grating would exhibit a noise level approximately 36 times higher. In addition, it was and still is beyond the state of ruling technology to form accurately shaped (and thus efficient) grooves at such high density.

For these reasons, the fan grating was discarded in favor of the in-plane VLS grating for use as the EUVE spectrometer design.

## c) Optical System Design

An exploded view of the EUVE spectrometer configuration[30] is shown in Figure 2-3 (also featured on the front cover of Applied Optics 15 June 1985 issue). A 40 cm diameter grazing incidence telescope of Wolter-Schwarzschild type II design collects the incident light. The primary and secondary mirrors are full surfaces of revolution of approximately conical sections. However, the primary deviates slightly from a paraboloid and the secondary from a hyperboloid, in order to provide the widest possible field-of-view. This occurs when the two-element mirror system is aplanatic, that is both lacks spherical aberration and obeys the Abbe sine condition (absent of field aberrations

Fig. 2-3. Exploded view of the EUVE flight spectrometer consisting of thre VLS grating channels which share the converging beam aperture of a grazing incidence telescope.

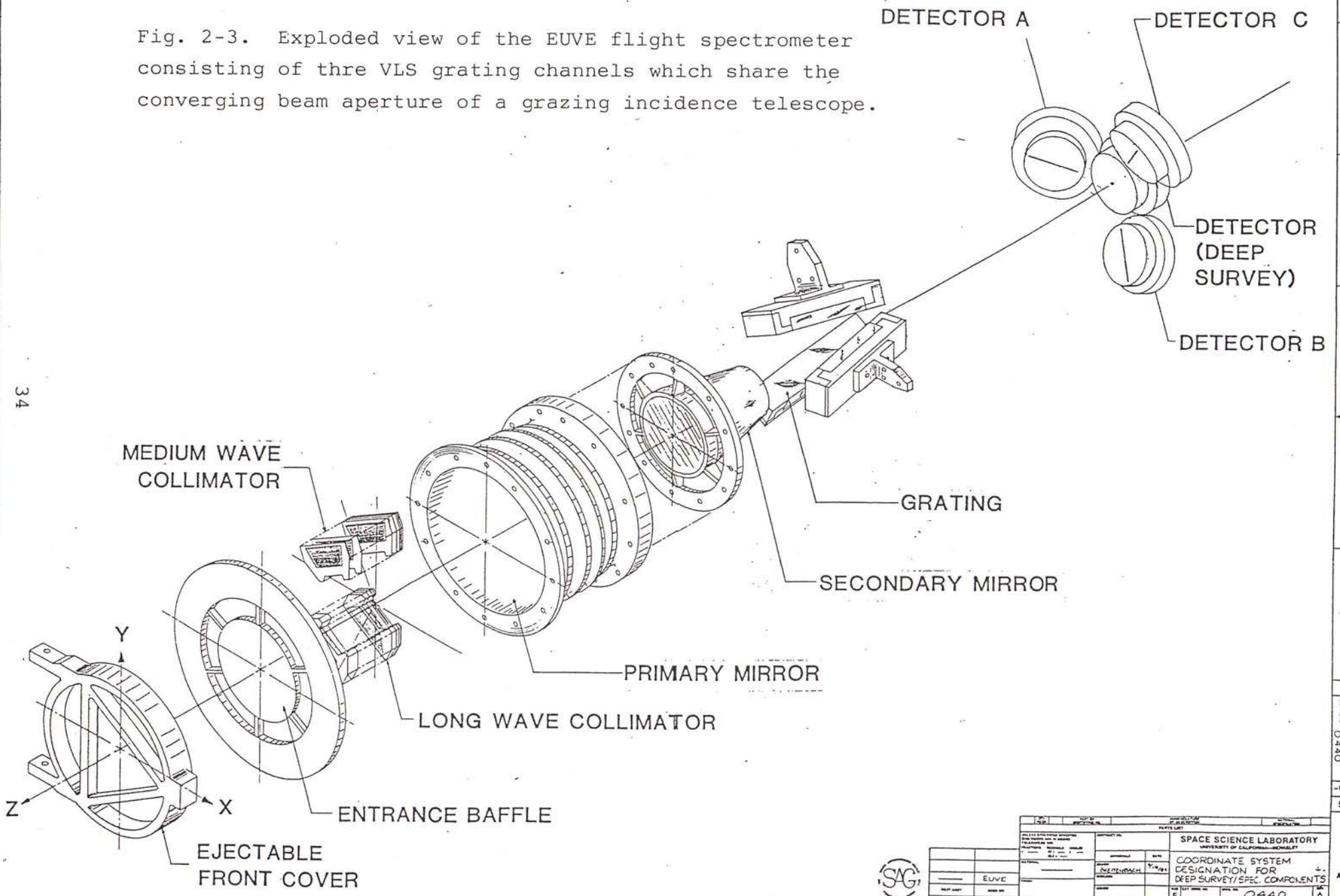

linear with the off-axis angle), according to Schwarzschild[31] and analyzed at grazing angles by Wolter[32] and others[33]. The prime focus of the telescope is imaged by a micro-channel plate detector located along the axis of symmetry of the telescope. As this telescope points in the anti-Sun direction, it allows a sensitive *deep survey* imaging of sources.

Spectroscopy is performed by three stationary gratings which each intercept approximately 1/6th of the beam converging from the telescope secondary mirror. Due to reflection by the grating, each of the three spectra is displaced from the telescope axis and is imaged by a dedicated micro-channel plate detector. Because of the stigmatic (point-like) imaging provided by the use of the VLS plane gratings in converging light, the spectra are placed as dispersed linear features approximately centered on the detector surfaces. Because of the small area occupied by the spectrum, the degradation of sensitivity due to background is minimized.

A cross-sectional drawing of the deep survey / spectroscopy instrument is shown in Figure 2-4. The total instrument length is 1.5 meters, and the drawing shows one of the three spectrometer channels. Because there is no entrance slit, the detectors are exposed to diffuse sky background due largely to backscatter of solar radiation from geocoronal helium and oxygen and interplanetary hydrogen. To reduce this unwanted radiation to tolerable levels, wire-grid collimators are employed to restrict the field-of-view of the telescope sections dedicated to medium and long wavelength spectra, and thin-film filters of different materials are placed over sections of the micro-channel plate detectors.

Due to the plane grating surfaces, the co-alignment required between the grating angle and the telescope is extremely loose, allowing for ease of construction with misalignments resulting primarily in a shift of the wavelength scale without degradation of resolution[28]. All optical components are stationary, with only the telescope and detector protective doors requiring movement to initiate operation.

The values of the major design parameters for the EUVE flight spectrometer are listed in Table I.

In combination, the three spectrometer channels provide simultaneous coverage from 70 to 760 Angstroms. This exceeded the specification of 100 to 600 Angstroms in order to provide additional capability for planetary work at the long wavelength end (proved useful during the Jupiter comet crash of 1994 !) and to provide access to more distant objects whose radiation would not be as highly absorbed by the interstellar medium at the short wavelengths.

The optical parameters were chosen to maximize spectral resolution and sensitivity in the desired channels. A discussion follows of the contributions to the two principal performance criteria of resolution and sensitivity.

## e) Focal Curves

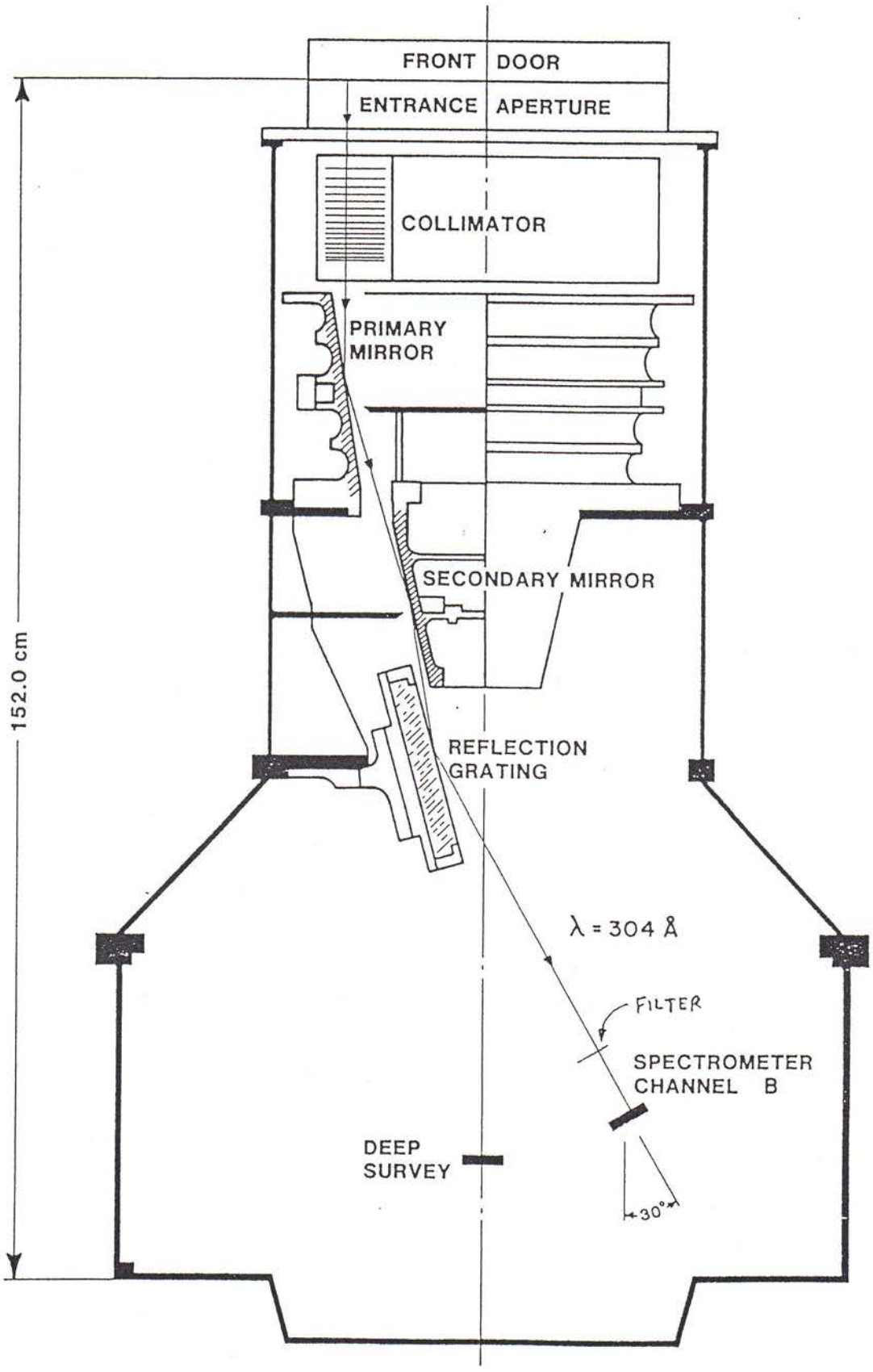


Fig 2-4. Cross-sectional view of the flight spectrometer, revealing three grazing reflections. The optics for one channel are shown, traced by the optical path of a 304 Å photon. The mechanical collimator acts as a field-limiting slit for long wavelength channels B and C.

Table I. EUVE Spectrometer Characteristics

| | |
|---|---|
| **Performance:** | |
| Spectral Channels (simultaneous) | A: 70-190 Å<br>B: 140-380 Å<br>C: 280-760 Å |
| Spectral Resolution (averages) | A: 0.5 Å<br>B: 1.0 Å<br>C: 2.0 Å |
| Spatial Resolution | 1.5 arc minutes |
| Effective area (100-600 Å) | 0.4 $cm^2$ |
| **Collecting Optics:** Wolter-Schwarzschild Type-2 | |
| Aperture | 40 cm diameter |
| Speed | F/3.4 |
| Reflective Coating | gold |
| **Grating:** Varied Line Space In-Plane Mounting | |
| Plate scale (averages) | A: 2.4 Å/mm<br>B: 4.8 Å/mm<br>C: 9.6 Å/mm |
| Groove density variations | A: 1675 - 3550 $mm^{-1}$<br>B: 830 - 1750 $mm^{-1}$<br>C: 415 - 875 $mm^{-1}$ |
| Plane surface ruled area | 80 x 200 mm |
| Blaze angle | 3.5° |
| Angle of incidence (average) | 82.9° |
| Reflective coating | rhodium |
| **Detector:** Micro-channel plate | |
| Aperture | 50 mm diameter |
| Resolution | 100 µm x 100µm |
| Filters | A: 0.3 µm parylene-N (1)<br>B: 0.15 µm aluminum (2)<br>C: 0.15 µm aluminum |
| Photocathode | Cesium Iodide (3) |

(1) changed to Lexan/Boron, (2) changed to Aluminum/Carbon,
(3) changed to KBr (Potassium Bromide)

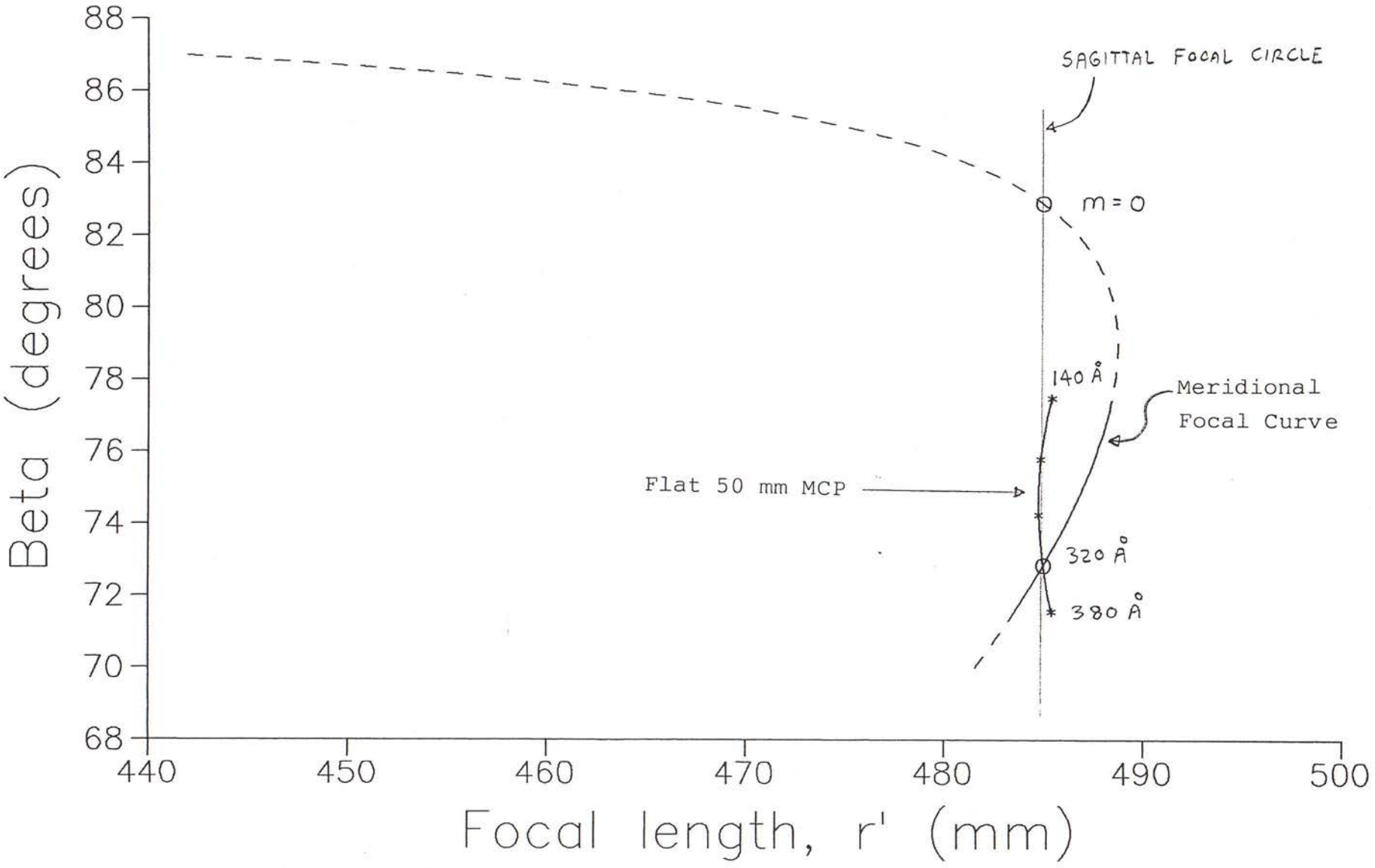


Fig. 2-5. Focal surfaces of VLS plane grating spectrograph as designed for EUVE.

Spectral resolution is optimized at the meridional focal curve, which can be derived from equations (1-1) and (1-5). For the plane grating, 1/R = 0, resulting in the following ruling coefficient in order to remove the defocusing term in F:

$$N_{20} = ( \eta \cos^2\alpha_o + \cos^2\beta_o ) / (2 m \lambda_o r'_o) \qquad (2\text{-}18)$$

where

$$\eta = r'_o / r_o \qquad (2\text{-}19)$$

Maintaining the incidence angle of $\alpha_o$ results in a spectrum of wavelengths $\lambda$ diffracted to corresponding angles $\beta$ using the grating equation. In order to maintain the focus ($F_{20} = 0$), equation (1-1) requires this spectrum lie along the following curve:

$$r' = r'_o \cos^2\beta / [(\cos^2\beta_o + \eta \cos^2\alpha_o) (\lambda/\lambda_o) - \eta \cos^2\alpha_o] \qquad (2\text{-}20)$$

where $\lambda/\lambda_o = (\sin\beta - \sin\alpha_o)/(\sin\beta_o - \sin\alpha_o)$. In the case of EUVE, $\eta = -1$, $\alpha_o = 82.9^o$, $\beta_o = 72.85^o$, $\rho_o = N_1 = 1150$ g/mm and $\rho_1 = 2N_2 = 4.618$ mm$^{-2}$, This results in the meridional curve given in Figure 2-5. It passes through the two correction points (m=0 and $\lambda=\lambda_o$). On this polar plot, the sagittal circle of radius $r'_o$ centered on the grating pole appears as the vertical line which also passes through the two stigmatic correction points.

## f) Spectral and Spatial Resolution

However, a flat micro-channel plate surface was available for the EUVE mission. To obtain high quantum efficiency, this detector should be oriented approximately normal to the diffracted rays. Figure 2-5 shows the polar coordinates of a flat detector which optimizes spectral resolution by positioning it to pass through the meridional focal surface at 320 Angstroms, and maintains high efficiency by orienting it normal to the diffracted ray striking the geometrical center of the detector ($\lambda$ = 250 Angstroms). This ray makes an angle of 15.5° angle relative to the grating surface. Along this flat focal surface, three-dimensional raytracings were performed using the following parameters for the medium channel of the spectrometer:

$r_o = -485$ mm
$r'_o = 485$ mm
$f_x = 22$
$f_y = 6.24$
$d_o = 8700$ Angstroms
$\lambda_o = 320$ Angstroms
$m = -1$

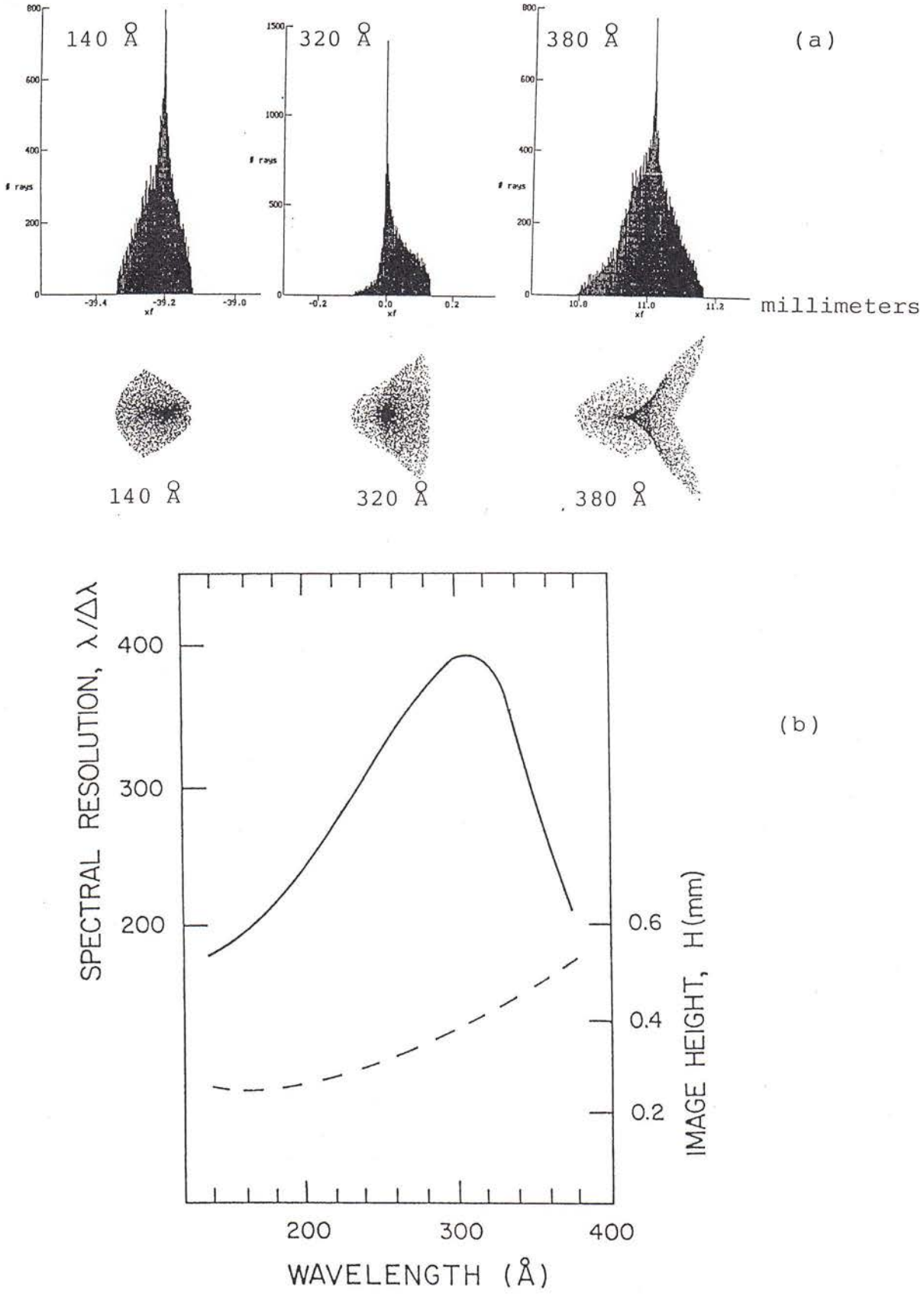


Fig. 2-6. a) Raytraced spot diagrams at the detector plane of the medium wavelength EUVE grating channel. b) Resulting limit to the spectral and spatial resolutions.

The raytrace used the full set of ruling coefficients, where the higher order meridional aberrations are removed by use of equations (1-1) and (1-8) to force $F_{30} = 0$ and equations (1-1) and (1-9) to force $F_{40} = 0$. This resulted in ruling coefficients of $\rho_2 = 3N_3 = +0.01354\ mm^{-3}$ and $\rho_3 = 4N_4 = +0.0000343\ mm^{-4}$. To analyze the grating aberrations alone, the object was an infinitesimally small point at the telescope focus. The spot diagrams of Figure 2-6a show the focal plane positions of 5000 photons at each of three wavelengths (140 and 380 Angstroms at the extreme edges of the usable spectrum and 320 Angstroms at the correction wavelength). The maintenance of high spectral and spatial resolution over the entire spectrum is clear, due to the image size staying within the range of 0.2 to 0.4 mm in each direction. Laboratory experiments[30] using a 1/4 size test grating resulted in a stigmatic image at 304 Angstroms which was approximately 10 times smaller in width (~ 20-30 μm) in keeping with equation (2-5). This width corresponds to a resolving power of ~ 2500.

By use of the known linear dispersion (~ 0.2 mm/Angstrom at the spectrum center), the extrema of the1-D spatial line profiles (enclosing 100% of the energy) are converted to spectral resolving power and plotted in Figure 2-6b as the solid curve. The dashed curve shows the extremum image size in the non-dispersive direction. However, to the grating images one must add the blurring due to the detector pixels and telescope pointing stability. The net convolution[30] results in an average FWHM resolving power of 150 to 300, with the latter being finally achieved (200-400 as a function of wavelength) due to enhanced pointing reconstruction using on-board star sensors. This also resulted in a minimum net image height of ~ 1 arcminute, dominated by the 0.42 mm from sagittal coma of the grating. This good spatial resolution greatly reduces the instrument background and provides simultaneous observation of multiple sources within the telescope field.

## g) Groove Shadowing Model and Measured Grating Efficiencies

Maxwell's differential equations provide the physical constraints for the electric and magnetic field vectors at the interface between two media. The solution to this boundary value problem yields the exact result for the energy reflected and transmitted for a surface of any shape. In the simple case of specular reflection from a smooth surface, the solution given by the Fresnel coefficients (Sec. 1.4). However, in the case of a diffraction grating, the solution cannot be expressed in closed-form, requiring extensive numerical iterative calculations[33]. A simple model is nonetheless required in order to guide the design of diffraction grating systems. In the following, a model is developed which, although by necessity not strictly correct, results in good agreement with experimental results at grazing incidence.

The absolute diffraction efficiency of a grating is for convenience considered to be the product of the reflectance of the coating and the relative diffraction efficiency of the grooves:

$$\varepsilon_{abs}(m,\lambda) = R(\lambda) \times \varepsilon_{rel}(m,\lambda) \tag{2-21}$$

The reflectance is a function of wavelength as given by the Fresnel equations. However, since the angles of incidence and reflection are not equal for a grating, one imagines that the reflectance must be specified at some effective average $<\alpha,\beta>$ of these two angles, which is a function of both the wavelength and the spectral order.

The relative diffraction efficiency depends on the shape of the grooves. Revising the scalar Kirchoff approximation[34] for optimum accuracy at grazing incidence, the relative diffraction efficiency resulting from a grating having grooves shaped as right triangles with apex angle $\delta$ (the called "blaze angle") is normalized as:

$$\varepsilon_{rel}(m,\lambda) = D_m(\lambda) / \Sigma_m D_m(\lambda) \tag{2-22}$$

where
$$D(m,\lambda) = \{\sin[\varpi_m(\lambda)]/\varpi_m(\lambda)\}^2/\sin[\beta_m^*(\lambda)] \tag{2-23}$$

$$\varpi_m(\lambda) = (\pi g/\lambda)\ \{\cos(\alpha^*+\delta) - \cos[\beta_m^*(\lambda)-\delta]\} \tag{2-24}$$

where a superscript * indicates the complement of the angle has been taken, so $\beta^* = \pi/2 - \beta$ = the graze angle of diffraction. The numerator of equation (2-23) is the Bessel function corresponding to the diffraction pattern from the illuminated part of an individual groove facet. At grazing incidence, this width is not equal to the groove spacing, but only to that portion which is not in the shadow of the adjacent groove, as illustrated in Figure 2-7a:

$$g = d\ [\ 1 - \tan\delta / \tan(\alpha^*+\delta)\ ]\ \cos\delta \tag{2-25}$$

The denominator in equation (2-23) accounts for the fact that the intensity pattern from an individual groove should be multiplied by the width of the interference peak of the spectral order, which scales as $1/\sin\beta^*$.

This revised Kirchoff theory correctly predicts both the wavelength and the efficiency at the peak ("blaze") of the diffraction efficiency curve. From equation (2-23), the peak clearly occurs when $\varpi = 0$ , which from equation (2-24) is when:

$$\alpha^* + \delta = \beta^* - \delta \tag{2-26}$$

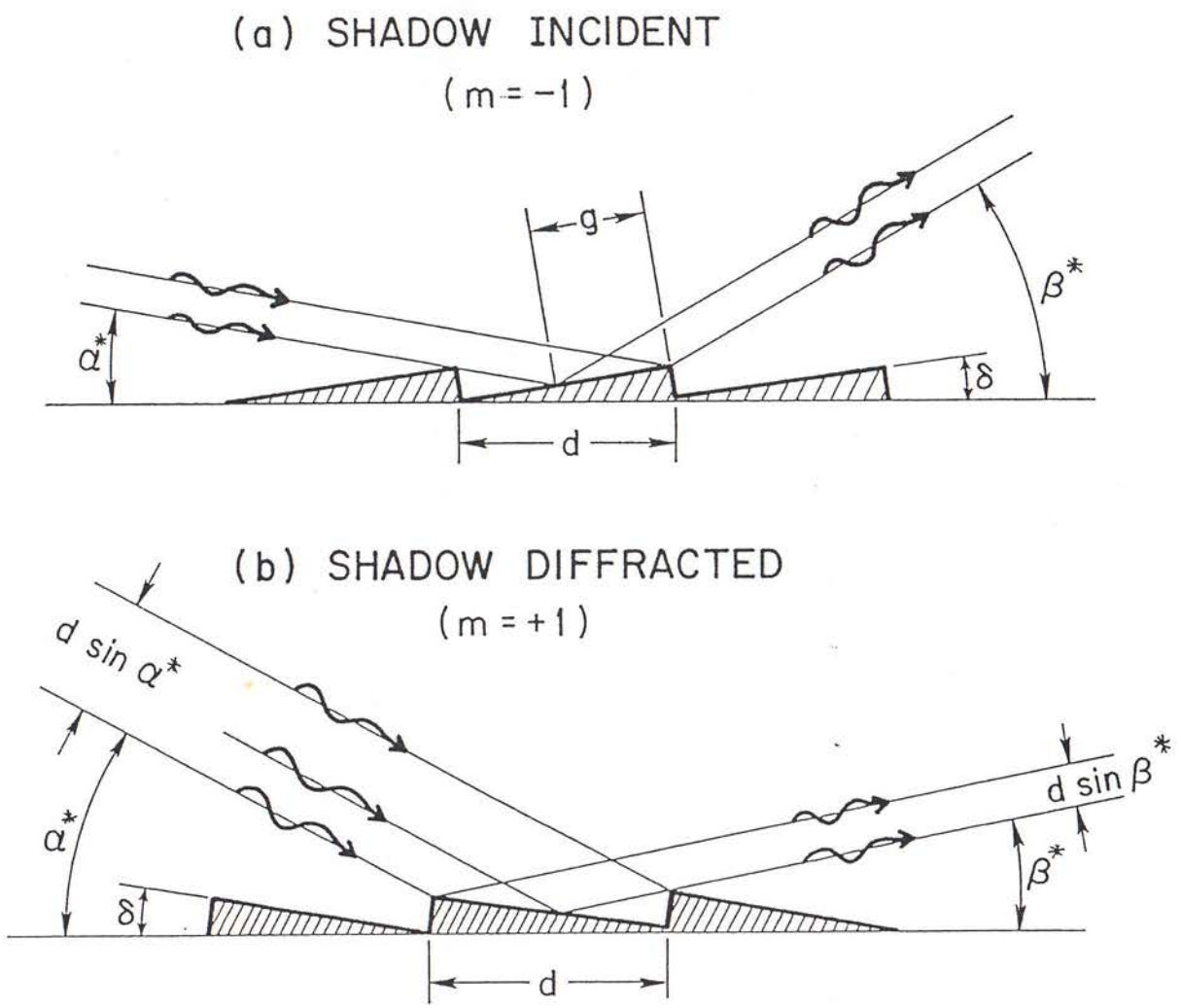


Fig 2-7. Geometry of groove shadowing. (a) blaze of an inside spectral order, (b) blaze of an outside spectral order. Shadow factors derived from these geometries may be used to accurately determine the blaze efficiency.

which when substituted into the grating equation yields:

$$\lambda_{blaze} = 2\ d \sin\delta \sin\gamma \qquad (2\text{-}27)$$

where $\gamma = \alpha^* + \delta = \beta^* - \delta$. This is the well-known condition in which the incident and diffracted rays are specular relative to the tilted facet of the groove. In other words, the graze angle of incidence and diffraction are equal ($\gamma$) relative to the facet surface.

The normalized relative efficiency at this peak is numerically calculated from the above equations to equal the well-known ratio:

$$\varepsilon_{blaze} = \sin\alpha^* / \sin\beta^* \qquad (2\text{-}28)$$

in agreement with the rigorous solution from electromagnetic theory[33]. This ratio can be understood more intuitively by reference to Figure 2-7b, in which the ray directions are reversed and the diffracted beam is now shadowed. Because of the principle of optical reversibility, such reversal maintains the same efficiency. This efficiency is obviously that fraction Q of the fraction of the illuminated groove which is not blocked by the adjacent groove:

$$Q = [\ 1 - \tan\delta\ /\tan(\alpha^*+\delta)]/[\ 1 + \tan\delta\ /\tan(\beta^*-\delta)] \qquad (2\text{-}29)$$

which equals ( $\sin\beta^* / \sin\alpha^*$ ) at the blaze ( $\beta^* = \alpha^* + 2\delta$ ). Thus, an alternate version of the efficiency model is to simply multiply the unnormalized Bessel function for fully illuminated facets (g=d) by the shadow factor of equation (2-29).

Figure 2-8 plots the results of efficiency measurements[30] of a test sample of the EUVE varied line-space grating, ruled by Dr. Tatsuo Harada at Hitachi. The grating was overcoated with rhodium due to its somewhat higher reflectance than gold in the extreme ultraviolet at the designed graze angles. The measured data points are fit by the above Kirchoff theory with the adjustable parameters being the blaze angle of the grooves and a constant factor to account for the ratio between actual and theoretical efficiency. The results of fitting the first order curves (versus wavelength or angle) are a blaze angle of $3.0^0$ to $3.5^0$ and a factor equal to 0.82 to 0.90, indicating that 82-90% of the theoretically predicted efficiency was obtained. The application of the Kirchoff theory is however limited, particularly for highly shadowed grooves and where the ratio between wavelength and apparent groove spacing is not significantly less than unity. This is evident from the departure of the predicted efficiency at 584 Angstroms and the difference (dashed versus solid curves) between use of equation (2-22) and the alternate (unnormalized) model which uses the shadow factor of equation (2-29).

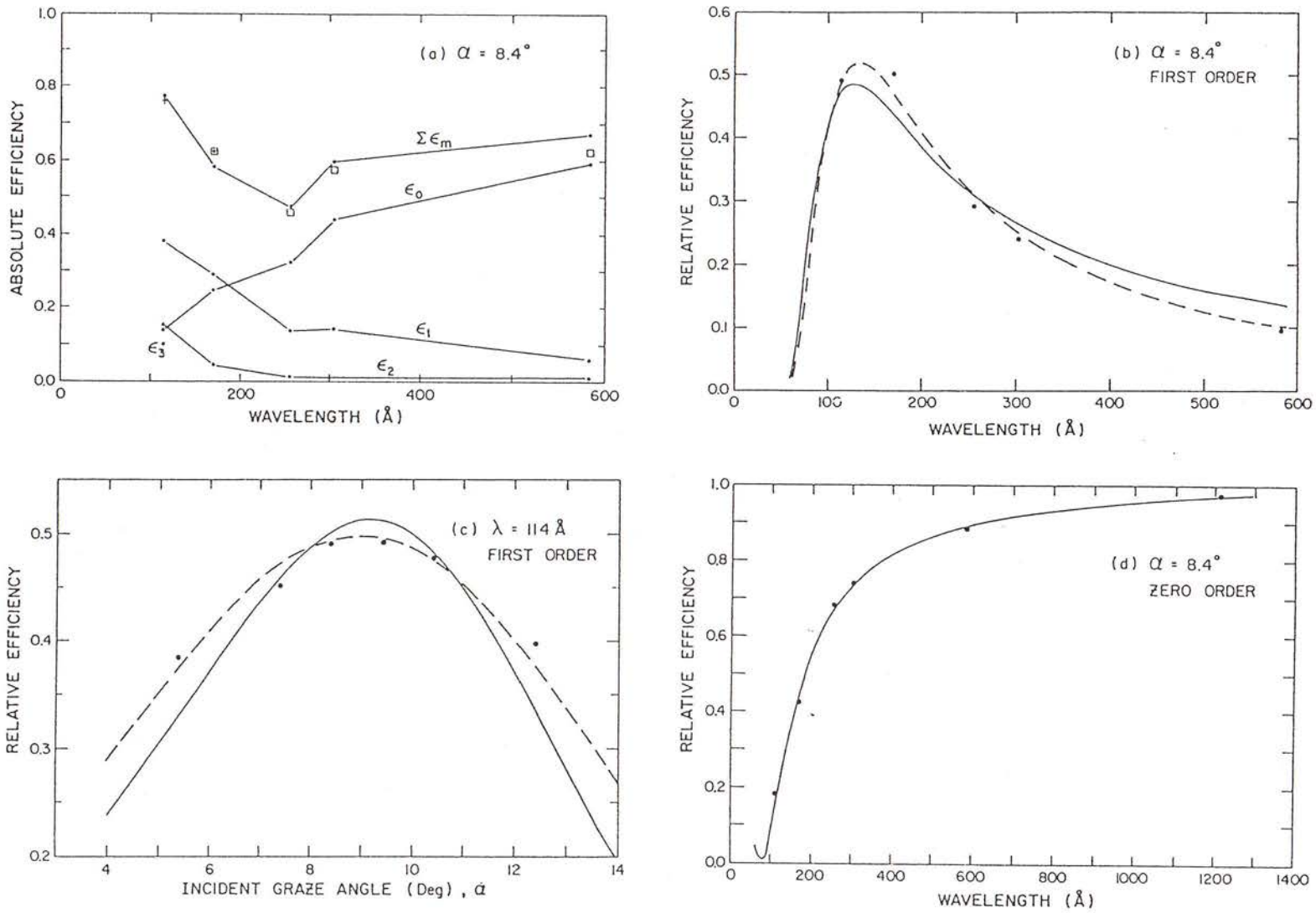


Fig 2-8. Measured grating efficiencies. (a) absolute efficiency in spectral orders 0, 1, 2, and 3 versus wavelength, at an 8.4° graze angle to the grating tangent (11.4° to groove facets). The sum $\Sigma\,\varepsilon_m = \varepsilon_0 + \varepsilon_1 + \varepsilon_2 + \varepsilon_3$ is compared to our reflectance measurements at 11.4° of a flat witness sample (+) and those found in reference 38 (□). (b) relative first-order efficiencies derived from left-hand panel, compared to theoretical curves times ~ 0.9. (c) relative first-order efficiencies versus angle at $\lambda$ = 114 Å, compared to theoretical curves times ~ 0.85. (d) zero order relative efficiencies versus wavelength at an 8.4° graze angle, compared to a theoretical curve times 1.06.

The measured absolute efficiency of 38% at 114 Angstroms is one of the highest efficiencies obtained in this wavelength region for a diffraction grating. Due to the varying angles of incidence and varying groove spacing across the ruled width, the diffraction efficiency curve resulting will become flatter as a function of wavelength for the full size flight gratings.

## h) Sensitivity

The last, and probably most important, performance criterion remaining to be analyzed in the sensitivity. Sensitivity is conveniently expressed as the minimum source flux necessary to allow detection above a threshold value in the signal-to-noise ratio. As diagrammed in Figure 2-9, this threshold is a function of a large number of interconnected terms. First, the strength of the signal is linearly proportional to the effective area of the instrument, which is a function of wavelength:

$$A(m,\lambda,\tau,p) = A_{geom} \times COLL(\tau) \times R(\lambda,p) \times \varepsilon_{rel}(m,\lambda) \times FILT(\lambda) \times QE(\lambda) \qquad (2\text{-}30)$$

where $A_{geom}$ is the geometrical aperture of the telescope, $\tau$ is the field angle of the telescope, COLL is the transmission of the wire-grid collimator, R is the reflectance of the 3-bounce optical system, $\varepsilon_{rel}$ is the relative diffraction efficiency of the grating, FILT is the thin-film filter transmission and QE is the detector quantum efficiency. The reflectance is a function of the degree of linear polarization (p) for the incident radiation. Details of the individual contributions to the factors in equation (2-30) are published by the author[30].

In the case of unpolarized incident light, Figure 2-10a plots the calculated effective area as a function of wavelength in spectral order m = -1. The area ranges between ~ 0.2 and 1 $cm^2$, with the three channels providing bandpasses limited by the filter transmission bands and the blaze peaks of the gratings. Below ~ 100 Angstroms, the reflectance drops sharply due to the high graze angles used. Above approximately 200 A in wavelength, the reflectance is a strong function of the incident polarization, hence rotation of spectrometer about the telescope axis allows the magnitude and direction of this polarization to be determined[30].

The noise level is due to photon counting statistics, and therefore equals the square root of the total number of events (real or otherwise) read-out in the spectral bin. The number of events scales linearly with instrument-induced noise such as the detector background per unit area (the "dark current") and the grating scatter, and with external sources of background such as the skyglow, all multiplied by the area occupied by the spectral image on the detector. This image size is in turn a function of the aberrations of the optics, the detector pixel size and the blurring due to instrument wobble during flight.

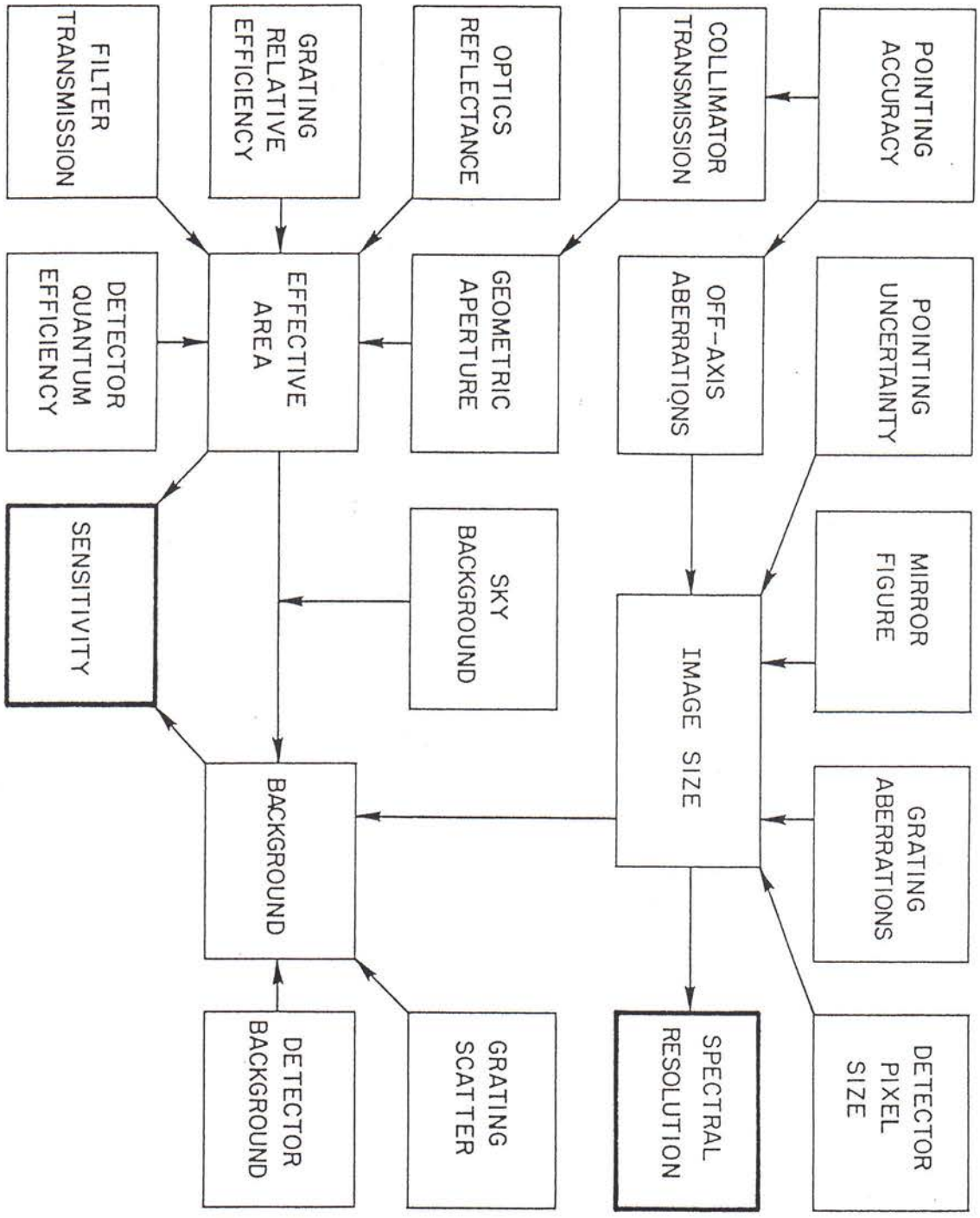


Fig. 2-9. EUVE instrument system block diagram, showing the relationships between many factors which contribute to the final resolution and sensitivity.

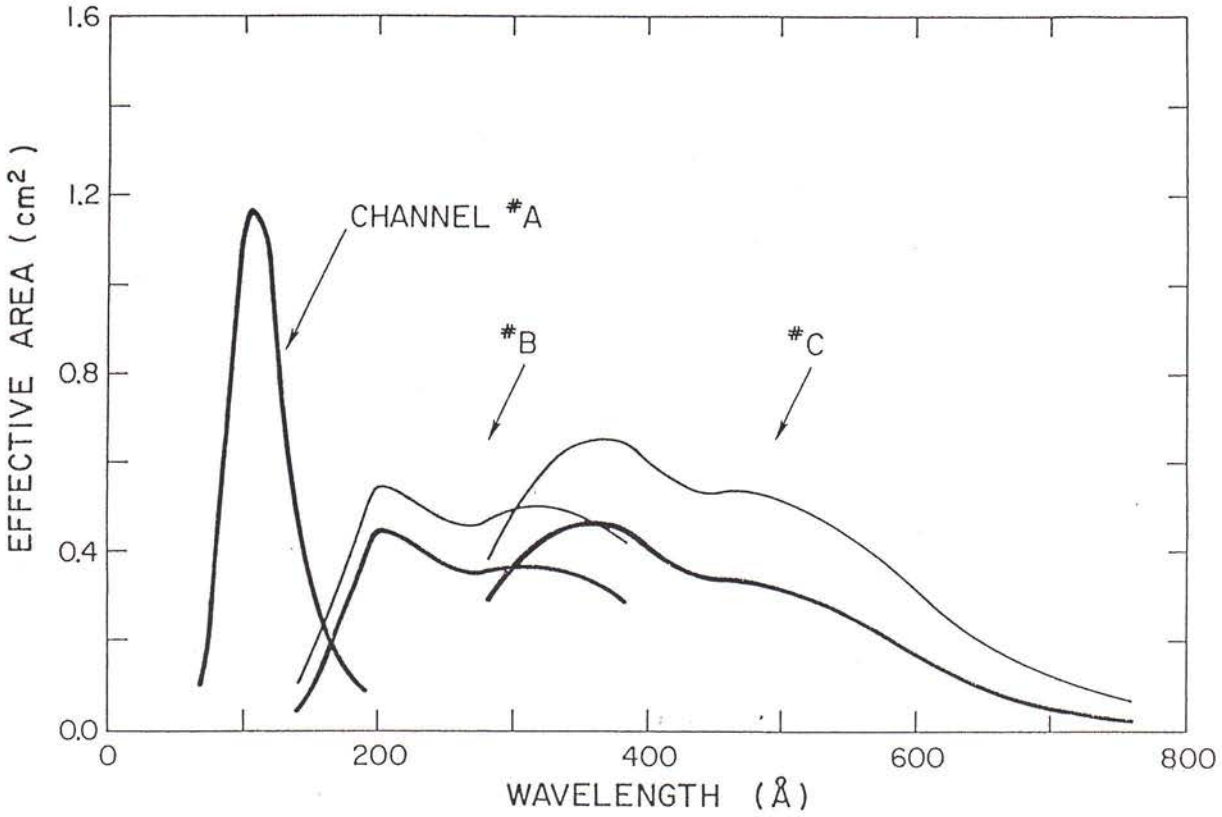


Fig. 2-10 a) Effective area as a function of wavelength, for on-axis pointing towards a spectroscopy target. For off-axis pointing, these values are lowered as discussed in the text. The upper (light) curves assume a thinner aluminum filter (1000 Å).

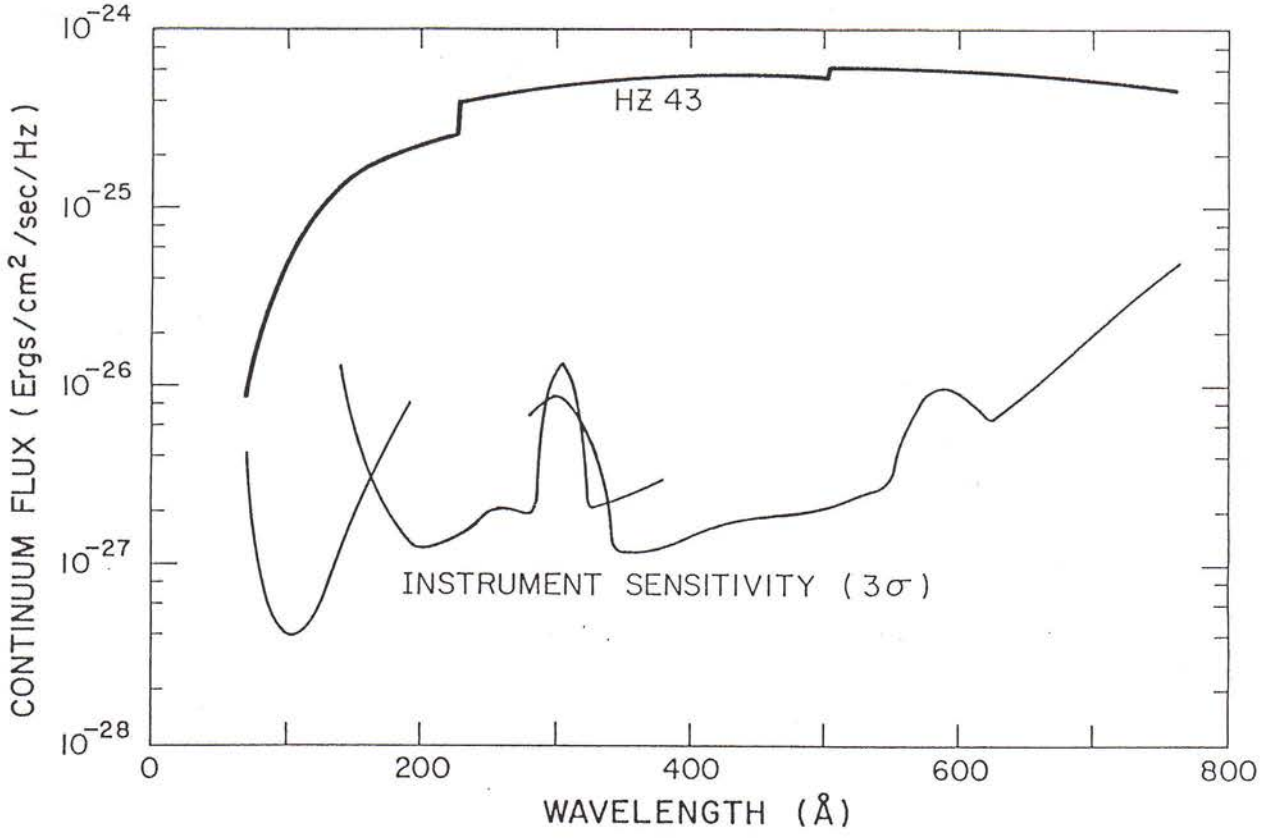


Fig. 2-10 b) Continuum flux from a known EUV source, HZ43, as a function of wavelength. This is compared to the limiting 3-σ spectrometer sensitivity after a 40,000 second observation, assuming a wavelength-binning resolution of $\lambda/\Delta\lambda = 100$. Sources approximately a factor of 100 dimmer than HZ43 will still be spectroscopically detectable.

Combining all these effects results in a general expression for the minimum detectable flux in a spectral line, assumed to be inherently narrower than the instrument resolution:

$$MDF_{line}(ph/cm^2/sec) = 1/2\{1+[1+(4/S^2)B(\lambda)t]^{1/2}\}S^2/[tA(\lambda)] \qquad (2\text{-}31)$$

where S is the S/N level of detection (e.g. S = 5 is a "5σ" detection), A(λ) is the effective area, t is the observing time and B(λ) is the background integrated over the resolution element. This can be easily converted to a sensitivity to continuum sources by use of the transformation:

$$MDF_{continuum}\ (ergs/cm^2/sec/Hz) = (\lambda/\Delta\lambda)\ h\ MDF_{line} \qquad (2\text{-}32)$$

where h = Planck's constant ($6.626 \times 10^{-27}$ erg/Hz) and where the spectral bin size (Δλ) may be increased during spectral analysis to provide better sensitivity.

Figure 2-10b plots the calculated minimum detectable flux for a continuum source at a spectral resolving power of 100, assuming a 3-σ detection in each wavelength bin and an observing time of 40,000 seconds (~12 hours). Away from the two bumps corresponding to high sky background (at 304 and 584 Angstroms), the level of detection is ~ $2 \times 10^{-27}$ ergs/cm$^2$/sec/Hz, which meets the scientific requirement by more than a factor of 2.

## i) Simulated Thermal and Coronal Plasma Spectra

Figure 2-10b also shows the source intensity[35] for one of the few extrasolar EUV sources known prior to launch, the hot white dwarf HZ43. This source is seen to be approximately 200 times brighter than the instrument sensitivity. Indeed, the sensitivity requirement was based on the conservative assumption that this is the brightest continuum source in the sky. Given predicted space densities of hot white dwarfs, the factor of 200 higher sensitivity than HZ43 was predicted to allow a fair sample of other hot white dwarfs to produce spectra of good signal-to-noise.

Detailed raw count-rate spectra are simulated in Figure 2-11. These were obtained by folding the source intensity through the effective area curve of Figure 2-10a, and adding Poissonian noise due to the sky and instrument backgrounds. The source intensity can be written as:

$$I(\lambda) = 4\ \pi\ W(\lambda)\ (\mathcal{R}_*/\mathcal{D})^2\ e^{[-\sigma(\lambda)N_H]} \qquad (2\text{-}33)$$

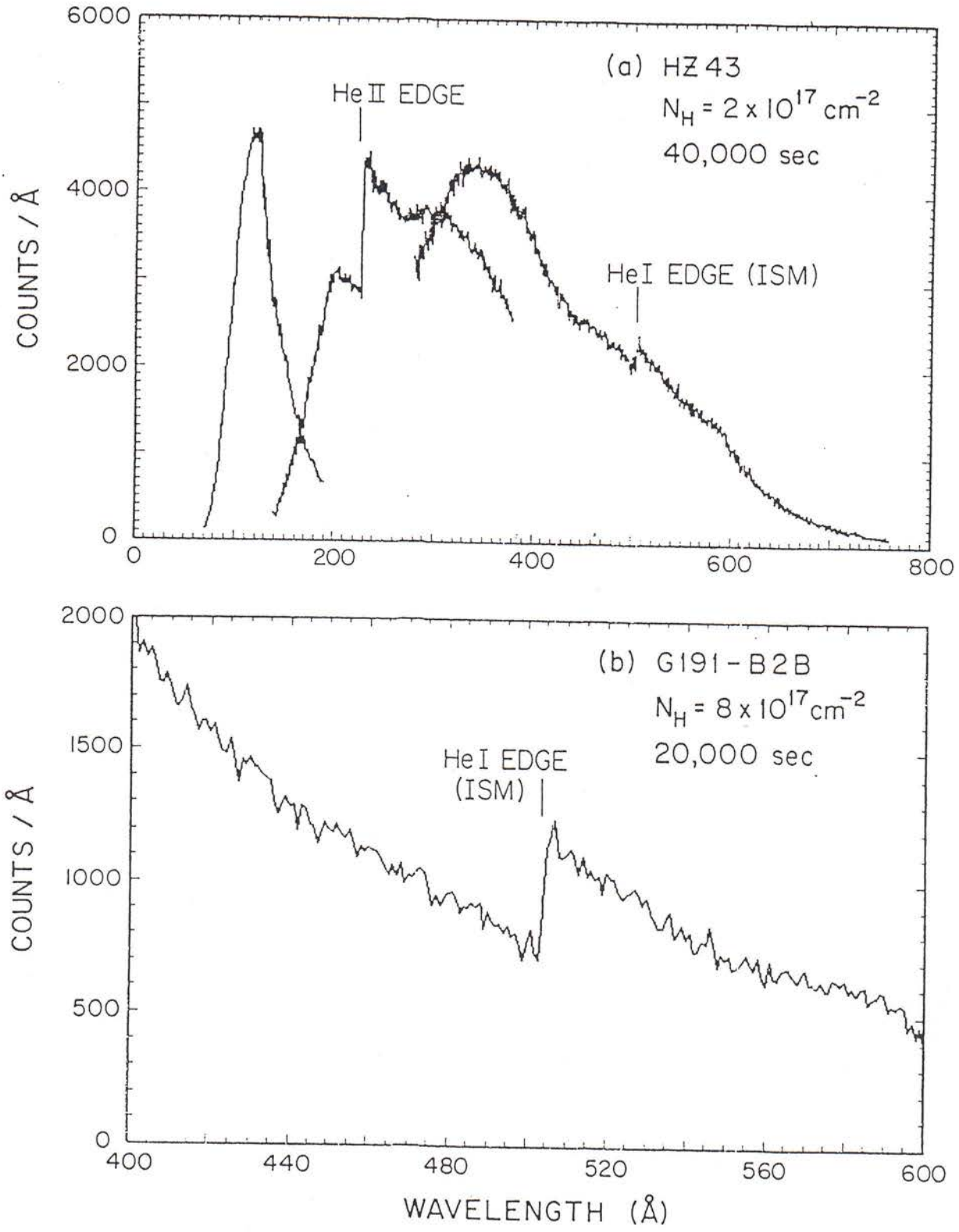


Fig 2-11. Accumulated counts per $\Delta\lambda = \lambda/100$ bin for observations of two hot white dwarfs. (a) HZ43 for 40,000 seconds, and (b) G191-B2B for 20,000 seconds. The smooth bumps and long wavelength decline are primarily due to the instrument effective area as plotted in Fig. 19. The noise is due to Poissonian counting statistics. The lower panel shows only a part of the long wavelength spectrometer channel near a simulated interstellar helium edge at 504 Å.

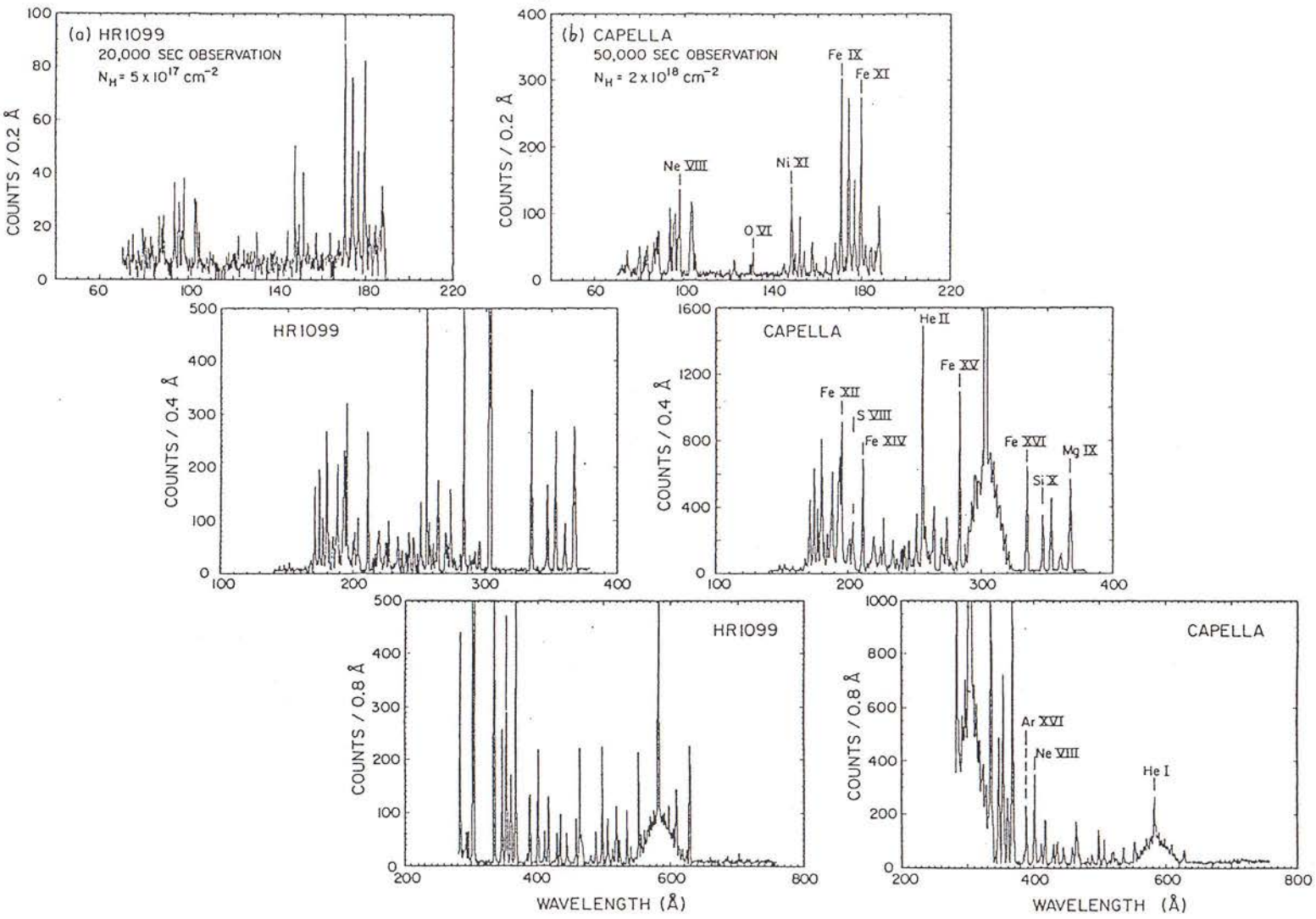


Fig. 2-12. Accumulated counts for simulated observations of two coronal sources. (a) HR1099 after 20,000 seconds down the Earth's shadow, and (b) Capella after 50,000 seconds. The lines observed in the short wavelength channel are sensitive to the temperature of the corona, while those appearing in the long wavelength channel are sensitive to the interstellar extinction along the line-of-sight.

where $W(\lambda)$ is the intensity at the surface of the star of radius $\mathcal{R}_*$, $\mathcal{D}$ is the distance to the star, $\sigma(\lambda)$ is the effective cross-section per neutral hydrogen atom in the interstellar medium (ISM) and $N_H$ is the column density of such hydrogen along the line of sight. $W(\lambda)$ was calculated from a white dwarf model atmospheres code using temperature and density parameters obtained from prior EUV observations[35]. A small fraction ($2 \times 10^{-5}$) of helium was included in the atmosphere to determine the spectrometer's ability to detect it. The atomic cross sections were taken from Cruddace et al[36] for cosmic elemental abundances, and a value of $N_H = 2 \times 10^{17}$ cm$^{-2}$ was used. The distance to HZ43 is 65 parsecs (1 parsec ~ $3 \times 10^{18}$ cm) and the stellar radius is $8.4 \times 10^8$ cm. After a simulated 12 hours of observation, the raw count spectrum (Figure 16a) shows two well-defined absorption edges in the white dwarf continuum, one at 228 Angstroms from ionized helium (HeII) and the other at 504 Angstroms from neutral helium. A second white dwarf (G191-B2B), believed to have a higher column density along the line of sight, shows a stronger interstellar HeI edge (Figure 2-11b). In an actual spectrum, these edges will allow the determination of the helium abundance in the stellar atmosphere and ISM, respectively. In addition, after de-convolving the calibrated spectrometer effective area, the continuum shape will allow accurate determinations of the temperature and density of the stellar surface and the column density of neutral hydrogen in the ISM.

Hot plasmas also surround several types of star, producing strong line emissions in the EUV and soft x-ray bands. Detailed extreme ultraviolet spectral measurements have been made on the Solar corona[37]. To provide a simple-minded source spectrum to fold through the EUVE spectrometer for other stars, the measured Solar EUV spectrum was scaled by the ratio of measured soft x-ray broadband luminosities, and factored by the transmission of the intervening interstellar medium as before. In the case of Capella, Figure 2-12 shows that a 50,000 second observation should allow intensity measurements of multiple stages of ionizations from various metals in the stellar corona. From such measurements in the short and medium wavelength spectrometer channels, stellar model parameters of temperature and density can be determined and used to predict the intensities of lines at other wavelengths. The ratio of observed to predicted intensities in the long wavelength channel then allows an accurate determination of the extinction due to the cooler circumsource and interstellar media.

## j) Flight Spectra

The Extreme Ultraviolet Explorer was launched in 1992 and successfully performed both its all-sky survey imaging mission and its spectroscopy phase of long-exposure pointings on selected targets of particular interest. Figure 2-13 is a set of spectra obtained by Dupuis et al[38] on six different hot white dwarfs. The exposure times varied between 20,000 and 80,000 seconds per star. Due to overlap of the wavelength coverage between the three grating channels (see Table I), these could be pieced together contiguously and flux-calibrated in the first spectral order (m=-1) to obtain the spectra

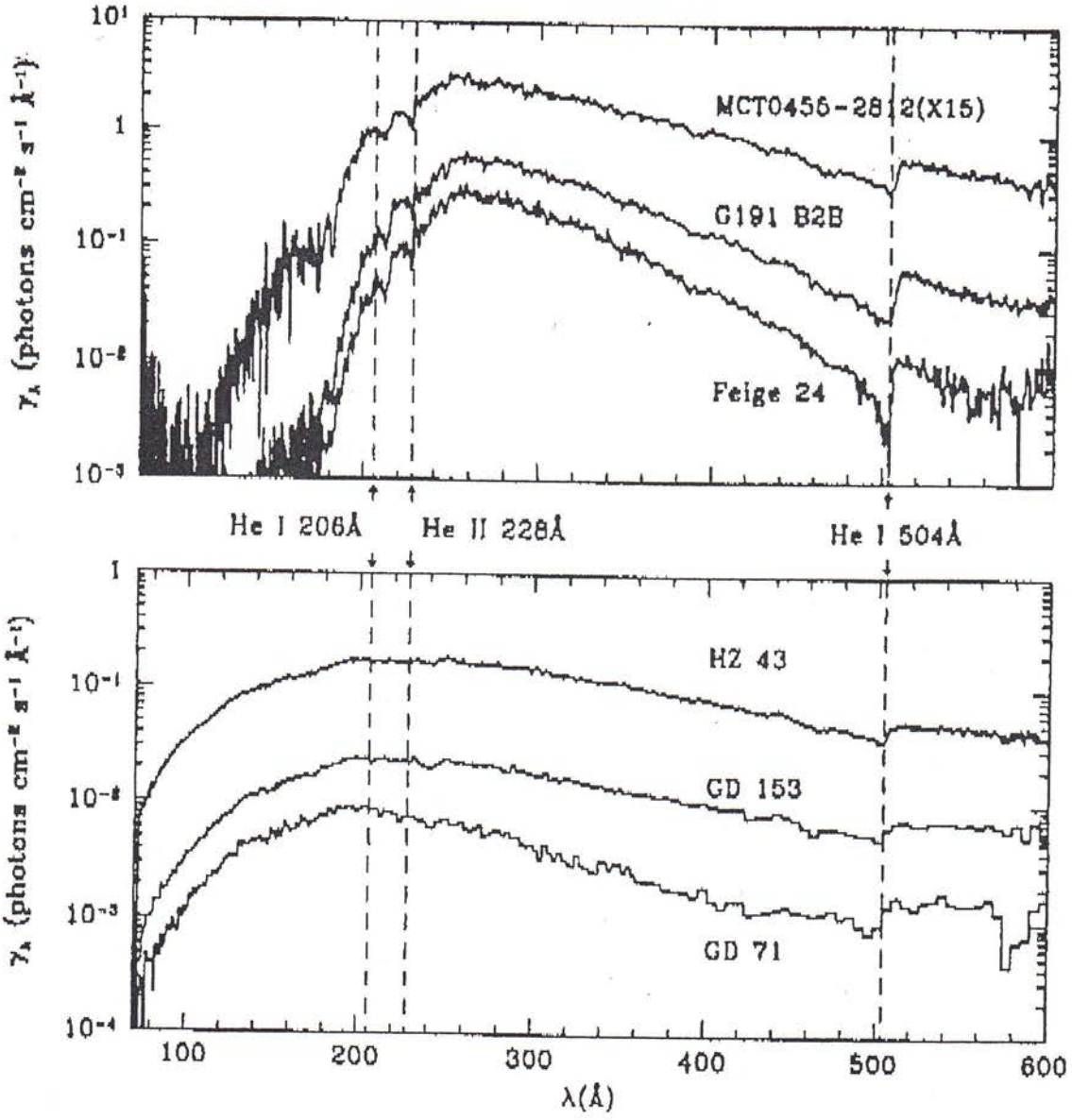


Fig. 2-13. EUVE spectra of hot white dwarfs as a composite of all three grating channels. The edge at 504 Å is due to photo-absorption by helium in the interstellar medium.

This figure is from Dupuis, Vennes, Bowyer, Pradhan and Thejil (Ap. J. vol. 455, p. 574, 1995).

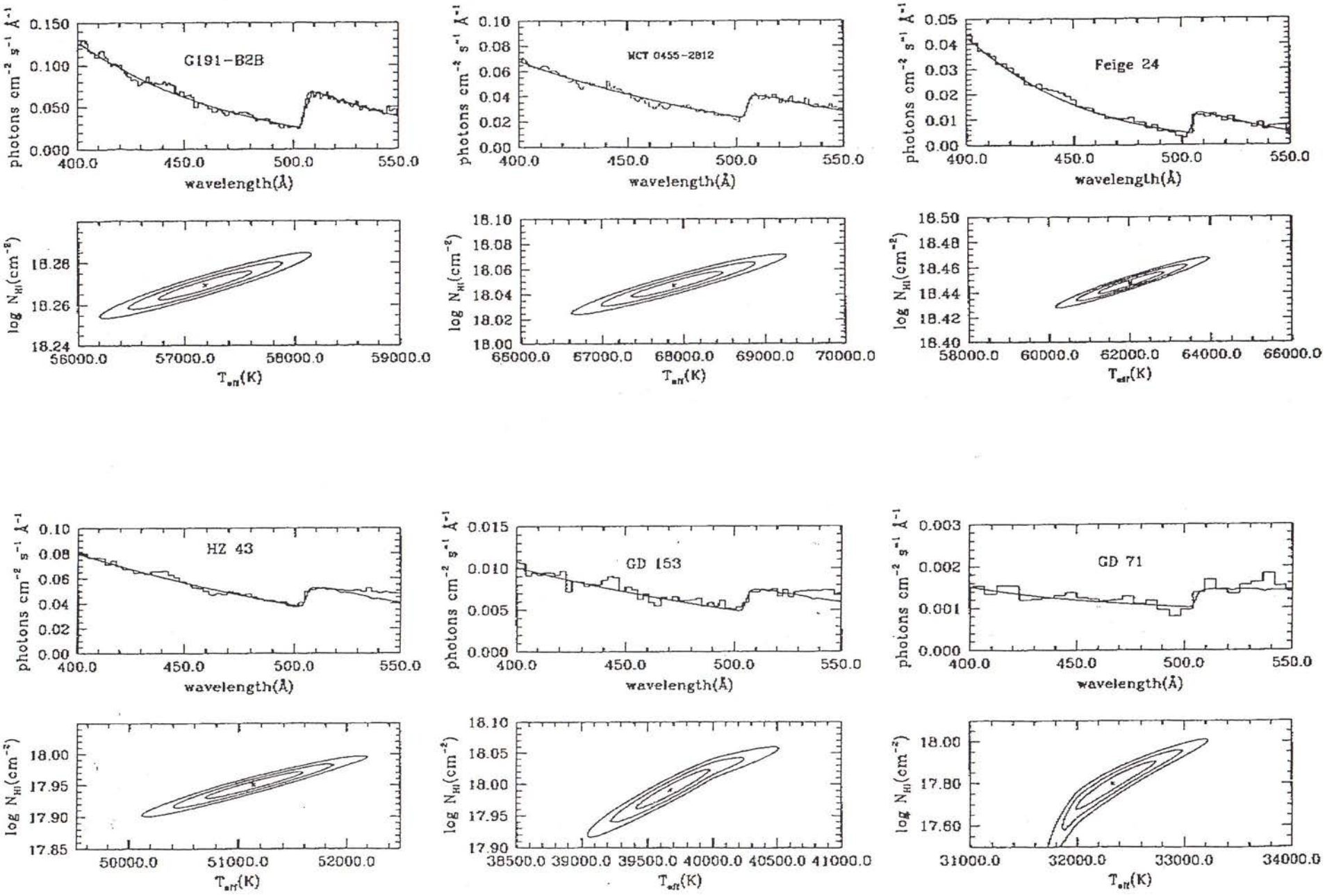


Fig. 2-14. Stellar temperatures and interstellar densities derived by Dupuis et al from Fig 2-13.

shown from 70 to 600 Angstroms. The intensity and shape of the dominant continuum are functions of the effective temperature and metallic content of the star, and the column density of hydrogen intervening along the line of sight in the ISM, while the strength of the photoionization edge at 504 Angstrom depends upon the ISM column density of helium. Figure 2-14 shows an example of the results obtained by model fitting of the data, resulting in the determination of the stellar temperatures and ISM column densities. Among the six targets, there is in excess of a factor of 4 range in the column densities and factor 2 in the temperatures. This exemplifies the scientific results for which the EUVE spectrometers were designed.

## *2.2 The X-Ray Multi-Mirror Spectrograph*

As seen in equation (2-31), the sensitivity improves linearly with the effective collecting area. However, large area telescopes of reasonable cost are of low spatial resolution (~ arcminute). To obtain spectral resolution sufficient ($\lambda/\Delta\lambda \sim 100$) for soft x-ray astronomy (0.5-2 keV) thereby requires high dispersion. As shown in Sec. 2.1, grazing incidence in-plane reflection gratings provide the unique combination of high dispersion and wide spectral coverage at high efficiency. They can therefore be coupled to such large, low resolution telescopes to yield moderate resolution spectroscopy of faint x-ray sources. This idea and a VLS grating stack concept became the basis for the X-Ray Multi-Mirror Spectroscopy Observatory[39,40] now being constructed and calibrated for flight.

The basic concept is the same as for the EUVE spectrometer (Sec. 2.2), using the grazing incidence VLS grating design of the in-plane variety to obtain maximum dispersion for a nearly stigmatic spectrum imaged by a flat detector surface oriented normal to the beam. Also as in the case of EUVE, the grating is placed in the converging beam from the secondary of a grazing incidence telescope. However, the higher energy photons for which XMM is targeted (in a two octave region centered near 1 keV ~ 12 Angstroms) requires shallower graze angles for both the telescope mirrors and for the grating. This causes a single grating of practical length to intercept only a small fraction of the large aperture beam from a nested array of telescope mirrors. Therefore, high throughput spectroscopy requires that multiple gratings be stacked in order to fill the aperture (Figure 2-15). This provides several hundred $cm^2$ in effective area[39].

A useful feature of the XMM spectrograph design is that identical VLS gratings can be used for all levels, provided either the incidence angle or the distance to the individual gratings varies slightly[39]. This results in individual grating spectra which coincide at the detector surface, and allows for the cost-effective production of the grating array as a stack of identical replicas from a single master design.

To determine the spectral resolution limited by the telescope and detector imaging, one differentiates the grating equation relative to both the angles of incidence and diffraction:

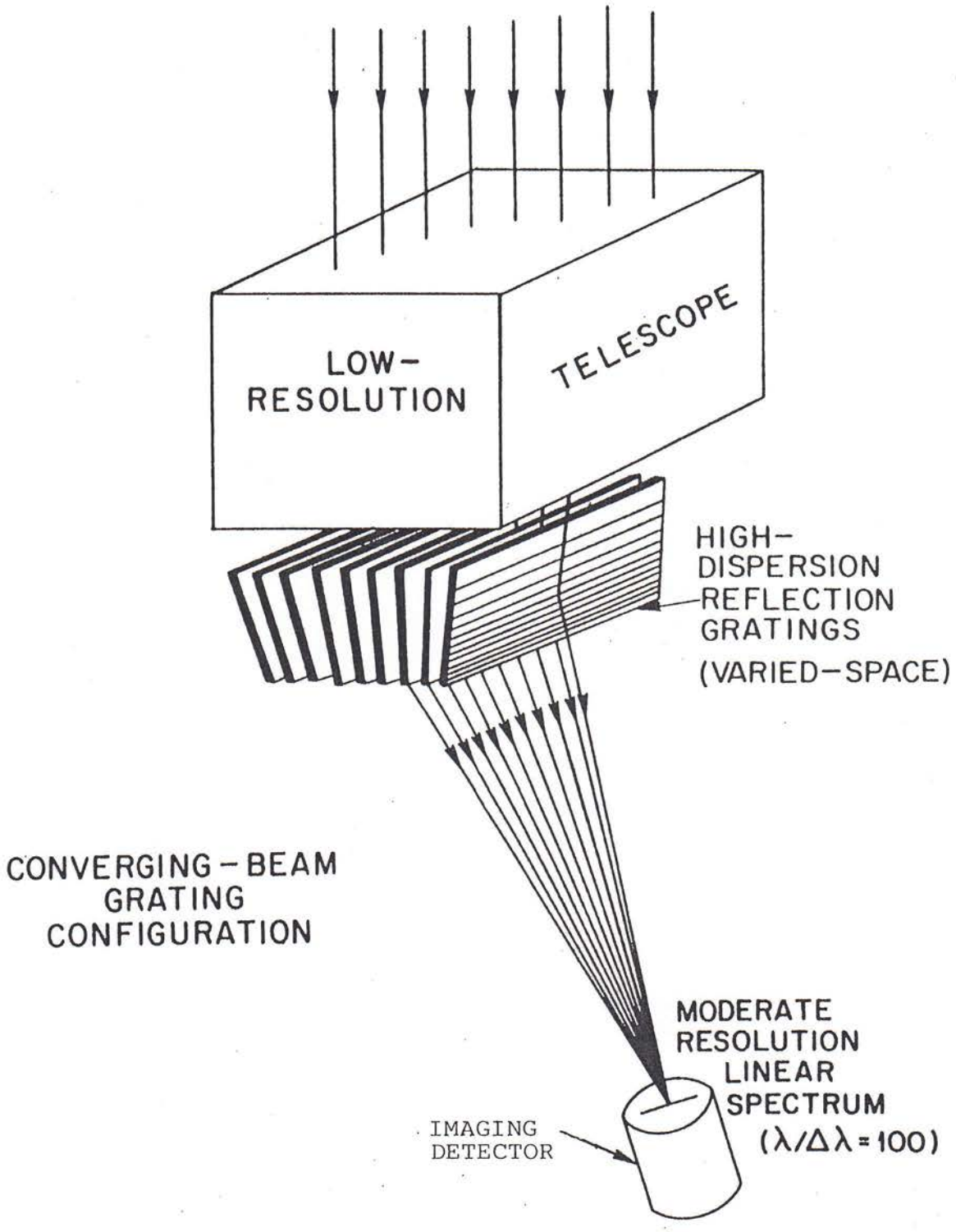


Fig. 2-15. VLS plane grating scheme for the X-ray Multi-Mirror Observatory, resulting in a large collection area spectrograph.

$$m\,\Delta\lambda / d = (\Delta\beta \cos\beta - \Delta\alpha \cos\alpha) \qquad (2\text{-}34)$$

Because both the telescope image and detector response profiles can be well approximated by normal (Gaussian) distributions and $\Delta\alpha$ is does not depend upon $\Delta\beta$, the widths should be summed in quadrature:

$$\Delta\lambda = (d/m)\,[\,(\Delta\beta \cos\beta)^2 + (\Delta\alpha \cos\alpha)^2\,]^{1/2} \qquad (2\text{-}35)$$

Dividing this by the blazed wavelength [equation (2-27)], making the sine approximations valid for grazing angles $\alpha^*$ and $\beta^*$, and substituting $\Delta\alpha = T\Delta\tau/r$ and $\Delta\beta = \Delta x_{det}/r'$, where the terms have been previously defined (Sec. 2.1), the resolving power can be expressed in convenient input parameters:

$$(\lambda/\Delta\lambda)_{blaze} \cong (r/T)(\varepsilon_{blaze}-1)\sin\gamma\,/[(\varepsilon_{blaze}\,\Delta\tau)^2 + (\Delta x_{det}/T)^2/\eta^2]^{1/2} \qquad (2\text{-}36)$$

where the absolute value is taken in the event of a negative value. Typically, we have a magnitude for $\eta = r'/r$ which is very close to unity for the VLS grating. Equation (2-36) reveals that there is a trade-off between spectral resolution and blaze efficiency ($\varepsilon_{blaze}$) in that low efficiency reduces the effect of the telescope blur through its demagnification [also see equation (2-17)].

In the case of the XMM spectrometer, the original design parameters were T = 8000 mm, r = 7500 mm, $\varepsilon_{blaze} = 0.5$, $\gamma = 2^o$, $\Delta\tau = 2.9 \times 10^{-4}$ radians (1 arcminute) and $\Delta x_{det}$ = 0.5 mm. Using equation (2-36), the resolving power is calculated to be ~ 100 at the blazed wavelengths (15 Angstroms in first order and 7.5 Angstroms in second order).

## *2.3 Laboratory High Resolution Erect Field Spectrometers (HIREFS)*

### a) Scanning Concept and Fermat Analysis

The spectrograph presented above delivers a fixed spectrum onto an imaging detector. This is adequate for astronomical observations, as the low signal flux from distant sources requires extremely long exposure times to accumulate the spectrum. The price paid for this multiplexing advantage and for the high throughput of a slitless astronomical spectrograph is a resolution limited by the image quality of the collecting mirror and the detector. Such resolution is often sufficient for the initial spectroscopic analysis of most astrophysical sources, whose spectral content is dominated by the cosmic abundance of hydrogen and helium (as exemplified in Figure 2-13).

However, laboratory sources of soft x-ray and extreme ultraviolet radiation contain a larger variety of elements, and such sources are also much more intense. The former condition requires higher spectral resolution to separate the large number of emission lines and other spectral features present, and the latter provides a means for doing this. If an exit slit of narrow width is used as the resolving element at the focal surface, then the dispersive contribution from the detector pixel width is eliminated. Use of an entrance slit similarly removes the contribution from the large, relatively low resolution telescope. The spectral resolution is limited only by the optical aberrations, with the dispersive contributions [equation (2-17)] made small by use of sufficiently narrow slit widths.

However, construction of a wavelength spectrum using a monochromator requires some means of adjusting the value in wavelength which passes through the exit slit. This slit could be translated along the focal surface or the grating could be rotated and the slits moved only along the fixed principal rays to compensate for any change in the focal length of the grating. Unfortunately, in either case, the distances over which the slits must move are enormous in the case of a conventional grating, due to the grazing incidence focal surface [equations (1-12) and (1-13), respectively].

The normal incidence focal surface of the VLS plane grating geometry, as shown for the example in Figure 2-5, provides a convenient solution to this problem. Consider placing an exit slit at the first order focus of the grating. As the focal lengths are the same in zero and first order, and as the plane grating surface provides no focusing power in the zero order image, it can be simply rotated about its central groove to bring the point-focused zero order image through this fixed exit slit. Due to the fact that the spectrographic focal lengths do not vary significantly between first and zero order, it is intuitively clear that the amount of defocusing present at the fixed exit slit for intermediate grating rotations must be small. For example, using the same focal length and groove density as for the classical concave grating (solid curve reproduced on this logarithmic scale from Figure 1-2b), the long-dashed curve of Figure 2-16 shows the defocusing (calculated from the light-path function) caused by rotation of a plane VLS grating in converging light. The dramatic reduction (a factor of ~100) in the optical aberration is "astronomical" in nature. Thus, while not originally intended with this

Fig. 2-16. Geometrical de-focusing aberration resulting from grating rotation using stationary slits. Solid curve is a conventional grating and dashed curves are different optimizations of a varied line-space plane grating.

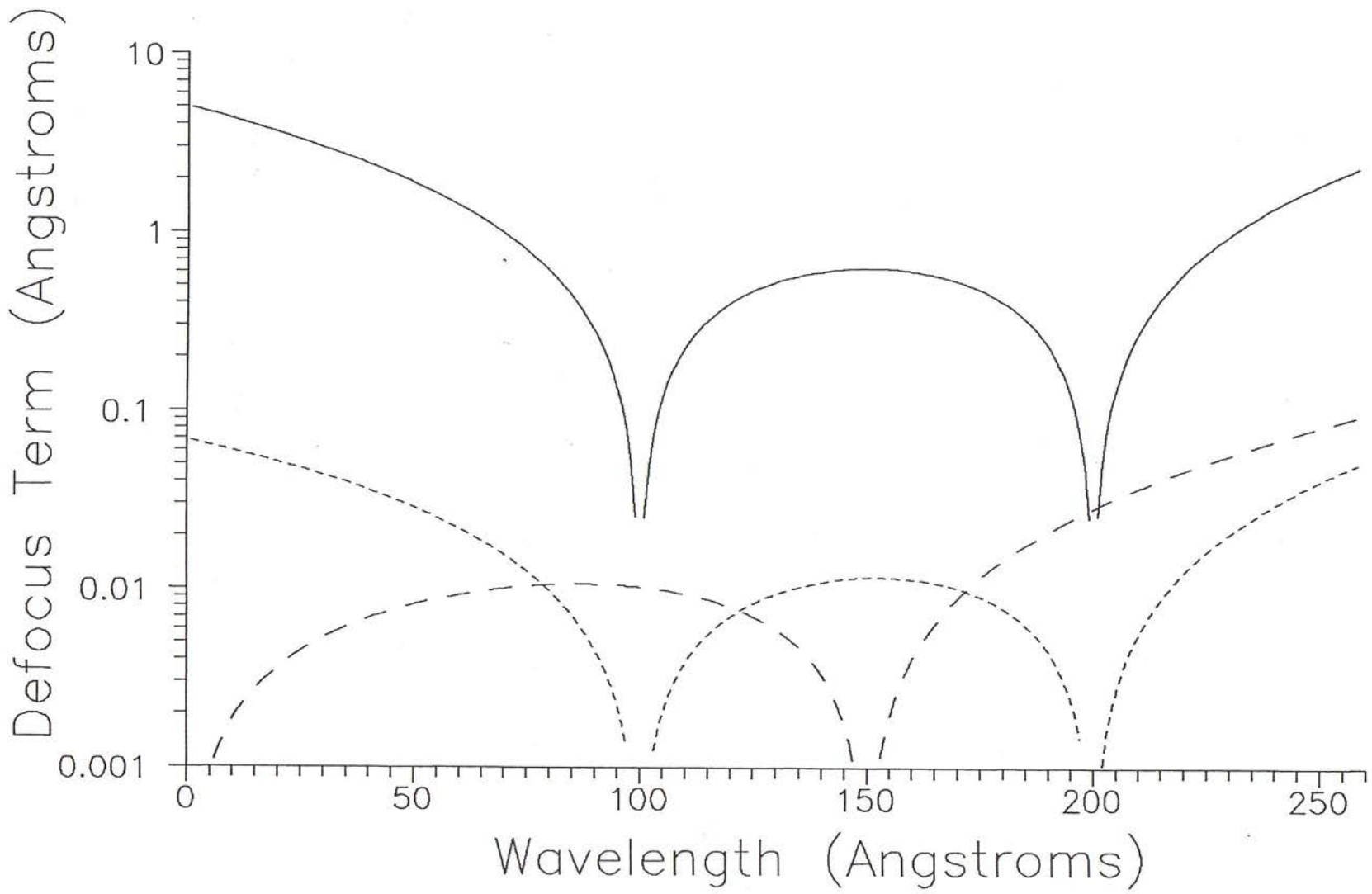

capability in mind, the plane VLS grating has enormous potential as a scanning monochromator, or to change the bandpass of the spectrum imaged by a stationary imaging detector. [The magnitude of such rotational aberrations was also found to be quite small during an error analysis done to determine the misalignment tolerances[30] in the mechanical design of the mounting structures for the EUVE spectrometers. It was found that the wavelength striking a fixed point on the detector would change without a significant broadening of the spectral width.]

One can minimize the spectral aberrations in the first order spectrum by moving the second correction point from zero order to a finite wavelength. Because of the normal incidence focal surface shown in Figure 2-5, this requires only a slight change in the focal distance. From Fermat's equations (1-1) and (1-5), the defocusing for a plane VLS grating at a wavelength other than $\lambda_c$ is:

$$F_{20} = 1/2(\cos^2\alpha /r + \cos^2\beta /r') - 1/2(\lambda/\lambda_c)(\cos^2\alpha_c /r + \cos^2\beta_c /r') \qquad (2\text{-}37)$$

where the focal distance r' is constant with wavelength. The second term of this equation results from choosing $N_{20}$ to cancel defocusing at the correction wavelength. Allowing the magnitudes of r' and r to be different provides the degree of freedom necessary to eliminate $F_{20}$ at a second wavelength, by specifying[41,42]:

$$\eta = r'_1/r = - [\cos^2\beta_2 - (\lambda_2/\lambda_1)\cos^2\beta_1] / [\cos^2\alpha_2-(\lambda_2/\lambda_1)\cos^2\alpha_1] \qquad (2\text{-}38)$$

where $\lambda_1$ is the original correction wavelength ($\lambda_c$) and where $\lambda_2$ is the new non-zero correction wavelength.

Now consider a simple rotational mounting, where the angle included between the incident and diffracted rays at the grating pole is constant ($2\theta = \alpha + \beta$). The incident and diffracted angles are determined by the grating equation more conveniently written as follows:

$$\alpha = \theta - \arcsin[m\lambda / (2d_o\cos\theta)] \qquad (2\text{-}39)$$

$$\beta = \theta + \arcsin[m\lambda / (2d_o\cos\theta)] \qquad (2\text{-}40)$$

With this condition on $\alpha$ and $\beta$, one finds through numerical calculations of equation (2-38) that $\eta$ is very close to minus unity for ***any*** included angle $2\theta$. This is a uniquely useful result, as it holds equally well for both normal incidence ($2\theta \sim 0$) and grazing incidence ($2\theta \sim \pi$) mountings. This is interpreted geometrically as simply re-affirming that the optimal spectral focal surface is at normal incidence to the diffracted beam

regardless of the angle of incidence to the grating (a condition initially forced by the use of varied spacings to provide nearly equal distances r' and r).

In the case of an inside spectral order (m<0), equation (2-38) results in the virtual distance -r being less than the focal distance r', that is abs($\eta$) > 1. In the outside order (m>0), abs($\eta$) < 1. Using the 1500 g/mm grating as before in the inside order with $\psi$ = 1640, the required value of $\eta$ is - 1.019. Such small differences required in the object and image distances have no deleterious effect upon the shape of the focal curve [equation (2-20), allowing the spectrometer to retain its use as an erect field spectrograph. Using Fermat's principle, the defocusing aberration of the optimized grating (with $\eta$ = -1.019) is shown by the short-dashed curve in Figure 2-16. While the spectral aberration no longer vanishes at a wavelength of zero, this is a spectroscopically useless wavelength undeserved of such correction.

The scanning concept of the VLS plane grating monochromator is illustrated in Figure 2-17 taken from the author's patent[42]. Rotation of the grating about its central groove, denoted here by the symbol G, results in a change of the (principal) wavelength directed along principal diffracted ray **90** through the fixed image position **I**. Either a slit **X** may be provided at this location, or the spectrum may be recorded on a normal incidence detector **178** which approximates the meridional curve **212**. This curve is still given by equation (2-20) which permits input of $\eta$ values other than -1. The image denoted **O** is for a generic wavelength (non-principal wavelength) in the dispersed spectrum The incident object point V is virtual (negative object distance is denoted by the dashed line), and is either slightly less than the focal distance (m<0) or slightly greater (m>0). The sagittal focal circle **214** is drawn for the original case of equal object and image distances.

The top panel of Figure 2-17 is a plot of the Fermat-calculated resolving power at the fixed image point as a function of scanned wavelength, for the case of a 1200 g/mm grating at an included angle of 164° in a simple rotational mount. The classical concave grating in divergent incident light is shown by the curve labelled **200** (PRIOR ART), and the two convergent beam plane VLS grating designs discussed above yield the curves labelled **204** ($\eta$ = -1) and **202** [optimized $\eta$ per equation (2-38)]. These curves include the higher-order aberrations of coma and spherical aberration, hence the resolving power does not become infinite at the correction points where defocusing is in fact exactly zero.

The ability to maintain the erect spectrographic field while changing the principal wavelength results in performance (e.g. resolution and efficiency) which is a function of both the *principal wavelength* $\lambda_p$ setting determined by the rotation angle of the grating and the *spectrum wavelength* $\lambda$ along the detection curve. Figure 2-18a is a three-dimensional plot of the Fermat-calculated optical resolution as a function of both the principal and spectrum wavelengths for a commercial Model HIREFS-164. The outside

Fig. 2-17. Scanning concept of VLS plane or large radius grating monochromator. Fermat calculations plotted in the top panel.

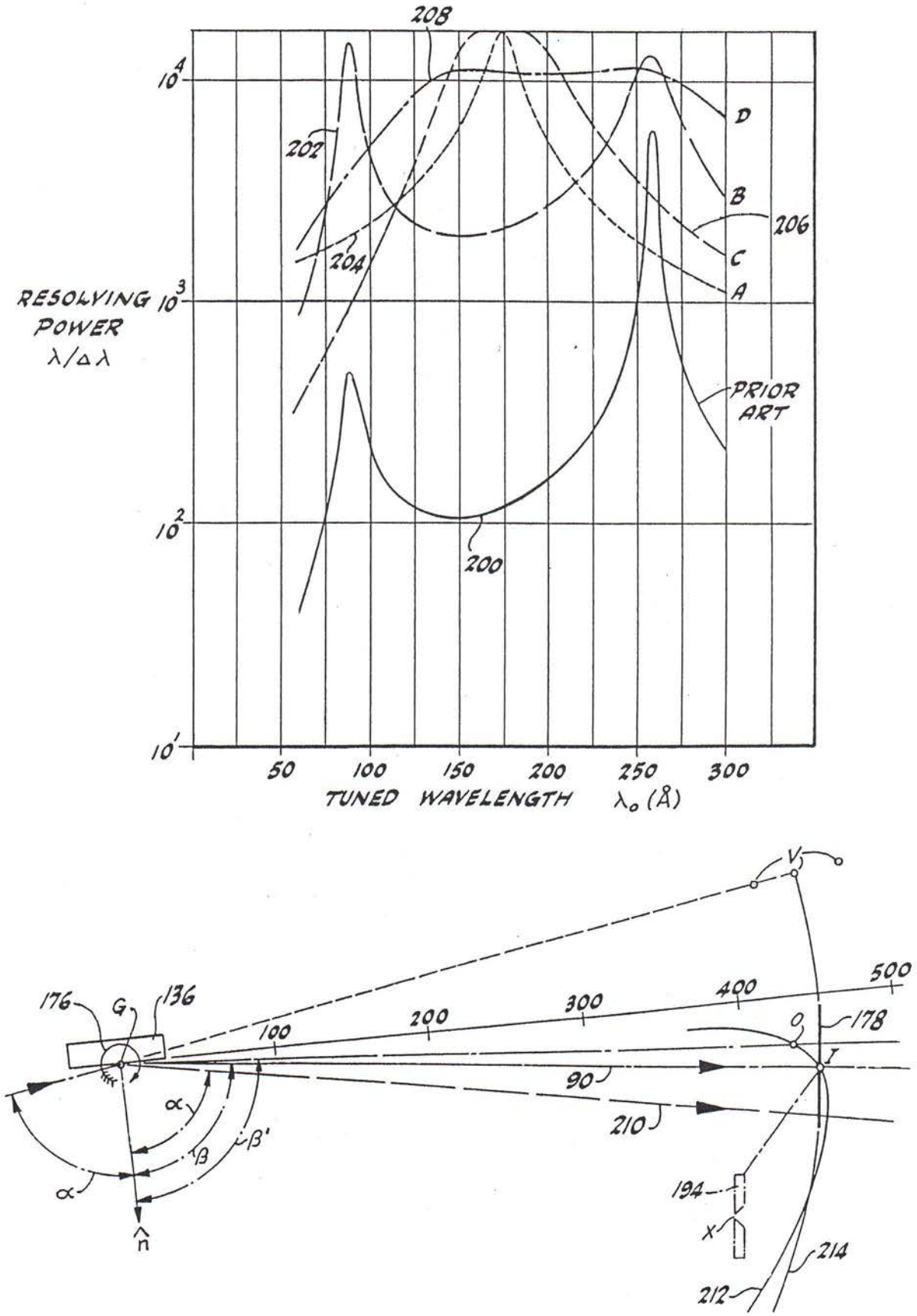

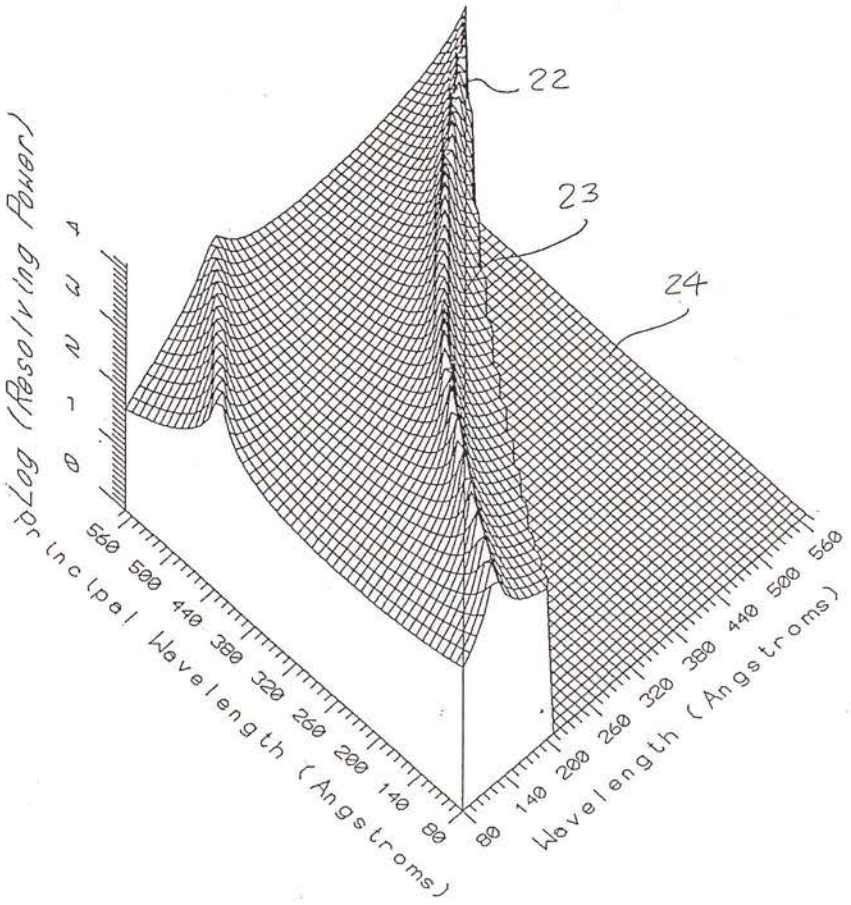


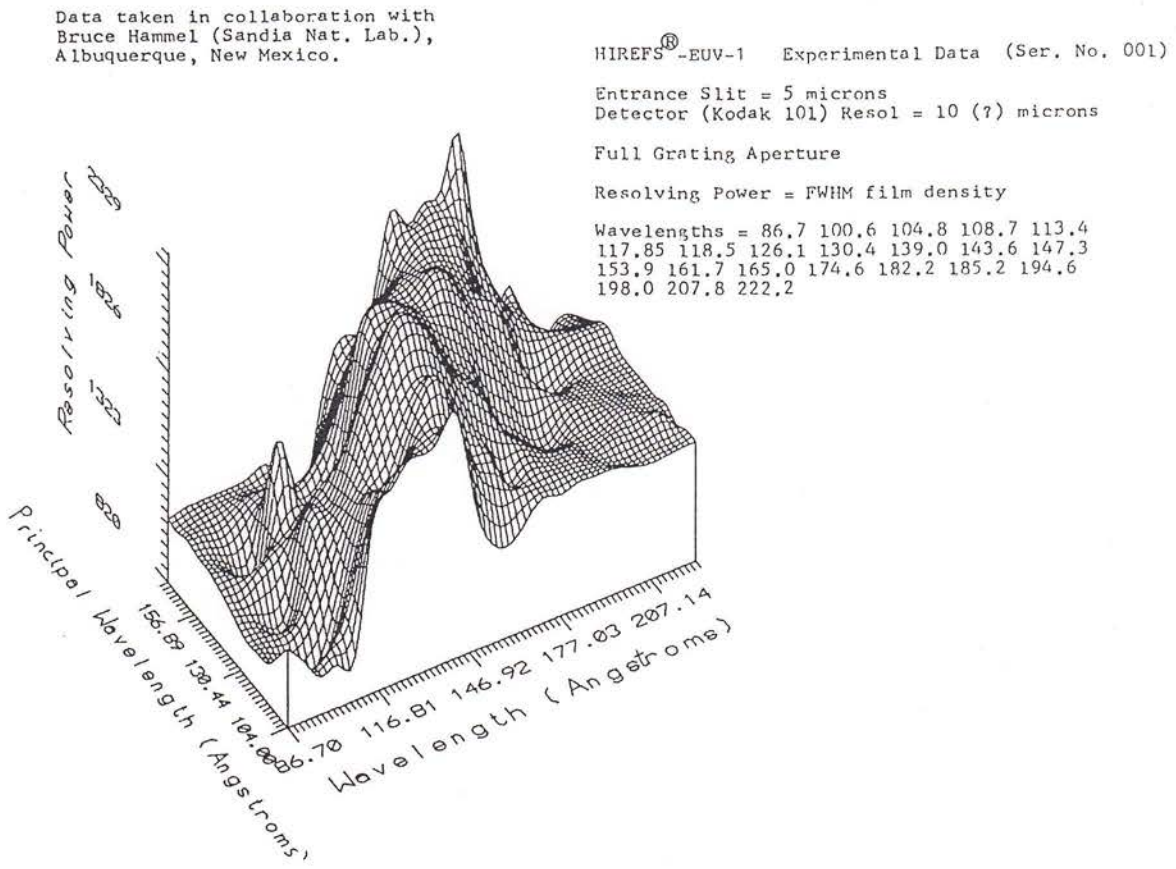


Fig. 2-18. Spectral resolving power as a function of principal (through fixed image position) wavelength and measured wavelength in the focal plane: a) limited by theoretical grating aberrations; b) measured using 5 micron entrance slit and film.

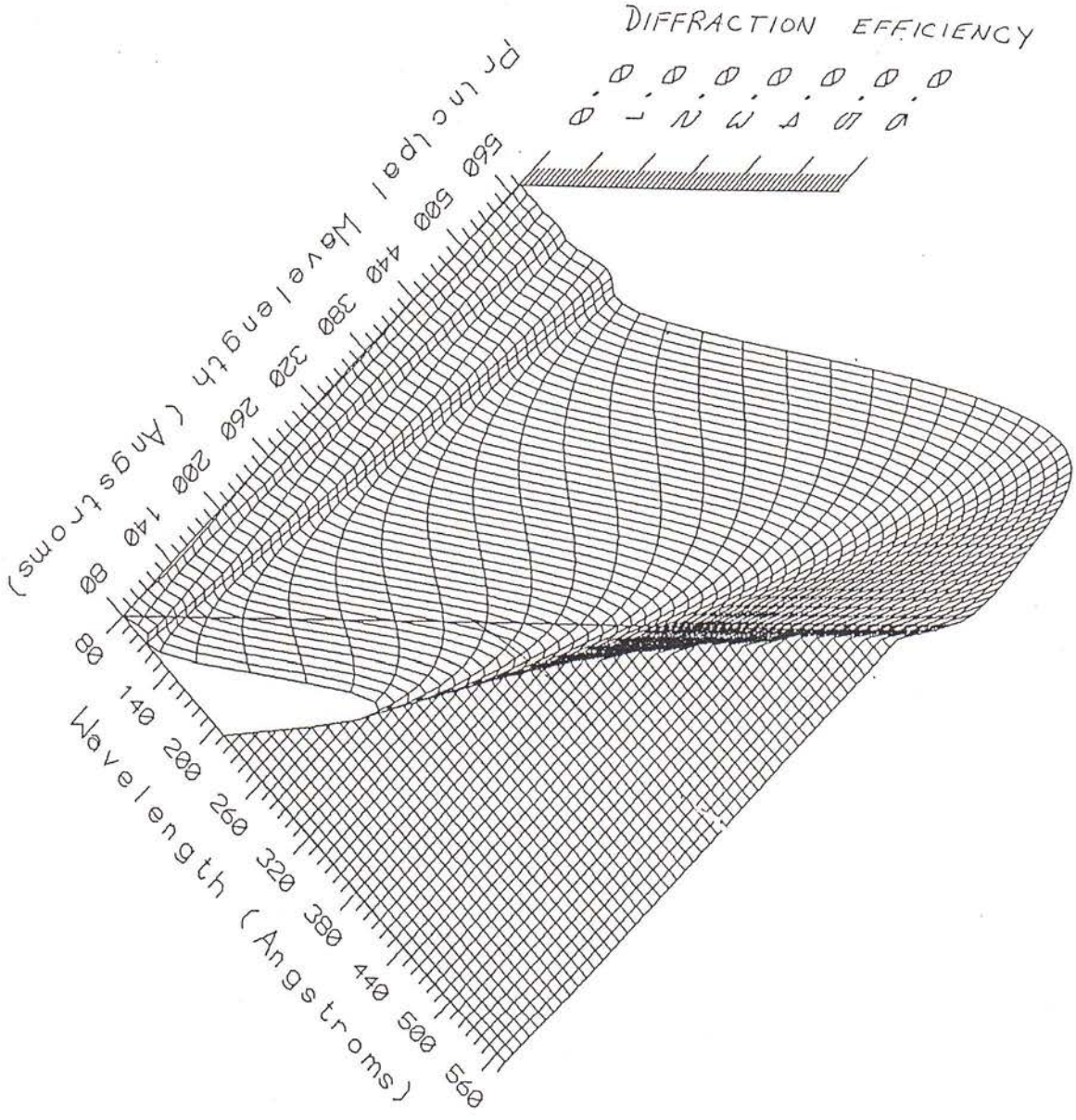


Fig. 2-19. Relative diffraction efficiency calculated from scalar Kirchoff theory, as a function of principal and measured wavelength.

spectral order is used for an active grating ruled width of 62.5 mm and the detection surface is the plane oriented perpendicular to the principal diffracted ray. The plane **23** is for $\lambda=\lambda_p$, corresponding to the fixed image position along the principal axis. The high resolution ridge **22** intersects this plane at two points corresponding to the two correction wavelengths in $\lambda_p$ for which defocusing is eliminated through use of equation (2-38). The correction wavelengths for this model are 180 and 520 Angstroms. At any one principal wavelength, the surface **24** of Figure 2-18a becomes a curve of resolving power versus wavelength in the dispersed spectrum. The decline in resolution away from the ridge corresponds to the flat and normal incidence detection surface deviating from the meridional focal curve. The abrupt drop to the right of the ridge corresponds to the long wavelength limit of the dispersed spectrum at the *horizon wavelength* which diffracts along the tangent of the grating surface. Measurements of the resolving power obtained with this spectrometer using a 5 micron entrance slit and film to minimize the dispersive aberrations, are shown in Figure 2-18b. The source of extreme ultraviolet radiation in this experiment was a capacitor discharge (Garton ) tube, believed to yield emission lines narrower than the spectrometer resolution.

Figure 2-19 is a three-dimensional plot of the relative blaze efficiency as a function of the principal and spectrum wavelengths. The calculations used the unnormalized method described in Sec. 2.1g). As in Figure 2-18a, curves of intersection with constant principal wavelengths represent the efficiency as a function of dispersed wavelength, while the curve of intersection with the plane $\lambda=\lambda_p$ represents the efficiency profile of the monochromator configuration at the wavelength diffracted to the fixed exit slit. While no such three-dimensional array of measurements were feasible to perform in the laboratory, the spectra obtained from this instrument showed the general trend of the more intense spectral lines occurring near the wavelengths predicted by these calculations.

## b) Variations on a Theme, and Ultra-Large Radii of Curvature

While maintaining the fundamental concept of this design, equation (2-38) can obviously be replaced by other aberration criteria tailored for optimum performance in specific high resolution applications. For example, if the highest possible spectral resolution must be maintained over a moderate wavelength centered on a single spectral feature, then one would seek to set $F_{20}$ and its first derivative with respect to wavelength ($\delta F_{20}/\delta\lambda$) equal to zero at that wavelength. In this case, a slightly different value of $\eta$ results[42]:

$$\eta = -\left[\cos^2\beta(\cos\alpha+\cos\beta) + 2\cos\beta\sin\beta(\sin\beta-\sin\alpha)\right] / \left[\cos^2\alpha(\cos\alpha+\cos\beta) - 2\cos\alpha\sin\alpha(\sin\beta-\sin\alpha)\right] \qquad (2\text{-}41)$$

The curve labelled **206** is the Fermat-calculated resolving power for this case, exhibiting the designed stationary value at the single correction wavelength of 150 Angstroms near which defocusing remains negligible.

The high resolution plateau may be widened further by gaining an additional degree of freedom through use of a finite radius of curvature (R) chosen to remove the defocusing term at a second wavelength while maintaining removing of defocusing and its first derivative at the first correction wavelength. Using the light-path function, this results in a set of three equations in three unknowns (r, $r'_I$, R). These are solved by hand, which after extensive algebraic manipulation yield[42]:

$$-r/R = (b_1a_2-b_2a_1)/(b_2c_1-b_1c_2) \tag{2-42}$$

$$r'_I/R = b_1/(c_1+a_1R/-r) \tag{2-43}$$

where

$$a_1 = -\cos^2\alpha_1(\cos\alpha_1+\cos\beta_1) + 2\cos\alpha_1\sin\alpha_1(\sin\beta_1-\sin\alpha_1) \tag{2-44}$$

$$a_2 = -\cos^2\alpha_1(\sin\beta_2-\sin\alpha_2) + \cos^2\alpha_2(\sin\beta_1-\sin\alpha_1) \tag{2-45}$$

$$b_1 = -\cos^2\beta_1(\cos\alpha_1+\cos\beta_1) - 2\cos\beta_1\sin\beta_1(\sin\beta_1-\sin\alpha_1) \tag{2-46}$$

$$b_2 = -\cos^2\beta_1(\sin\beta_2-\sin\alpha_2) + \cos^2\beta_2(\sin\beta_1-\sin\alpha_1) \tag{2-47}$$

$$c_1 = -2(1-\sin\beta_1\sin\alpha_1 + \cos\beta_1\cos\alpha_1) \tag{2-48}$$

$$c_2 = (\cos\alpha_2+\cos\beta_2)(\sin\beta_1-\sin\alpha_1) - (\cos\alpha_1+\cos\beta_1)(\sin\beta_2-\sin\alpha_2) \tag{2-49}$$

The resulting resolving power curve is shown by curve **208** in Figure 2-17, displaying the very broad plateau intended by this optimization procedure. For outside spectral orders, the radius of curvature is negative (convex), while for inside orders it is positive (concave). The magnitude of the radius is extremely large, in the example used to generate curve **208** it was 300 times larger than the focal length of the grating. Such an ultra-large radius of curvature grating surface is nearly flat.

Because of the finite radius of curvature, the focal curve deviates from that given in equation (2-20) for a plane surface, and is found by solving for $F_{20}$=0 at all wavelengths from equations (1-1) and (1-5) while substituting the above quantities and the value of $N_{20}$ obtained by forcing $F_{20} = 0$ at $\lambda_1$. The result is:

$$r'/R = \cos^2\beta/[c(\sin\beta-\sin\alpha_I)+\cos^2\alpha/(-r/R) + \cos\alpha + \cos\beta_I) \qquad (2\text{-}50)$$

where

$$c = [-\cos^2\alpha_1/(-r/R)+\cos^2\beta_1/(r'_I/R) - (\cos\alpha_1+\cos\beta_1)]/(\sin\beta_1-\sin\alpha_1) \qquad (2\text{-}51)$$

## c) VLS Correction of Geometrical Mirror Aberrations

For an object of infinitesimal or randomized width, equations (1-1) and (1-8) are used to determine the varied-space parameter $N_{30}$ which eliminates grating coma at one wavelength of choice. Similarly, equations (1-1) and (1-9) allow the elimination of grating spherical aberration through use of a non-zero value for $N_{40}$. The Fermat calculations given in the preceding sections, including Figures 2-17 and 2-18 removed these higher order aberrations at a wavelength chosen near the center of the scanned wavelength spectrum. This procedure is optimum when the mirror which provides convergent radiation onto the grating is free of aberrations, or has aberrations which are not precisely correlated with meridional aperture by a smooth analytical function.

However, the mirror used to provide the converging beam to the grating resolution is often a simple spherical section. Even at unit magnification ($r'_M = r_M$), such a mirror exhibits some spherical aberration, which can be calculated using equation (1-8) with $\alpha = \beta = \phi$ for a mirror. This aberration can be negated at one wavelength by offsetting the value of $N_{40}$ from that given above:

$$\Delta N_{40} = -1/4\ (r_M/r^4)\cos^4\alpha\ \tan^2\phi\ /(m\lambda) \qquad (2\text{-}52)$$

Numerical raytracings of Figure 2-20 confirm the removal of spherical aberration at the chosen wavelength of 180 Angstroms, and a significant reduction in spherical aberration across the spectrum (e.g. the factor of ~ 4 reduction at 520 Angstroms), due to the slow variation of the optimum correction as the angle of incidence changes in the rotational mount to change the wavelength. These VLS corrections to the mirror aberrations were made to the commercial HIREFS beginning with the first units manufactured in 1987.

In addition to allowing for correction of mirror spherical aberration, the author's patent[42] also indicated that correction of mirror coma can be provided by the same procedure of adjusting the corresponding ruling coefficient, and that such coma is significant for mirror magnifications away from unity. This aberration is contained in the $L_{30}$ term of the light-path function of a spherical mirror [see equation (1-8) with $\alpha = \beta = \phi$], requiring a balancing by use of a $\Delta N_{30}$ term in the varied spacings, the magnitude

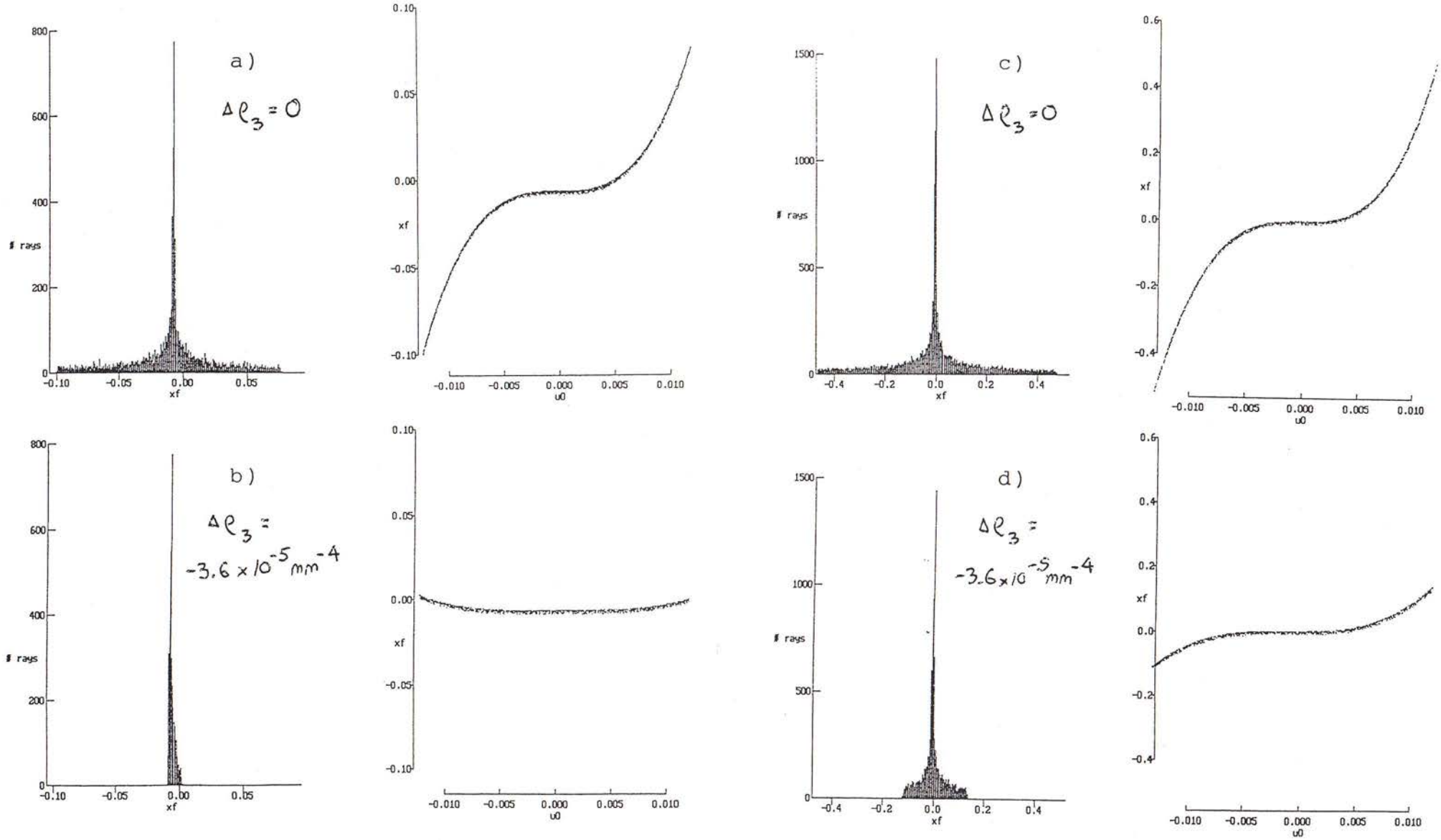


Fig. 2-20. VLS correction of spherical aberration from converging mirror in HIREFS model 164. At 180 Angstroms: a) no correction, b) with correction. At 520 Angstroms: c) no correction d) with correction optimized at 180 Angstroms. The phase spot diagrams to the right of each line profile plot the ray aberration position versus the angular aperture incident to the mirror. The S-shaped spot diagrams signify spherical aberration.

of which depends upon the magnification of the mirror and the spectral correction wavelength desired for the grating.

There are other such corrections possible, by using the ruling coefficients to balance the aberrations of other optics in the system. The magnitude of these corrections depends upon the detailed parameters of the optics. Adjustment of the ruling parameters can even be employed to correct for unintended imperfections in the shape of the other optical elements, provided they can be accurately characterized. The salient point is that such aberration correction is provided by the additional degrees of freedom inherent in this grating design.

## d) Stigmatic Configurations for Spatial Imaging

The above analysis has so far been restricted to spectral aberrations, that is those occurring in the meridional plane of incidence. However, as discussed in Sec. 1.3 b), removal of astigmatism is also often required in order to provide spatial resolution in the non-dispersive sagittal direction. In the case of the EUVE spectrometer, this was accomplished by use of a point object for the grating produced by a telescope mirror system comprised of surfaces of revolution. However, in the laboratory a simpler spherical mirror surface is advantageous in order to obtain the highest possible resolution. The meridional and sagittal focusing conditions for a spherical mirror are the same as those for a spherical grating [equations (1-5) and (1-6), respectively] where the angles of incidence and diffraction are replaced by the angle of incidence $\phi$ (equal to the angle of reflection). This results in the Coddington equations for a mirror:

Meridional Focusing: $$1 / r_M + 1 / r'_M = 2 / ( R_M \cos \phi ) \qquad (2\text{-}53)$$

Sagittal Focusing: $$1 / \underline{r}_M + 1 / \underline{r}'_M = 2 \cos \phi / R_M \qquad (2\text{-}54)$$

where the underlined quantities signify the values in the sagittal direction.

In the case of a near normal incidence mirror, the sagittal focal length is slightly longer than the meridional focal length. This can be exploited to provide a stigmatic spectrum by matching the offset between the image distance and the meridional object distance of the grating ($\eta$ not equal to 1). For example, to minimize the mirror aberrations, consider the case of unit magnification in the meridional direction (though other choices are possible due to the freedom to partially correct for mirror aberrations as shown above), and a point object for the mirror ( $\underline{r}_M = r_M = r'_M$). Then dividing equation (2-54) by equation (2-53) yields:

$$\kappa = r'_M / \underline{r}_M' = 2 \cos^2 \phi - 1 \qquad (2\text{-}55)$$

As the plane grating provides no focusing in its sagittal direction, removal of astigmatism at the meridional focus of the grating requires that the mirror focus in the grating dispersion direction at a distance of r behind the grating, and focus in the grating non-dispersive direction at a distance r' behind the grating. If the mirror and grating reflect in the same plane, then this stigmatic condition becomes:

$$(1/\kappa - 1) = [1 - 1/\mathrm{abs}(\eta)]\ r' / r'_M \qquad (2\text{-}56)$$

where $\eta = r'/-r$. As discussed previously, $\mathrm{abs}(\eta) > 1$ when the spectral order is negative. In this case, the bracketed term is a small positive number, and there is always a positive solution for $k < 1$, enabling choice of a finite incidence angle from equation (2-55). However if a positive spectral order is used then $\mathrm{abs}(\eta) < 1$, resulting in no stigmatic solution in this configuration. A solution is obtained in this case if the mirror and grating are crossed, so that the meridional plane of the mirror is the sagittal plane of the grating, and vice-versa. Equation (2-56) then changes to:

$$(1 - 1/\kappa) = [1 - 1 /\mathrm{abs}(\eta)]\ r'/r'_M \qquad (2\text{-}57)$$

The required angle of incidence $\phi$ is generally quite small, due to the value of $\mathrm{abs}(\eta)$ always being near 1. For example, consider the grating of Figure 2-16 where $\eta = 1.019$ Using a value of $r'/r'_M = 0.9$ to account for the fact that the mirror precedes the grating, equation (2-56) results in $\phi = 5.2^\circ$. This provides a stigmatic point at the correction wavelength. The astigmatism remains zero on the anastigmatic focal curve equal to the circle of radius r' centered on the grating, and is very small along the meridional focal curve. In the case of a monochromator, the astigmatism is zero at all wavelengths passing through the fixed exit slit.

This combination of a near-normal incidence spherical mirror and a grazing incidence VLS plane grating was constructed as a spectrograph to analyze a laser-produced plasma[43]. The mirror was coated with a Mo/Si multilayer[44] in order to provide normal incidence reflectivity for ionized aluminum lines near 160 Angstroms. The removal of astigmatism in the spectra provided spatial information on the dynamically expanding laser-plasma sphere which appeared spread out in the non-dispersive direction by an amount which depended on the level of ionization. Such spatial resolution provided by a stigmatic configuration is useful in studying the dynamics and cooling times of pulsed sources, and is useful in studying the steady-state condition of spatial variations within stable plasmas such as those provided by magnetic confinement.

Unfortunately, this simple configuration does not provide efficient results over broad spectral ranges, due to the narrow bandpass of the multilayer and its use at near-normal incidence for which access to wavelengths below approximately C-K (44 Angstroms) are problematic. A more general solution to the problem of providing a stigmatic spectrum is obtained by use of a grazing incidence mirror. Unfortunately,

equations (2-53) to (2-55) reveal that the ratio of sagittal to meridional focal length goes towards infinity as the angle of incidence approaches 90° for a spherical mirror. At an 85° angle (5° graze), the sagittal focal length is two orders of magnitude longer than the meridional, resulting in no practical reduction of astigmatism. In principle, this could be corrected by use of an ellipsoidal or toroidal mirror, however, the surface accuracy obtained at reasonable expense for such shapes are not sufficient to obtain the arcsecond image quality needed when limited by slits of narrow width.

The solution to this problem is shown in Figure 2-21, consisting of the insertion of an additional mirror **12** which is crossed relative to the converging mirror **108**. Mirror **12** has as its object the soft x-ray source **174** and focuses only in the non-dispersive (astigmatism) direction of the grating. Mirror **108** has as its object the narrow width of an entrance slit **92** and focuses only in the dispersive direction to provide the virtual object in the spectral direction. The two mirrors in combination form a Kirkpatrick-Baez mirror system[45], in which the focusing in the two directions is almost completely de-coupled at grazing incidence. In its application to providing a stigmatic spectrum, this de-coupling is exploited in two ways. First, the image quality in the non-dispersive direction need not be to the level of arcseconds, which allows the astigmatism mirror to be a moderate resolution bent mirror. Such a mirror can be inexpensively fabricated with a large aperture and thus provide a high collection angle for the spectrometer. Secondly, such a bent mirror can be adjusted in shape to provide adjustment of astigmatism independent of the spectral resolution. Therefore, this mirror will hereinafter be referred to as the *astigmatism control mirror.* By appropriate choice of the mirror shape, the astigmatism can be made to vanish, to be large or to be of any desired intermediate value useful for a particular experiment.

Figure 2-22 is a photograph showing a manufactured unit in accordance with the optical schematic of Figure 2-21. The incident beam passes through an entrance slit which is out of view to the right, strikes the astigmatism control mirror shown as the long assembly mounted to a large rotary bearing, proceeds to the meridional focusing mirror (covered by the circular protective metal plate) and then to the grating (underneath the rectangular metal piece which is attached to a sine-bar located along the bottom edge of the vacuum chamber. Vacuum feedthroughs allow selection of the slit width (5, 10, 20, 50, 100 or 200 microns), the bent mirror radius and radius gradient, the meridional mirror angle of incidence (fine tuning), the grating (4 positions) and the grating rotation angle (center wavelength), while under vacuum.

This grazing incidence system, composed of a rotatable VLS plane grating and a crossed grazing incidence mirror system, is a spectrograph/monochromator device which has been designed and manufactured as a commercial instrument by Hettrick Scientific Inc. under the tradename HIREFS. Models ranging in graze angle from 8° for use at extreme ultraviolet wavelengths to 2° for coverage down to the soft x-ray, have been tested using many different sources and detectors. The unique combination of an erect spectrographic field, a tunable wavelength at high resolution to a fixed image point,

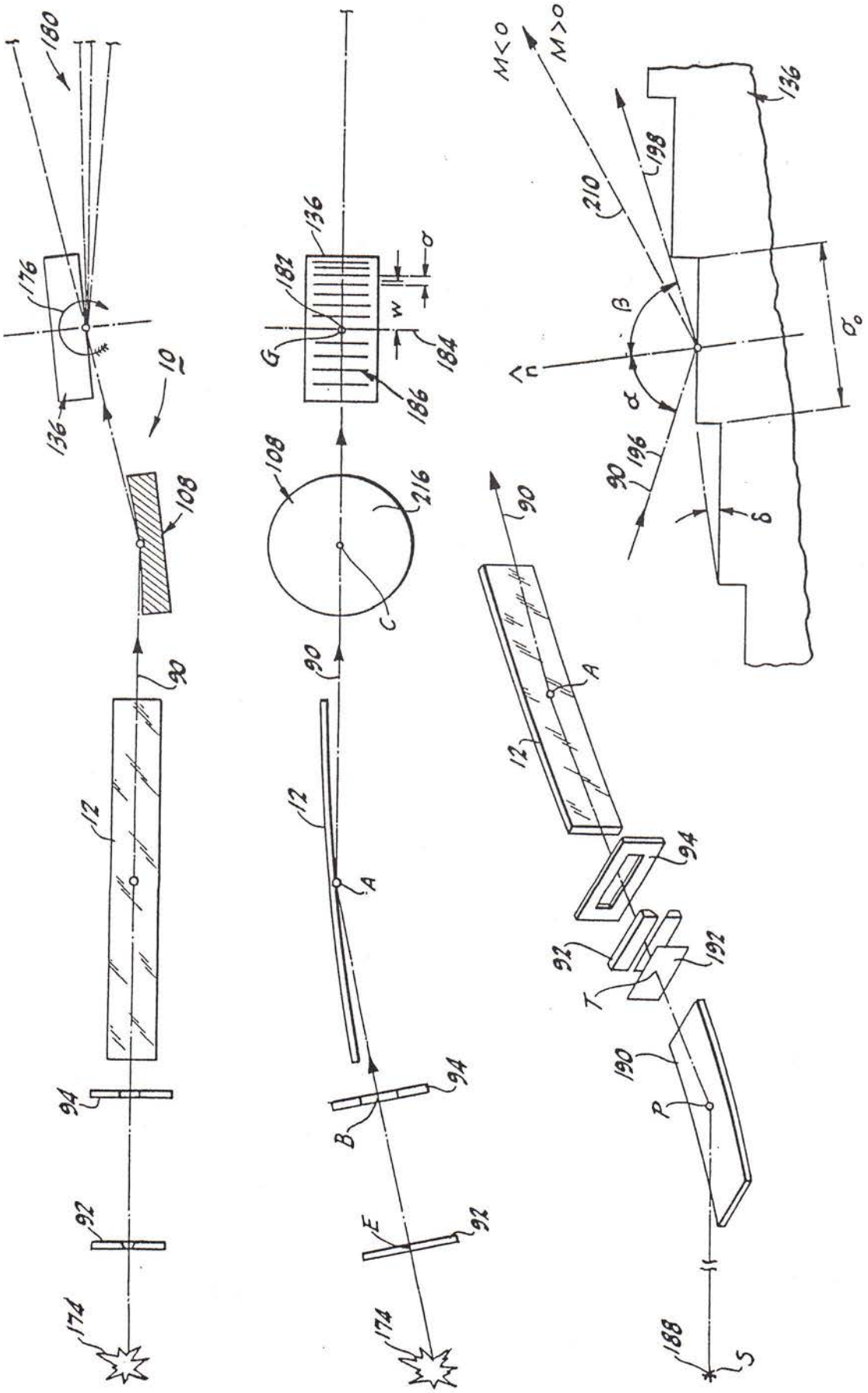


Fig. 2-21. HIREFS optical configuration, providing stigmatic spectra as a spectrograph or monochromator at grazing incidence.

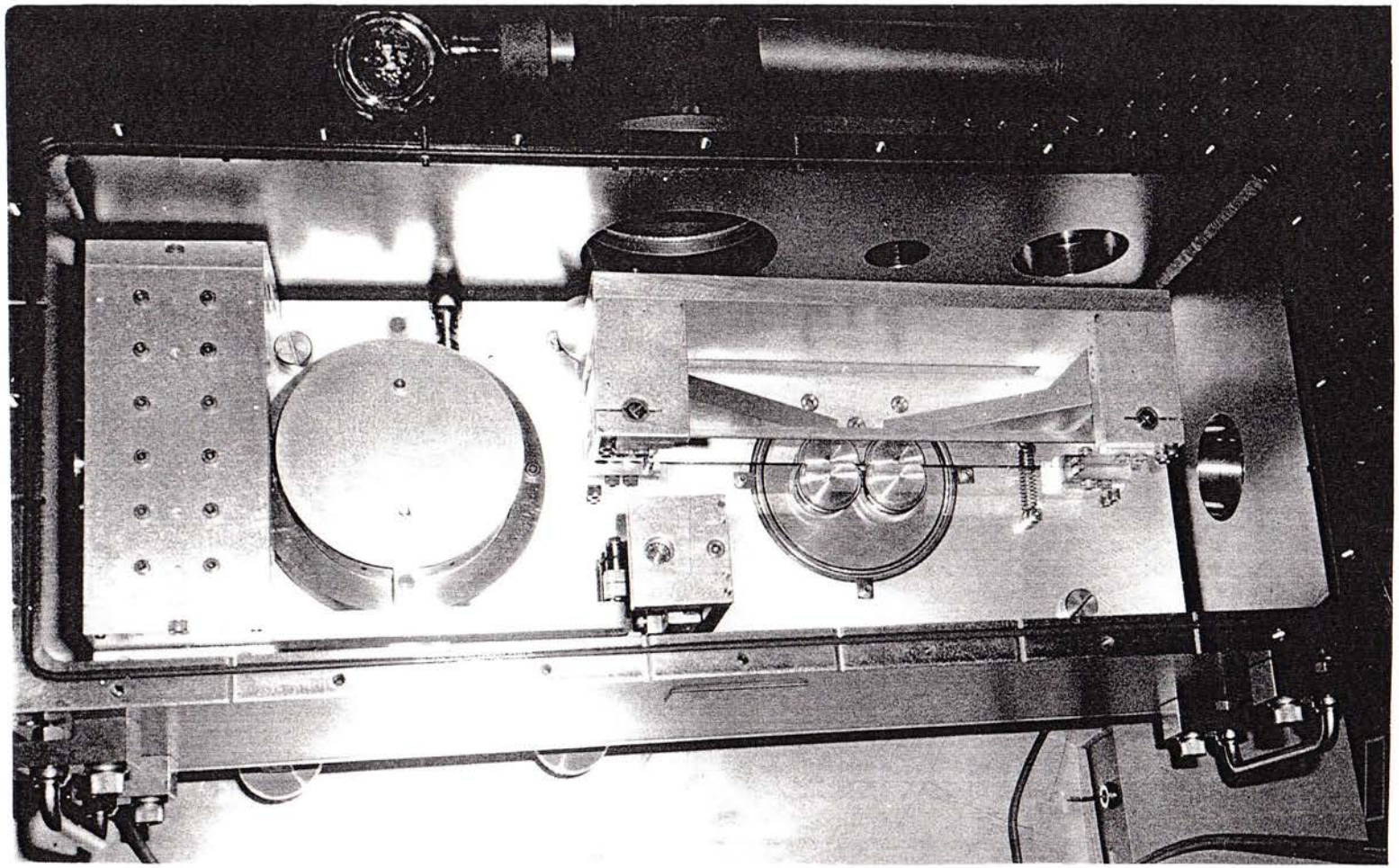

Fig. 2-22. Photograph of a commercial HIREFS showing the interior of optics chamber.

Hettrick Scientific, Inc.
SOFT X-RAY OPTICAL SYSTEMS
904 WRIGHT AVENUE UNIT #8
RICHMOND, CALIFORNIA 94804
(415) 234-3996
FAX (415) 234-3997

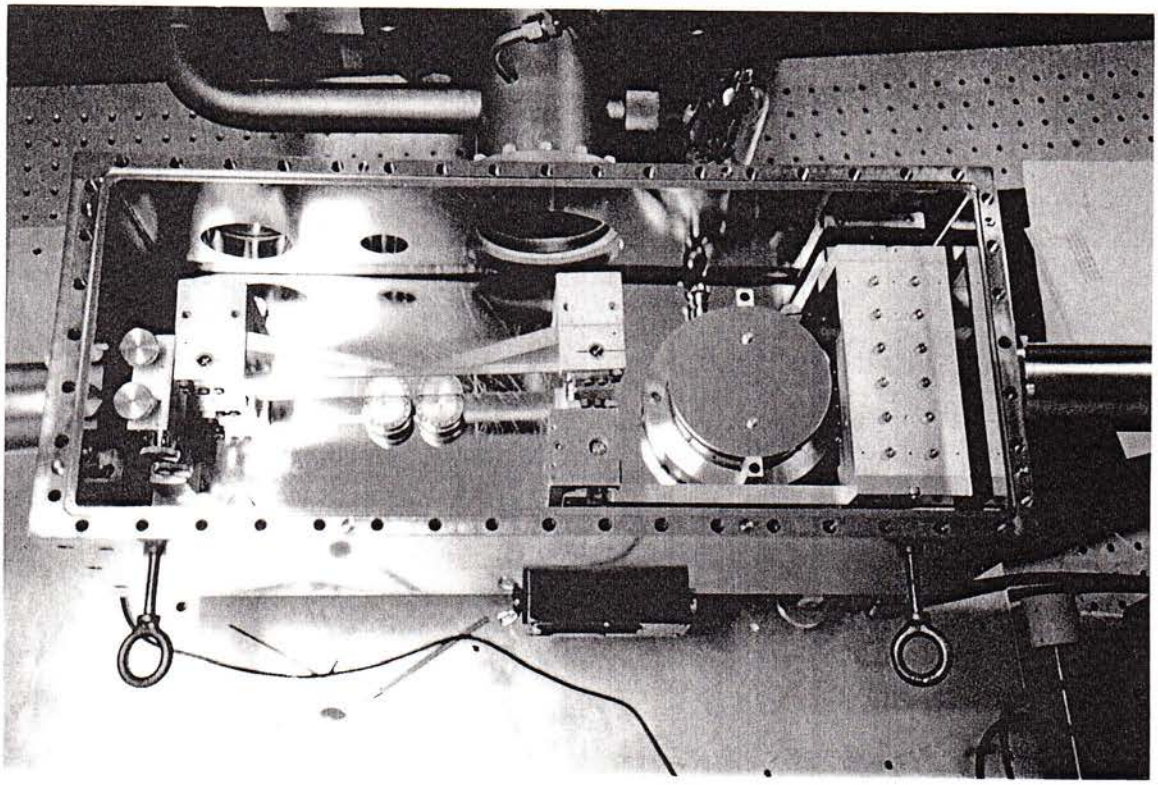

Fig. 2-22. b) Photograph of ultra-high vacuum stainless HIREFS monochromator, constructed and tested by the author (1989).

Fig. 2-23. HIREFS model SXR soft x-ray spectra of laser-produced aluminum plasma. The six spectra, recorded on a single piece of film, exhibit different astigmatism controlled by radius adjustment of a mirror reflecting in the non-dispersive direction. The stigmatic spectrum provides spatial imaging of ~ 5 arcseconds and a spectral resolving power of ~ 2000.

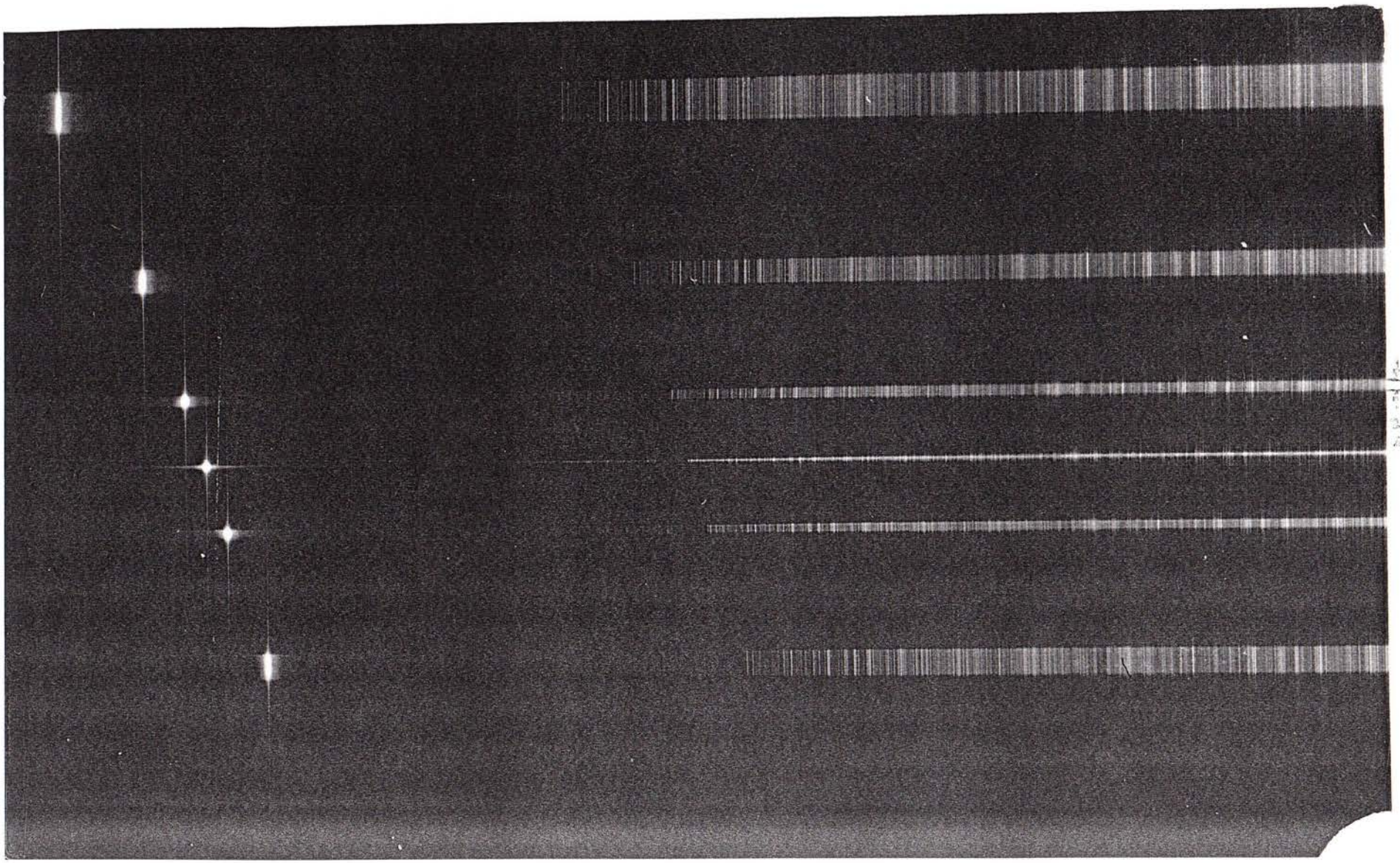

Fig. 2-23. HIREFS model SXR soft x-ray spectra of laser-produced aluminum plasma. The six spectra, recorded on a single piece of film, exhibit different astigmatism controlled by radius adjustment of a mirror reflecting in the non-dispersive direction. The stigmatic spectrum provides spatial imaging of ~ 5 arcseconds and a spectral resolving power of ~ 2000.

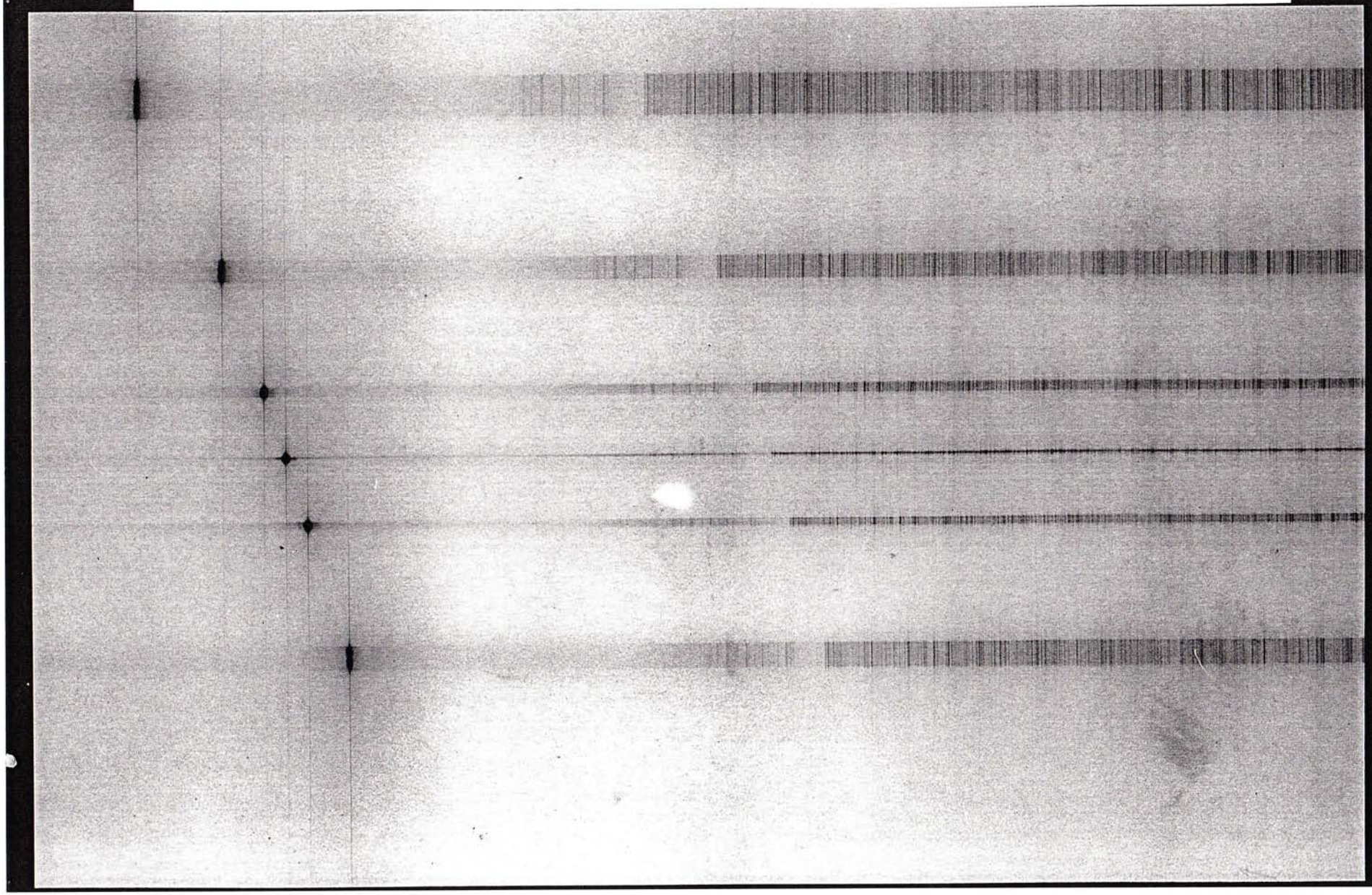

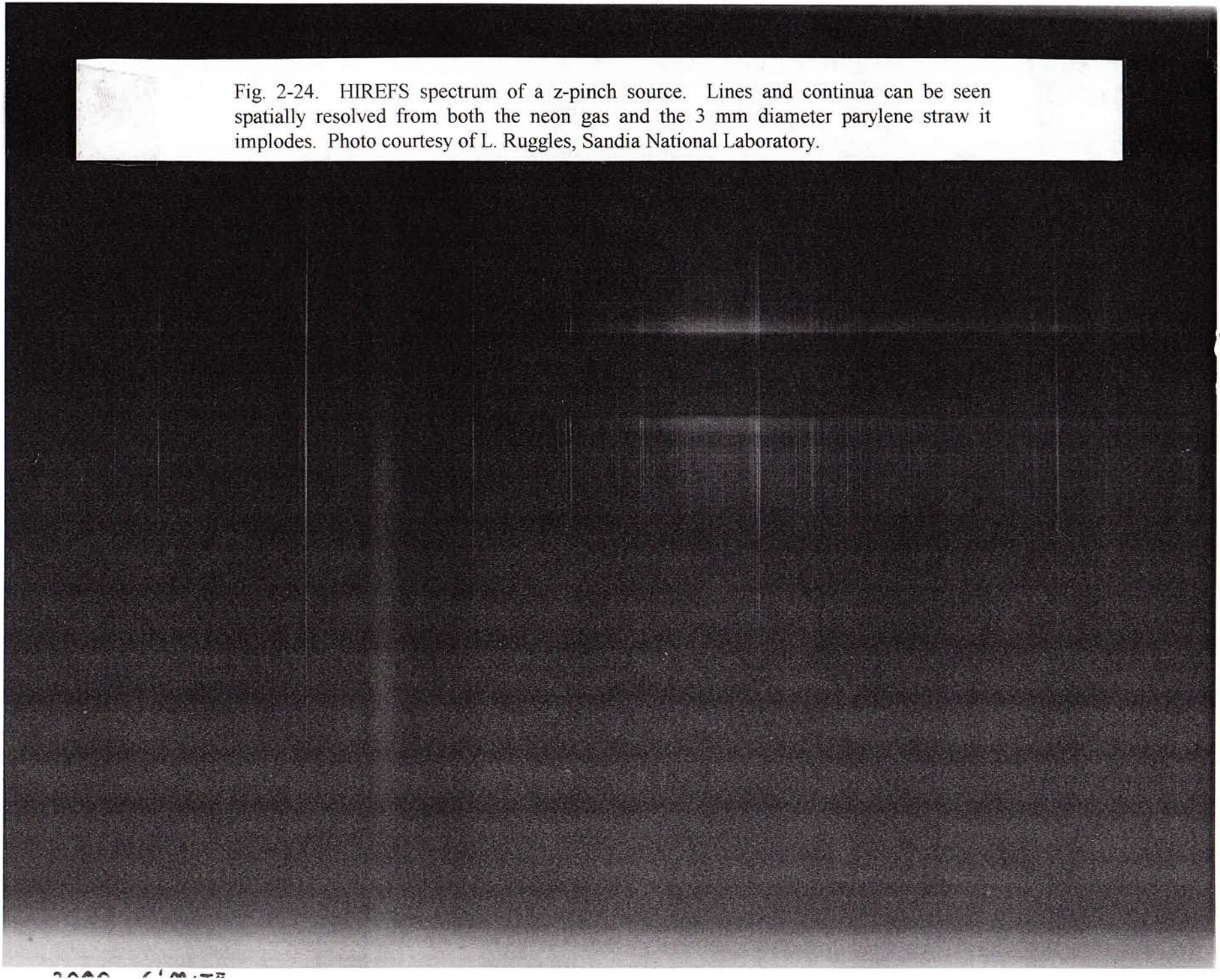

Fig. 2-24. HIREFS spectrum of a z-pinch source. Lines and continua can be seen spatially resolved from both the neon gas and the 3 mm diameter parylene straw it implodes. Photo courtesy of L. Ruggles, Sandia National Laboratory.

stigmatism (or adjustable astigmatism) and the use of only simple optical surfaces, allowed the HIREFS to become a versatile instrument in a wide variety of applications. A few of the experimental results obtained during calibration of the HIREFS by the author, and in the use of the instrument at customer facilities[46-57] are next presented.

## e) Stigmatic Plasma Focal Plane Spectra

Figure 2-23 is a set of spectra taken using HIREFS model SXR (2° graze angles) in spectrographic mode, with a flat strip of high resolution x-ray film (Kodac T-grain) at normal incidence to the diffracted beam near the center of the spectrum. To calibrate the settings of the bent mirror which remove astigmatism, successive spectra were taken with different feedthrough settings for the radius of curvature of this mirror, while offsetting the spectra in both directions to prevent overlap. The nominal groove density of the grating was 160 $mm^{-1}$ and all optical surfaces were coated with gold. The source was an aluminum plasma produced by a Q-switched Nd:YAG laser of 1.064 microns wavelength pulsed at 10 Hz with a pulse width of approximately 2.5 nsec and pulse energy of approximately 300 mJ. The source target was a solid aluminum rod, upon which the laser was focused to 25-50 microns in diameter using a beam expander and aplanatic lense. The resulting point source was refocused by a pre-mirror through the 5 micron entrance slit of the spectrograph and spectrum exposures of 2 minutes were made on the film. The enlargement of the directly exposed 35 mm film shows the zero order images to the left of each spectrum, and a dark absorption region near the center of the spectrum at approximately 100 Angstroms in wavelength. The most stigmatic spectrum is ~ 25 microns in image height (~ 0.025 mrad = 5 arcseconds), while maintaining spectral image widths of approximately 15 microns. This meridional imaging yields spectral resolving powers of approximately 2,000. Similar gratings at higher and lower groove densities (1440, 480 and 65 grooves/mm) yields the same resolving powers at wavelengths in the region from below 10 Angstroms to several hundred Angstroms.

Figure 2-24 shows how this spatial resolution was exploited by a customer (Sandia National Laboratory) to analyze a plasma produced by a z-pinch source[48]. The imaging spectrum shows the outline of the 3 mm hollow parylene straw imploded by the pinch. The continuum and emission lines from the straw material are seen at the edges of the straw, including the broad helium-like carbon line at ~ 44 Angstroms. The narrow lines from the neon gas surrounding and imploding the straw are seen spatially extended. These full-time integrated "spectral photos" were followed by multiple time-gated results to allow investigation of the dynamics of the plasma during and after the implosion.

Some of the most interesting results obtained with the HIREFS were done in combination with a CCD detector developed by MIT[54]. This configuration provides high dispersive spectral resolution on the small flat CCD operating at a normal orientation to the beam, and separation of spectral orders by use of the inherent energy resolution of the CCD. The two-dimensional spectra produced by this arrangement allows both the spectrograph and the CCD to be calibrated. For example, Figure 2-25

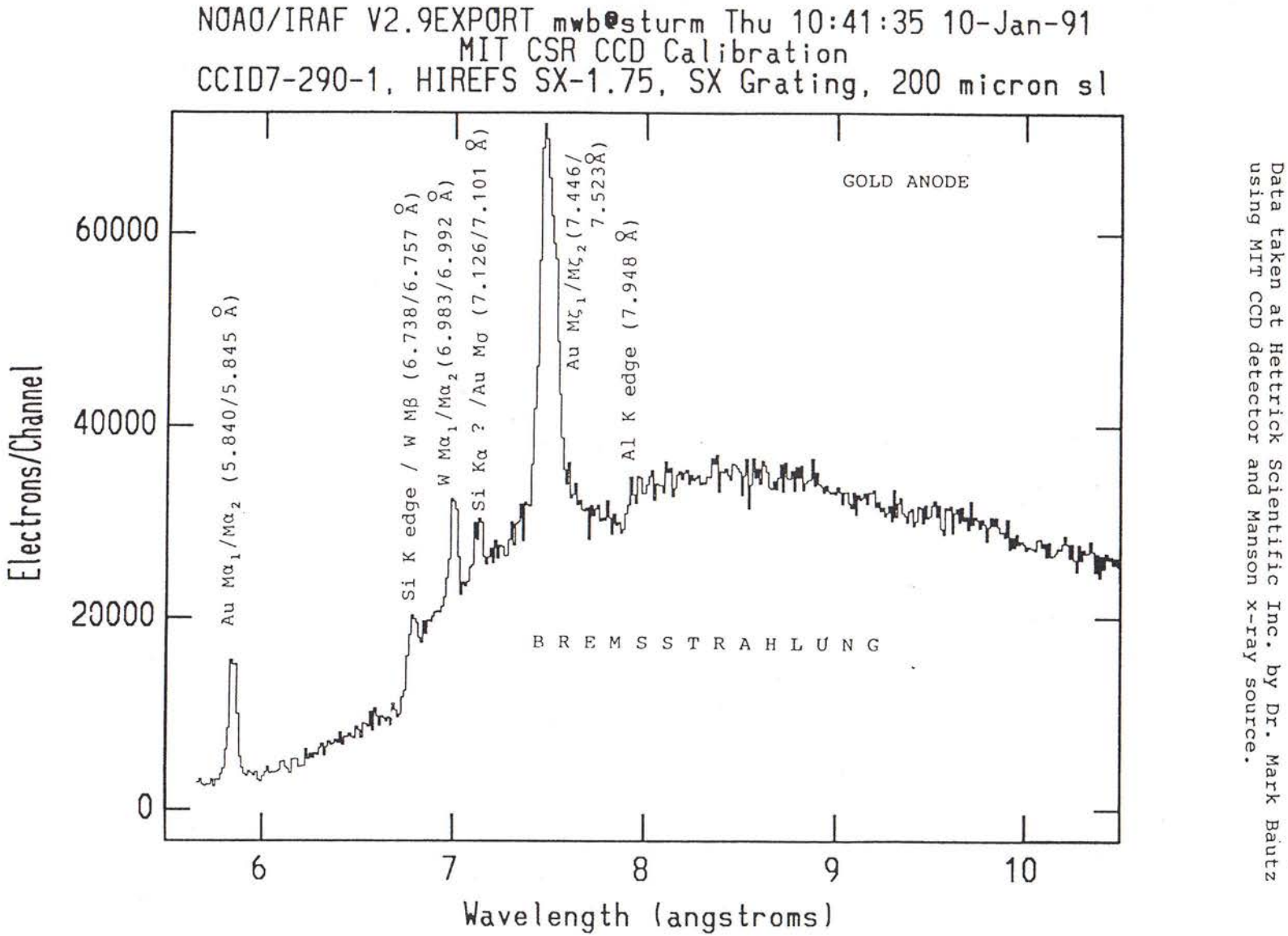


Fig. 2-25. HIREFS model 176 spectrum of electron beam source recorded in spectrographic mode by MIT CCD at the focal plane.

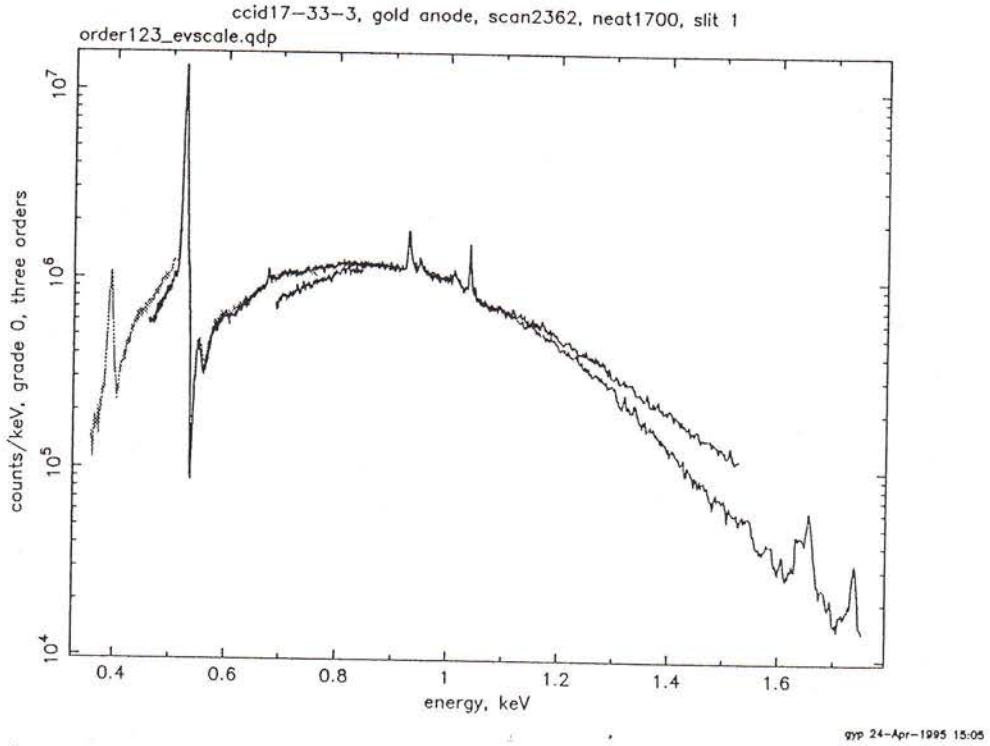


a) Intensity as a function of energy for three orders of the spectrometer with a gold target in the X-ray source.

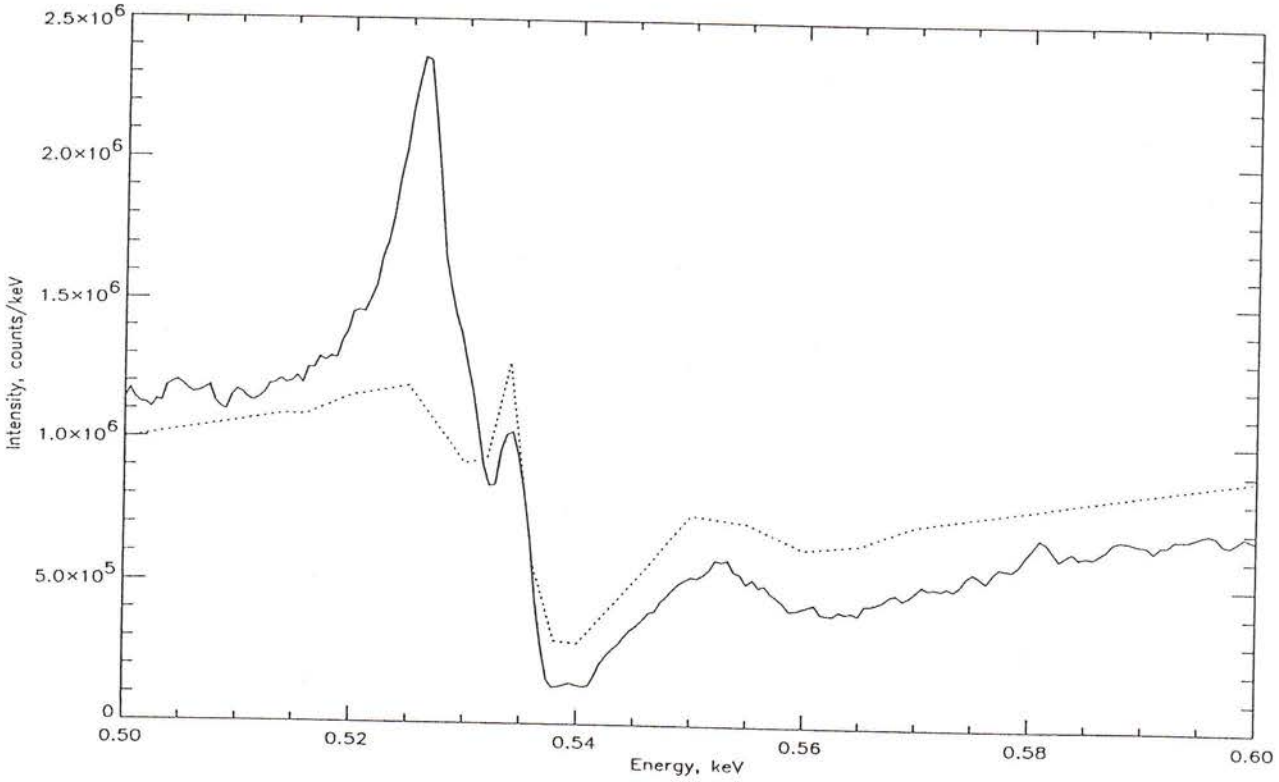


b) Intensity as function of energy in the vicinity of the oxygen edge (solid line). Dotted line represents QE plot of the CCD multiplied by a factor of $4 \times 10^6$ to match the scale.

Fig. 2-26. XAFS spectra taken by Prigozhin, Bautz, Gendreau and Ricker, using the HIREFS in spectrographic mode.

shows a short wavelength spectrum of an electron impact source operating at 5 kV accelerating voltage, taken using a high density (1440 g/mm) grating in the spectrograph. Bremsstrahlung from the high-z target material (gold) is clearly evident, as are the characteristic x-ray lines from gold and contaminants such as tungsten (and oxygen and carbon at longer wavelengths) coating the anode surface. In addition, the aluminum filter inserted in front of the CCD to eliminate visible background, and the $SiO_2$ contained in the CCD structure itself produced absorption edges in the continuum. These edges allowed analysis of the thickness of these films. The gold M-shell line at 5.84 Angstroms is the shortest wavelength detected with this spectrometer. Figure 2-26 is a high resolution spectrum showing X-ray Atomic Fine Structure (XAFS) at the oxygen edge originating primarily from the $SiO_2$ in the CCD. The known position of the lines and edges allows an accurate calibration of the dispersed wavelength, from which measurement of the linearity of the CCD gain is made at all wavelengths in the continuum.

Using electronic detectors (microchannel plates and CCDs) of resolution 25-50 microns, one obtains spectral resolving powers of 500-1000 (up to 3000 using film) with the 1.75 meter long HIREFS with $2^o$ graze angles. To obtain significantly higher resolving power requires increasing the linear dispersion per fractional wavelength, which is realized by an increase in the system length or the graze angle (and thus wavelength at a given efficiency). This can be seen in equation (2-36) by the linear dependance of resolving power on the focal length r and the graze angle $\gamma$. For example, a system length of 6 meters and a graze angle of $9^o$ resulted in a resolving power of 35,000 at a wavelength of 160 Angstroms[41], and a commercial HIREFS Model 170.5-XUV-5.5 with 5.5 meter length and $4.75^o$ graze angle obtained a resolving power of 16,000 at a wavelength of 236 Angstroms. An initial line profile[49] taken with the latter spectrograph is shown in Figure 2-27a, tuned to a high gain lasing line of Ne-like Ge for which the intensity was sufficient to overexpose the Airy disc of the image and make the diffraction pattern visible. This diffraction pattern is modelled by including the physical optics effect of finite illuminated aperture to a 2-D raytracing of the grating focusing. The calculated result shown in Figure 2-27b shows excellent agreement between the observed fringe spacing of 28.2 microns and the spacing of 26.5 microns calculated from the predicted illuminated aperture based upon the instrument mechanical parameters. As physical optics (and not geometrical aberrations) was limiting the resolution, the optimum grating width is larger than the illuminated width in that initial experiment.. Removal of an aperture limiting beam directing mirror allowed a larger grating aperture to be illuminated in subsequent experiments[51] for which the spectral resolution should be close to the theoretical value. This value equals the number of grooves on the grating surface (375 g/mm x 62.5 mm = 23,500) for infinitesimal width entrance slits and detector resol and in the absence of geometrical aberrations, and decreases to approximately 16,000 using 10 micron slit and detector resol.

The geometrical aberrations of the grating used in the above ultra-high resolution HIREFS was corrected (during its manufacture in 1990) for coma of the mirror which

(#10215)

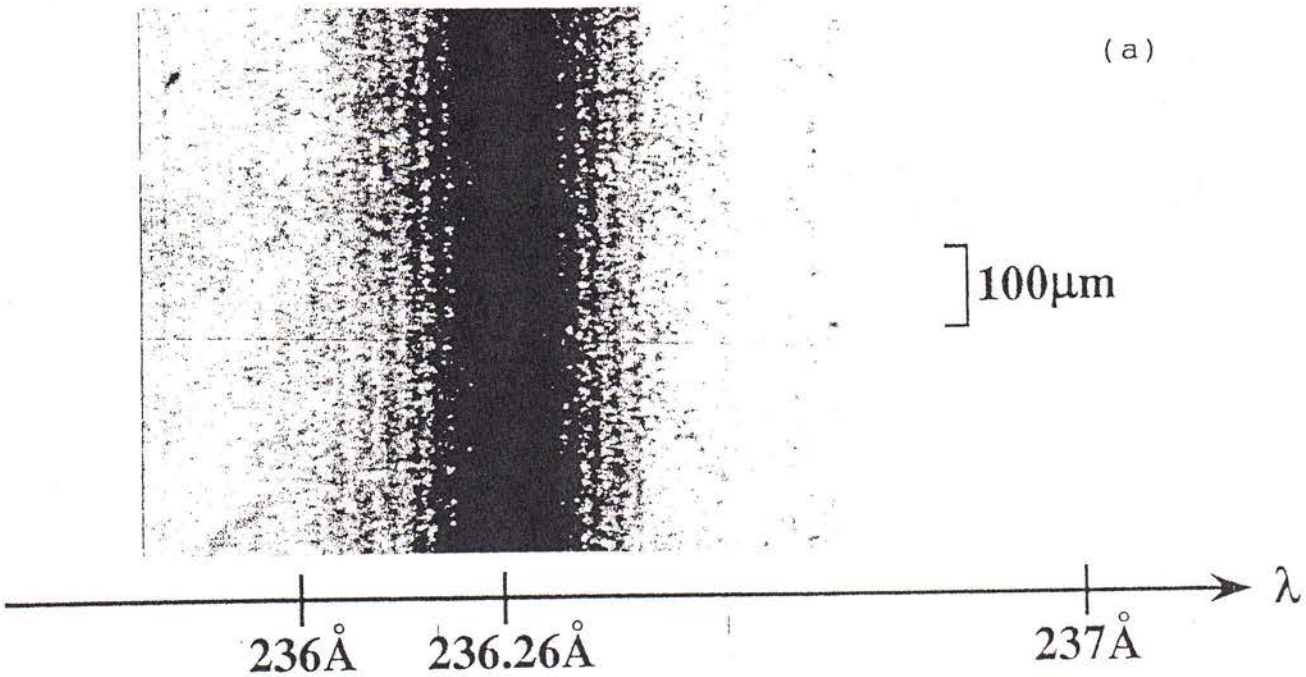


Fringe space on film is 28.2μm,
which corresponds to $\Delta\lambda$=24.9mÅ.

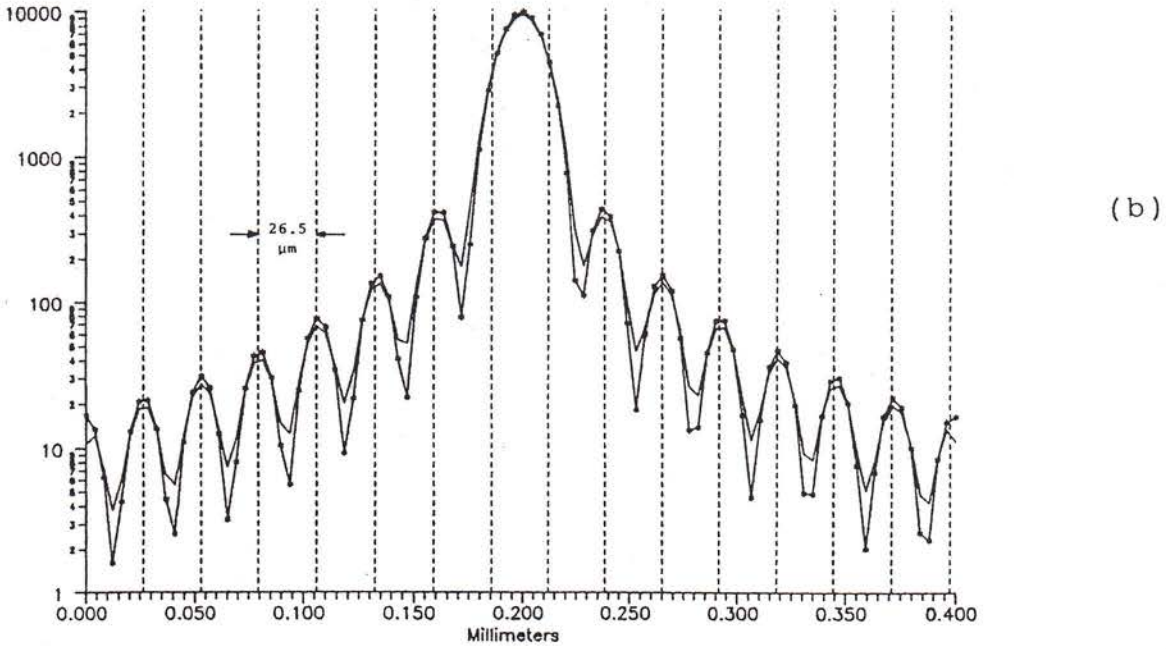


(b)

Fig. 2-27. Ultra-high resolution HIREFS tuned to Ne-like Ge laser line. a) experimental result by Kato et al, b) raytrace simulation including the diffraction effects from a finite number of grooves.

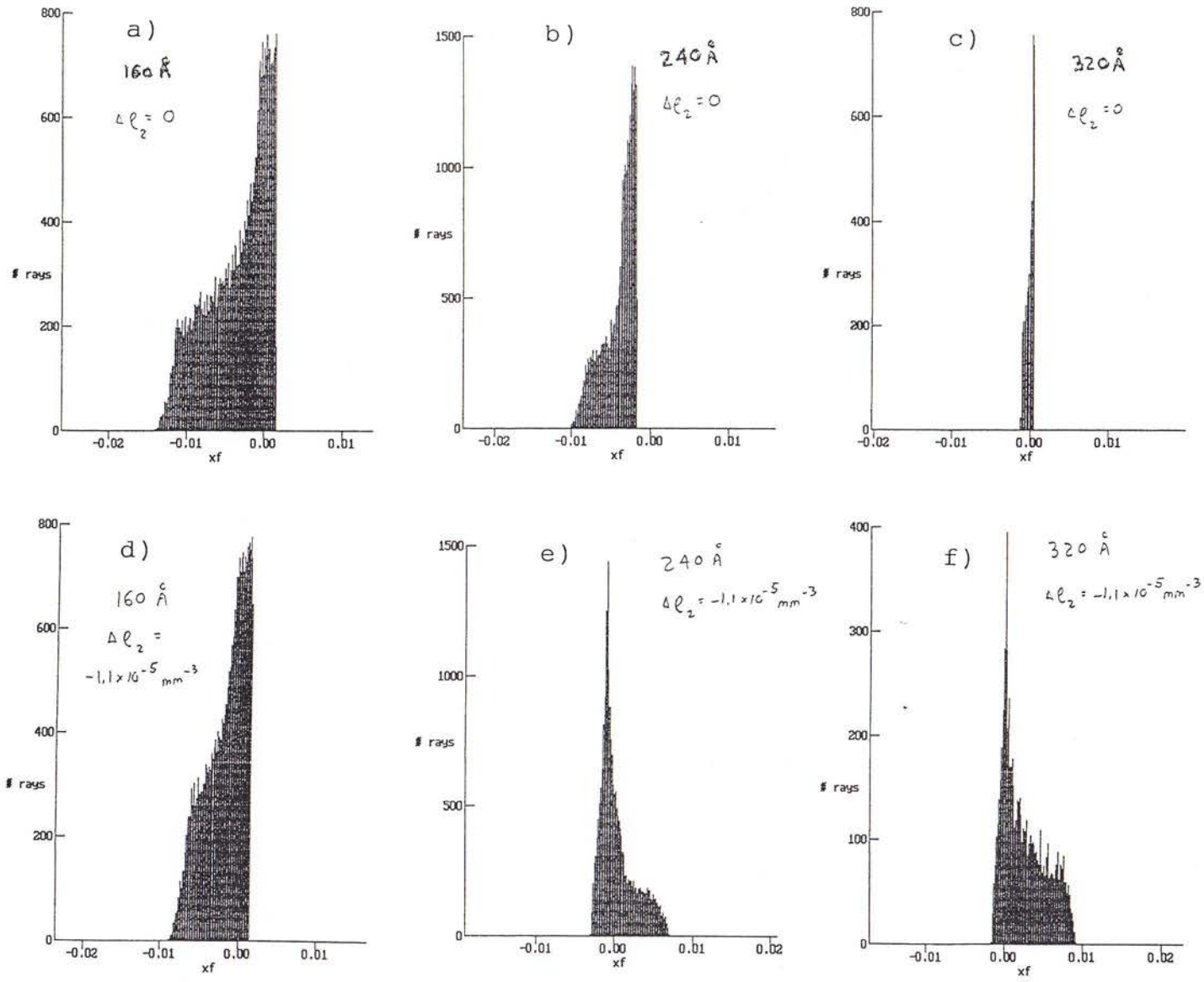


Fig. 2-28. VLS correction of coma from converging mirror with non-unit magnification in HIREFS model 170.5.

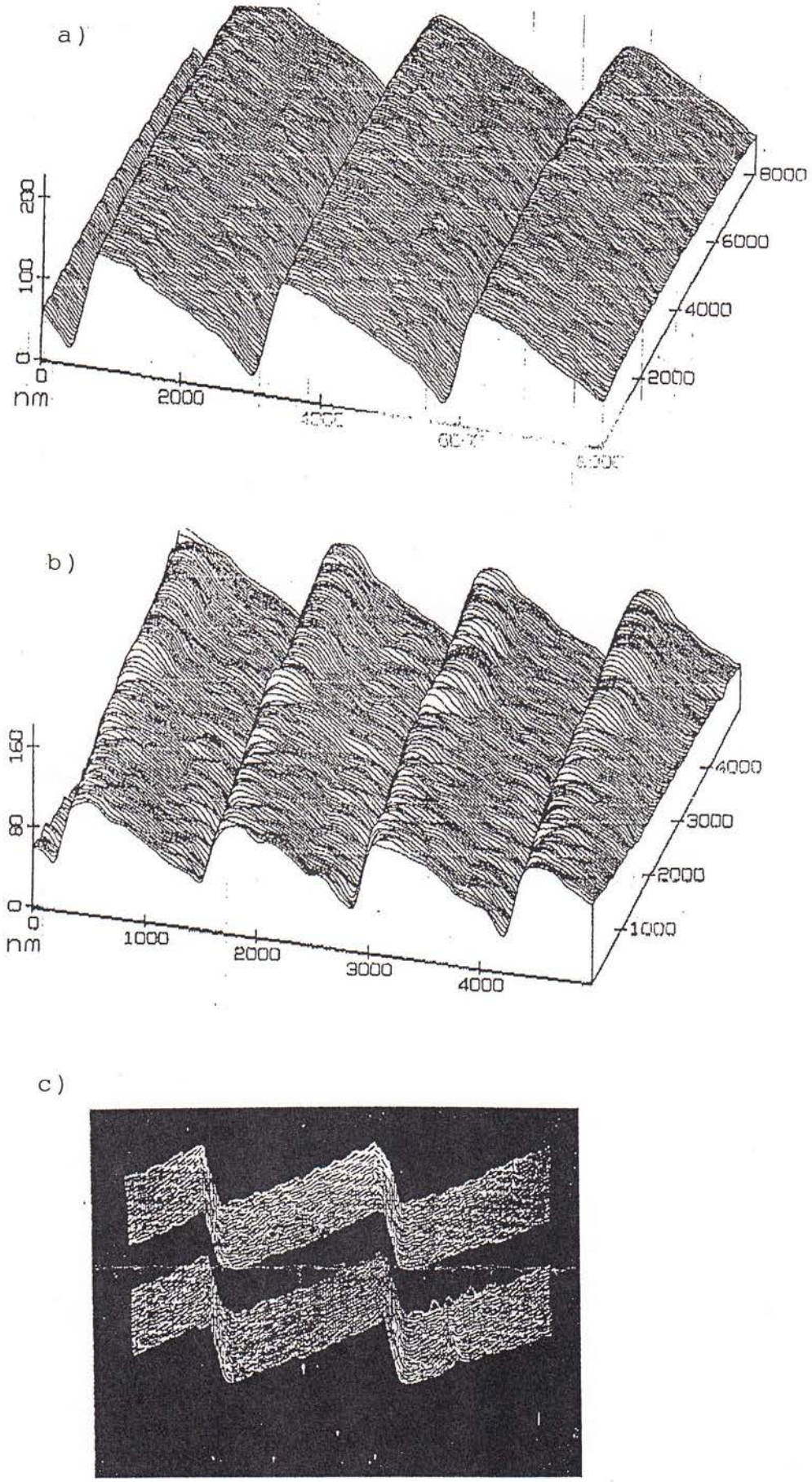


Fig. 2-29. Scanning tunneling micrographs (STMs) of grating grooves for HIREFS model 170.5: a) nominal 375 g/mm grating; b) nominal 750 g/mm grating and c) nominal 1500 g/mm grating.

provided the converging beam to the grating, as explained in Sec. 2.3 c) above. The mirror coma was not zero because it was operated at a magnification of 3 to minimize the distance from this mirror to the entrance slit. Figures 2-28a-c show the first order line profile which would result at three different scan wavelengths from use of the ruling coefficient $N_{30}$ derived from the light-path function for the grating alone [equations (1-1) and (1-8)], while Figures 2-28d-f show the profiles calculated from the non-zero coma correction term $\Delta N_{30}$ used in the optimized grating. The optimum coma correction is not the same for all wavelengths, thus a value was chosen to minimize the largest coma (in microns) as a function of scan wavelength.

This tunable spectrograph also contains gratings of nominal groove density 750 g/mm and 1500 g/mm, allowing coverage to wavelengths as short as 35 Angstroms at high resolution. The 4.75° graze angle and the nearly perfect blazed groove profiles shown by the scanning tunneling micrographs of Figure 2-29 should provide high efficiency for all gratings.

## f) AXAF Monochromator and Test Scans of Plasmas

As discussed in Sec. 2.3 a) above, the tunable spectrograph design is converted into a monochromator by insertion of a stationary exit slit at the focal plane. Several such HIREFS monochromators were designed and fabricated for applications which included the testing of multilayers[46,47] and detectors, the spectral analysis of femtosecond laser-produced plasmas[55,56] and the characterization of large astronomical x-ray telescopes[57]. A photograph of one such HIREFS monochromator is shown in Figure 2-30. The entrance slit is located to the far right, the optics chamber (housing the astigmatism control mirror, meridional focusing mirror and gratings) in the center and the exit slit to the left. All chambers are mounted to a breadboard which can be aimed both vertically and horizontally to illuminate the Advanced X-ray Astrophysics Facility (AXAF) telescope located at a distance of approximately 500 meters. The object point for the telescope is a monochromatic stigmatic image at the exit slit of the monochromator. The 2° graze angles for the optics and the ability to select any one of four gratings ($\rho_o$ = 1440, 480, 160 or 65 mm-1) provides access to first order wavelengths from approximately 6 Angstroms to 300 Angstroms at a resolving power up to approximately 2000.

Calibration of this monochromator was performed using a laser-produced aluminum plasma as described in the preceding section. The monochromatic radiation transmitted through the exit slit was detected using a silicon photodiode. As the photo-electron yield of silicon is known (1 $e^-$ per 3.63 eV incident photon energy) and the diode surface had only a thin stable oxide layer, the current read out by an electrometer could be converted into photons/sec emerging the monochromator exit slit. Figure 2-31 is a plot of the spectrum, intensity calibrated for the first order lines. The 160 g/mm grating, 20 micron entrance slit and 10 micron exit slit were selected. The spectral resolving power was

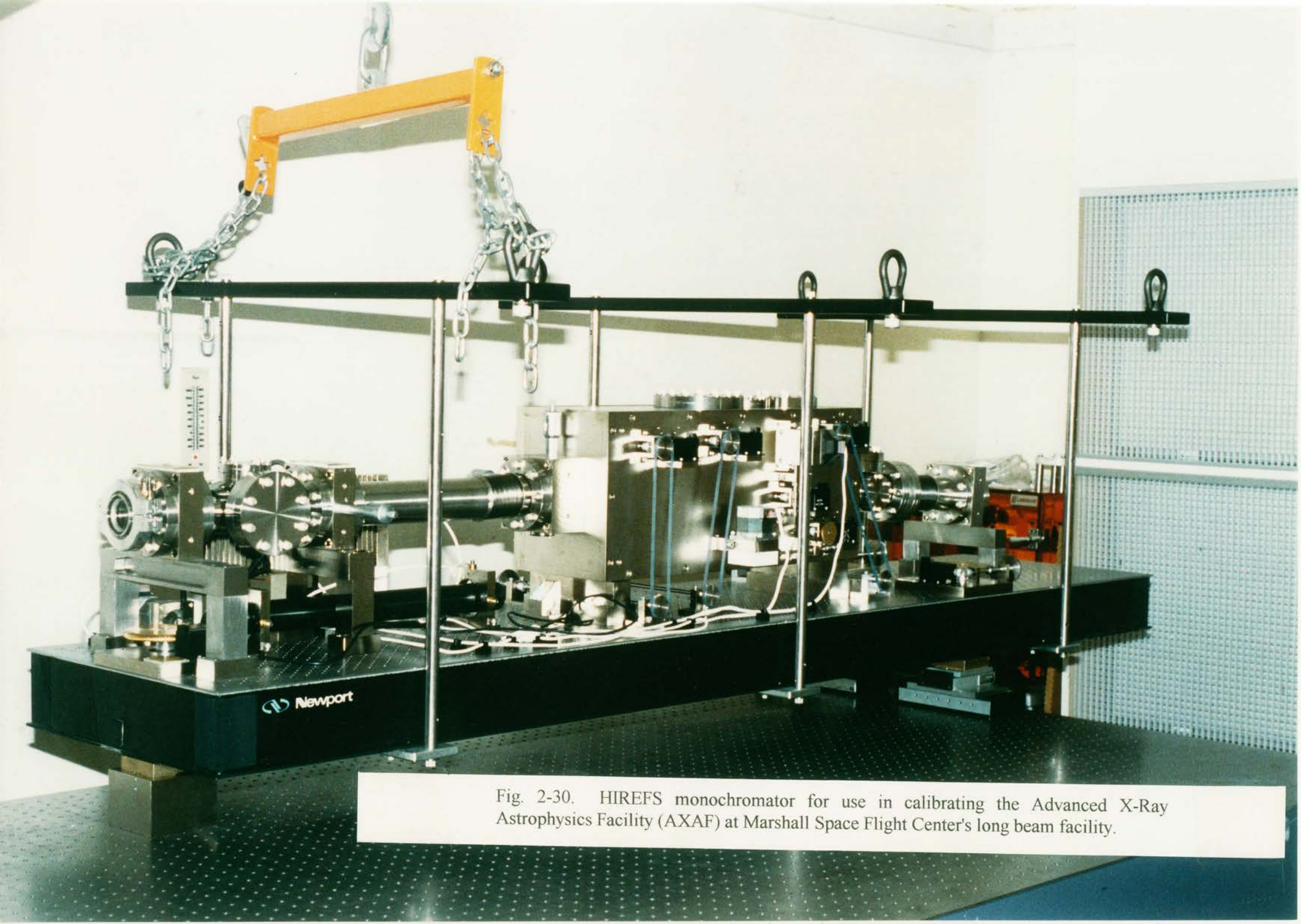


Fig. 2-30. HIREFS monochromator for use in calibrating the Advanced X-Ray Astrophysics Facility (AXAF) at Marshall Space Flight Center's long beam facility.

Fig. 2-31. HIREFS monochromator spectrum of aluminum laser-produced plasma. Entrance slit was 20 microns in width and exit slit 10 microns.

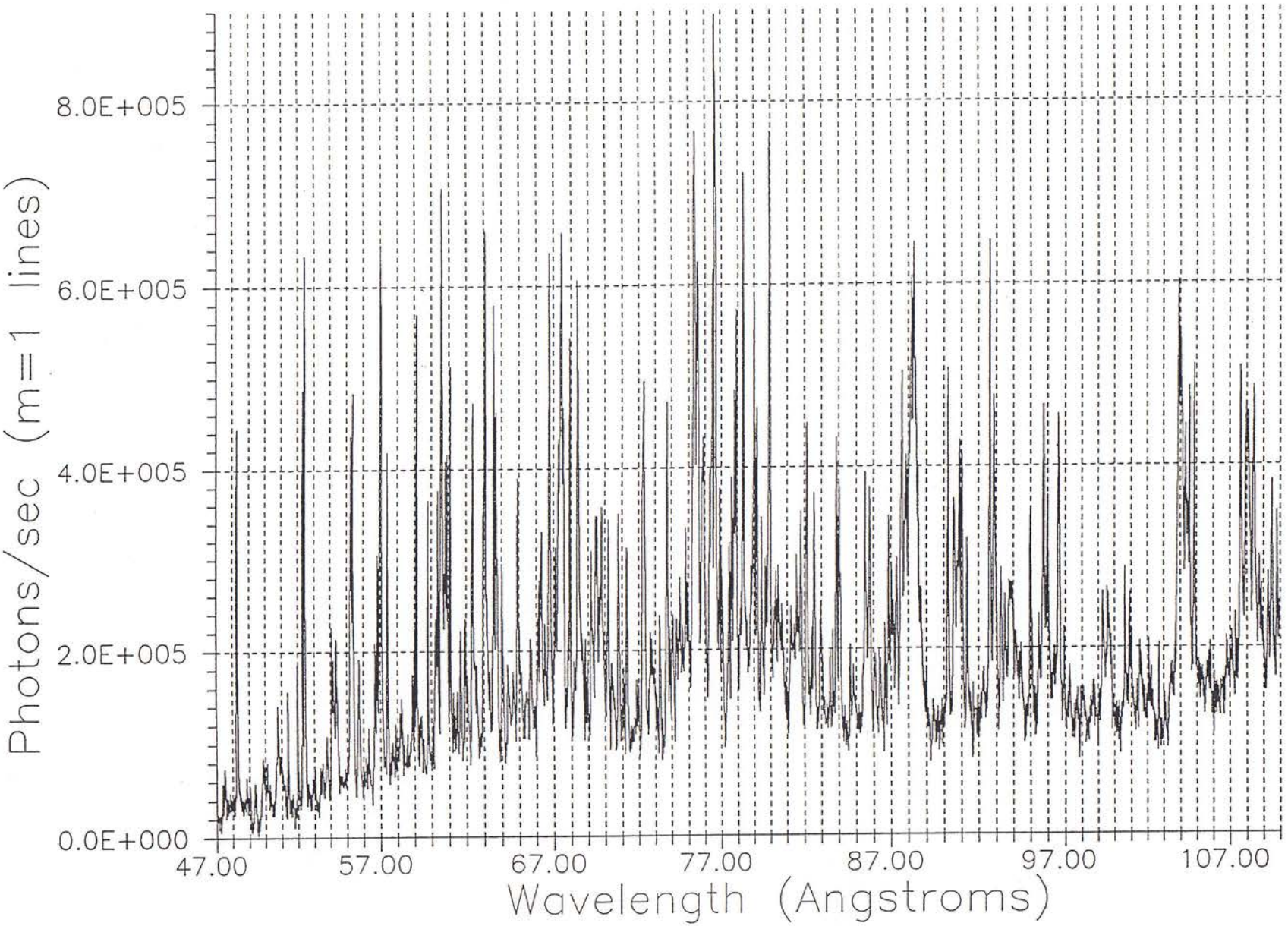

Fig. 2-32. High resolution profile taken of Aluminum XI line using 10 micron entrance slit and 5 micron exit slit of HIREFS monochromator: a) experimental result; b) numerical raytrace simulation.

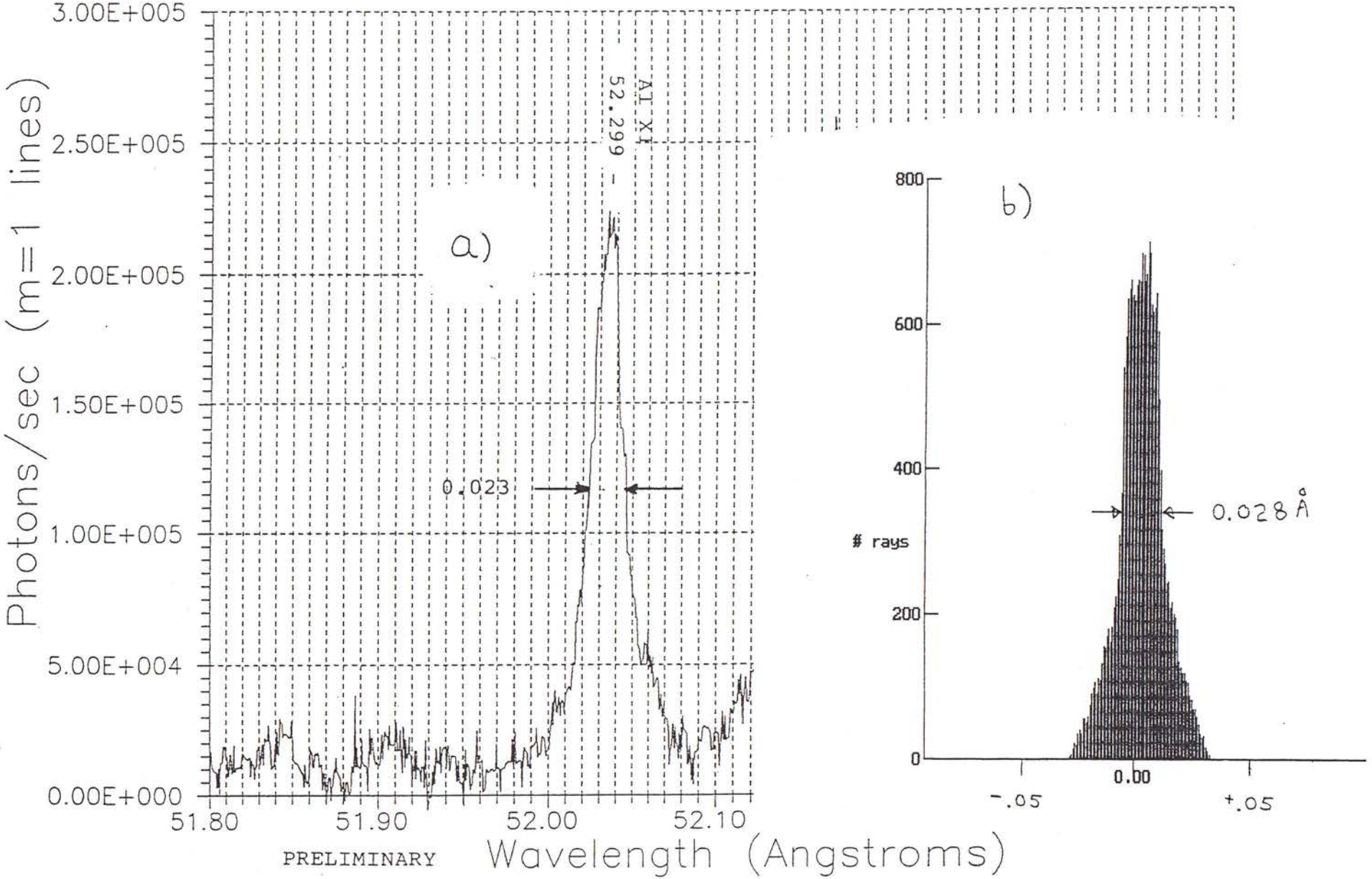

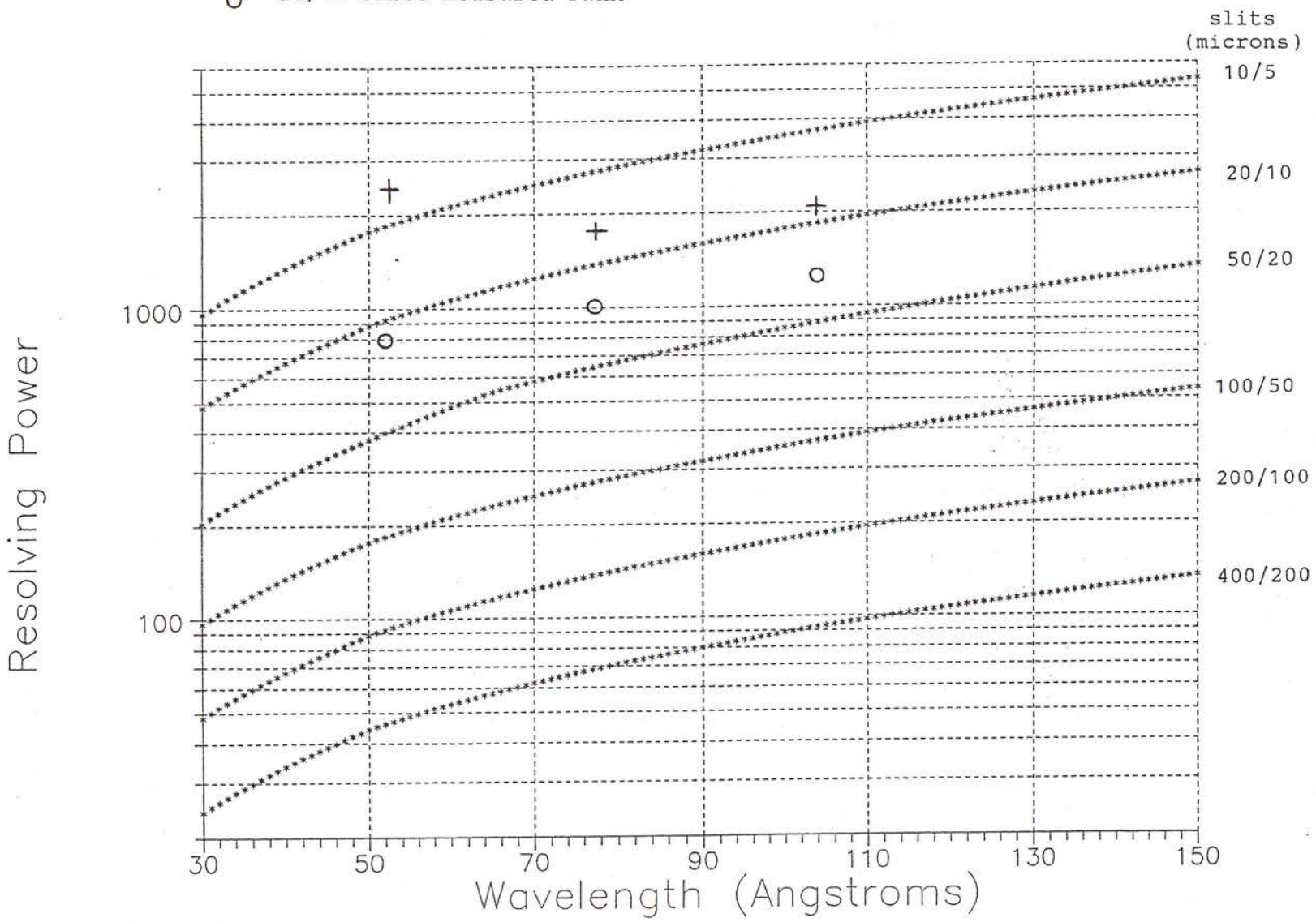


Fig. 2-33. Grating SB
****** theoretical resolution
data points - measurements.

Fig. 2-34. Strong continuum from gold target laser-produced plasma. Plasma was used as a point source in place of the entrance slit to provide high intensity through a stigmatic HIREFS monochromator.

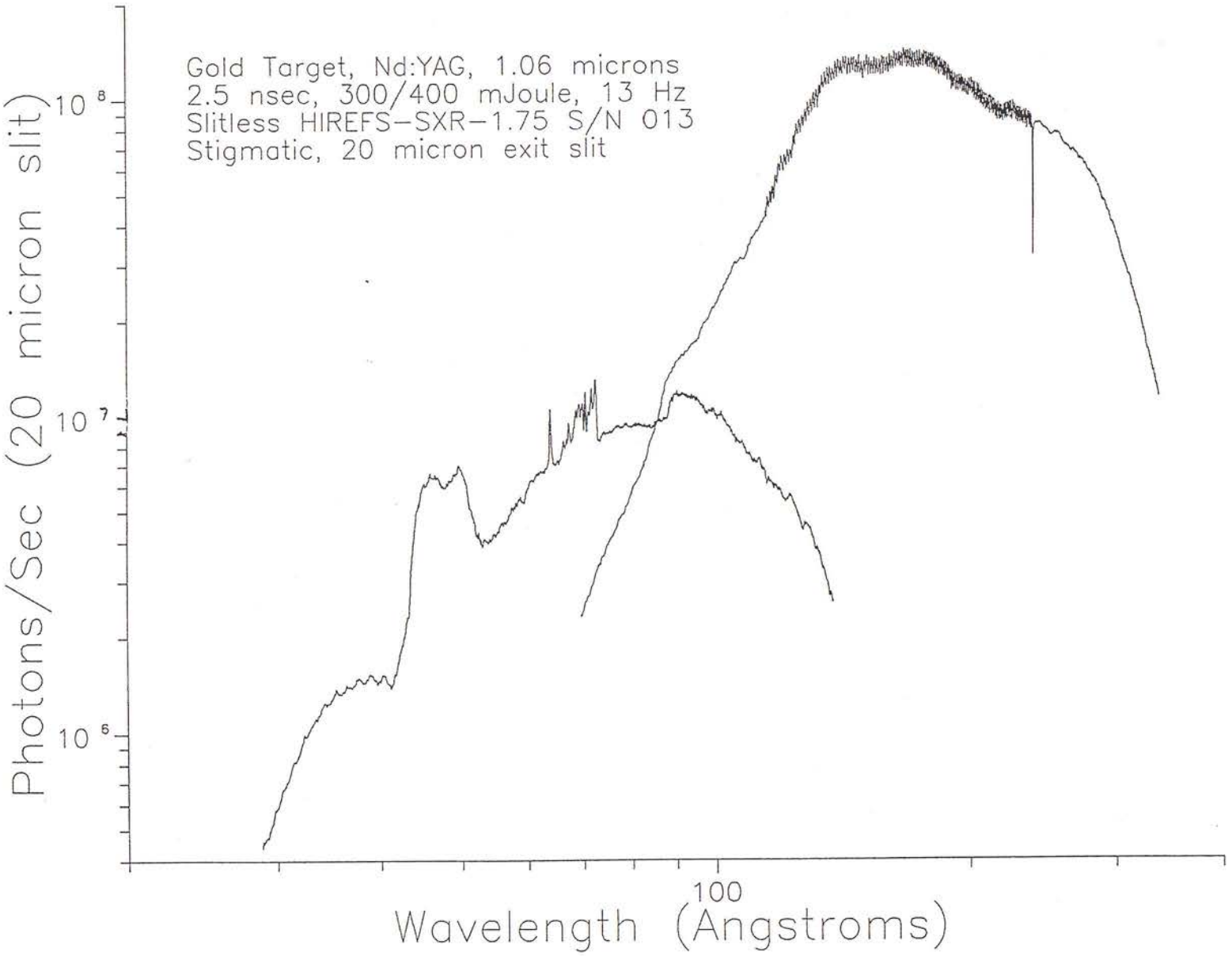

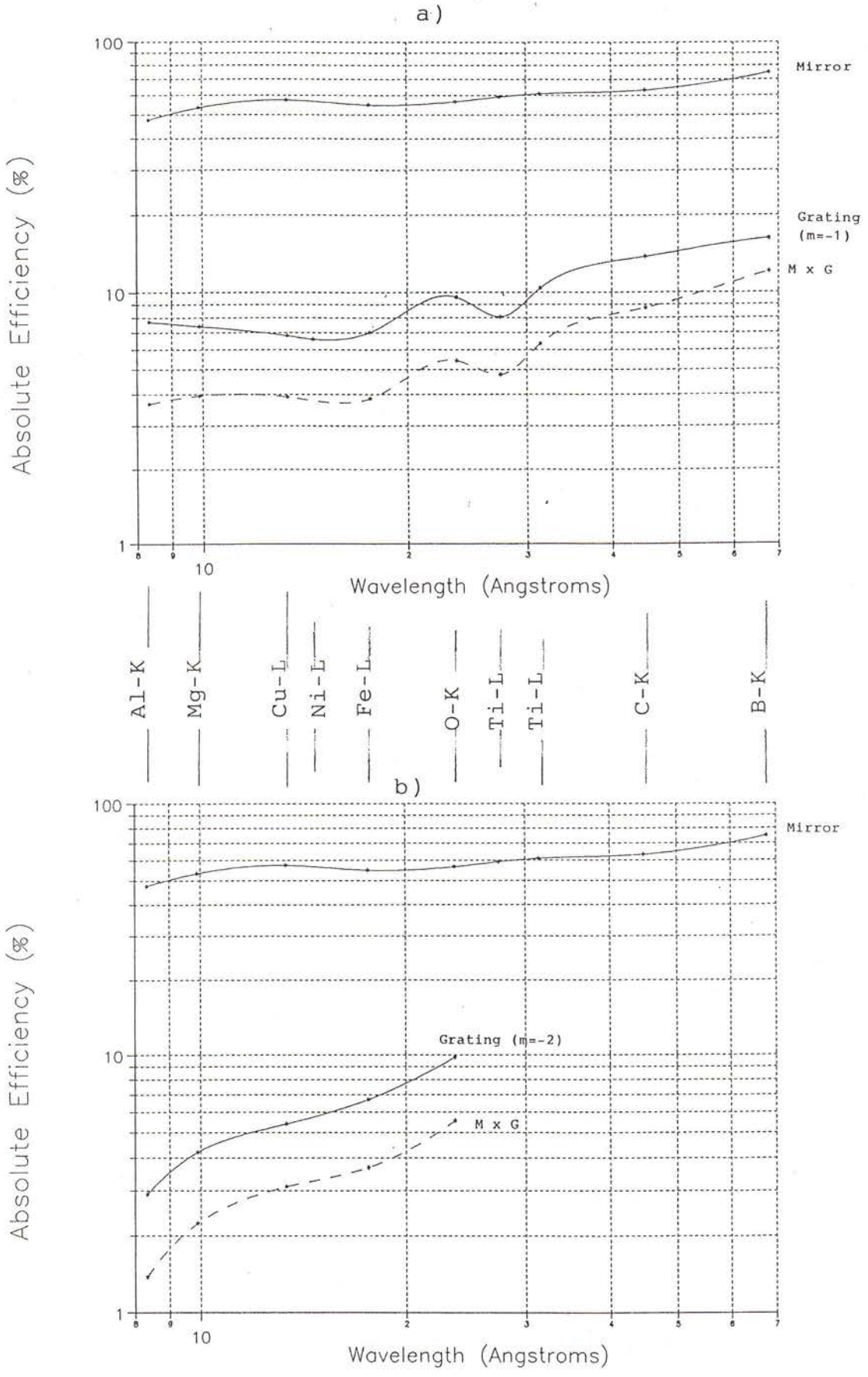


Fig. 2-35. Absolute efficiency measurements of 480 g/mm grating in a) first spectral order and b) second spectral order. The series efficiency of the grating-mirror combination is plotted as the dashed curve in each figure. This calibration was done at 10 characteristic x-ray lines produced by an electron beam source.

measured to be approximately 1000 across this spectrum. To test the limit of the instrument resolution, narrower slits (10 micron entrance and 5 micron exit) were selected, and the profile of the Al XI line at 52.299 Angstroms scanned (Figure 2-32a). The measured FWHM of ~ 0.023 Angstroms compares well with the numerical raytrace (Figure 2-32b) which shows a FWHM of approximately 4.8 microns at exit slit plane. Convolving this with a 5 micron exit slit should yield a transmitted FWHM of ~ 7.4 microns. Dividing this by the linear dispersion of 0.264 mm/Angstrom results in a predicted FWHM of 0.028 Angstroms. Measurements made at other wavelengths and slit settings are plotted in Figure 2-33 and compared to the resolving power curves generated from including the effect of slit widths assuming negligible contribution from optical aberrations. Deviations of the measurements from the theory can be due to optical aberrations, figure error aberrations, misalignment errors, signal noise and unidentified spectral components causing line blends. While higher resolutions have been obtained in particular measurements, the resolving power appears to typically level off at a value near 2000 for this spectrograph of 2° graze angles and 1.76 meters length from slit to slit. This monochromator was coupled to a Rigaku water-cooled rotating anode light source to obtain strong continua using a tungsten anode.

The application of this monochromator as a high intensity continuum light source at high spectral resolution is illustrated in Figure 2-34. Using a gold target in the laser-plasma source, and placing this point source at the entrance slit plane of the monochromator, strong continua are shown using the 160 $mm^{-1}$ and 65 $mm^{-1}$ gratings and a 20 micron exit slit. The continua are augmented by both broad and narrow emission features from gold and a carbon-k absorption edge which appears in both first order (43.6 Angstroms) and second order (87.2 Angstroms). In the region near 100 eV photon energy, the detected flux at this resolving power of ~ 500 is over $10^8$ photons/sec. This compares well with fluxes achieved using much more inherently powerful light sources such as synchrotrons.

## g) Measured Soft X-Ray Efficiencies

The absolute efficiency of a 480 g/mm HIREFS grating and meridional mirror was measured using an electron beam source with various anodes to obtain 10 different calibration wavelengths. The angle of incidence to the gold grating was fixed at 89° and the diffracted angle was 88.1° at Al-K to 85.3° at B-K. The grating efficiency in first order as plotted in Figure 2-35a is seen to be approximately 10% in this short wavelength region. The gold mirror reflectivity (at an 88° angle of incidence) is shown to be approximately 60%. The values are consistent with the theoretical reflectivity of gold and a relative grating efficiency of ~ 16% in first order.

A 16% relative grating efficiency equals half of the theoretical *peak* relative efficiency of 33% calculated from equation (2-28) using $\alpha^* = 1°$ and $\beta^* \sim 3°$. As this peak is calculated at the blazed wavelength, the average efficiency over such a broad band as measured here must be reduced by at least a factor of two. Thus, while the

Fig. 2-36. The change in geometrical aperture incident and diffracted from the HIREFS grating due to rotation of the grating as a function of wavelength.

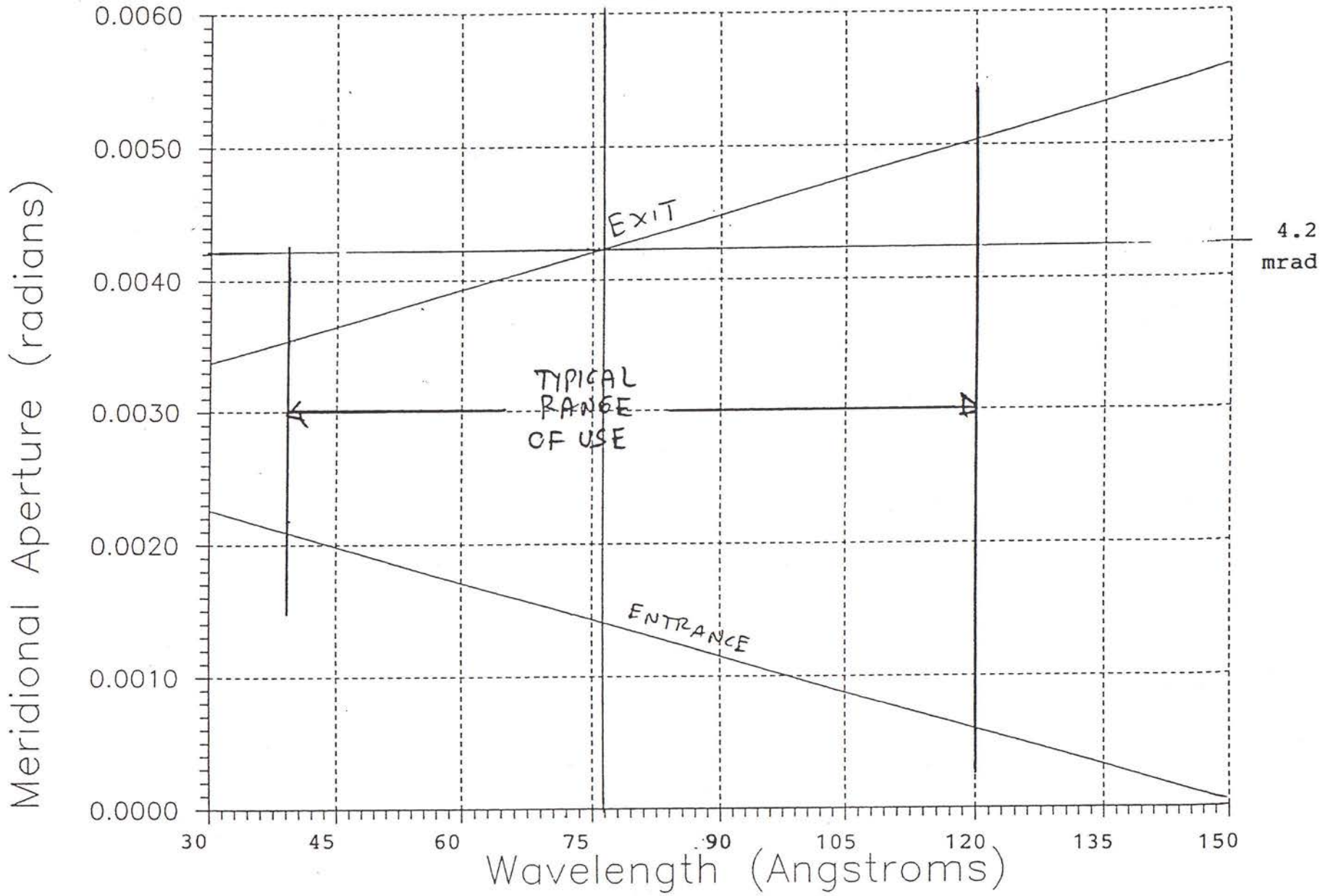

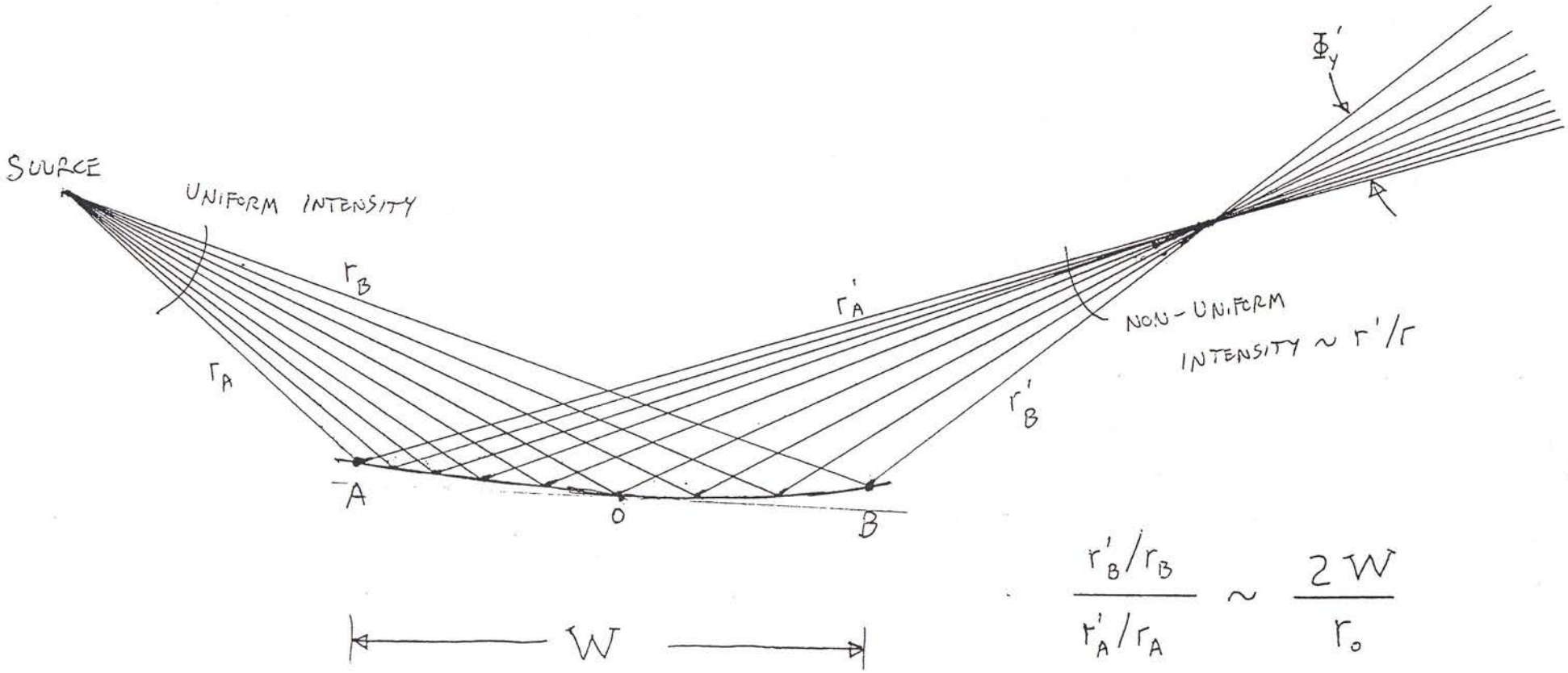


Fig. 2-37. Variation in angular brightness caused by a grazing incidence mirror.

measurements do not result in as high a peak efficiency as predicted, the average efficiency over a broad wavelength region is at least as high as predicted on the basis of perfectly blazed grooves.

One expects that the observed broadening of the diffraction efficiency curve, combined with a lowering of the peak, is a result of deviations in the groove forms from triangular profiles. This is consistent with second order measurements of the grating efficiency (Figure 2-35b) which were a factor of two lower than first order even though the reflectivities were comparable. Distortions from a perfectly flat groove will distort the local wavefront and thus lower the diffraction efficiency in higher orders before having a substantial effect upon the first order. Thus, provided such deviations are not dramatic, they can actually be desirable for use in a spectrometer which is to cover a spectral range of at least one octave, or in which higher order spectra must be minimized in intensity. Therefore, a sinusoidal or rectangular (laminar) groove profile is also acceptable, especially given that shadowing of triangular profiles brings the theoretical relative efficiency to below 50% in most grazing incidence applications.

## h) Spatial Uniformity

The meridional aperture of the incident beam converging to the grating is given approximately as:

$$\Phi_x = 1/f_x \cong [W/abs(r)] \cos \alpha \qquad (2\text{-}58)$$

where $\alpha$ is given by equation (2-39) as a function of wavelength. The meridional aperture of the diffracted beam converging to the exit slit is given approximately as:

$$\Phi_x' = 1/f_x' \cong [W/r'] \cos \beta \qquad (2\text{-}59)$$

where $\beta$ is given by equation (2-40) as a function of the wavelength. In these equations, W is the illuminated width of the grating. In the limit of small graze angles $\alpha^*$ and $\beta^*$, the sine approximation leads to:

$$\Phi_x \cong [W/abs(r)] [\gamma + m\lambda/(2d_o\gamma)] \qquad (2\text{-}60)$$

$$\Phi_x' \cong [W/r'] [\gamma - m\lambda/(2d_o\gamma)] \qquad (2\text{-}61)$$

where $\gamma = (\alpha^* + \beta^*)/2 = (\pi - \psi)/2$ is the effective graze angle in the constant angular deviation mounting. Thus, the incident and diffracted meridional apertures vary linearly upon wavelength, as plotted in Figure 2-36 using the parameters for the HIREFS discussed above. Thus, $\gamma = 0.0349$ radians ($2^o$), W = 62.5 mm, $r' \sim -r \sim 775$ mm and $d_o = 1/160$ mm. The choice of the inside spectral order (m = -1) minimizes the percentage

variation of the diffracted aperture, while resulting in a large percentage change in the incident aperture. This choice was made due to the customer's application of feeding the exit beam to a fixed size telescope for diagnosis.

Within these apertures, spatial variation of intensity can occur due to a number of causes, including 1) unintentional variation in groove profile across the ruled grating, 2) designed variation in groove density and angles of incidence in the ruled width, 3) overillumination of the exit slit due to geometrical aberrations, 4) variation in source intensity as a function of angle and 5) intensity distortion due to finite size optics at grazing incidence. As illustrated in Figure 2-37, the latter effect causes an intensity variation even if the incident source illumination is uniform with aperture. This is due to the intensity per unit angular aperture scaling poportional to the local magnification r'/r along the mirror surface, resulting in an intensity variation:

$$\text{Intensity Variation} \sim 2\ W / r_o \sim (2/\gamma)\ \Phi \qquad (2\text{-}62)$$

in the case when $r'_o \sim r_o$. The raytraced exit aperture shown in Figure 2-38a shows $\Phi_y \sim$ 7 mrad, revealing an intensity variation of ~ 40% in the non-dispersive direction of the spectrometer due to the long astigmatism control mirror (W = 234 mm, r ~ 1000 mm). In the dispersive direction, the meridional focusing mirror also produces some variation in combination with the pre-mirror used in both these raytracings and in the experiment. However, due to the smaller aperture in this direction, the variation due to this effect is only ~ 6% as shown in Figure 2-38b. The experimental result (Figure 2-38c) shows a larger variation (~ 20%) which is believed due mostly to practical effects such as a) temporal stability of the source (e.g. laser window contamination and target run-out) over the finite time during which the measurements were made, b) variable surface contamination on the pre-mirror by plasma debris and c) detector noise.

However, the fact that the experimental result shown in Figure 2-38c measures the full predicted aperture of $\Phi_x' = 4.2$ mrad (ref. Figure 2-36) demonstrates that the diffracted beam is essentially in perfect focus through the 10 micron exit slit used to obtain this data.

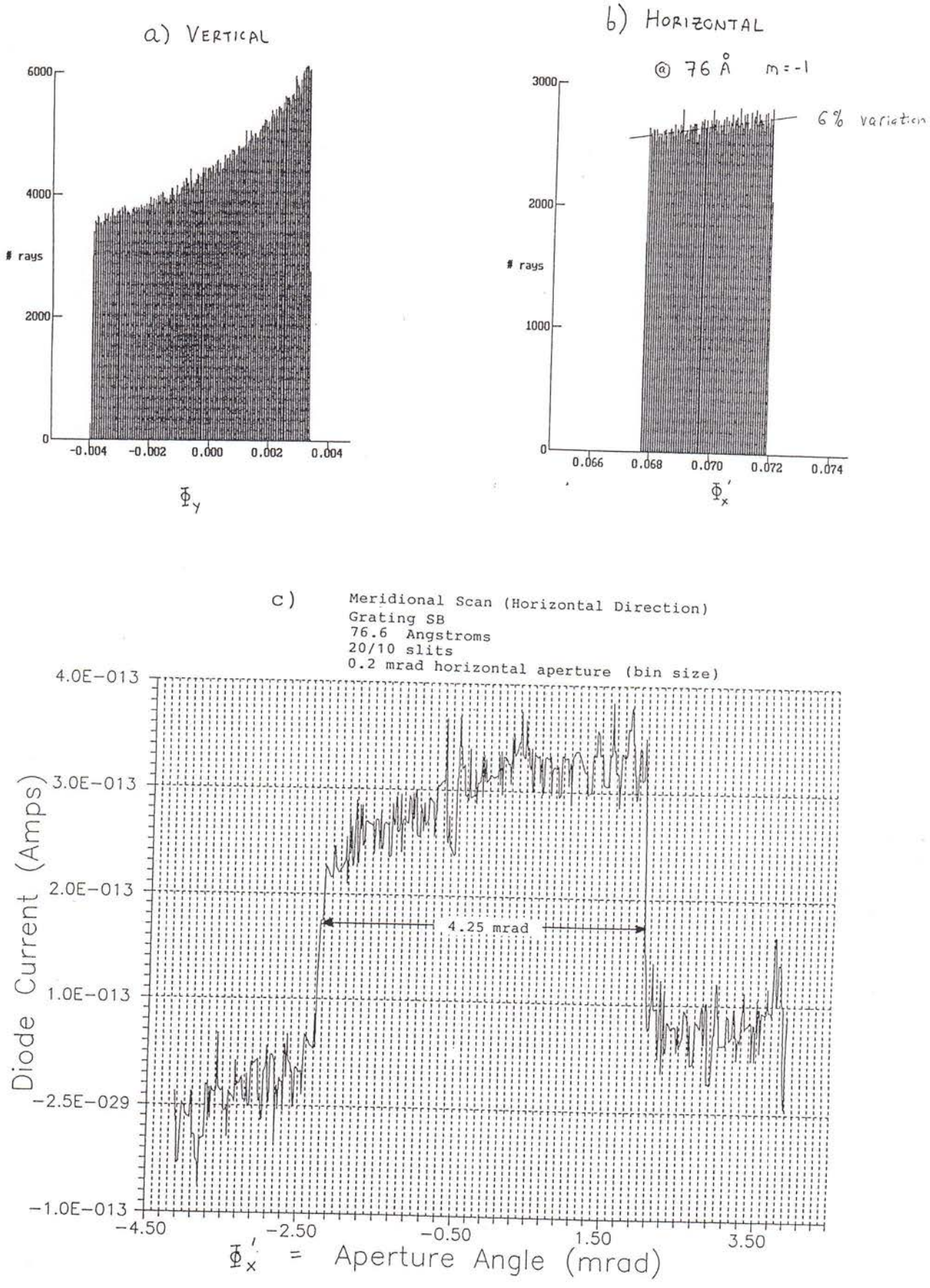


Fig. 2-38. Angular aperture brightness variations raytraced for a) astigmatism control mirror and b) meridional focusing mirror of the HIREFS. Meridional measurements plotted in c) using narrow slits.

# 3. In-Focus Monochromators (IFM)

## *3.1 Geometrical Concept and Fermat Analysis*

While a significant improvement over previous grazing incidence designs, the varied line-space plane grating spectrometers described above are not self-focusing. The radiation diverging from the source or entrance slit must be focused by use of an auxiliary mirror to provide a converging beam to the grating. This mirror introduces some aberration due to geometrical optics, figuring and alignment errors, and some loss in throughput due to its finite reflectivity and scatter. In addition, the focal condition is met at only two wavelengths in the spectrum when using stationary slits, and coma is corrected at only one wavelength. A self-focusing grating which maintains fixed slits and provides images absent of all low order aberrations is the next step in the development of an ideal spectrometer.

If the erect spectral field of the above design is not required, then higher throughput and resolution can be obtained by a new monochromator[58,59] employing a self-focusing grating as illustrated in Figure 3-1. The slits are again fixed in space, and the grating rotates to select the wavelength. However, in order to remove the defocusing which occurs at all but one or two correction wavelengths, the grating is also translated in the direction of its surface tangent. If the grating has varied groove spacings, such translation has the effect of changing the groove spacing and all its derivatives at the position where the fixed principal ray strikes the grating surface. Defocusing is thereby eliminated at *all* wavelengths in the continuum, rather than at one or two wavelengths. This in-focus monochromator (IFM) design is not specific to the angle of incidence, so can be used at grazing incidence without the aberrations inherent of other self-focusing grazing incidence geometries adapted from classical normal incidence designs. The combined rotation and translation of a varied space grating is a new mounting not anticipated in classical optics.

There are a limitless variety of parameterizations of this design. However, one particularly useful solution is presented here in closed form. To minimize the amount of translation required, consider removal of the lowest order aberrations at two wavelengths through rotation alone. Fermat's equations for defocusing and coma [(1-1), (1-5) and (1-8)] at two such correction points ($\lambda_1$ and $\lambda_2$) are given by:

$$\cos^2\alpha_1 /r - \cos\alpha_1 /R + \cos^2\beta_1 /r' - \cos\beta_1 /R + 2\,(\sin\beta_1 - \sin\alpha_1)\, N_{20}/N_{10} = 0 \qquad (3\text{-}1)$$

$$\cos^2\alpha_2 /r - \cos\alpha_2 /R + \cos^2\beta_2 /r' - \cos\beta_2 /R + 2\,(\sin\beta_2 - \sin\alpha_2)\, N_{20}/N_{10} = 0 \qquad (3\text{-}2)$$

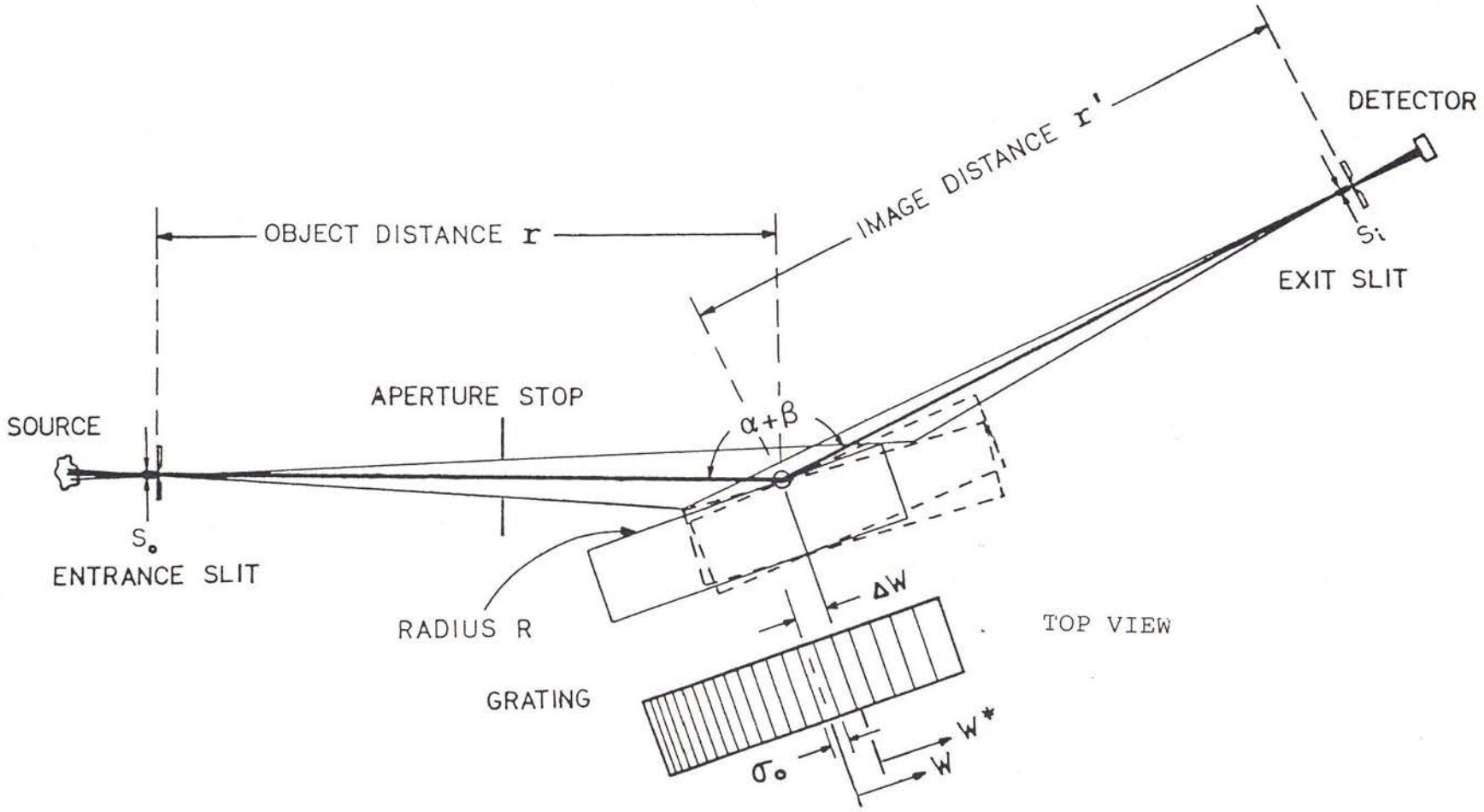


Figure 3-1. IFM grating simultaneously rotates about an axis parallel to its grooves and translates along surface tangent. Groove spacings vary across aperture.

$$-(\sin\alpha_1/r)(\cos^2\alpha_1/r - \cos\alpha_1/R) + (\sin\beta_1/r')(\cos^2\beta_1/r' - \cos\beta_1/R) + 2(\sin\beta_1 - \sin\alpha_1)N_{30}/N_{10} = 0 \quad (3\text{-}3)$$

$$-(\sin\alpha_2/r)(\cos^2\alpha_2/r - \cos\alpha_2/R) + (\sin\beta_2/r')(\cos^2\beta_2/r' - \cos\beta_2/R) + 2(\sin\beta_2 - \sin\alpha_2)N_{30}/N_{10} = 0 \quad (3\text{-}4)$$

where $\alpha$ and $\beta$ are determined from the wavelength according to equations (2-39) and (2-40), respectively. Equations (3-1) to (3-4) are four equations in four unknowns (r, r', $N_{20}=\rho_1/2$ and $N_{30}=\rho_2/3$), where the fixed parameters are the radius of grating curvature (R), the included angle ($2\theta$) and the central groove density ($N_{10} = \rho_o$). Both defocusing ($F_2$) and coma ($F_3$) are made to vanish at each of $\lambda_1$ and $\lambda_2$ by solving the above equations simultaneously, which is possible if the grating is concave ($R > 0$), resulting in:

$$1/r = \{ [ b^2 - 4ac ]^{1/2} - b \} / (2aR) \quad (3\text{-}5)$$

$$1/r' = \zeta / r - \xi / R \quad (3\text{-}6)$$

$$\rho_1 = [(\cos^2\alpha_1/r - \cos\alpha_1/R) + (\cos^2\beta_1/r' + \cos\beta_1/R)] / (m\lambda_1) \quad (3\text{-}7)$$

$$\rho_2 = 3/2\,[(\cos^2\alpha_1/r - \cos\alpha_1/R)\sin\alpha_1/r - (\cos^2\beta_1/r' - \cos\beta_1/R)\sin\beta_1/r'] / (m\lambda_1) \quad (3\text{-}8)$$

where the dimensionless parameters are:

$$a = \chi\sin\alpha_1\cos^2\alpha_1 - \sin\alpha_2\cos^2\alpha_2 - \chi\zeta^2\sin\beta_1\cos^2\beta_1 + \zeta^2\sin\beta_2\cos^2\beta_2 \quad (3\text{-}9)$$

$$b = -\chi\sin\alpha_1\cos\alpha_1 + \sin\alpha_2\cos\alpha_2 + 2\chi\zeta\xi\sin\beta_1\cos^2\beta_1 - 2\zeta\xi\sin\beta_2\cos^2\beta_2 + \chi\zeta\sin\beta_1\cos\beta_1 - \zeta\sin\beta_2\cos\beta_2 \quad (3\text{-}10)$$

$$c = -\chi\xi^2\sin\beta_1\cos^2\beta_1 + \xi^2\sin\beta_2\cos^2\beta_2 - \chi\xi\sin\beta_1\cos\beta_1 + \xi\sin\beta_2\cos\beta_2 \quad (3\text{-}11)$$

$$\zeta = (\chi\cos^2\alpha_1 - \cos^2\alpha_2) / (\cos^2\beta_2 - \chi\cos^2\beta_1) \quad (3\text{-}12)$$

$$\xi = [\chi(\cos\alpha_1 + \cos\beta_1) - (\cos\alpha_2 + \cos\beta_2)] / (\cos^2\beta_2 - \chi\cos^2\beta_1) \quad (3\text{-}13)$$

$$\chi = \lambda_2/\lambda_1 \quad (3\text{-}14)$$

With input parameters of $\rho_o$ = 1500 mm$^{-1}$, R = 10 m and 2$\theta$ = 164°, one finds the solution results in design parameters of r = 1011.488 mm, r' = 964.542 mm, $\rho_1$ = -1.63766 mm$^{-2}$ and $\rho_2$ = +0.00267255 mm$^{-3}$. These differ significantly from those of the conventional design (r = 624.23 mm, r' = 2304.24 mm, $\rho_1$ = 0, $\rho_2$ = 0), in particular the more nearly equal values for object and image distances in the VLS design. While the resulting defocusing shown by curve **200** in Figure 3-2a is comparable to that obtained for the conventional grating (curve **100**) previously plotted in Figure 1-2b, the coma shown by curve 202 in Figure 3-2b is significantly lower than that of the conventional grating (curve **102**). This indicates that a removal of defocusing would allow high spectral resolution at all wavelengths. The non-zero value of $\rho_1$ obtained above allows for such removal at all wavelengths in the continuum by a surface translation ($\Delta$w) of the grating. Fermat's equations still hold provided w, $\rho_o$, $\rho_1$, $\rho_2$, $\rho_3$, etc. are replaced by the adjusted values relative to the new grating pole. These are w*, $\rho_o$*, $\rho_1$*, $\rho_2$*, $\rho_3$*, etc. as follows:

$$w^* = w - \Delta w \quad (3\text{-}15)$$

$$\rho_o^* = \rho_o(1\text{-}1/2\ \varphi^2) + \rho_1(1\text{-}2/3\ \varphi^2)\Delta w + \rho_2\Delta w^2 + \rho_3\Delta w^3 \quad (3\text{-}16)$$

$$\rho_1^* = -\rho_o\varphi/R + \rho_1(1\text{-}2\varphi^2) + 2\rho_2\Delta w + 3\rho_3\Delta w^2 \quad (3\text{-}17)$$

$$\rho_2^* = -\rho_o\varphi^2/(4R^2) - 3/2\ \rho_1(1\text{+}2/9\ \varphi^2)\varphi/R + \rho_2(1\text{+}1/2\ \varphi^2) + 3\rho_3(1\text{+}1/6\ \varphi^2)\Delta w \quad (3\text{-}18)$$

$$\rho_3^* = -2/3\ \rho_o\varphi/R^3 - 4/3\ \rho_1(\varphi/R)^2 + 4/3\ \rho_2\varphi/R + \rho_3(1\text{+}2\varphi^2) \quad (3\text{-}19)$$

where

$$\varphi = \arcsin(\Delta w/R) \quad (3\text{-}20)$$

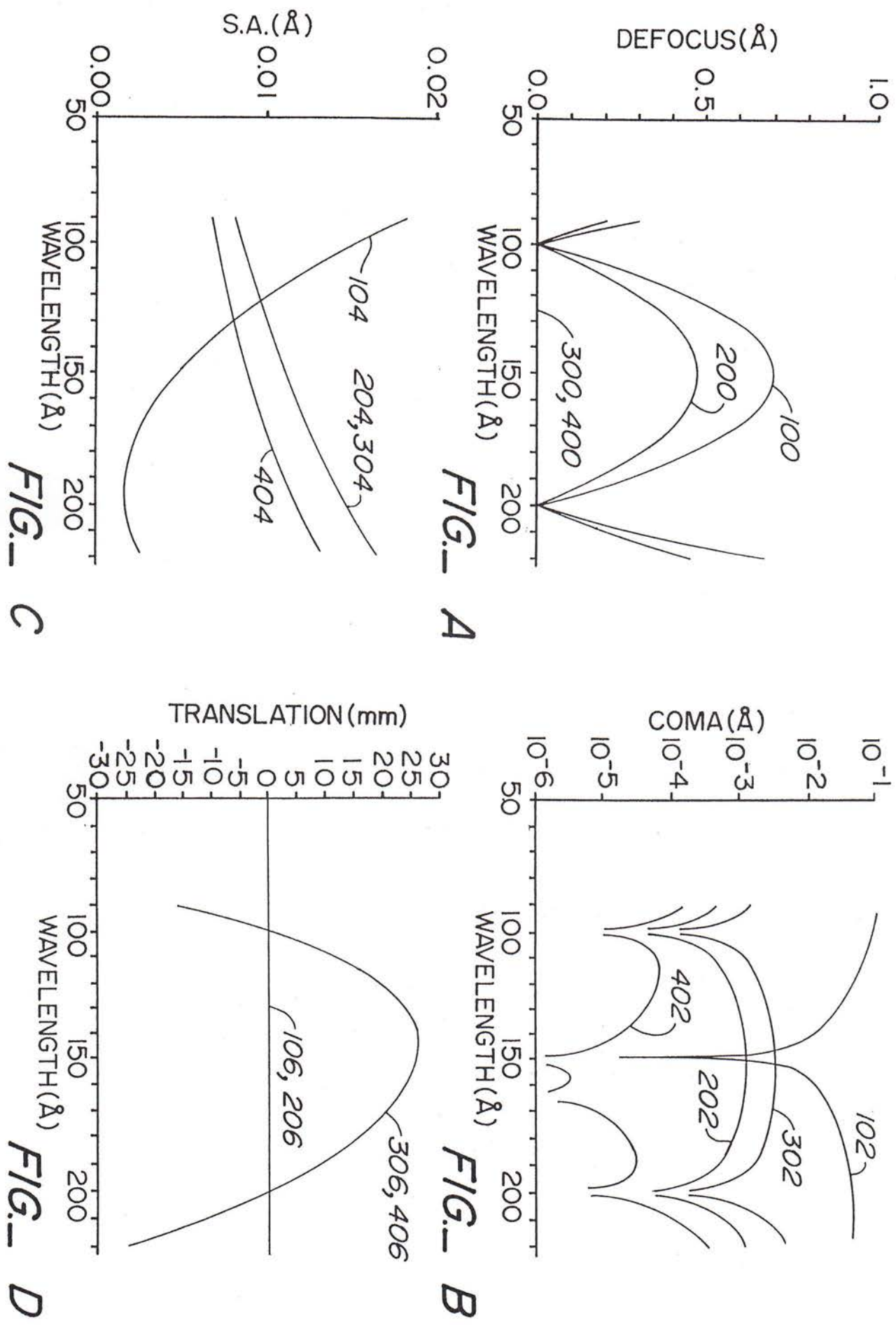


Fig. 3-2. Fermat calculations of the geometrical aberrations of a rotating and translating IFM grating (curves 30X and 40X) versus rotation of classical grating (curves 10X).

The fixed principal ray now strikes ruled width coordinate $w = \Delta w$, and $w^*$ is measured relative to this new pole. **This degree of freedom for aberration elimination is not present for a classical (equally-spaced) grating, as translation parallel to its surface would have no first order effect.**

The amount of translation is obtained by numerically iterating equations (3-16) to (3-18) at each wavelength to force $F_{20} = 0$. Setting the last free parameter $\rho_3$ to zero results in the curve **302** for coma of only ~ .001 Angstroms as shown in Figure 3-2b. While this is already below the physical diffraction limit, it can be reduced even further by taking advantage of the dependence of $p_2^*$ upon $\rho_3$ indicated in equation (3-18). For example, setting $\rho_3 = -7 \times 10^{-7}$ mm$^{-4}$ results in the elimination of coma at a third wavelength near the center of the spectral range, as shown by curve **402** in Figure 3-2c. All wavelengths are now sharply in focus, the limit to the optical resolution being spherical aberration (curve **404** in Figure 3-2c). The extremum spherical aberration of ~ .01 Angstroms corresponds to a FWHM of ~ .0025 Angstroms, and is thus a factor of 250 improvement over the 0.7 Angstrom resolution obtained with the conventional design. The translation required to accomplish this dramatic reduction in aberrations is shown by curve **406** in Figure 3-2d. Because the grating rotation provides for the broad selection of wavelength, the amount of translation required is small (~ 25 mm) and easily obtained with a simple stage. As the translation functions only to remove a small residual amount of defocusing, the translational accuracy required is low. For example, since 25 mm corrects for 0.5 mm defocusing, even a (large) 0.1 mm error in the translation will introduce a defocusing aberration of only ~ 0.5/250 = 0.002 Angstroms. Secondly, the small amount of translation results in the concave grating still intersecting the fixed principal ray at nearly the same vertical position, allowing the translation to be in a straight line.

The amount of space variation required is also modest, due to the use of a concave grating surface to provide the main focusing power. In the above example, a space variation of only ~ 7% is required across the 65 mm meridional width. Such variation is easily obtained and causes little change in the diffraction efficiency across the grating aperture.

## *3.2 UV Experimental Results at Grazing Incidence*

The IFM exhibits its most advantageous performance at grazing incidence, where the conventional designs suffer from highly degraded performance. Experimental verification of the above IFM theory was made initially by construction of an atmospheric monochromator having a 20° graze angle ($2\theta = 140°$). The grating parameters were chosen to enable operation in the ultraviolet and visible, resulting in $\rho_0 = 200$ mm$^{-1}$, $\rho_1 = -0.37169$ mm$^{-2}$, $\rho_2 = +0.00257$ mm$^{-3}$, $\rho_3 = +0.000001$ mm$^{-4}$, R = 1001 mm, r = 301.5 mm, r' = 316.6 mm and a grating ruled width of 45 mm. At each wavelength tested, the translation was adjusted to maximize the power transmitted

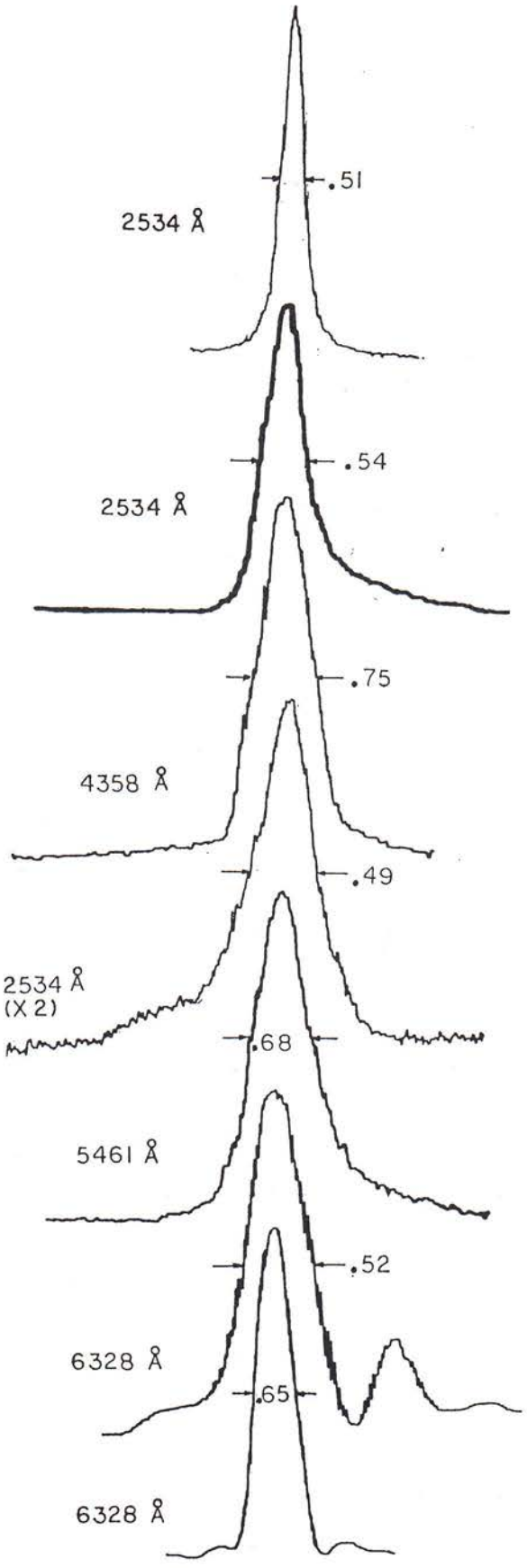


Fig. 3-3. First experimental results with an IFM, demonstrating theoretical spectral resolution at all scanned wavelengths in a grazing incidence mounting with fixed slits.

Table II. **Predicted and Measured Monochromator Performance**[a]

| $m$ | $\lambda$(Å) | $\Delta w$(mm) Theory | $\Delta w$(mm) Actual | $\Delta\lambda_d$(Å) | $s_0$($\mu$m) | $s_i$($\mu$m) | $\Delta\lambda_0$(Å) | $\Delta\lambda_i$(Å) | $\Delta\lambda$(Å) Actual |
|---|---|---|---|---|---|---|---|---|---|
| Uncertainty (±) | | | 0.2 | | 1 | 1 | 0.08 | 0.05 | 0.05 |
| 1 | 2534 | 0.00 | 0.12 | 0.28 | 10 | 10 | 0.68 | 0.88 | 0.82 |
| 1 | 2534 | | | 0.28 | 10 | 5 | 0.68 | 0.22 | 0.73 |
| 1 | 2534 | | | 0.36[b] | 5 | 5 | 0.34 | 0.22 | 0.51 |
| 1 | 3126 | 6.10 | 6.30 | 0.35 | 20 | 20 | 1.41 | 0.81 | 1.35 |
| 1 | 3126 | | | 0.35 | 10 | 10 | 0.70 | 0.40 | 0.75 |
| 1 | 3650 | 8.39 | 8.37 | 0.41 | 20 | 20 | 1.46 | 0.76 | 1.35 |
| 1 | 4047 | 8.86 | 8.82 | 0.45 | 10 | 10 | 0.75 | 0.36 | 0.72 |
| 1 | 4358 | 8.88 | 8.67 | 0.48 | 10 | 10 | 0.76 | 0.35 | 0.75 |
| 2 | 2534 | 6.84 | 6.52 | 0.14 | 10 | 10 | 0.40 | 0.16 | 0.49 |
| 1 | 5461 | 5.14 | 4.97 | 0.61 | 10 | 10 | 0.81 | 0.30 | 0.68 |
| 1 | 5461 | | | 0.61 | 5 | 10 | 0.40 | 0.30 | 0.56 |
| 1 | 6328 | 0.00 | 0.00 | 0.70 | 10 | 5 | 0.85 | 0.13 | 0.64 |
| 1 | 6328 | | | 0.70 | 5 | 5 | 0.42 | 0.13 | 0.52 |
| 1 | 6328 | | | 0.87[b] | 10 | 5 | 0.85 | 0.13 | 0.65 |
| 1 | 6328 | | | 0.87[b] | 5 | 5 | 0.42 | 0.13 | 0.65 |

[a] $m$, spectral order; $\lambda$, wavelength; $\Delta w$ (theory), predicted grating translation; $\Delta w$ (actual), measured grating translation relative to 0-$\mu$m reading for optimized imaging at $\lambda$ = 6328 Å; $\Delta\lambda_d$, diffraction-limited resolution, assuming a full grating aperture; $s_0$, entrance slit width; $s_i$, exit slit width; $\Delta\lambda_0$, entrance slit-limited resolution; $\Delta\lambda_i$, exit slit-limited resolution; $\Delta\lambda$ (actual), measured FWHM of traced line profile.

[b] Grating width stopped to 36 mm, centered at the rotation axis.

through the exit slit, then a high resolution scan across the spectral line was traced on a chart recorder. Two light sources were used: a low pressure mercury lamp for lines at 2534, 3126, 3650, 4047, 4358 and 5461 Angstroms and a Helium-Neon laser for the red line at 6328 Angstroms. The mercury discharge was ~ 5 mm in diameter and placed behind the entrance slit whereas the pencil He-Ne beam ~ 0.6 mm in diameter was diffracted by the narrow entrance slit to fully illuminate the grating.

Figure 3-3 shows the wavelength profiles obtained for three strong emission lines of the Hg lamp and the red He-Ne line. These traces reveal a symmetrical in-focus image at each wavelength. As listed in Table II which includes an additional three (weaker) lines, all measured resolutions are attributed entirely to either the finite slit widths or the physical diffraction-limited resolution (9000 grooves full aperture). In agreement with both geometrical (Fermat) calculations and numerical raytracing of the line profiles, the measured FWHM resolution of < 1 Angstrom is approximately 1/4 times the calculated extremum spherical aberration of 3-5 Angstroms for wavelengths from 2534 to 6328 Angstroms. A few of the profiles shown in Figure 3-3 appear slightly asymmetrical, due to the 9 mm grating translation which weights the aperture and thus the spherical aberration to one side of the grating pole. This effect is removed by stopping down the aperture slightly to maintain a symmetrically illuminated grating aperture, resulting in the symmetrical profiles shown in the top and bottom traces. The diffraction-limited profile at 6328 Angstroms is evidenced by the presence of subsidiary maxima. **The measured FWHM** of these profiles, using slit widths of 5-10 microns, **corresponds to resolving powers of 5,000-12,000**. Considering the grazing angle, the short length (~ 0.6 m) and the large aperture (~ 50 mrad), this resolution is quite high, and is **a factor of ~ 300 improvement over that attainable using a conventional rotating grating with fixed slits and the same angular deviation.**

Table II also demonstrates that the experimentally measured amount of translation is within 0.2 mm of that calculated according to the above theory. This translation was simple linear motion in the direction of the grating tangent at the rotation axis which was fixed in space.

## *3.3 Compact Soft X-Ray IFM*

The ability to maintain a perfect spectral focus at all wavelengths with fixed slits and a large grating aperture provides a higher combination of resolution and throughput than previous designs, making the IFM particularly advantageous when operated with soft x-ray radiation. Reducing the graze angle from the 20° in the proof-of-concept IFM to 2° in a commercial model IFM-SXR-0.5 provided a high throughput moderate resolution monochromator for use throughput the soft x-ray region. A compact physical envelope of 0.5 meters slit-to-slit was obtained by use of the following input parameters: $2\theta = 176°$, R = 8 m , $\rho_o = 600$ mm$^{-1}$ ($\lambda_1 = 11.5$ Angstroms and $\lambda_2 = 22$ Angstroms). Longer wavelength gratings are of lower groove density as indicated in the advertisement reproduced here as Figure 3-4.

Fig. 3-4. IFM compact model specs.

# ◇ IFM™ IN-FOCUS MONOCHROMATOR

HETTRICK SCIENTIFIC INC.
904 Wright Ave. #8 Richmond, CA 94804
TEL (415) 234-3996 FAX (415) 234-3997

U.S. PATENT 4,991,934

- ◇ **Self-Focusing Grating (High Throughput)**
- ◇ **Grazing Incidence (Soft X-Ray Use)**
- ◇ **Fixed Position Slits**
- ◇ **No Defocusing Over Entire Spectrum**
- ◇ **Highly Symmetrical Line Profiles**
- ◇ **Five Grating Bands Available**
- ◇ **Gratings/Slits Selected Under Vacuum**
- ◇ **Compact Affordable Design**

## OPTICAL PRINCIPLE

The IFM is based on a new grazing incidence focusing condition*, whose essential features are illustrated below. A reflection grating consists of grooves whose spacings vary systematically along the dispersion plane. Selection of the wavelength transmitted between fixed entrance and exit slits is accomplished by rotation of the grating combined with a simultaneous translation along its surface tangent. Due to the varied spacing, the translation provides a new set of grating parameters where the principal ray strikes the grating surface. This new degree of freedom eliminates defocusing at every wavelength. Second order (coma) aberration is also well corrected by higher order terms in the varied-space function. This yields symmetrical line shapes, and provides a physically compact instrument having a large collection angle.

The optical aberrations of the IFM are typically a factor of 10-100 smaller than a conventional spherical or toroidal grating in a single-element fixed slit mounting. Equivalently, the throughput gain is 10-100 at that limiting spectral resolution.

The fixed slits permit practical use with immovable sources of light and detection, and hence represent an attractive and cost-effective alternative to the Rowland circle monochromator.

*M.C. Hettrick, "In-focus monochromator: theory and experiment of a new grazing incidence mounting," Appl. Opt. **29**, 4531-4535 (1990).

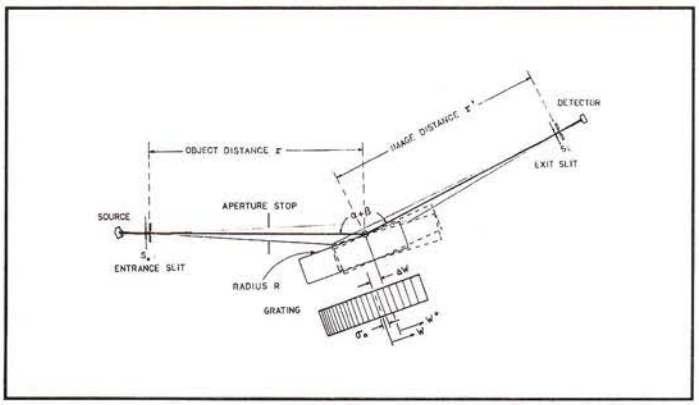


Optical systems based on the IFM are protected by U.S. Patent 4,991,934 and by other foreign patents pending. Licensing is available from Hettrick Scientific Inc. for customers who wish to manufacture special (e.g. UHV) IFM systems for in-house use.



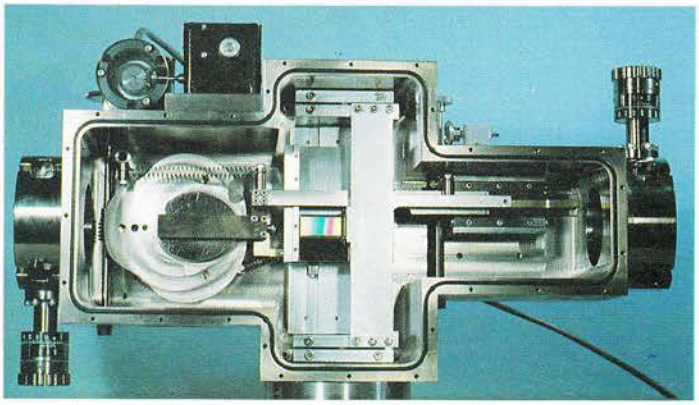

## CONSTRUCTION

The design philosophy for compact model IFM-SXR-0.5 is maximum throughput at moderate spectral resolution. It employs an axis of rotation fixed in space near the grating pole, and a spherical concave grating surface located approximately midway between the slits. This results in minimal required translation, and a nearly fixed direction for the emerging ray.

The grating mounting plate is lapped optically flat to ensure accurate co-alignment of up to five gratings interchangeable under vacuum. In addition, six discrete slit widths are selectable under vacuum using a feedthrough incorporating a centering adjustment which is factory present for optimal resolution and wavelength calibration. The wavelength scanning is accomplished by means of a double cam residing under vacuum and machined to automatically correlate the combined grating rotation and translation. This is driven by a single externally mounted stepper motor, providing a linear wavelength scale.

## SOFT X-RAY RESULTS

A laser-produced, (1.06 μm, 300 mJ, 2.5 nsec, 13 Hz) aluminum plasma was focused through the entrance slit of the IFM-SXR-O.5 by means of a relay mirror. The spectrum recorded by a commercial silicon soft x-ray photodiode is shown below. The peak line intensities of 700 pico-Amps correspond to 6 x $10^7$ photons/sec. With 200 μm slits, $4x10^8$ ph/sec are detected emerging the exit slit! Because the internal drive cams have bilateral symmetry within the spectral operating range of the gratings, the scan direction automatically reverses as one scans passed the maximum wavelength. This provides for an efficient accumulation of data, and requires no limit switches. As evident in the experimental results shown here, the two spectra are excellent mirror images of each other, wavelength calibration being maintained. *The IFM delivers spectra coming and going!*

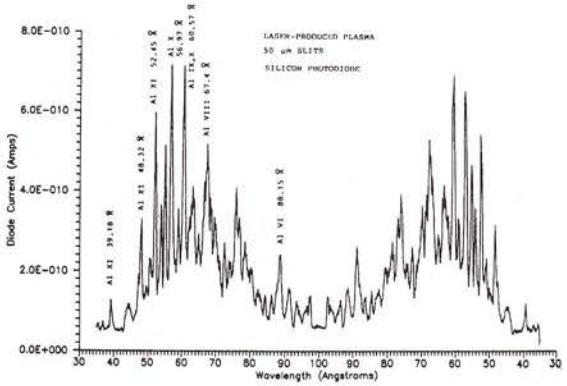

## IFM-SXR-0.5 SPECIFICATIONS

| | |
|---|---|
| Mounting | Hettrick, U.S. Patent 4,991,934, Spherical Grating |
| Angular Deviation | $4^{o}$ (Fixed). Nominal graze angle of $2^{o}$ |
| Grating Format | Gold Surface. Active Aperture 62 mm Meridional x 15 mm Sagittal. 5 Positions Selectable Under Vacuum. |
| External Drive | Single Micro-Stepped Motor with Compumotor SX57-51 Indexer/Drive w/RS232C interface port. |
| Scan Speeds | 0.1 - 100 mÅ/sec (Grating A) |
| Wavelength Linearity | ±0.5% |
| Backlash | <0.05 Å (Grating A) |
| Reproducibility | ±0.01Å (Grating A) Same Slits, per Pumpdown. |
| Slits | Feedthrough Selectable Widths of 5, 10, 20, 50, 100 and 200 microns. Lengths Are All 15 mm. |
| Vacuum Chamber | Weld-Free 6061 Aluminum, Electroless Nickel Plated, Captive Viton 0-Ring Sealed Lid. 1/4-20 Mtg. Inserts. |
| User Ports (e.g. Pumping) | O-Ring Sealed. Bottom Port Accepts 4.5" Conflat Flange, Side Port Accepts 2.75" Conflat Flange. |
| Total Weight | 22 kg, Including Innards, Lid, Motor and Counter. |
| Length | 0.47 meters (Slit-Slit), 0.5 meters (Flange-Flange) |
| Aperture (vs. Wavelength) | 11.2-14.9 mrad (f/89 to f/67) at Entrance Slit<br>7.2-3.5 mrad (f/139 to f/285) at Exit Slit |
| Aperture Center | Shift vs. Wavelength < ± 6 % of Above Values |

## GRATING SPECIFICATIONS

| Grating Code | HX | X | A | B | C |
|---|---|---|---|---|---|
| Nominal g/mm | 1200 | 600 | 300 | 150 | 75 |
| Operating Range (Å) | 6*-12.5 | 8.75-25 | 17.5-50 | 35-100 | 70-200 |
| Plate Scales (Å/mm) | | | | | |
| Entrance Slit | 1.5-2.0 | 3.0-4.0 | 6.0-8.0 | 12.0-15.9 | 24.0-31.8 |
| Exit Slit | .96-.48 | 1.9-1.0 | 3.9-1.9 | 7.7-3.8 | 15.4-7.6 |
| Nominal Resolution (Å) | | | | | |
| 50 micron Slits | 0.07 | 0.15 | 0.3 | 0.6 | 1.2 |
| 10 micron Slits | 0.02 | 0.04 | 0.07 | 0.15 | 0.3 |

*Short wavelength limit depends upon source intensity.

## ACCESSORIES

A monochromator system typically integrates some of the following accessories. During soft x-ray spectral testing at our facility, we can align and test the completed assembly prior to shipment. In additon to this hardware, we encourage the customer to use our consulting and installation services to facilitate a successful interfacing and operation at the customer's facility.

RELAY MIRRORS can be used to focus point sources through the entrance slit, collimate or re-focus the exit slit onto the user's detector.

VISIBLE ALIGNMENT MODULES direct a He-Ne pencil beam through the monochromator from the entrance slit end, exit slit end, or both. Particularly useful in conjunction with relay mirrors to back-aim the incident beam through the entrance slit under vacuum.

FILTER ASSEMBLIES increase the S/N ratio when the user's detector is sensitive to a broad band of wavelengths. Model VSA-100 is supplied with four filter holders, clear rectangular aperture 3.8 x 17.2 mm to match the acceptance aperture of the monchromator. Filters available on request.

APERTURE ASSEMBLIES are useful when a defined rectangular aperture at the output is needed (e.g. for feeding test optics), or when the beam intensity must be decreased without changing slit size. Model VSA-200 is available with 6 apertures (various sizes) selectable under vacuum.

MOUNTING BREADBOARDS are particularly important when co-aligning the monochromator to other optics (e.g. relay mirrors) or when interfacing to sources or detectors which cannot be directly mounted to the monochromator. We offer rigid lightweight custom breadboards containing either simple 4-point or precision 3-point adjustable screws. Stands, gate valves, and other accessories are available on request, and may be integrated into the breadboard or other structure specified by the custormer.

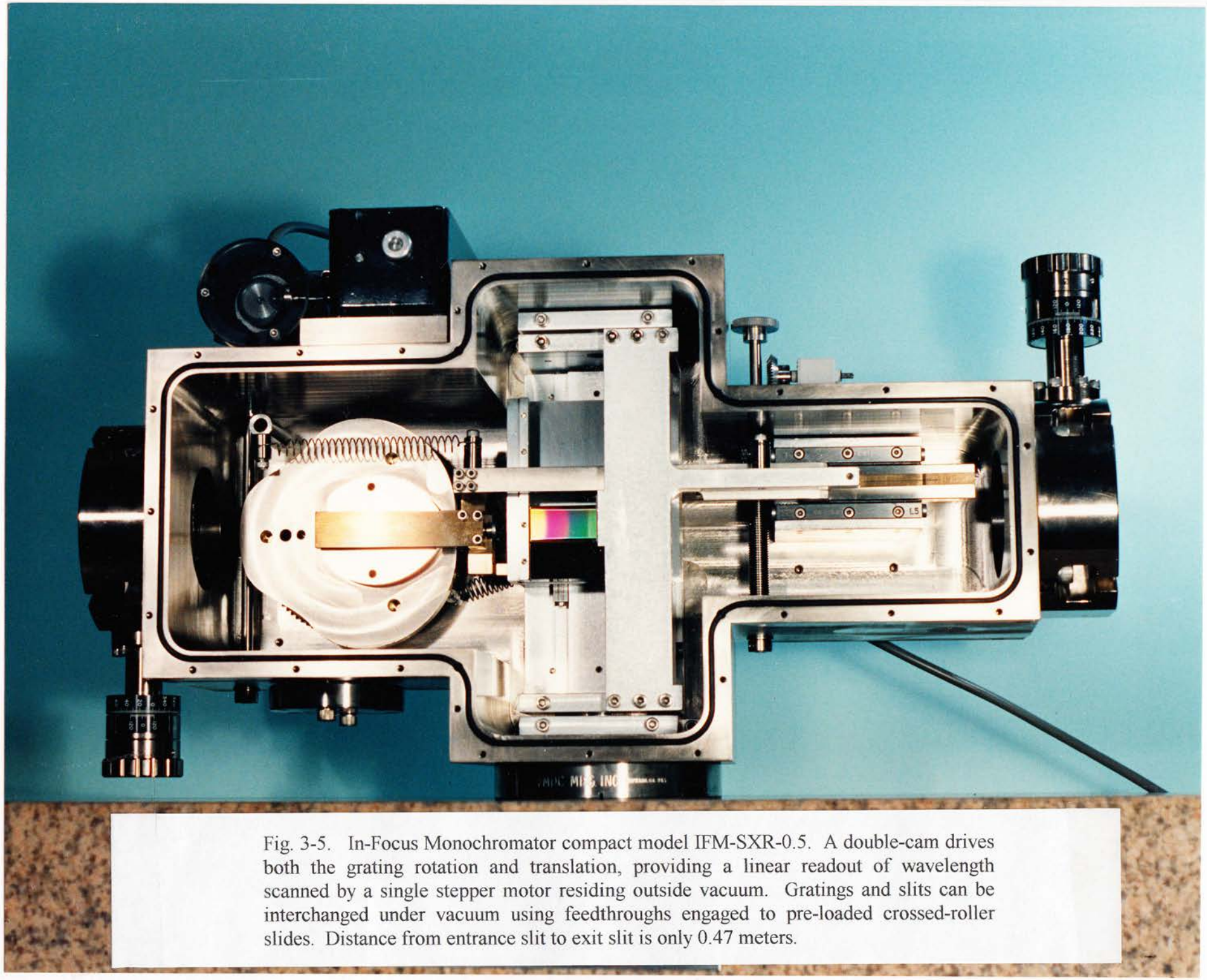

Fig. 3-5. In-Focus Monochromator compact model IFM-SXR-0.5. A double-cam drives both the grating rotation and translation, providing a linear readout of wavelength scanned by a single stepper motor residing outside vacuum. Gratings and slits can be interchanged under vacuum using feedthroughs engaged to pre-loaded crossed-roller slides. Distance from entrance slit to exit slit is only 0.47 meters.

Fig. 3-6. Required translation of soft x-ray IFM grating along its surface tangent.

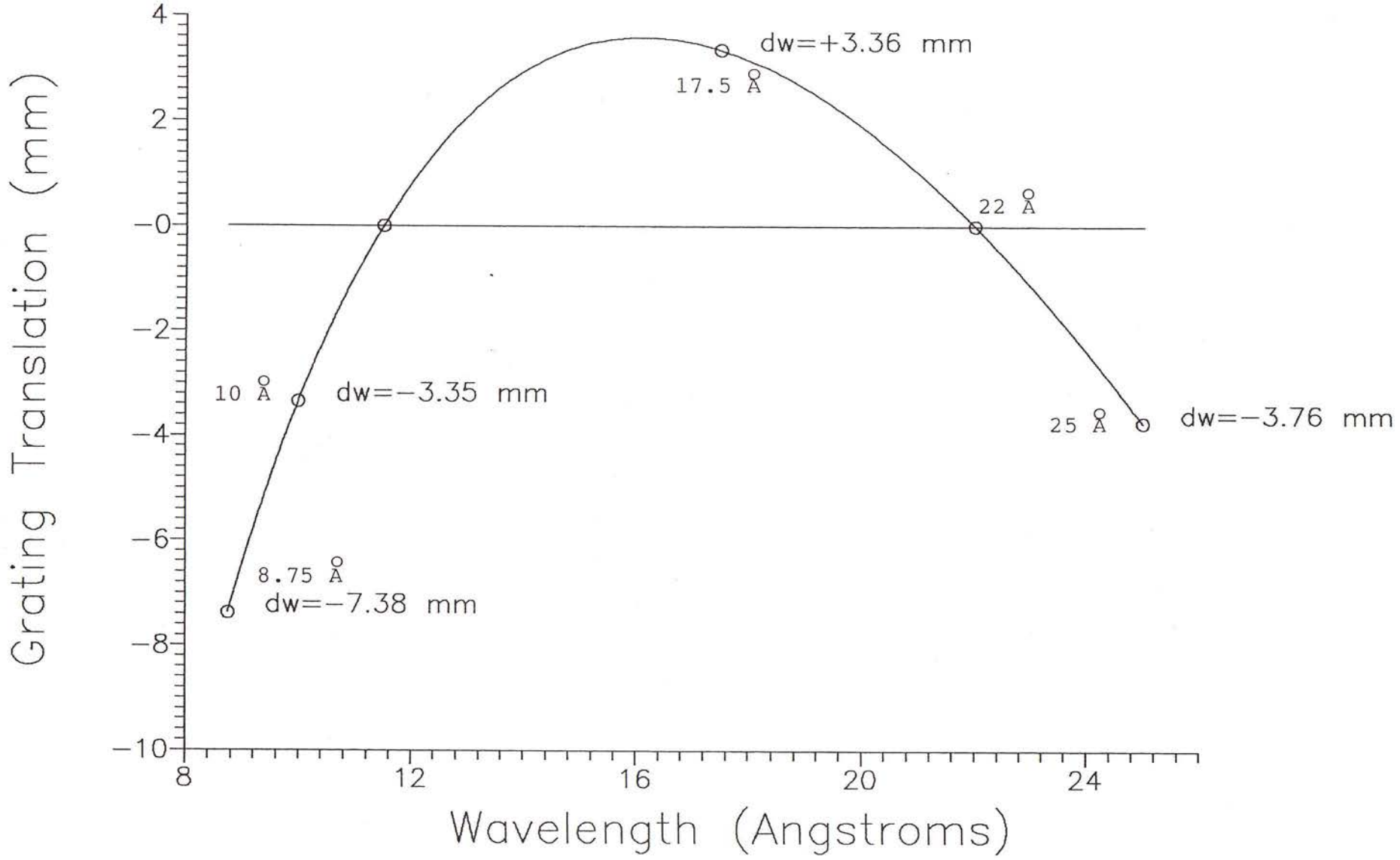

A convenient feature of the mechanical design, shown in Figure 3-5, is that the grating rotation and translation are driven by a double-cam which automatically correlates the two motions and provides a linear readout of wavelength from the rotation of a stepper motor shaft residing outside the vacuum chamber. The required translation as a function of wavelength is plotted in Figure 3-6. At the two correction wavelengths, the translation is zero. Originally designed to cover the 10-25 Angstrom region, the 600 g/mm grating need only translate by ~ +/- 3.5 mm. Extension to shorter wavelengths (8.75 Angstrom) required a maximum translation of -7.38 mm. In practice, this allowed access to the important Al-K line at 8.34 Angstroms.

## a) Raytrace Simulations (2-D and 3-D)

The line profiles shown in Figure 3-7 result from 2-D meridional raytraces of Model IFM-SXR-0.5 at the exit slit plane, using an entrance slit of 5 microns width. The horizontal scales have been converted to Angstrom units, revealing a nearly constant FWHM resolution of ~ 0.02 Angstroms. When convolved with a 10 micron exit slit, the This represents a typical resolving power is ~ 500 at the center of the band. Away from the two correction wavelengths, the line profiles exhibit some asymmetry due to non-zero coma. This asymmetry is small in comparison to the line width resulting from all but these narrowest of slits.

Full 3-D raytraces are shown in Figure 3-8 at the same wavelengths. The sagittal beam diverged by 30 mrad to simulate a full illumination of the 15 mm long exit slits used in the actual monochromator. This results in the small amount of sagittal coma appearing as image curvature in the spot diagrams. The image width in the dispersion (vertical) direction is dominated by the magnification of the 5 micron entrance slit by the factor $\cos \alpha / \cos \beta$ which ranged from ~ 1.6 to 4.2 as a function of the wavelength, due to use of the outside (+) spectral order.

## b) Measured Soft X-Ray Efficiencies

Due to the use of only a single optical element, the efficiency of this soft x-ray monochromator is the efficiency of the grating. To determine this efficiency, absolute reflectometry measurements were made on four IFM gratings [X(600 g/mm), A(300 g/mm), B(150 g/mm) and C(75 g/mm)] ruled according to the author's specifications by Dr. George Hirst and Stan Coles (Perkin Elmer Corp.). The spectral bands are denoted . Each grating was mounted to allow rotation to the desired angle of incidence and translation to center the grating in the monochromatic beam provided by an IFM-SXR-0.5 monochromator used to select spectral lines from a laser-produced plasma light source. The angle of incidence was adjusted at each wavelength to simulate the constant angular deviation mount of $2\theta = 176^{\circ}$ used in the monochromator, and a silicon photodiode detector translated into the beam diffracted from the test grating to measure its intensity. This was converted to absolute efficiency by also measuring the incident intensity after translating the grating sample out of the beam.

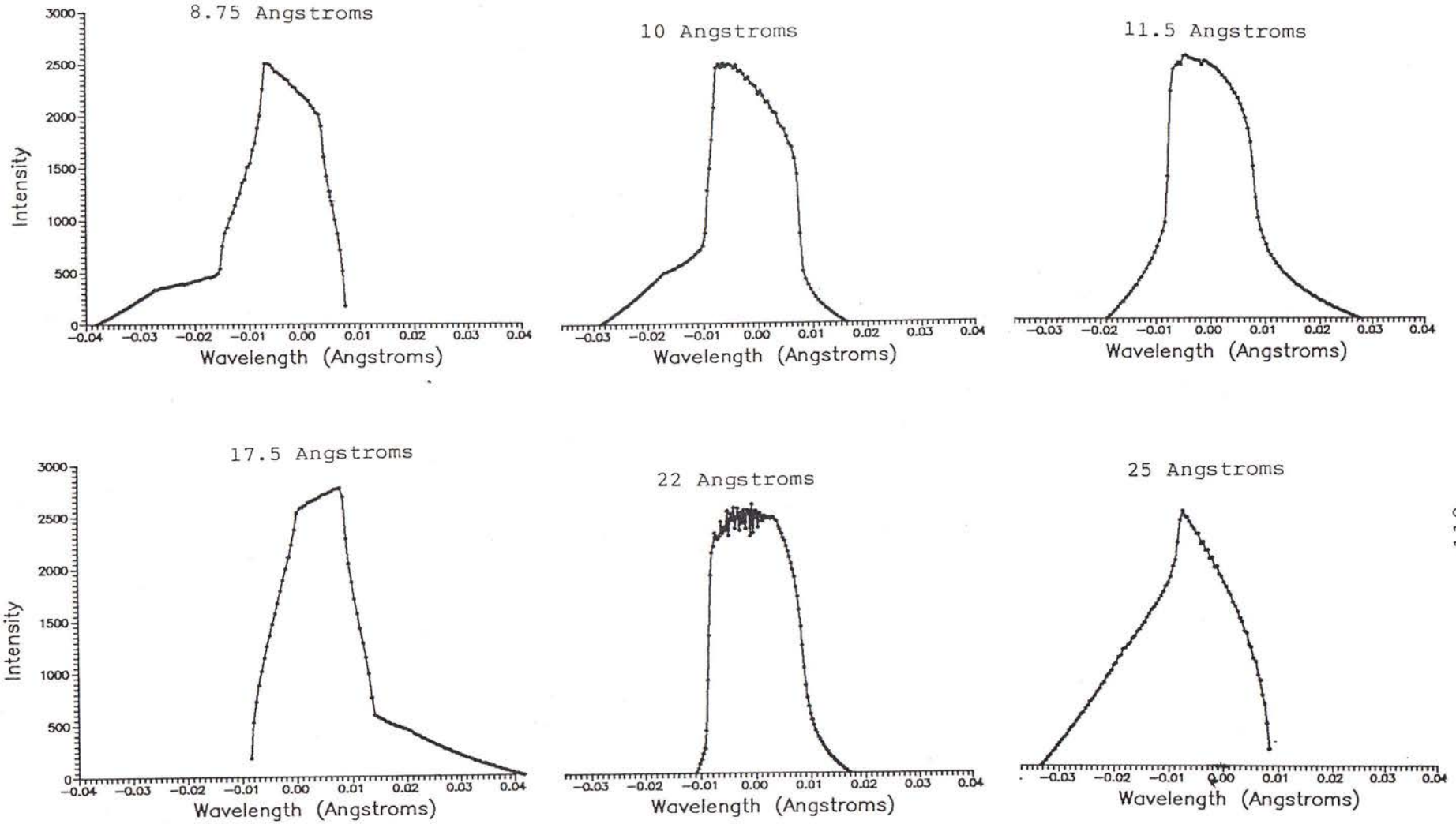


Fig. 3-7. Line profiles at exit slit plane calculated using a 2-D numerical raytrace code. The required translation at each wavelength is given in Fig. 3-7. Note symmetrical profile at 11.5 and 22 Angstroms where translation and therefore coma aberration is forced to zero. Entrance slit was 5 microns, and only the meridional rays were traced (no sagittal aperture).

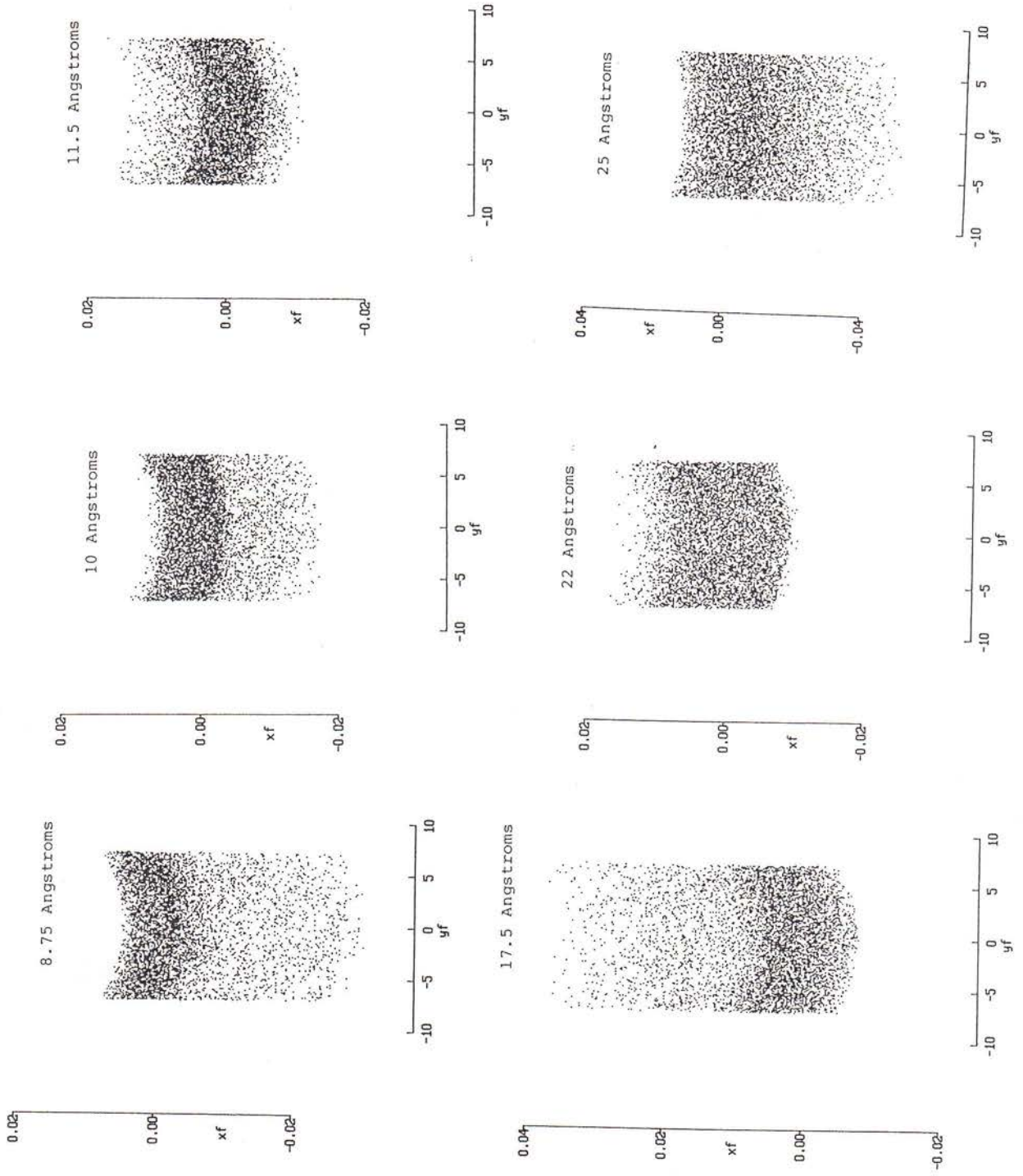


Fig. 3-8. Spot diagrams resulting from 3-D numerical raytracings. Focal plane coordinates are in millimeters. Note the increased magnification of the 5 micron entrance slit as wavelength increases, and the image curvature due to the large (30 mrad) sagittal aperture.

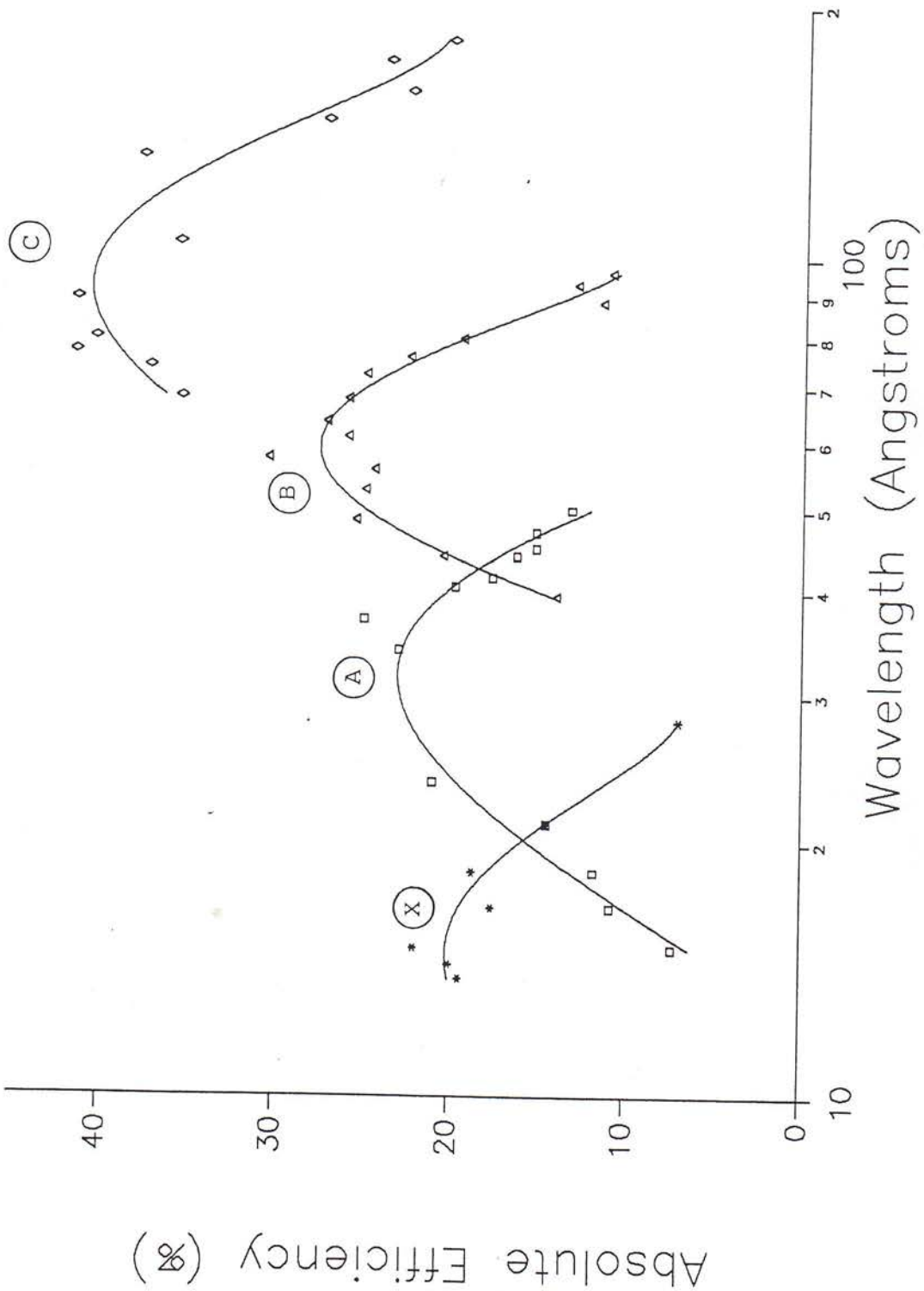


Fig. 3-9. Measured absolute grating efficiencies for four different IFM gold-coated gratings. A region near the center of each grating was sampled and the grating rotated in a reflectometer to select wavelength in a $2\theta = 176^{\circ}$ mount. Incident wavelength was pre-monochromatized by an IFM and laser-produced plasma light source.

The measured results are plotted in Figures 3-9 for the four gratings, and fit to third degree polynomials. The first order absolute efficiencies peak at ~ 20% for the short wavelength gratings (X and A), rise to 25% for the medium wavelength grating (B) and further increase to ~ 40% for the long wavelength grating (C). These results are essentially equal to the theoretical values at the blazed wavelength. These theoretical values equal the shadow factor Q (see Sec. 2.1f) which is ~ 50% in this case, times the reflectance of gold which ranges from ~ 50% at the short wavelengths to ~ 70% at the long wavelengths.

The angular acceptance of the monochromator in the meridional direction is due to the 62.5 mm grating width, resulting in 11.2 mrad to 14.9 mrad as a function of wavelength as the grating rotates. In the sagittal direction, the 15 mm long exit slit limits the acceptance angle to ~ 30 mrad for sources placed near the entrance slit. The resulting solid angle of acceptance is the product of these, or ~ 400 μrad. Multiplying this geometrical value times a typical measured efficiency of 25% results in en effective solid angle of ~ 100 μrad. This value can be multiplied by the intensity of a narrow source located at the entrance slit plane to determine the approximate intensity emerging the exit slit. However, if a diffuse source is located behind the entrance slit, the solid angle must be diminished by the ratio of the entrance slit width to the source size. This assumes the source is placed at the optimum distance from the slit, resulting in full illumination of the grating.

## c) First Soft X-Ray Results

Figure 3-10 shows laboratory photographs and a chart recorder trace of the first soft x-ray results obtained with Model IFM-SXR-0.5 on February 28, 1991. The spectral lines arise from various ionization states of the aluminum laser-produced plasma, and the instrument resolution is determined by analysis of only the narrowest of these lines, to avoid including multiple component line blends.

The predicted resolution is determined by assuming the optical aberrations are negligible and considering only the dispersive resolution at the two slits. As shown by the raytraces above, this is a good approximation when the slit widths are 10 microns or larger. As each slit contributes a square profile to the line shape (unlike the Gaussian profiles of the space astronomy spectrograph of Sec. 2.2), the convolution of both slits is a trapezoidal profile with a FWHM equal to:

$$\Delta\lambda = \text{MAX}\,(A,B) + 1/2\ \text{MIN}\,(A,B) \qquad (3\text{-}21)$$

where

$$A = (d_o/m)\,(\Delta x_{ent}/r)\,\sin\{\pi/2 - \theta + \arcsin[m\lambda/2/d_o/\sin(\pi/2-\theta)]\} \qquad (3\text{-}22)$$

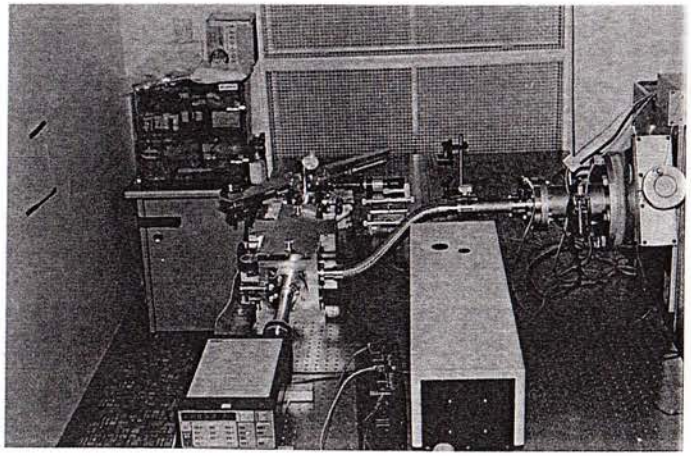

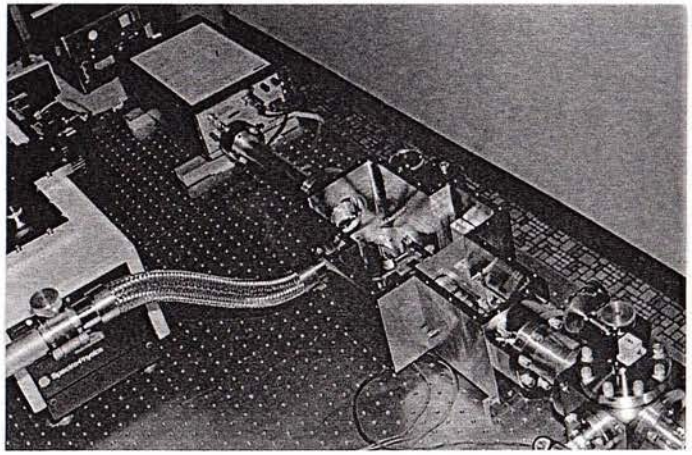

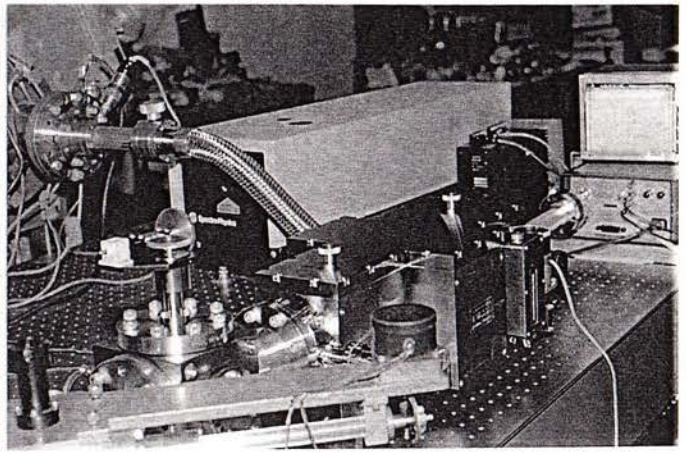

Photos The monochromator is tested for spectral resolution and calibration using the narrow line radiation from a laser-produced plasma. A pico-ammeter used to record the spectra is shown at the top of the photo.

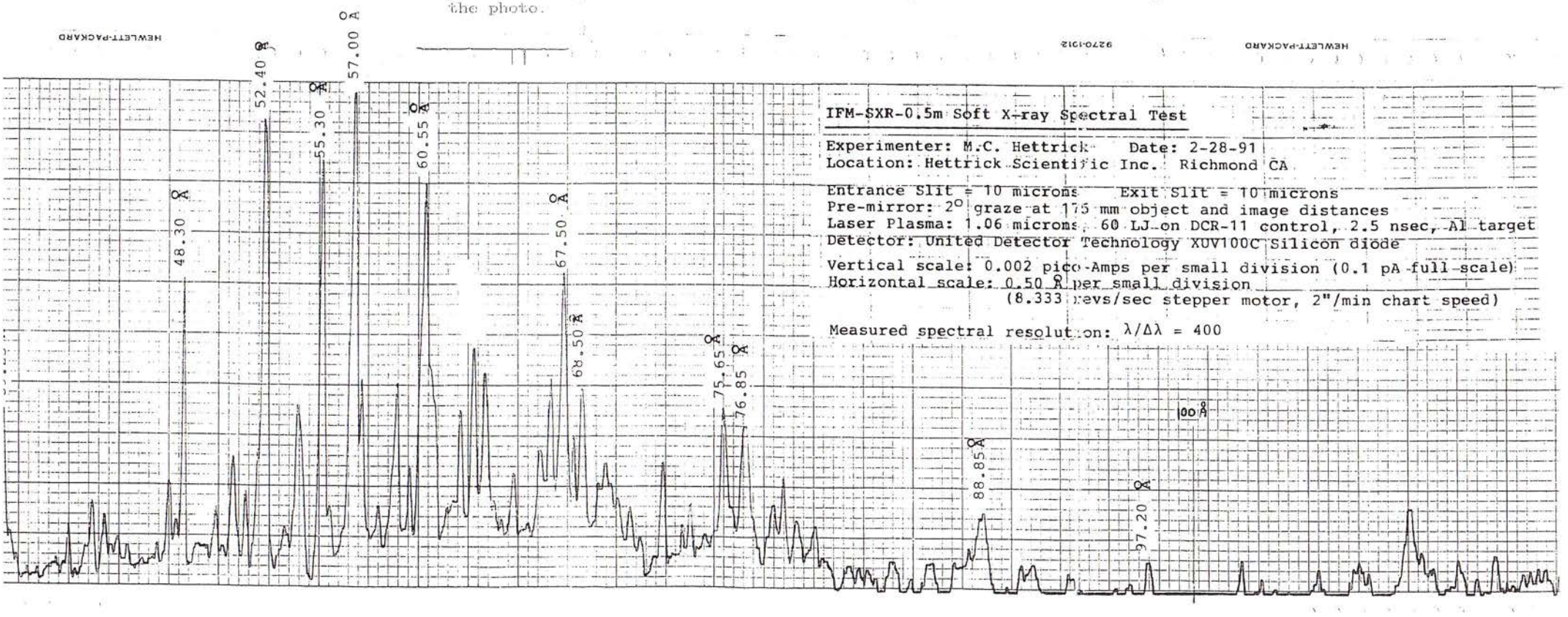


Fig. 3-10. The first soft x-ray spectrum taken using an In-Focus Monochromator (IFM). This data was recorded on Feb. 28, 1991 at Hettrick Scientific Inc. with the compact commercial model IFM-SXR-0.5 in the configuration photographed at the top.

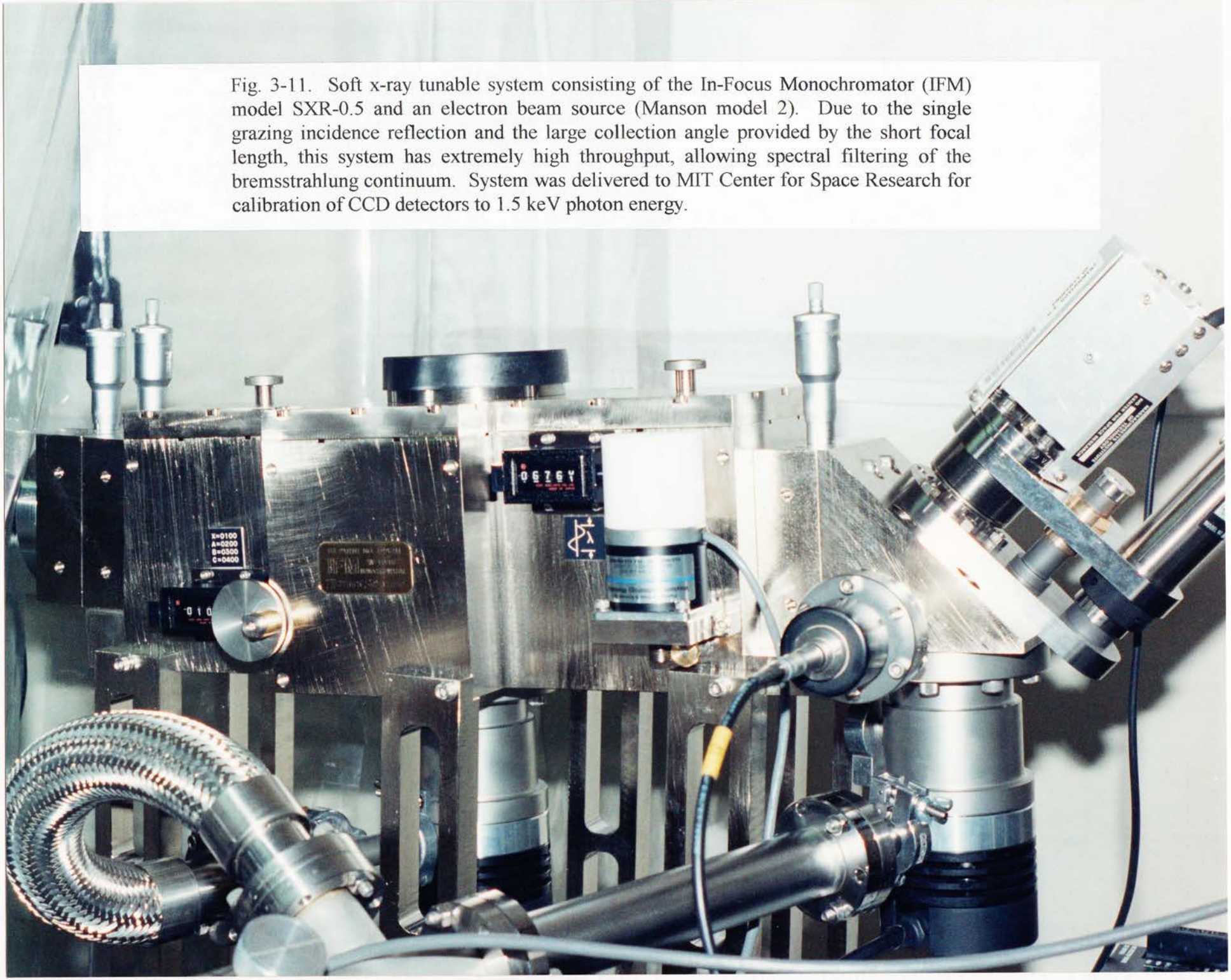

Fig. 3-11. Soft x-ray tunable system consisting of the In-Focus Monochromator (IFM) model SXR-0.5 and an electron beam source (Manson model 2). Due to the single grazing incidence reflection and the large collection angle provided by the short focal length, this system has extremely high throughput, allowing spectral filtering of the bremsstrahlung continuum. System was delivered to MIT Center for Space Research for calibration of CCD detectors to 1.5 keV photon energy.

$$B = (d_o/m)\ (\Delta x_{ex}/r')\ \sin\{\pi/2 - \theta - \arcsin[m\lambda/2/d_o/\sin(\pi/2-\theta)]\} \qquad (3\text{-}23)$$

and where $\Delta x_{ent}$ is the width of the entrance slit and $\Delta x_{ex}$ is the width of the exit slit. Substituting $d_o$ = 66,667 Angstroms (grating B), m = +1, $\theta = 88^o$ and $r \cong r' \cong 236$ mm, and using the sine approximation for small angles, the above equations become:

$$A \cong \Delta x_{ent}\ (.00986 + .0000607\ \lambda) \qquad (3\text{-}24)$$

$$B \cong \Delta x_{ex}\ (.00986 - .0000607\ \lambda) \qquad (3\text{-}25)$$

where $\Delta x$ are in micron units and $\lambda$ is in Angstrom units. Using $\Delta x$ = 10 microns results in $\Delta\lambda \cong$ 0.16-0.18 Angstroms over the 35-100 Angstroms band. This is in good agreement with the measured resolution of ~ 0.2 Angstroms.

This spectrum represents the first grazing incidence fixed slit spectrometer which recorded in-focus spectral images at all scanned wavelengths using a single optical element. This first IFM is in operation at the Los Alamos National Laboratory using an electron beam light source. An additional five IFMs were manufactured and are in operation at various laboratories using e-beam, laser-plasma and other sources in the wavelength region from ~ 8 Angstroms to ~ 400 Angstroms. Two such IFM configurations are next presented, including the results from tests made at Hettrick Scientific Inc.

## d) Calibration of E-Beam Source Line Spectra

The calibration of single-photon counting detectors, such as micro-channel plates and CCDs, requires a low intensity stable source which emits both line and continua throughout the soft x-ray region. This is provided by an electron beam source which is placed near the entrance slit in order to fill the grating aperture. As astigmatism is not only tolerable but actually preferred in order to fill the detector aperture, a single-element IFM may be used. Figure 3-11 is a photograph of such a system configured with a Manson Model 2 soft x-ray source attached to an adjustment feedthrough and compact triangular chamber near the entrance slit assembly. A turbo-molecular pump attached directly to the source chamber maintains a pressure below $10^{-7}$ torr in order to minimize the accumulation of hydrocarbons on the source anode.

The spectra obtained using gratings X and A and detected by current readings through a silicon photodiode are plotted in Figure 3-12a. The slit widths were 100 microns, and the K-lines of neutral Aluminum, Magnesium, Oxygen and Carbon readily appear from the aluminum anode. The magnesium is due to the alloy of aluminum used, and the oxygen and carbon are due to hydrocarbons accumulated on the anode surface after an extended period of operation. The known wavelengths of these lines allow an

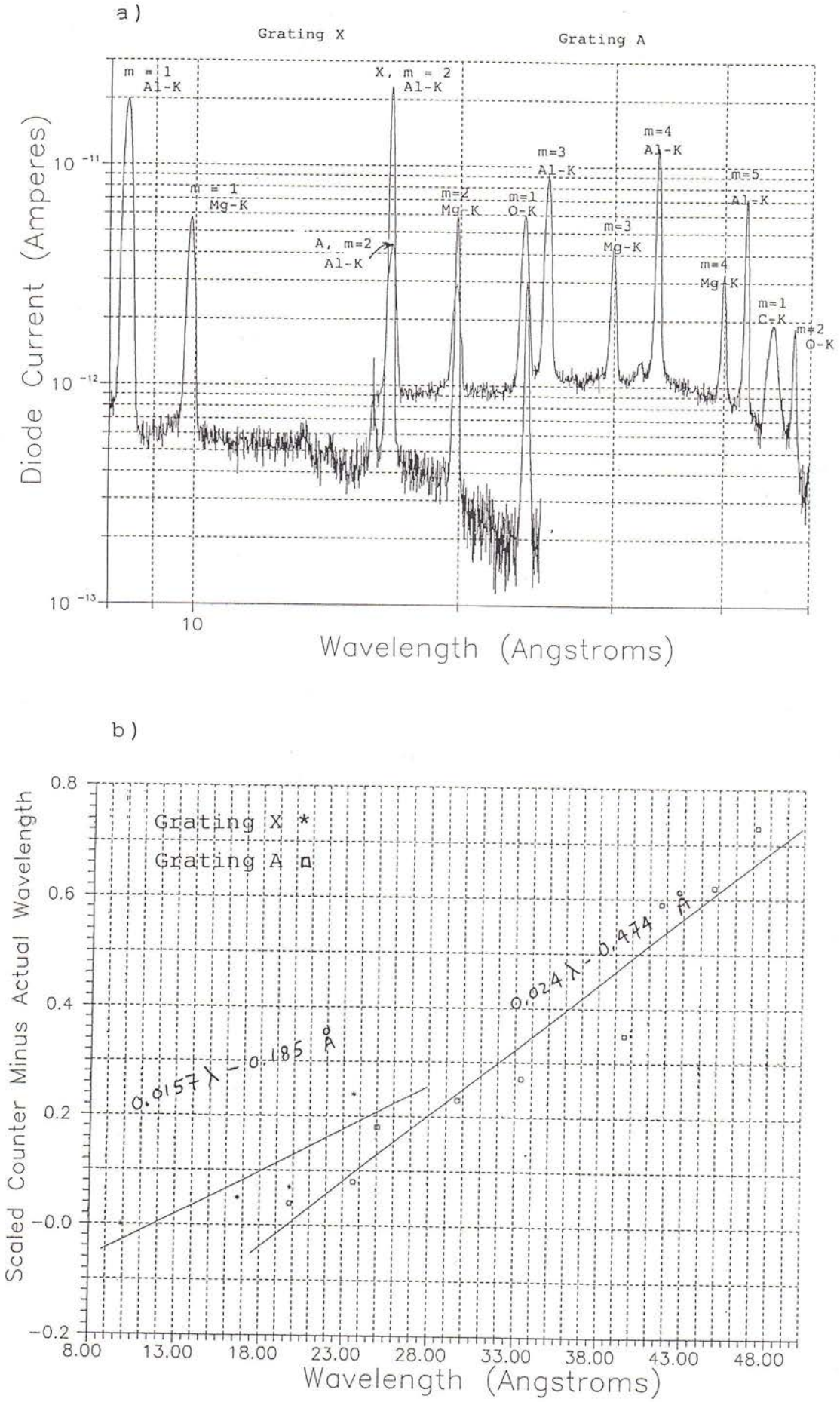


Fig. 3-12. E-beam calibration of IFM: a) spectrum using 100 micron slits with aluminum alloy anode; b) absolute wavelength calibration.

Fig. 3-13. High resolution profile of the narrow Al-K alpha line from e-beam source diffracted in second spectral order by the IFM using an entrance slit of 5 microns and an exit slit of 10 microns. The measured resolving power is approximately 500.

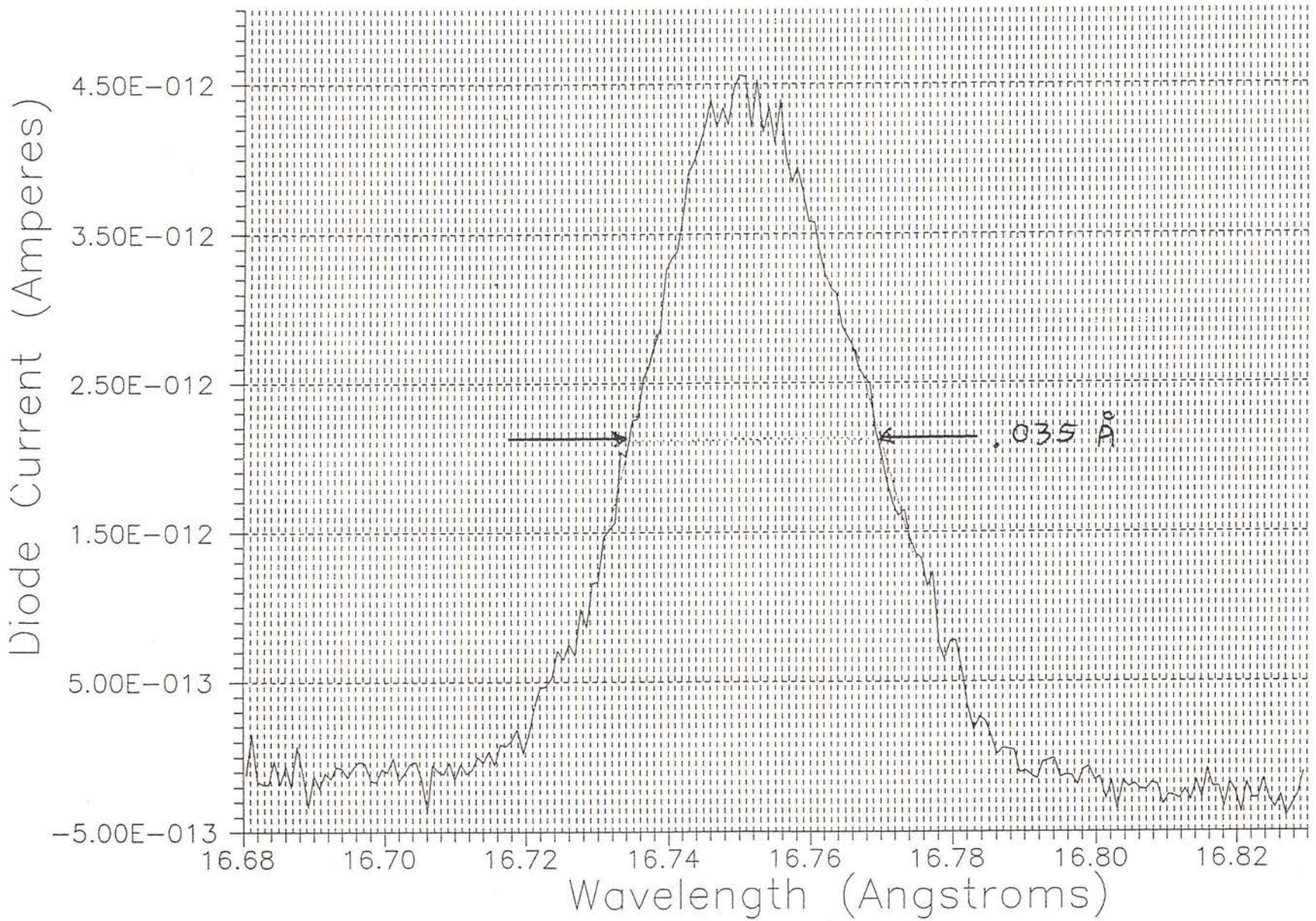

absolute calibration of the wavelength scale. The cam wavelength drive allows for a precise linear fit to the data, as plotted in Figure 3-12b, with residual errors less than 0.5% in wavelength.

The FWHM of the line profiles in Figure 3-12a corresponds to a resolving power of ~ 50-100 as a function of wavelength, consistent with equation (3-21). The low-z lines of aluminum and magnesium are inherently narrow, and therefore serve as probes of the instrument resolution. Selecting an entrance slit of 5 microns and exit slit of 10 microns, Figure 3-13 plots a higher resolution profile taken of the second order Al-K line. The measured FWHM of ~ 0.035 Angstroms corresponds to a resolving power of ~ 500 at this spectral wavelength.

By insertion of other anodes and attachment of foils on Copper or Aluminum based anodes, the astigmatic IFM has provided lines to wavelengths as short as P-K (6.1 Angstroms) and has discovered intense Ti-L lines at 27.42 Angstroms and 31.36 Angstroms, the latter being in near wavelength coincidence with the elusive N-K line. Such additional lines have provided a useful tunable monochromatic light source for calibration of CCD detectors and other optical components.

## e) Bremsstrahlung Spectra and Laminar Grating

The electron beam source also emits bremsstrahlung easily detected with single-photon counting devices following the exit slit of the monochromator. Even the uncooled silicon photodiode detector used to calibrate the IFM showed measurable bremsstrahlung continuum at all wavelengths. Figure 3-14a shows one such spectrum at long wavelengths using grating C and an aluminum anode. Unfortunately, the blazed grating has triangular groove profiles which produce good efficiency in high spectral orders. Thus, any features in the continuum are overwhelmed by the presence of multiple order lines of aluminum from the anode. This spectrum, taken using a 50 micron entrance slit and 100 micron exit slit, shows the aluminum-K line at 8.34 Angstrom reproduced all the way through spectral order m ~ 20!

To reduce the intensity of these higher order lines, and thus provide a spectrum dominated by the first order continuum, a laminar profile VLS grating model D was made for the IFM by the author using a new grating fabrication technique developed by Hettrick Scientific Inc. Figure 3-14b, taken using a 20 micron entrance slit and a 50 micron exit slit, shows the self-absorption edge of the aluminum anode at Al-L, clearly measurable due to the removal of the higher order lines by the laminar groove profile. The correct fabrication of the designed groove density variation is also confirmed by the measured sharpness of the absorption edge.

## f) Stigmatic IFM for Plasma Spectra

With the addition of a mirror to remove the astigmatism, the IFM provides a point-like monochromatic image of extremely high brightness. Figure 3-15 is a sketch of such

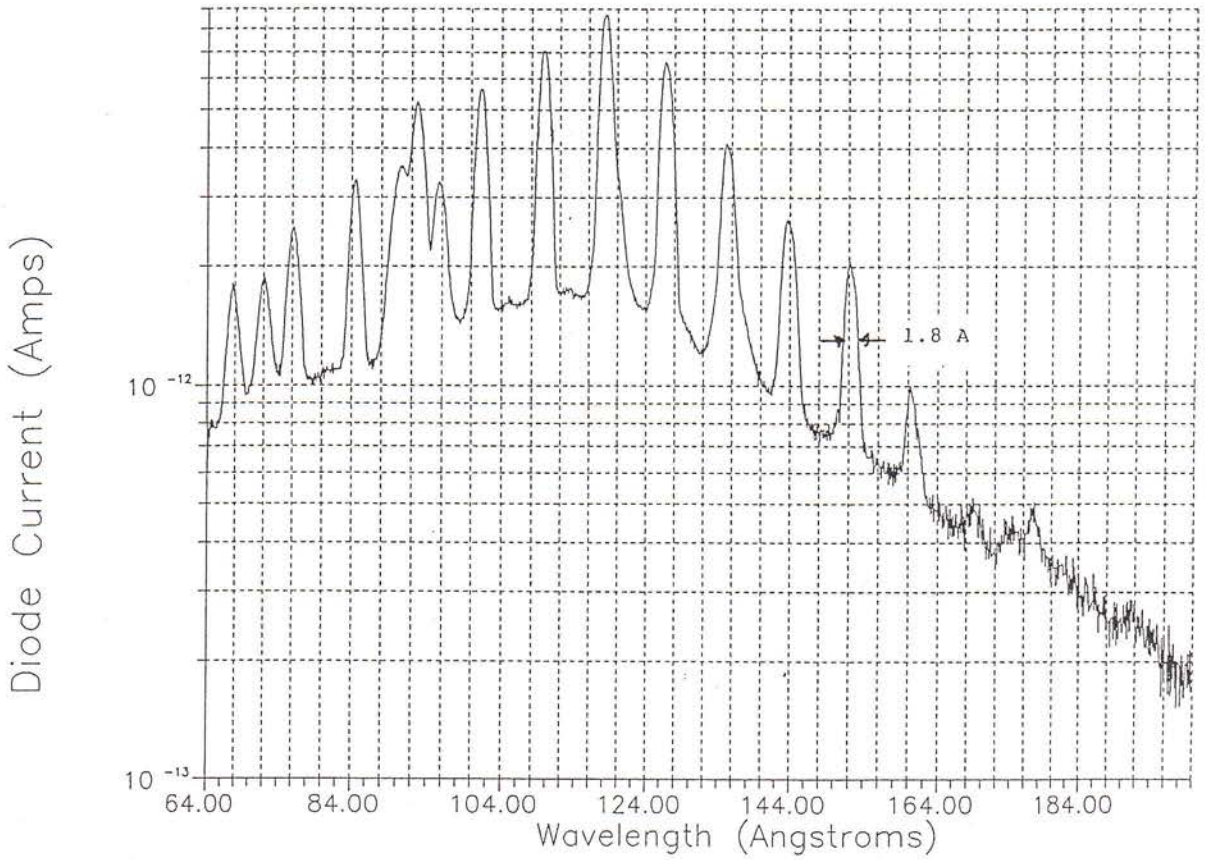


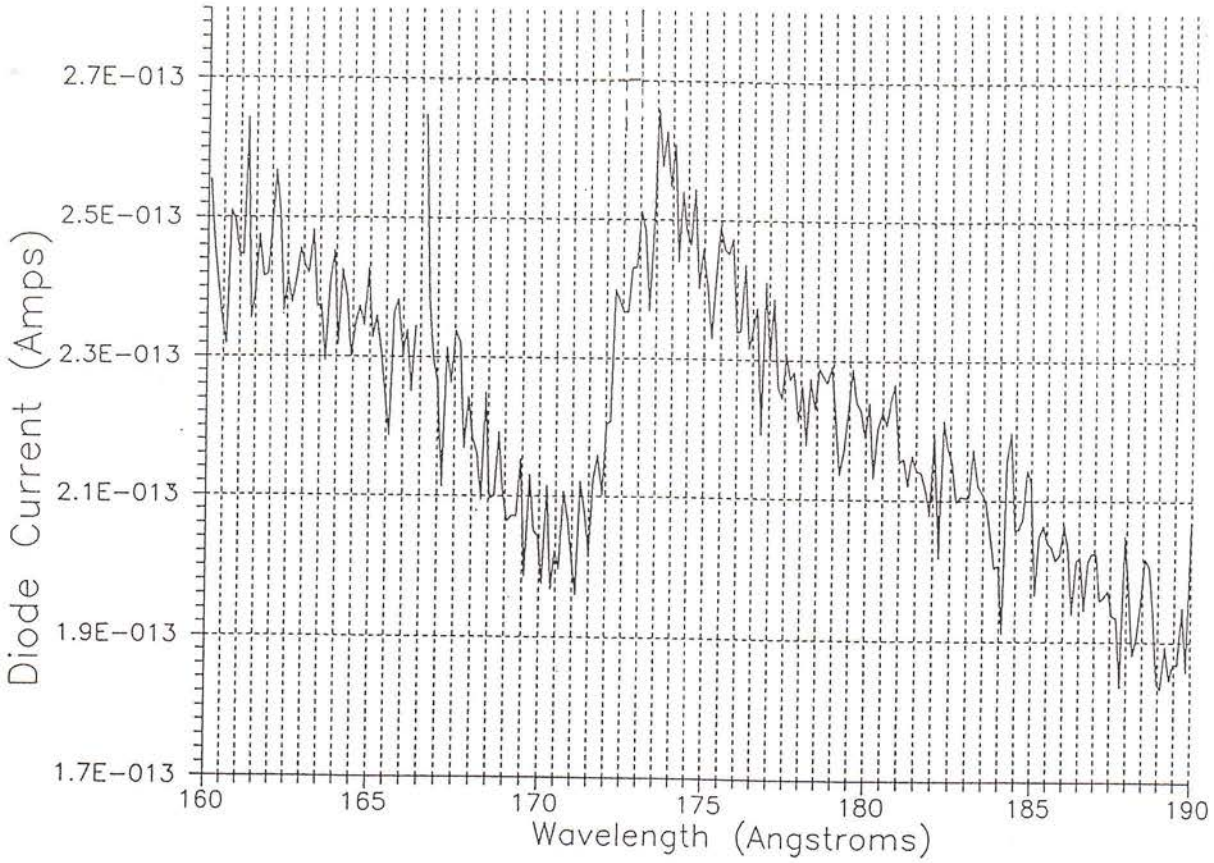


Fig. 3-14a) Grating C (75 g/mm) spectrum using 50/100 micron slits, dominated by high spectral orders of Al-K line, from blazed grating. b) Laminar grating D spectrum using 20/50 micron slits, revealing first order continuum spectrum and Al-L absorption edge from anode.

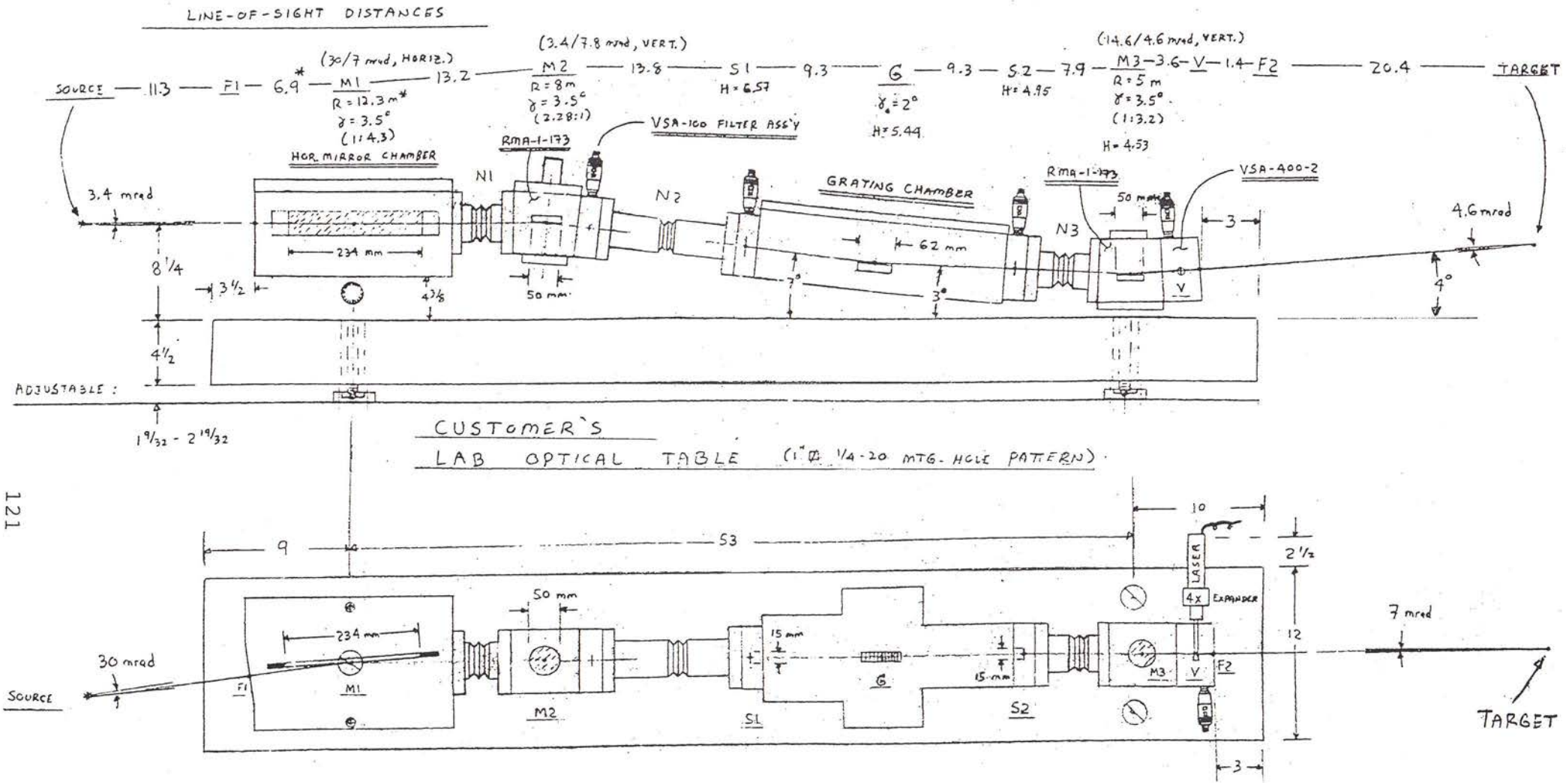


Fig. 3-15. Assembly of stigmatic IFM, delivering ultra-bright point monochromatic images to a target which resides in ultra-high vacuum.

**Hettrick Scientific, Inc.**
SOFT X-RAY OPTICAL SYSTEMS
904 WRIGHT AVENUE UNIT #8 RICHMOND, CALIFORNIA 94804
TEL (510) 234-3996 FAX (510) 234-3997

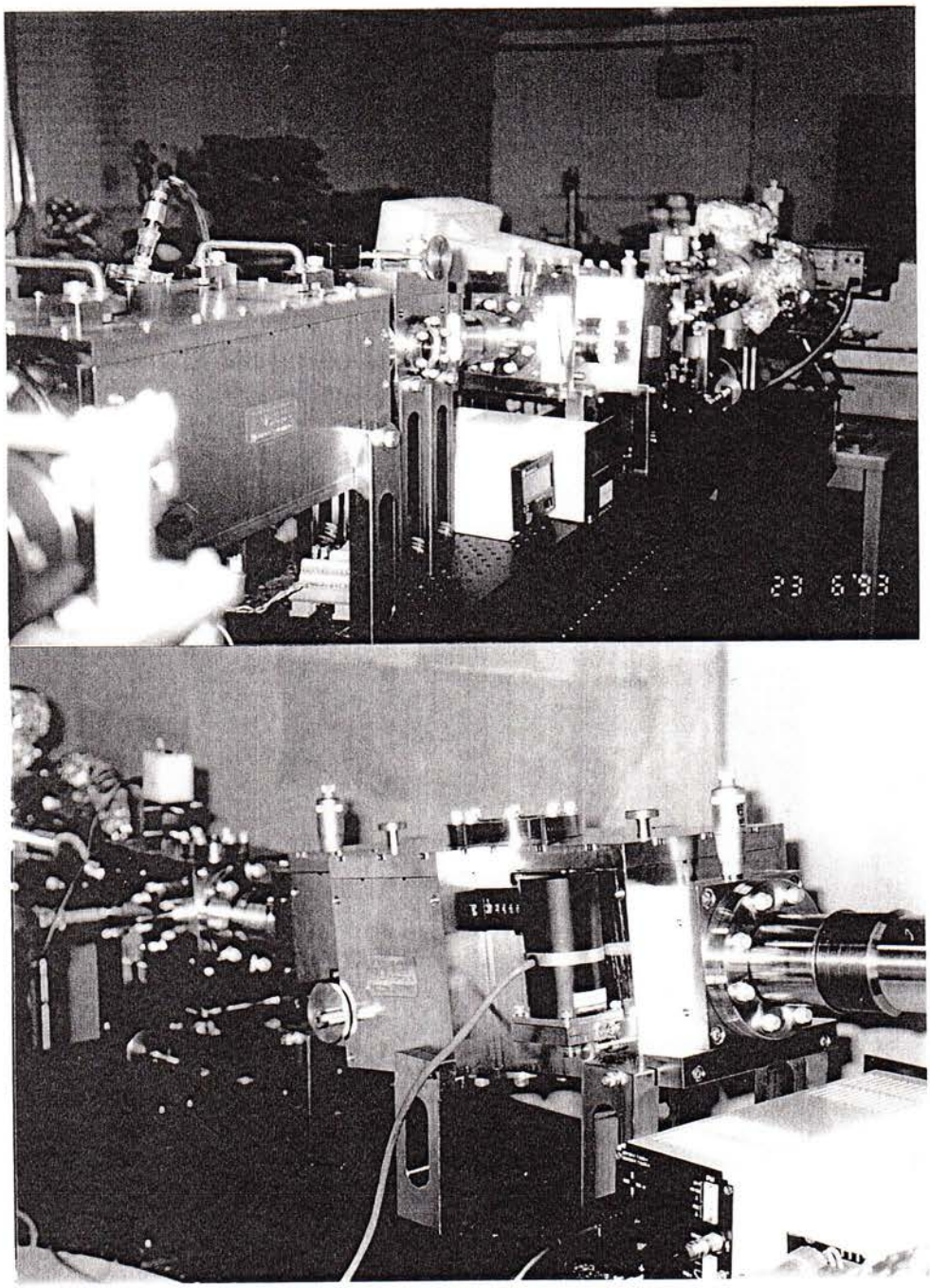


IFM-TYPE II-SXR-0.5 end-to-end system.

Fig. 3-15. b) Photographs of stigmatic IFM system drawn in Fig. 3-15 during laser-plasma testing of resolution and efficiency at author's company.

Fig. 3-16. Stigmatic IFM grating C spectrum of aluminum laser-produced plasma. Entrance slit was 5 microns and exit slit 10 microns.

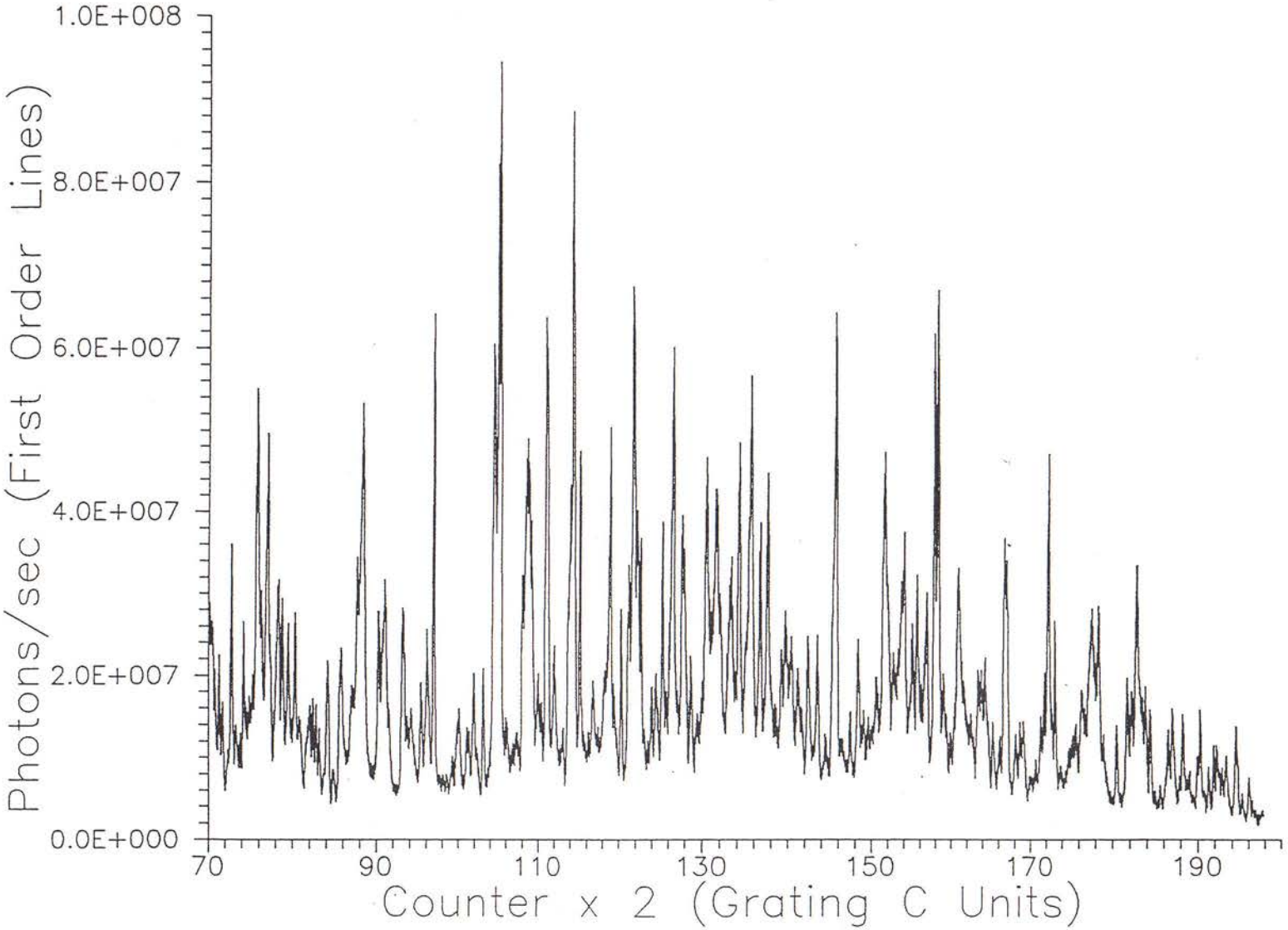

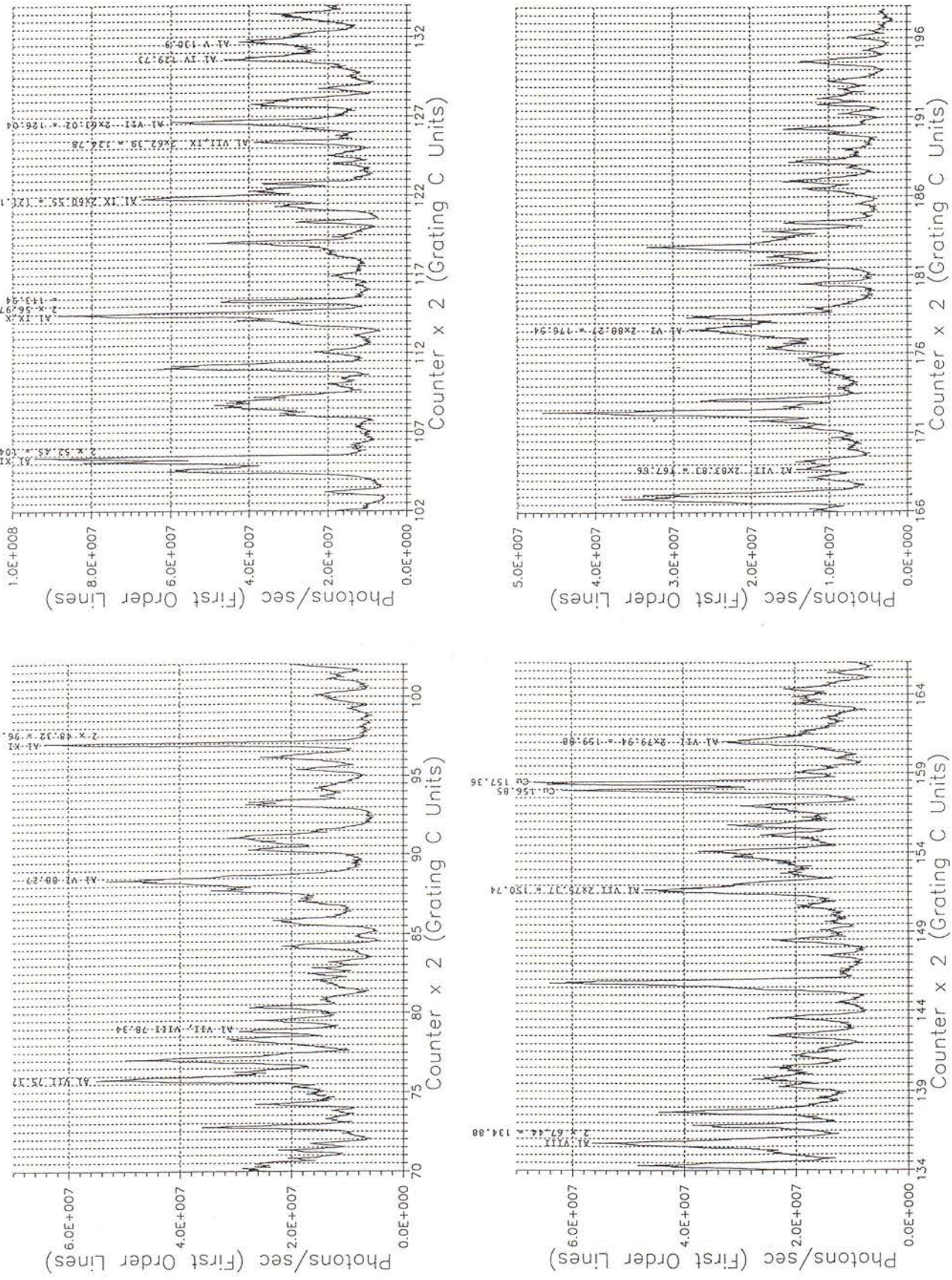


Fig. 3-17. Expanded trace of Fig. 3-16 including line identifications.

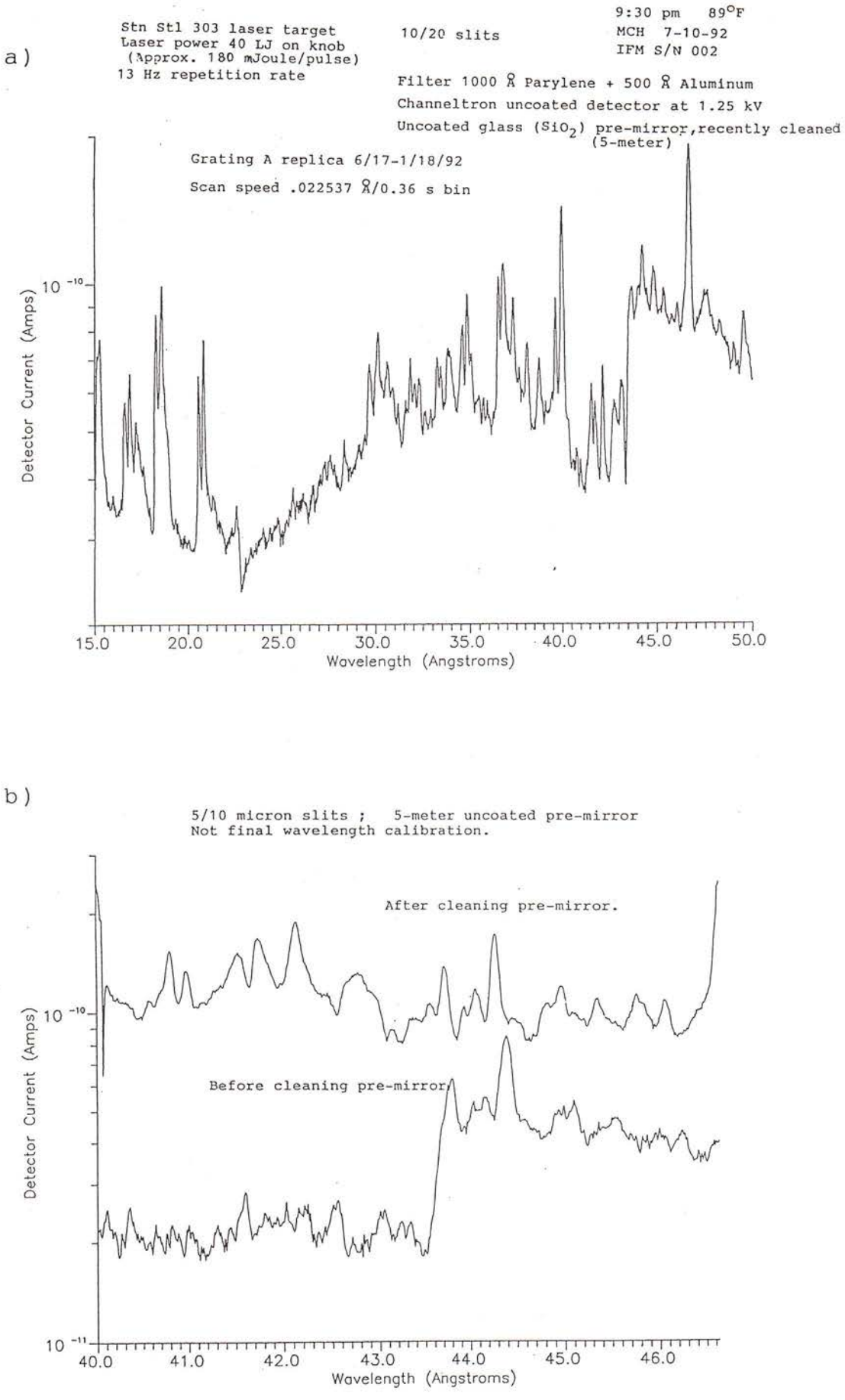


Fig. 3-18. a) Indication of Carbon-K edge in IFM spectrum. b) Verification of Carbon contamination of pre-mirror from laser-produced plasma source.

a stigmatic IFM constructed for use with a laser-produced plasma light source. The astigmatism control mirror has a large angular acceptance (30 mrad) and is oriented with its surface normal at right angles to the dispersion plane. The exiting monochromatic beam was refocused by a post-mirror to provide a point image at the user's target. The magnification factors derived from Figure 3-15 are 3.2 relative to the exit slit width in the dispersion direction and 4.3 relative to the source in the non-dispersive direction. Thus, for a 0.1 mm source and 0.05 mm exit slit, the image focused onto the target is approximately 0.5 mm x 0.2 mm. The resulting intensity per unit area at the target was sufficient to produce photo-electrons subsequently analyzed to study the chemistry and structure of the target surface[60]. To minimize contamination of the target surface, the monochromator is maintained at near UHV pressures ($10^{-9}$ torr region). This is made possible by clean construction practices and choice of materials.

Figure 3-16 is a full-range spectrum of a laser-produced aluminum plasma taken with the stigmatic IFM grating. Grating band C was used and the slits were 5 microns and 10 microns. The ionization species identified for some of the multitude of lines is given in the expanded horizontal scales of Fig. 3-17. The lines which are not obviously blends have measured FWHMs in the range of 0.18 to 0.22 Angstroms, corresponding to a resolving power of ~ 650 at the band center. This is exactly the amount of aberration predicted using the above dispersion equations (3-21) to (3-23). This clearly demonstrates that the geometrical aberrations are small even in comparison to the 5 micron slit. The calibration of absolute wavelength using the known wavelengths of the identified lines resulted in linearity to within 0.5%.

## g) Diagnosis of Laser Plasma Contamination

While the testing of spectrographs and monochromators at Hettrick Scientific Inc. was mainly for the purpose of performance verification and calibration, this also provided information on the laser-produced plasma source used for some of these measurements. It is well known that such sources eject both gaseous and particulate debris which contaminate the surface of windows and other optics in view of the source. However, the pre-mirror used to refocus the plasma point source through the entrance slit of the IFM is at a 2° graze angle relative to the line-of-sight to the plasma. This results in a very slow accumulation of such debris and thus a sensitive means of monitoring the different phases of the coating of a mirror by the plasma. For example, Figure 3-18a reveals the presence of a Carbon-K edge, whose strength was correlated with the visual appearance of a brownish-gold discoloration coating a bare pre-mirror. Indeed, cleaning the mirror removed this edge, as shown in Figure 3-18b. This carbon contamination apparently precedes the deposition of the heavier metallic component of the plasma debris. A precise monitoring of the deposition rate of such films can be obtained by use of the numerous lines and edges available in the soft x-ray region, combined with the high throughput and resolution provided by a monochromator such as described here.

# 4. Surface Normal Rotation (SNR) Monochromators

In further development of the ideal monochromator, one can list the limitations of the above VLS designs as follows: 1) a large variation in the aperture size as a function of wavelength, 2) a high required precision of grating rotation to obtain an accurate selection of wavelength and 3) a narrow range in wavelength efficiently diffracted by a blazed grating, due to the change in the angles of incidence and diffraction upon grating rotation. Conventional designs exhibit additional problems including the defocusing of the image or the need to scan auxiliary mirrors or the slits. All these limitations arise from the fact that scanning is performed within the dispersion plane normal to the grooves and the grating surface. This scanning has comprised rotation of the grating about an axis parallel to its grooves, sometimes accompanied by translation of the grating or rotation and translation of mirrors within the dispersion plane. This limited range of scanning motions has been honored by all grating spectroscopy instruments, whether they be used at normal or grazing incidence, for in-plane or off-plane diffraction, in reflection or transmission, and even when the groove spacings have been varied by holographic or mechanical means.

Unfortunately, such motions within the dispersion plane alter the focusing properties of the grating, a detrimental effect which is most pronounced at grazing incidence. This has historically been corrected by the introduction of auxiliary mirrors and complicated scanning motions for the optics and slits to maintain a well-focused image. Even with the use of varied spacings to provide this correction, the grating has still been rotated about an axis parallel to its grooves, leaving the three limitations listed above. In particular, the resulting wavelength-dependent numerical aperture causes a non-ideal illumination of targets to which the monochromatic radiation is directed. In the past, a constant numerical aperture and fixed beam direction could only be obtained by resorting to the even less desirable condition of huge translations of both the entrance and exit slits to maintain adherence to the Rowland circle.

## *4.1 Geometrical Concept*

As a new alternative[61,62], consider the rotation of a diffraction grating about an axis *normal* to its surface as shown in Figure 4-1a. The optical surface of the grating is unchanged in position and orientation during such a motion, and should therefore maintain its focusing properties through fixed slits. The only change is the orientation of the grooves, which are now tilted by an angle $\Theta$. An incident light ray therefore views a groove spacing within the plane of incidence which has in effect increased by $1/\cos\Theta$. This results in a corresponding increase in the wavelength diffracted to a fixed image position within this plane:

$$\lambda = \lambda_o / \cos \Theta \qquad (4\text{–}1)$$

where

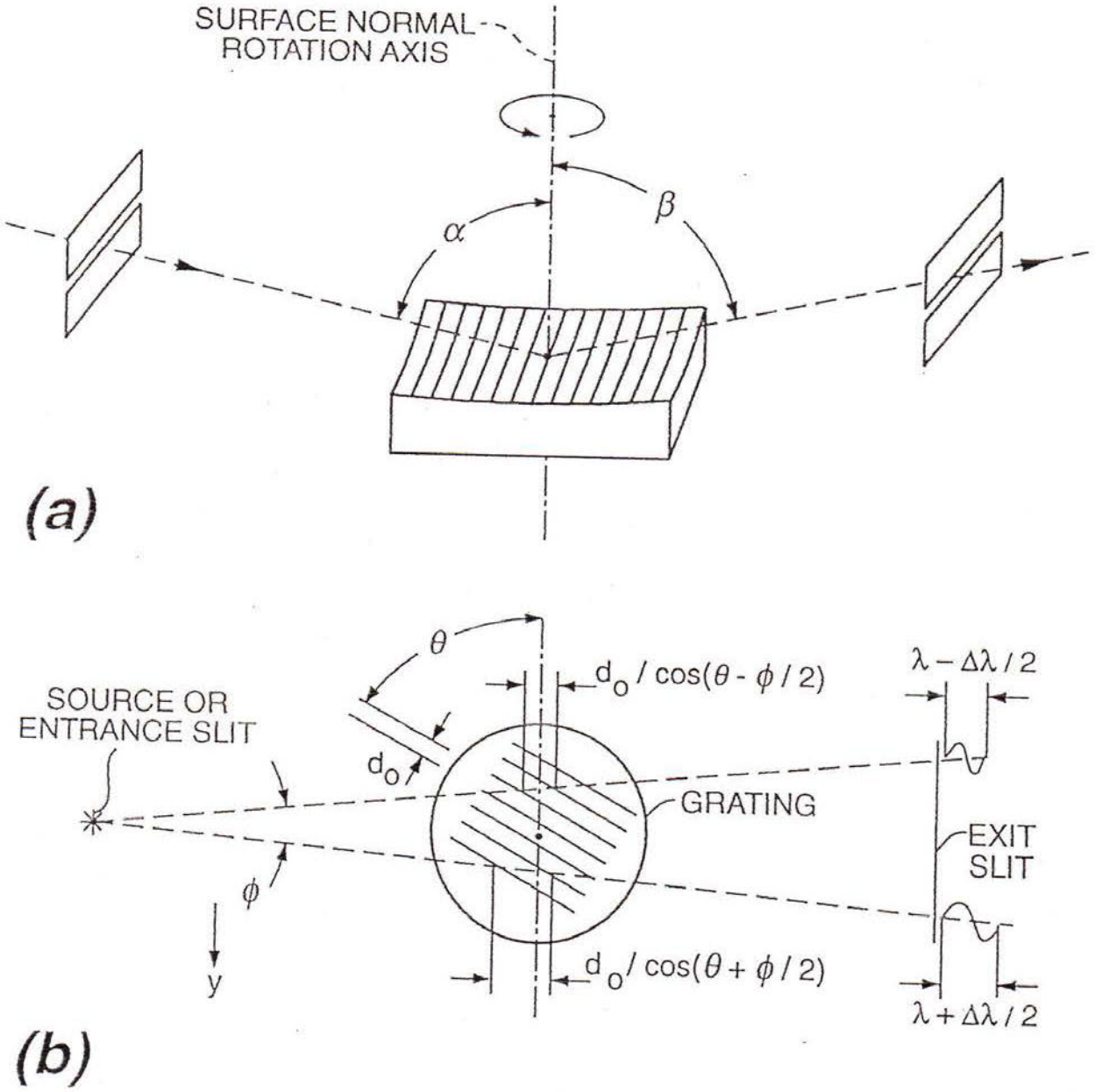


Fig. 4-1. Geometry of a simple surface normal rotation (SNR) fixed slit grating monochromator. In (a) a 3-D perspective is shown where the grating is oriented to diffract the minimum wavelength through the exit slit. In (b), a top view of the rotated grooves shows the groove spacings projected upon the sagittal incident rays, resulting in a limit to the spectral resolution. The same rotation scan technique may be used to construct other optical systems, including plane grating designs, those employing auxiliary mirrors, and where the slit(s) may move.

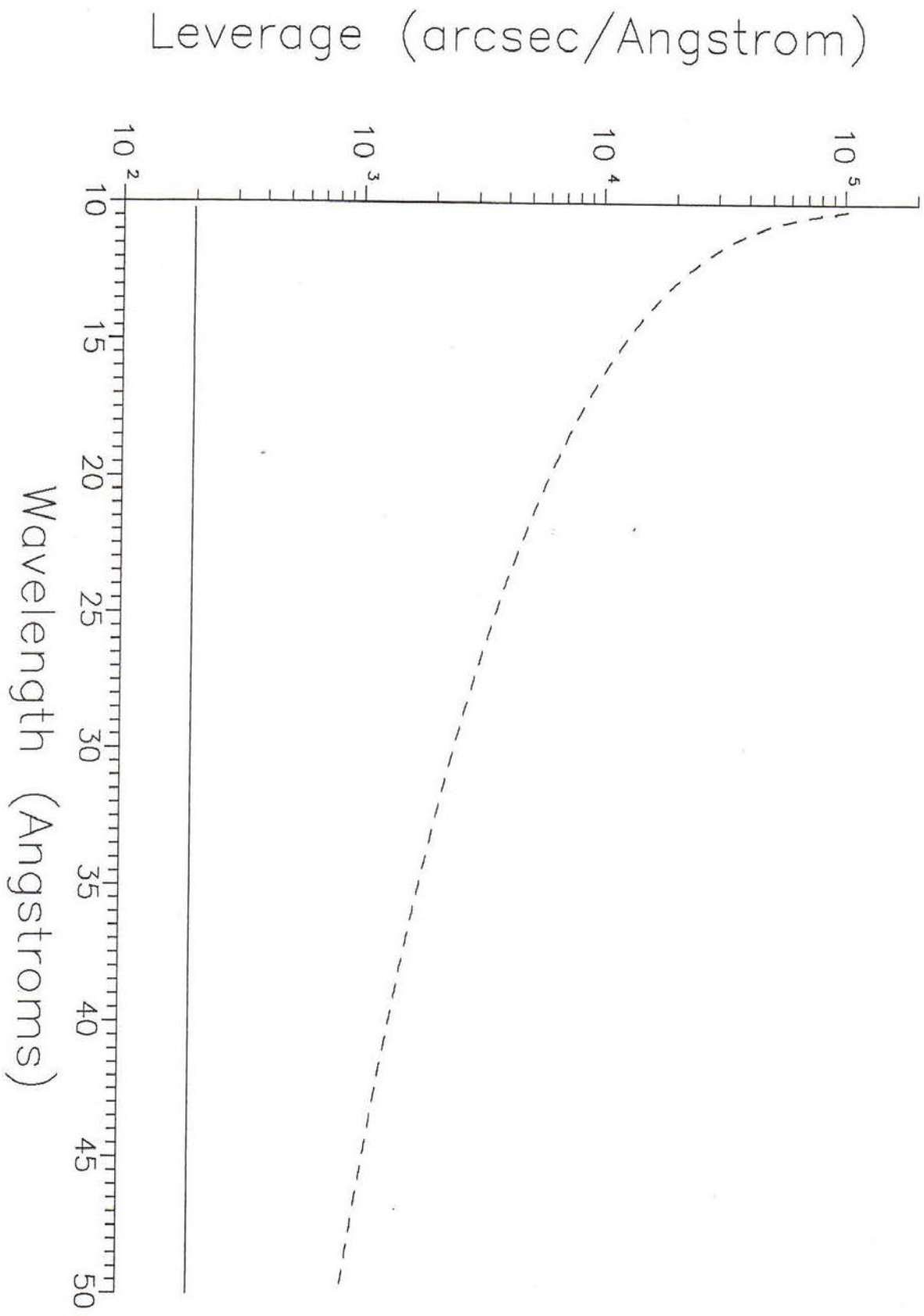


Fig. 4-2. Allowable error in mechanical rotation angle of SNR grating (dashed) versus conventional rotation (solid) for a 750 g/mm grating at an included angle of 2θ = 175.5 degrees. The surface normal rotation provides significant leverage and thus greatly reduced mechanical tolerances on the rotation stage.

$$\lambda_o = (\sin\beta - \sin\alpha)\, d_o / m \qquad (4\text{-}2)$$

is the wavelength diffracted to this position at a rotation angle of zero wherein the grooves are normal to the dispersion plane. The wavelength $\lambda_o$ is the minimum accessible wavelength in spectral order m. Since $\alpha$ and $\beta$ are unchanged during rotation of the grating, the focal length and numerical aperture of the grating are also fixed in this Surface Normal Monochromator, or SNR.

Equations (4-1) and (4-2) can also be derived from application of the light-path function. Due to the rotation, the groove term **N** is now a function of both the meridional coordinate $w$ and the sagittal coordinate $\ell$:

$$\mathbf{N} = (w,\ell) = (w/d_o)\cos\Theta + (\ell/d_o)\sin\Theta \qquad (4\text{–}3)$$

Thus, $N_{10} = (1/do)\cos\Theta$ and $N_{01} = (1/do)\cos\Theta$. From equations (1-1) and (1-4), the grating equation now reads:

$$\sin\alpha - \sin\beta + m\lambda N_{10} = \sin\alpha - \sin\beta + (m\lambda/d_o)\cos\Theta = 0 \qquad (4\text{-}4)$$

This is equation (4-1) and specifies a change in wavelength proportional to the inverse *cosine* of the rotation angle. This results in the desirable advantage of a slow change in wavelength through a large change in rotation angle. The solid line in Figure 4-2 is the required change in rotation angle per change in wavelength for conventional rotation of a grating about an axis parallel to its grooves. This is for a constant included angle of $2\theta = 175.5^o$ and a 750 g/mm grating, resulting in approximately 200 arcseconds per Angstrom. A resolving power of 1000 at 10 Angstroms therefore requires an accuracy in the rotation angle of 2 arcseconds. To put this tolerance in perspective, 2 arcseconds is only 1 part in 1800 of one tooth of a 360 tooth spur gear. Clearly, such accuracy requires extremely high precision gear trains combined with the leverage provided by long rotation arms. In contrast, the dashed curve in Figure 4-2 the required change in rotation angle per Angstrom using the surface normal rotation scan geometry. The huge leverage provided (factor of 10-100 looser than conventional rotation) is appreciated from the cosine dependence in equation (4-1) resulting in a factor of 2 change in wavelength upon a $60^o$ rotation angle.

The presence of a non-zero $N_{01}$ term results in a shift of the image out of the plane of incidence. From equations (1-1) and (1-10), the shift of the principal ray is

$$y' = r'\,\delta\mathbf{F}/\delta\ell = r'\,m\lambda\,\delta\mathbf{N}/\delta\ell = r'\,(m\lambda/d_o)\sin\Theta = r'\,(m\lambda_o/d_o)\tan\Theta \qquad (4\text{-}5)$$

From equation (4-2) it can be seen that the factor $(m\lambda_o/d_o)$ is small at grazing incidence where angles $\alpha$ and $\beta$ approach $\pi/2$. At such angles, the movement of the image in the y'-direction is therefore small. However, at normal incidence this movement would be large and typically disadvantageous. This is perhaps the only known case in grating design where the performance becomes better towards grazing incidence. The residual aberrations in this case are dependent upon the geometry of the incident beam as given in Secs. 4.2 and 4.3.

## *4.2 Diverging Beam SNR Geometries*

### a) Simple Rotation SNR and Aberration Computations

In the simplest configuration where the single grating accepts the radiation diverging from a source or entrance slit, Figure 4-1b indicates that opposite ends of a grating groove present slightly different effective spacings as viewed by the incident ray. This is due to the finite numerical aperture, $\Phi_y$ in the sagittal direction, resulting in a contracted effective spacing $d_{min} = d_o/\cos(\Theta-\Phi/2)$ at the top of the grating groove and an elongated effective spacing $d_{max} = d_o/\cos(\Theta+\Phi/2)$ at the bottom. The relative difference between these spacings results in a relative difference in the diffracted wavelengths as follows:

$$\Delta\lambda/\lambda = \Delta d/d = \Delta[d_o/\cos(\Theta+\Phi_y/2)-d_o/\cos(\Theta-\Phi_y/2)]/(d_o/\cos\Theta)$$

$$= (\cos\Theta)\,(\sin\Theta/\cos^2\Theta)\,[\Phi_y/2 - (-\Phi_y/2)]$$

$$= \Phi_y \tan\Theta \qquad (4\text{-}6)$$

This result also results from application of the light-path function. Consider the sagittal position y' given in equation (4-5). From Figure 1-1, the geometrical light-path distance from the in-plane object to this image can be written as

$$L \cong \{[r'(m\lambda_o/d_o)\tan\Theta-\ell]^2+[r'\sin\beta-\omega]^2+[r'\cos\beta-\omega^2/(2R)-\ell^2/(2R)]^2\}^{1/2}$$

$$+ \{\ell^2+[r\sin\alpha+\omega]^2+[r\cos\alpha-\omega^2/(2R)-\ell^2/(2R)]^2\}^{1/2} \qquad (4\text{-}7)$$

By expanding this as a series in $\omega^i\,\ell^j$, the new term of lowest order is the mixed term which produces image tilt:

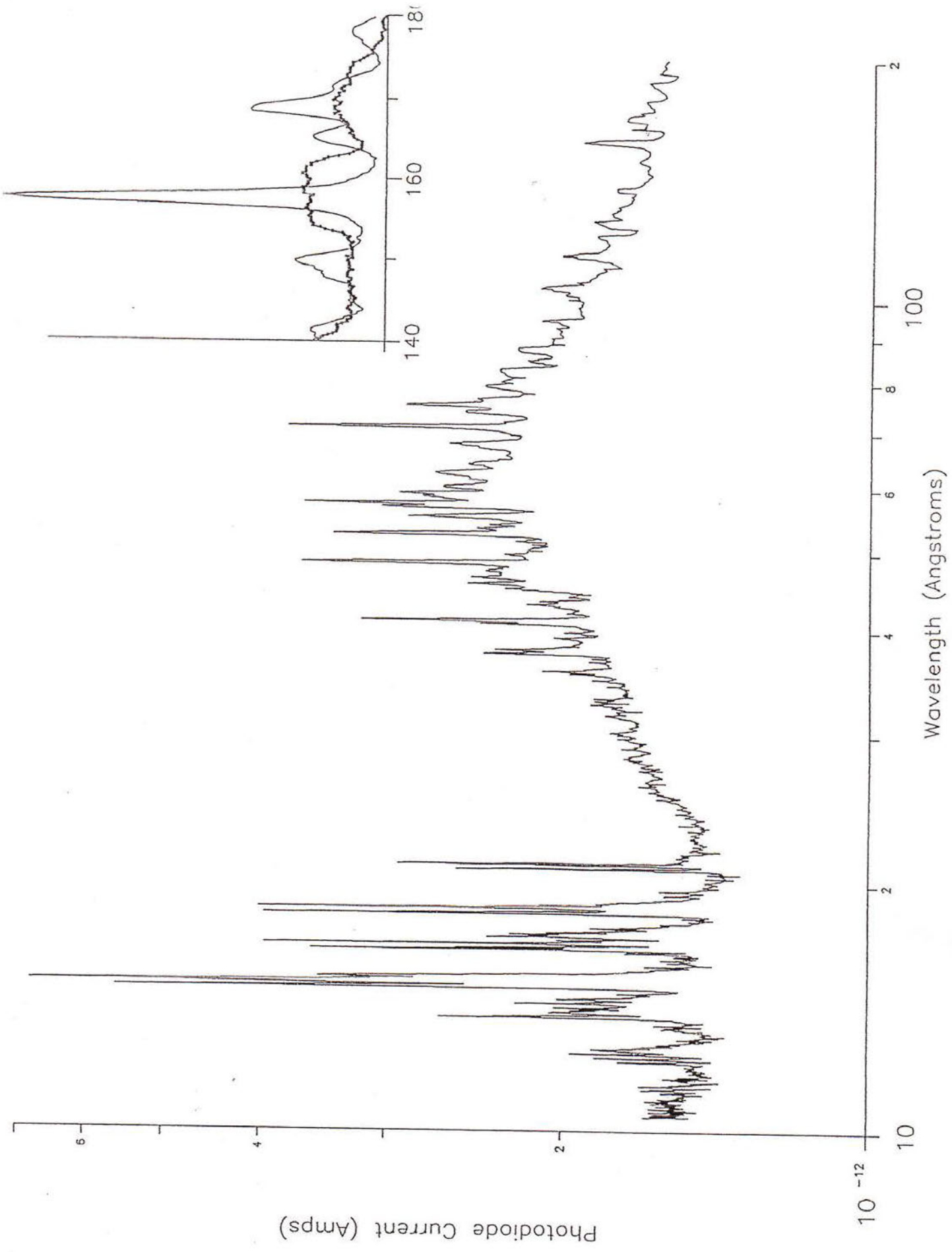


Fig. 4-3. SNR spectrum of 303 stainless steel laser plasma through a sagittal aperture of 1 mrad. Inset shows degradation caused by a 4 mrad aperture and the improvement obtained by tilting the exit slit.

$$L_{11} = - (m\lambda_o/d_o) \tan\Theta \sin\beta / r' \qquad (4\text{-}8)$$

which from equation (1-11) yields

$$\Delta\lambda_{11} /\lambda = d/(m\lambda)\, \delta\mathbf{F}/\delta\omega = (d/m)\, \delta\mathbf{L}/\delta\omega$$

$$= d/(m\lambda)\, L_{11}\, \ell$$

$$= \Phi_y \tan\Theta \sin\beta$$

which at grazing incidence $\cong \Phi_y \tan\Theta$ (4-9)

## b) First Soft X-Ray Results

To test the above theory, a soft x-ray SNR monochromator was constructed, consisting of a slitless laser-produced plasma source, a selectable series of sagittal apertures, a palladium coated concave grating of radius R = 20 m and ruled area 32 x 32 $mm^2$ and a selectable series of exit slit widths. The instrument length from source to exit slit was ~ 1.5 m, the angular deviation was $2\theta = 176^o$ and the minimum wavelength was $\lambda_{min}$ ~ 10.4 Angstroms. To minimize the meridional aberrations, the source and exit slit were located on the Rowland circle of the grating. A silicon photodiode detector measured the intensity of the beam transmitted through the exit slit as the grating rotation angle $\Theta$ was scanned by a stepper motor. The rotation angles were converted to absolute wavelength values by use of equation (4-1) and one known line in the spectrum.

Figure 4-3 presents the resulting spectrum of a stainless steel target taken by the test SNR monochromator. A sagittal aperture of 1 mrad was selected. Equation (4-6) thus predicts a geometrical aberration of 1/730 at 17 Angstroms, 1/250 at 41 Angstroms, 1/140 at 71 Angstroms and 1/66 at 158 Angstroms. When the blur of ~ 1/360 is added due to the dispersive aberration from the 20 mm exit slit and comparable size slitless source, the predicted net aberration is 1/290, 1/185, 1/117 and 1/60 respectively. These are in good agreement with the measured FWHM values from Figure 63 of 1/335, 1/149, 1/118 and 1/66.

## c) High Energy SNR Monochromator for Astro-D Calibration

Figure 1-5 reveals that a $1^o$ graze angle provides usable reflectivity to wavelengths as short as ~ 3 Angstroms (4 keV photon energy). A SNR monochromator with $2\theta = 178^o$ was built for high energy calibration of an astronomical telescope and focal plane CCD detector. One of the main goals of the calibration was to measure the spectral

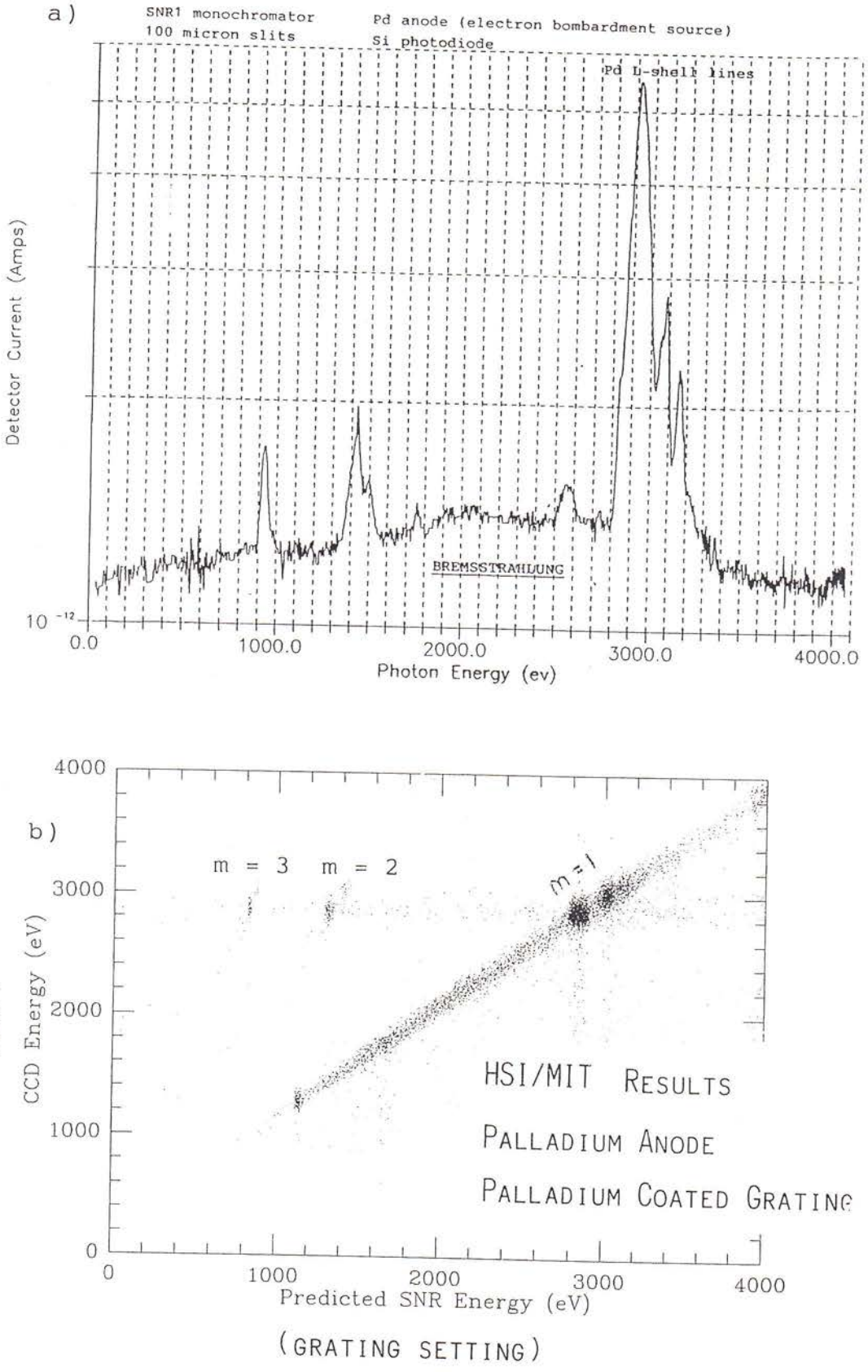


Fig. 4-4. High energy SNR using 1 degree graze angle: a) spectrum recorded by photo-diode; b) pulse-height determined photon energy from CCD detector versus dispersion determined energy from grating rotation angle. Separation of grating spectral orders is obtained. CCD results courtesy of MIT Center for Space Research.

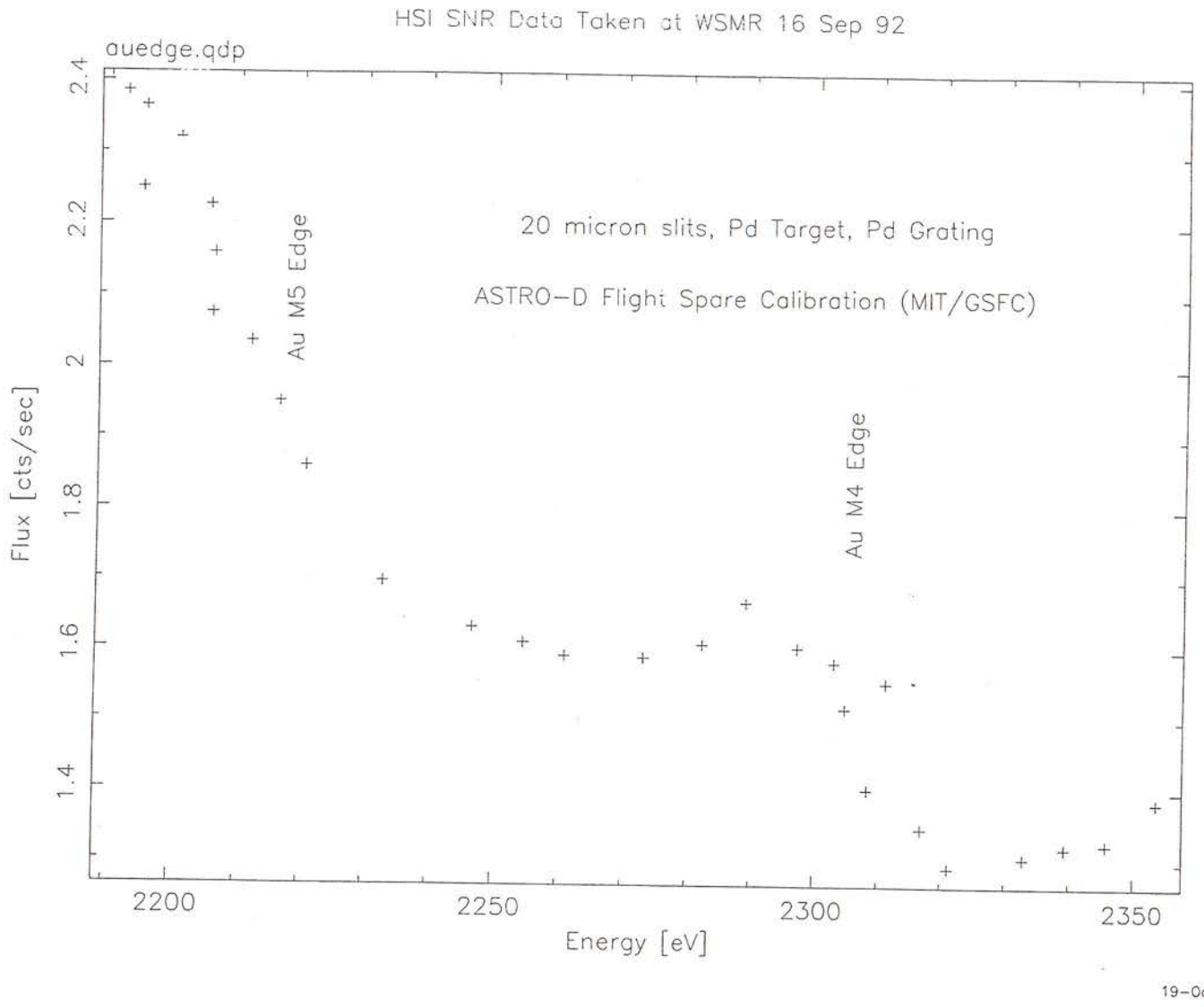


Fig. 4-5. Gold M-shell structure in the reflectance of the gold coated ASTRO-D telescope mirrors. Data obtained by MIT Center for Space Research using high energy SNR monochromator.

variations in the reflectivity of the telescope due to its gold coating. The radiation was bremsstrahlung provided by an electron beam source, and the both the source anode and grating coating were palladium to prevent instrumental gold M-shell edges being present in the spectrum emerging the monochromator.

Figure 4-4a is a low resolution scan of the spectrum produced by the monochromator and source in the 0.5-4 keV region, using 100 micron entrance and exit slits. A smooth level of continuum is present at the position of the gold M-shell edges at 2.2 and 2.3 keV. The bremsstrahlung extends all the way to ~ 4 keV, as seen from the confirming CCD pulse-height results plotted in Figure 4-4b. These energies were previously the exclusive domain of crystal spectrometers. Such spectrometers require the accurate rotation of two crystals and the translation of one in order to maintain fixed position slits and beam directions, and thus was experimentally attempted but found to provide inadequate performance for use in the calibration task.

To direct the exiting beam at the fixed position telescope ~ 300 meters distant, the source was intermittently translated in the non-dispersive direction to correct for the movement which would otherwise occur in the exiting beam according to equation (4-5). The results of the telescope calibration are shown in Figure 4-5, clearly revealing the strength of two gold M-shell edges at a resolution of ~ 100 eV ($\lambda/\Delta\lambda \sim 200$). These flux data were used to remove the telescope response from the in-flight data obtained by ASCA (the flight mission of ASTRO-D).

## d) Double Rotation Geometrical Concept and Raytracings

The limit to the spectral resolution of the simple rotation SNR, as shown in Figure 4-1b, is due to the change in wavelength due to rays striking the grating in the sagittal direction. Equation (4-6) shows that this change is linear with the sagittal aperture coordinate, hence yields a tilted image at the exit slit plane. If the exit slit is tilted an equal amount:

$$\psi = (m\lambda_o/d_o)\ \tan\Theta\ /\ (1+r_y/r')\ /\ \cos\beta \qquad (4\text{-}10)$$

then this limit to the spectral resolution is eliminated. In this equation, $r_y$ is the distance from the source to the grating pole. Returning to the test SNR described in Sec. b) above, the inset to Figure 4-4 shows that a tilt of the exit slit by the predicted amount of $6^o$ results in a factor 6 reduction in the spectral aberration at a sagittal aperture of $\Phi_y = 4$ mrad.

However, for sources extended by a distance $\Delta y$ in the sagittal direction of the entrance slit, there will remain an effective $\Delta\Phi_y = \Delta y / r_y$ which enters into equation (4-6) as follows:

$$\Delta\lambda/\lambda = (\Delta y / r_y) \tan \Theta \qquad (4\text{-}11)$$

For example, a 2 mm source size would contribute an effective sagittal blur of 4 mrad at a grating 500 mm away, resulting in a spectral aberration of 1/50 at a rotation angle of $\Theta = 78.46^{\circ}$ required to scan to $\lambda = 5\ \lambda_{min}$. To eliminate this source of spectral aberration, the grating is tilted instead of tilting the exit slit. This is equivalent to tilting both slits by equal angles relative to the grating. The unit magnification from entrance slit to exit slit on the Rowland circle grating means that an extended source has no significant effect upon the resolution, due to the one-to-one mapping of the slits along their lengths. Such a double-rotation SNR therefore provides high spectral resolution over a broad spectral range.

The required grating tilt, $\Psi_G$ is determined by considering the effect of rotation about the $\omega$-axis upon the light path distances. This has the main effect of changing the u-value of the grating coordinate by an amount $\ell \sin\Psi_G$, which must be added to the value $u = (\ell^2 + \omega^2)/(2R)$ used in equation (4-7). With this substitution, expansion of this light-path distances now results in an image tilt term:

$$L_{11} = \cos\Psi_G \left[(m\lambda_o/d_o)\tan\Theta \sin\beta + (\cos\alpha + \cos\beta)\tan\Psi_G\right] \qquad (4\text{-}12)$$

which at grazing incidence is removed by the following choice of grating tilt:

$$\begin{aligned} \tan\Psi_G &\sim -(m\lambda_o/d_o)\tan\Theta / (\cos\alpha + \cos\beta) \\ &\sim -(m\lambda_o/d_o)\tan\Theta / (2\cos\theta) \end{aligned} \qquad (4\text{-}13)$$

Numerical raytracings confirm this, for example a grating tilt of $\sim 2.7^{\circ}$ at a wavelength of 50 Angstroms given an included angle $2\theta = 175.5^{\circ}$ and a groove density of 750 g/mm. Figure 4-6a plots the result of 3-D raytracing of monochromatic lines at the minimum wavelength (10 Angstroms), at 30 Angstroms and at 50 Angstroms. The grating has a 20 meter radius of curvature and a 123 mm x 123 mm aperture ($\Phi_x = 123/20{,}000 = 6$ mrad). The dispersive resolution for slits placed on the Rowland circle can be written as simply:

$$\Delta\lambda_{FWHM} / \lambda = 1.5\ \Delta x\ (d_o / \lambda_o) / R \qquad (4\text{-}14)$$

where $\Delta x$ is the width of each slit. Using the 750 g/mm grating ($d_o = 13{,}333$ Angstroms), the fractional dispersive resolution is a constant 1/1,000 at all wavelengths using 10 micron slits. However, there is a small amount of broadening seen in the at the 50

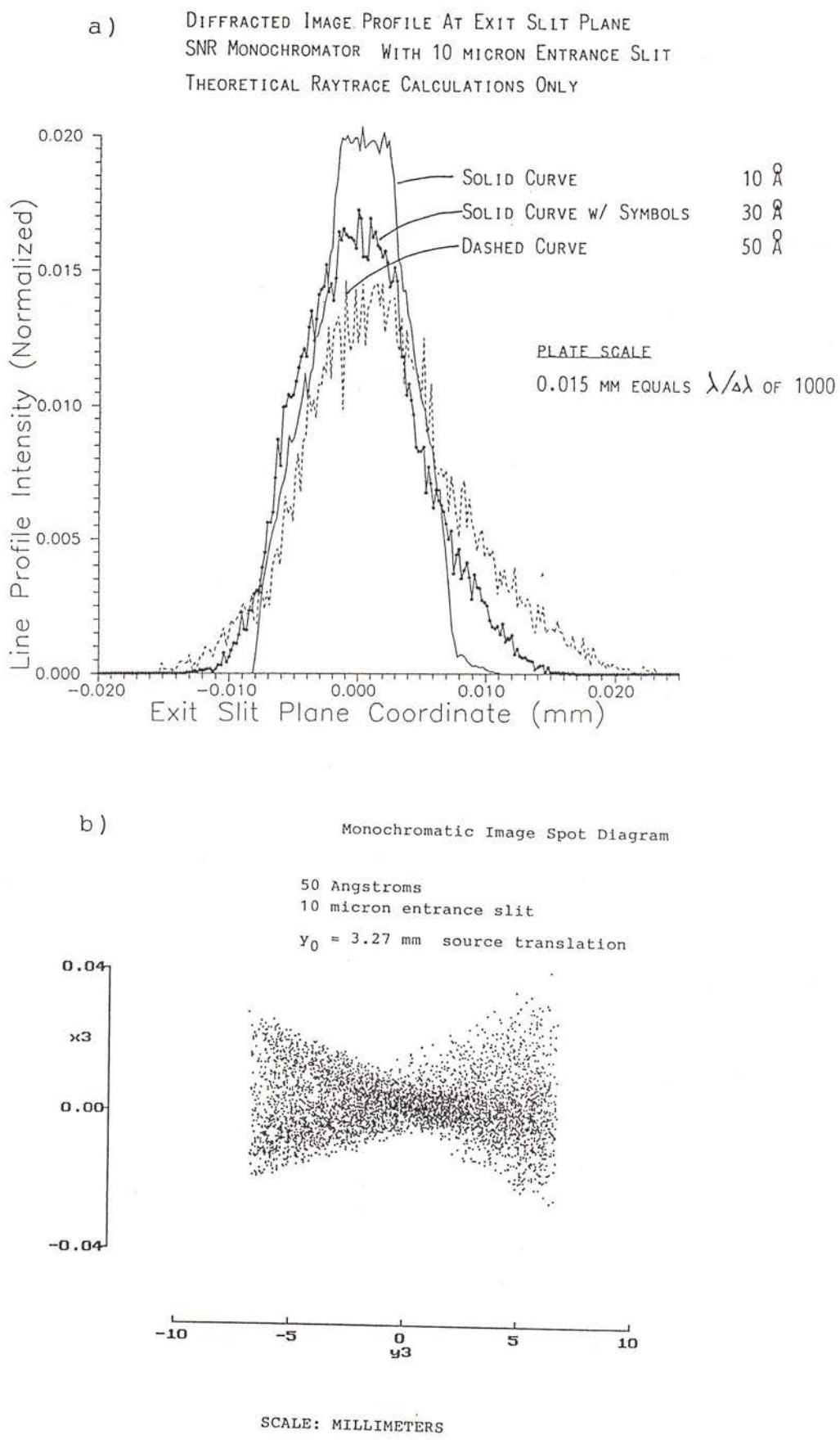


Fig. 4-6. Double-rotation SNR numerical raytracings: a) line profiles at exit slit plane; b) spot diagram of 50 Angstrom image at exit slit plane showing long wavelength degradation in spectral resolution. Sagittal aperture was 7 mrad and meridional aperture was 6 mrad.

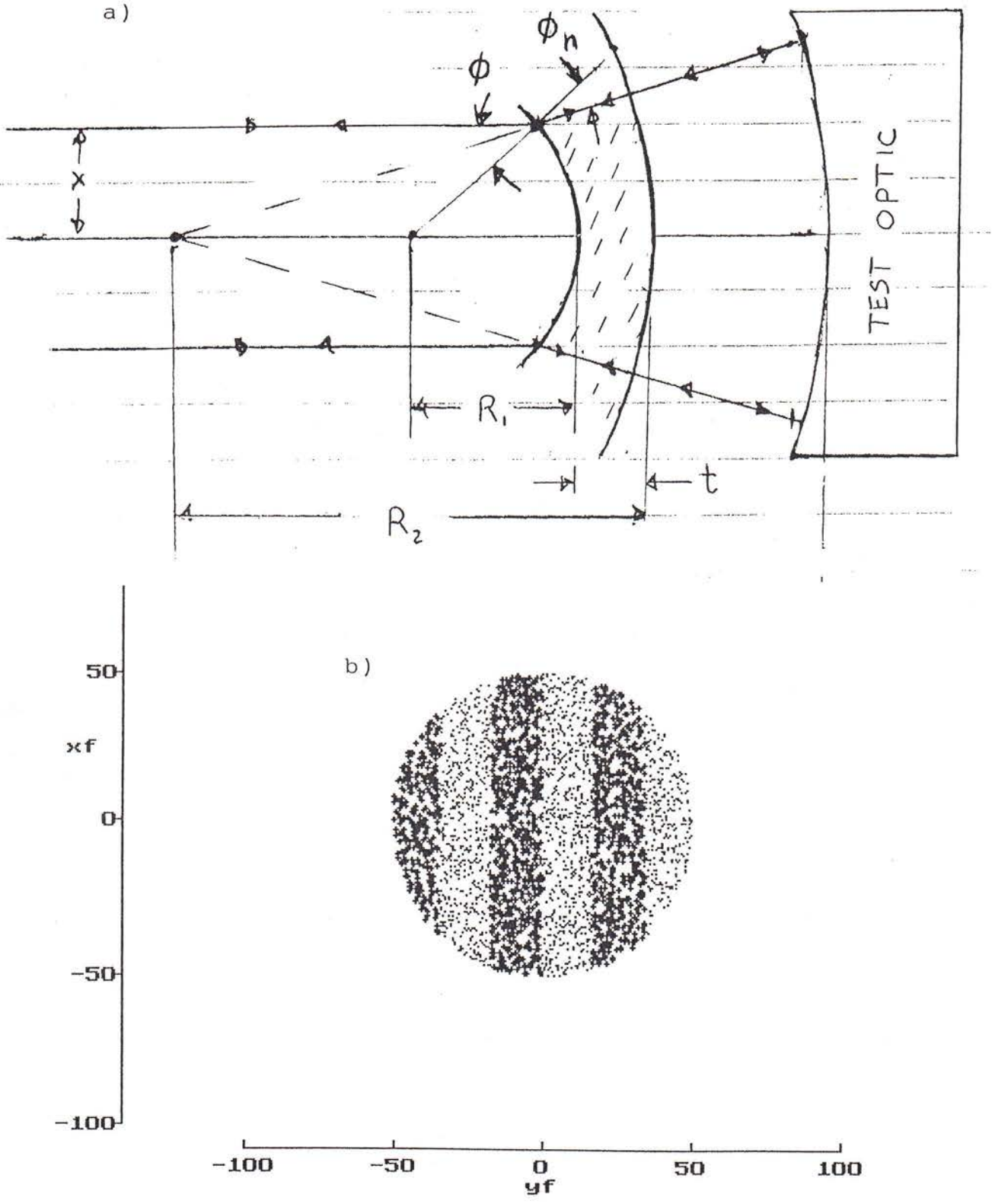


Fig. 4-7. a) Design parameters of a transmission sphere lense for Fizeau interferogram measurement of spherical surface test optic (long radius grating blank). b) Numerical raytrace simulation of interference fringes resulting from use of spherical surfaces for the transmission sphere lense.

Fig. 4-8. Fizeau interferograms of two grating blanks, taken using the transmission sphere lense of Fig. 4-7. The test pieces showed asphericity less than 1/5 fringe (1/10 wave) and were radius calibrated to enable knowledge of SNR monochromator focal length.

110 mm Ø aperture

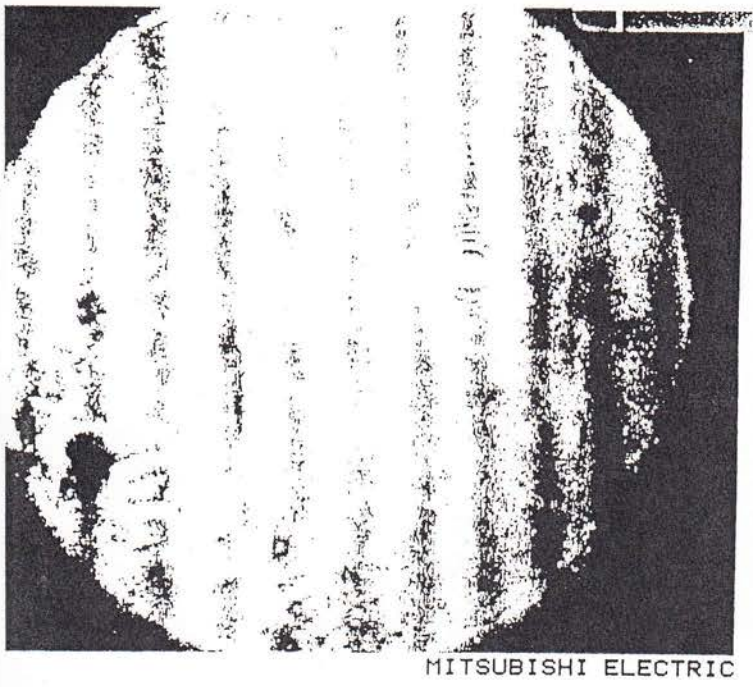


No. 1 (BACK-UP)

R = 20.38 meter

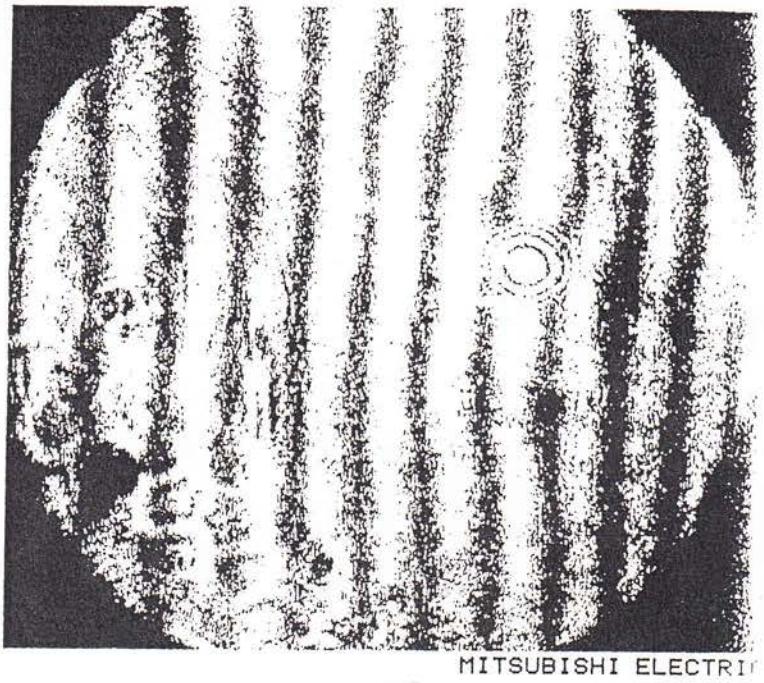


No. 2

R = 20.18 meter

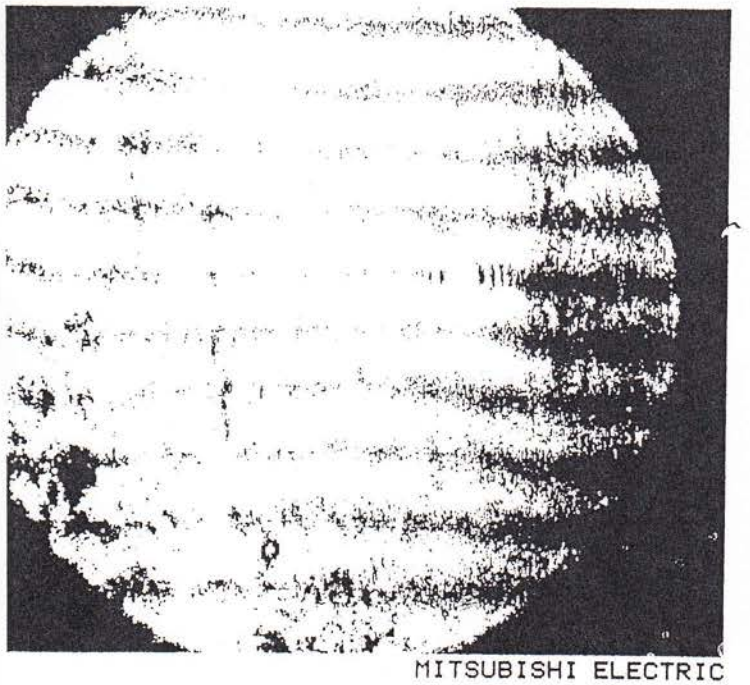


No. 1 (BACK-UP)

R = 20.38 meter

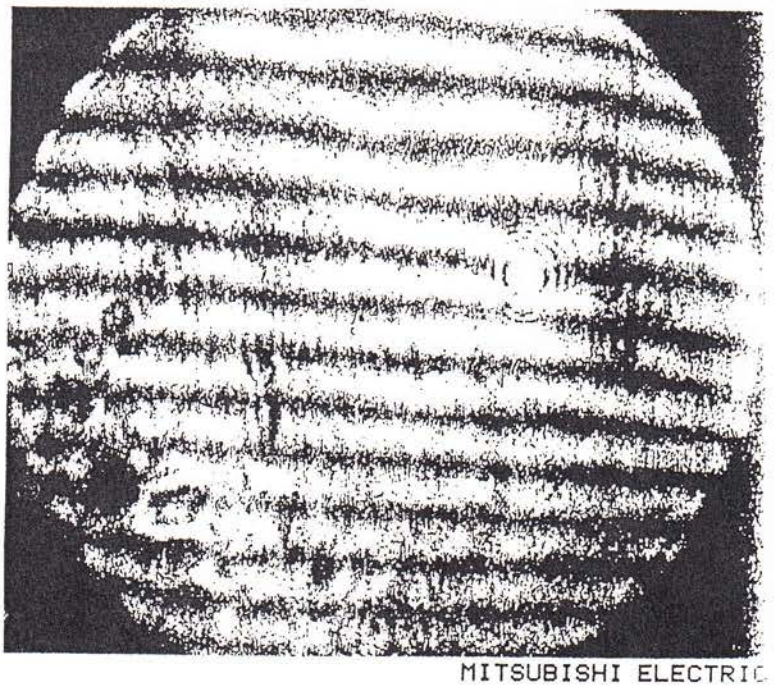


No. 2

R = 20.18 meter

Angstrom line profile, due to the sagittal geometrical aberration appearing in the spot diagram of Figure 4-6b.

The high spectral resolution made possible with this double-rotation grating motion ($\Theta$ about the surface normal and $\Psi_G$ about the $\omega$-axis) is necessary to calibrate the high resolution spectrograph designed for the XMM satellite (see Sec. 2.2 above).

## e) Fizeau Transmission Sphere Measurement of Grating Curvature

In order to obtain the theoretical resolution, the grating surface must be accurately figured to a spherical shape over its large ruled aperture. To perform a precise measurement of deviations from a sphere, and to calibrate the exact radius of curvature, an interferometric fixture was devised based on a Fizeau interferometer. To accommodate the need for collimated beams exiting and entering the interferometer, a transmission sphere was designed to transform the collimated incident beam into one diverging into the grating spherical surface from an effective point located at the center of curvature. As shown in Figure 4-7a, the reference surface of the transmission sphere must be concentric with the grating surface (the transmission sphere must be a retro-reflector) so that phase differences between the light reflected from this surface and that returning from the test grating surface are a measure of surface errors of the grating. This geometry requires the following condition:

$$\sin \phi = x / R_1 \tag{4-15}$$

$$\sin \phi_n = x / R_1 - x / (R_2 - t) \tag{4-16}$$

which by substitution of Snell's law ($n \sin\phi_n = \sin \phi$) provides the following relation for the radii of the two surfaces of the transmission sphere:

$$R_1 / R_2 = (1 - 1 / n) (1 - t / R_2) \tag{4-17}$$

Strictly speaking, this derivation ignored the spherical aberration of the two surfaces of the transmission sphere, but such aberration was found to be negligible by raytracing simulations such as displayed in Figure 4-7b, revealing a total distortion of less than 1/100 of a wave. The experimental result on the actual grating blank is shown in Figure 4-8, verifying the achievement of ~ 1/10 wave (1/5 fringe) on the grating surface. This also provided a measurement of the grating radius of curvature to within approximately 20 mm, by calibrating the transmission sphere reference surface against a known radius mirror. This allowed the design of the absolute object and image distances to place the entrance and exit slits on the Rowland circle of the grating. The resulting length of the

Fig. 4-9. Double-Rotation SNR:

SURFACE NORMAL ROTATION (SNR) MONOCHROMATOR MODEL 2.25-1.57M-SPECIAL READY FOR DELIVERY TO THE EUROPEAN SPACE AGENCY. SYSTEM INCLUDES (FROM LEFT TO RIGHT) ENTRANCE SLIT ASSEMBLY, GRATING CHAMBER, LASER VISIBLE ALIGNMENT MODULE, EXIT SLIT ASSEMBLY, VERTICAL OUTPUT BAFFLE ASSEMBLY AND FILTER ASSEMBLY ALL MOUNTED TO RIGID SLIMLINE BREADBOARD. BREADBOARD IS EQUIPPED WITH 3-POINT BALL SCREW AIMING SYSTEM. ONE POINT OF WHICH IS STEPPER MOTOR DRIVEN. GRATING ROTATION SELECTION OF TRANSMITTED WAVELENGTH IS ALSO STEPPER MOTOR DRIVEN. THIS SYSTEM WAS USED TO CALIBRATE THE RESOLUTION AND SCATTERING OF THE X-RAY MULTI-MIRROR (XMM) REFLECTION GRATING SPECTROMETER ELECTRO-OPTICAL BREADBOARD IN THE 10-50 Å REGION.

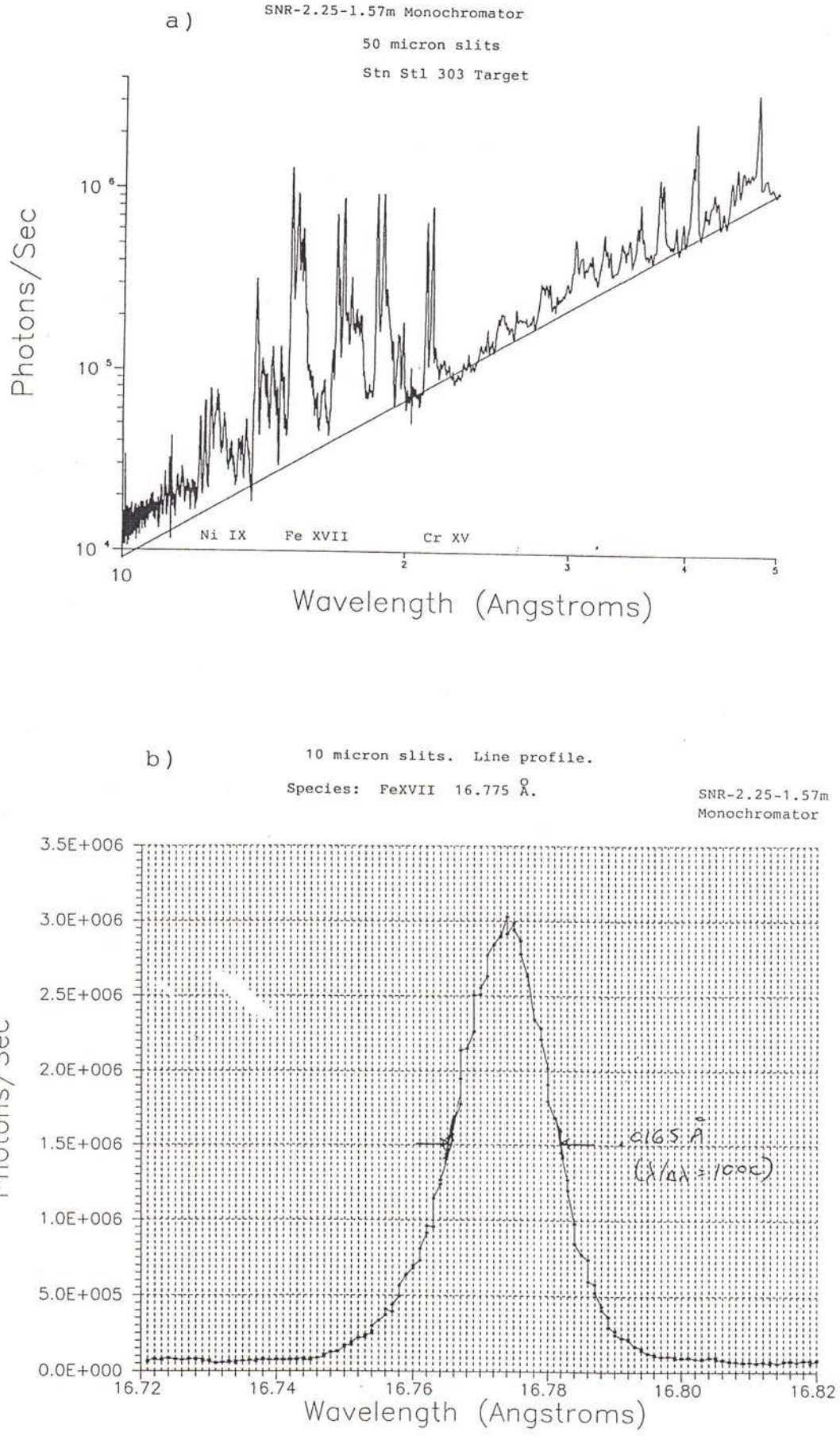


Fig. 4-10. Double-rotation SNR for XMM calibration: a) spectrum of laser-produced plasma showing lines and continuum extending to and remaining in good focus at all wavelengths; b) line profile demonstrating the designed resolving power of 1000 using 10 micron slits.

monochromator was 1.57 meters from entrance slit to exit slit, and the grating included angle $2\theta$ was $175.5^{\circ}$ resulting in a nominal graze angle of $2.25^{\circ}$.

## f) Double-Rotation SNR for XMM Calibration

A photograph and description of the SNR constructed for this task is shown in Figure 4-9. The soft x-ray source used by the experimenters was a water-cooled electron beam. The emitted line radiation was viewed at a $6^{\circ}$ angle relative to the anode surface in order to maximize the soft x-ray intensity. However, for testing of the instrument resolution, a laser-produced stainless steel plasma was used, and spectral scans made as shown in Figure 4-10a. The nearly power-law fit of the continuum baseline all the way to the shortest wavelengths suggests the absence of significant scatter in the monochromator. This was confirmed by inserting thin-film filters to provide absorption edges at various wavelengths throughout the spectrum. The resulting near elimination of the signal to the high energy side of each edge indicates that the continuum was real and not scattered white light.

Use of 10 microns slits and intrinsically narrow emission lines provided experimental verification of the spectral resolution such as shown in Figure 4-10b. Results at the longest wavelengths near 50 Angstroms showed a small degradation in resolution ($\lambda/\Delta\lambda \sim 850$) due to the sagittal aberration revealed in the raytracing of Figure 4-6b.

## g) Soft X-Ray Efficiencies of SNR Grating

The surface normal rotation increases the groove spacing in proportion to the diffracted wavelength. This maintains the blazed wavelength of equation (2-27) much closer to the diffracted wavelength than in classical rotation. Secondly, the new scheme rotates the groove facets out of the highly shadowed condition endemic to in-plane diffraction, thus decreasing the shadow factor of equation (2-29) as the wavelength increases. These two advantageous effects[62] are plotted in Figure 4-11a. The net result is a more gradual decline in the relative diffraction efficiency as a function of wavelength, resulting in a wider bandpass at good efficiency. A witness sample grating to the high resolution SNR described above was measured for absolute efficiency at 5 wavelengths, as the grating was rotated about its surface normal to select these wavelengths in a reflectometer. The results plotted in Figure 4-11b show usable efficiency over a factor of ~ 5 in wavelength, though details of the efficiency curve are not available due to the limited number of test wavelengths. The efficiency of the actual grating finally used in the monochromator is believed to have an even broader efficiency curve due to the subsequent optimization (deepening) of the groove depth during the set-up for its fabrication.

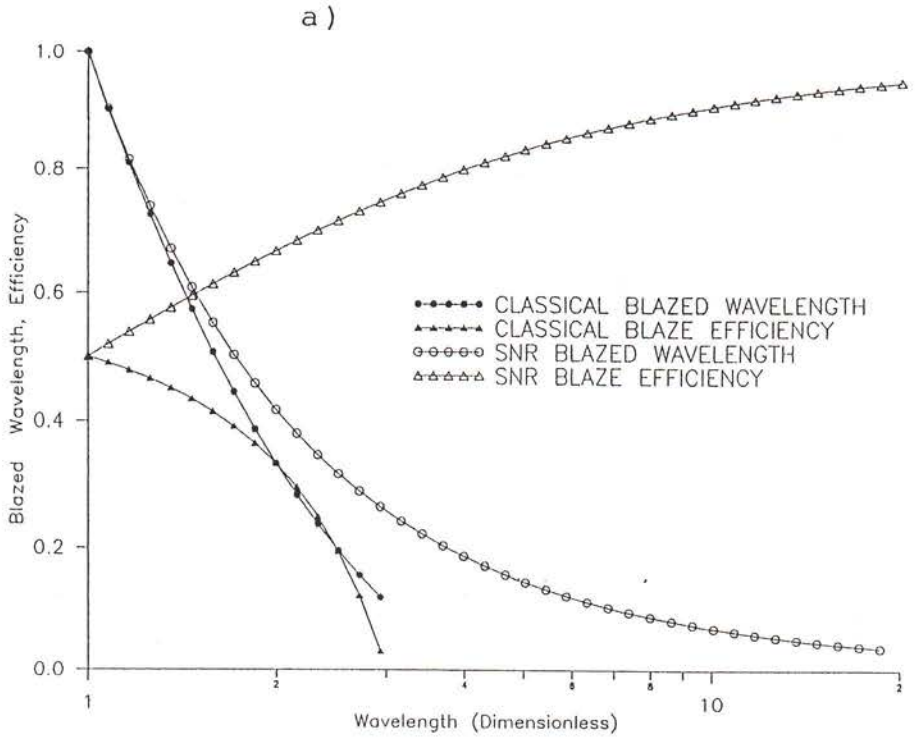


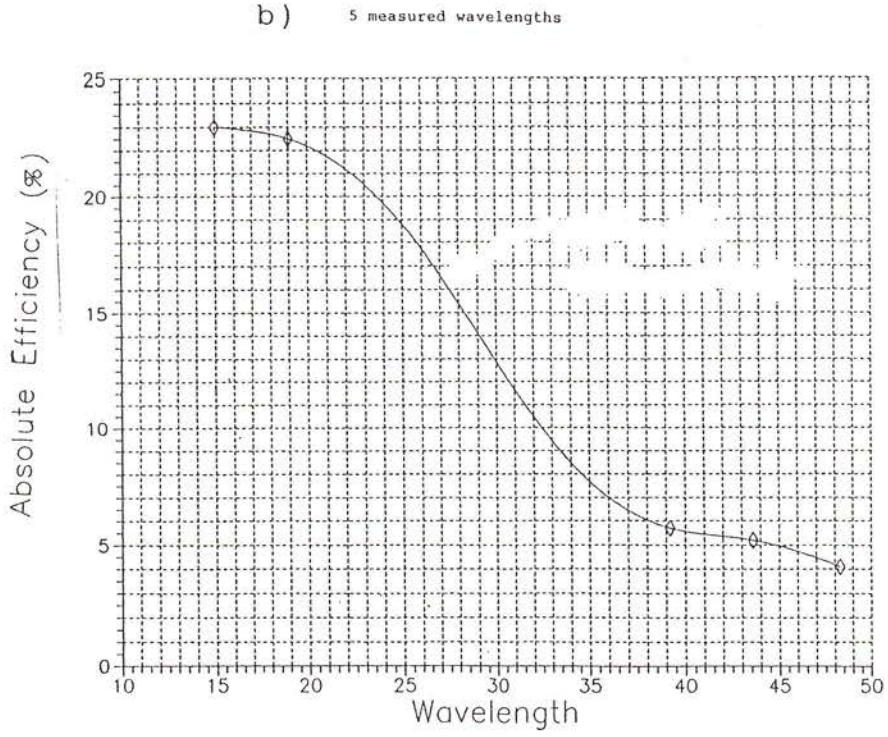


Fig. 4-11. a) Theoretical blazed wavelength and peak relative grating efficiency in classical versus surface normal rotation. b) Measured absolute grating efficiency in surface normal rotation.

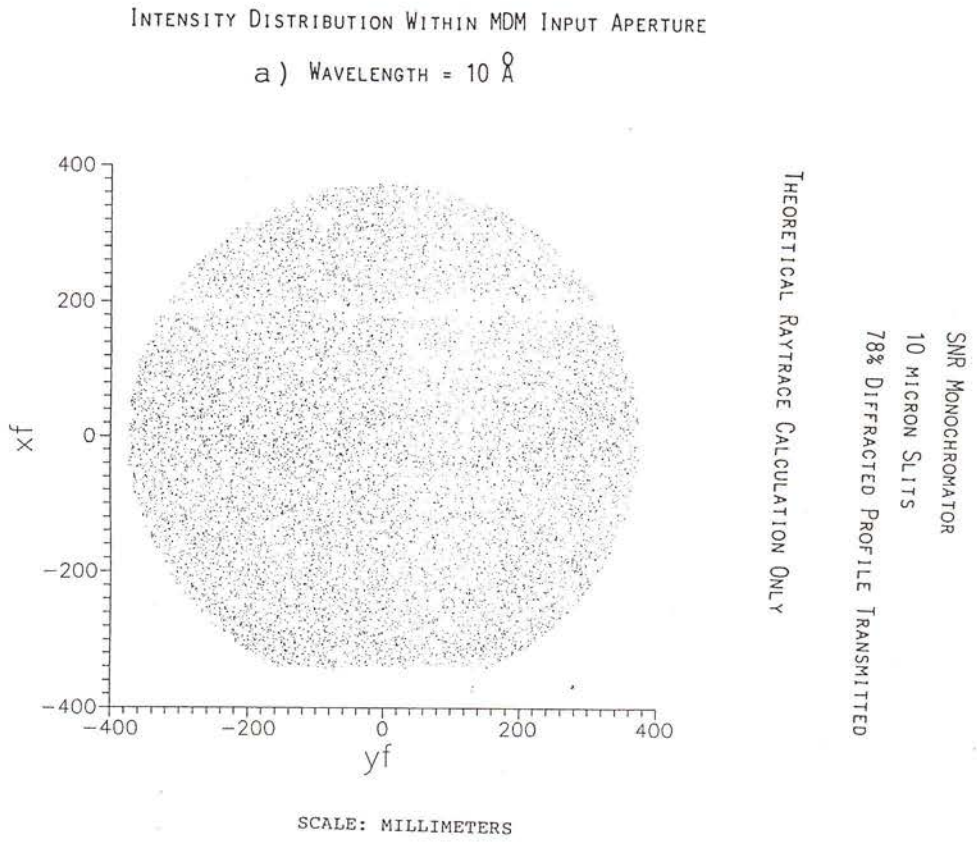


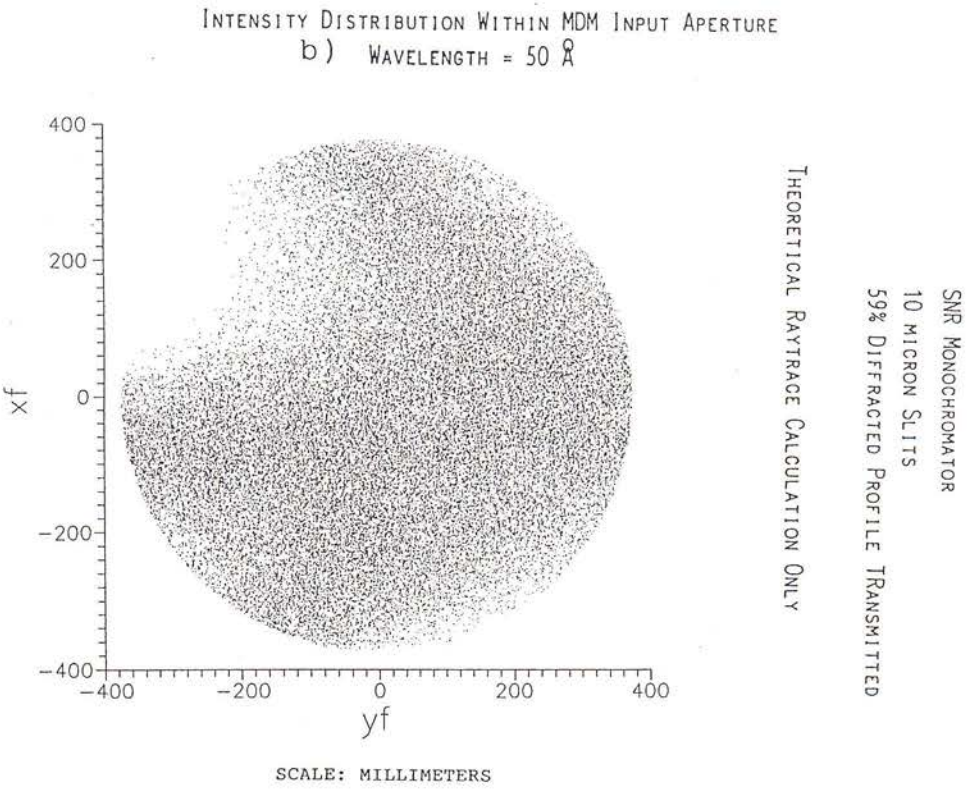


Fig. 4-12. Numerical raytracings of exit aperture of double-rotation SNR at a) 10 Angstroms and b) 50 Angstroms.

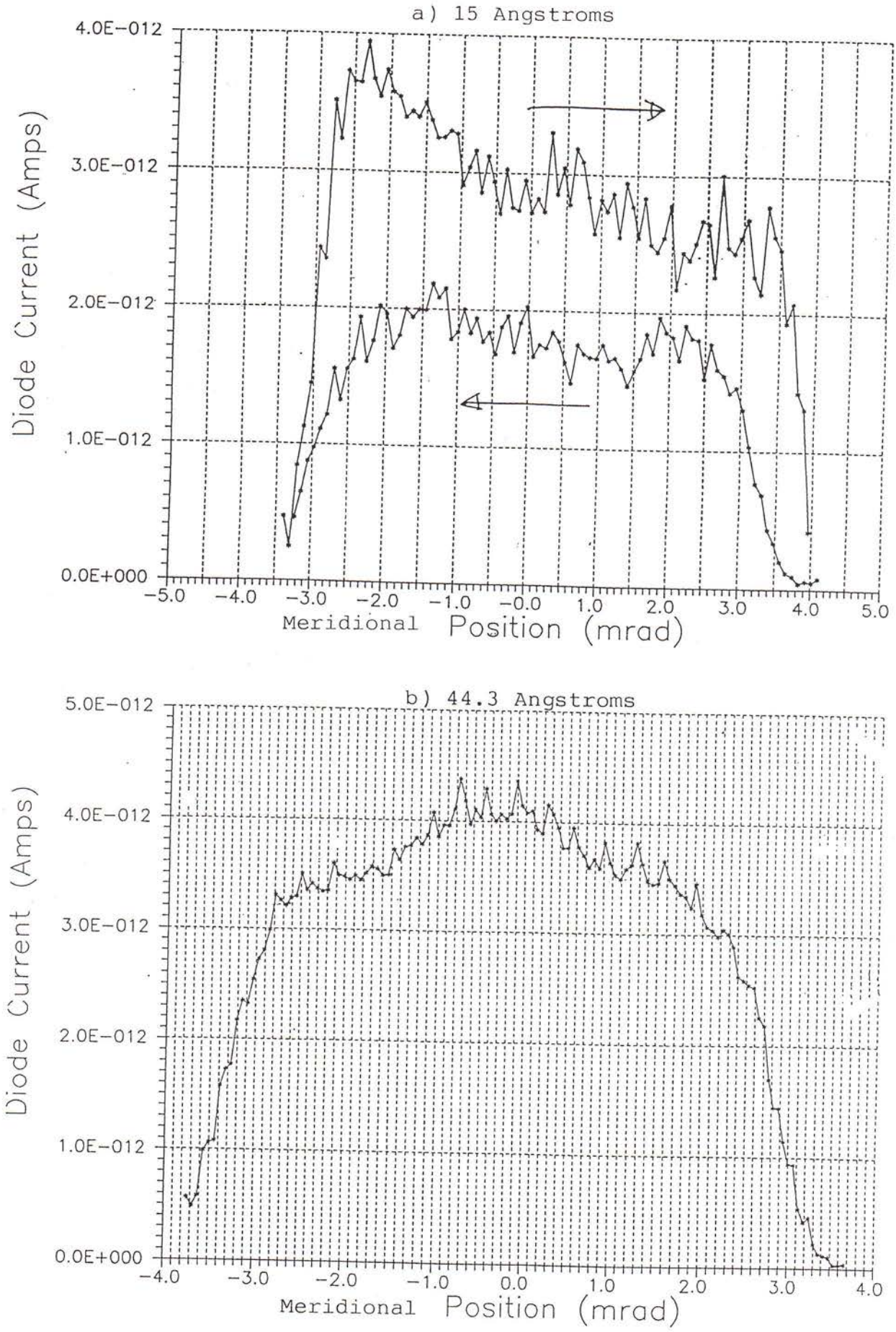


Fig. 4-13. Measured intensity as a function of position in the dispersion direction of the diffracted beam, integrated in the non-dispersive direction, for the double-rotation SNR.

### h) Spatial Uniformity

The single optical element and the use of equally-spaced grooves each minimize the variation in efficiency across the diffracted aperture. The main variation occurs from the geometrical aberrations which set in at the longest wavelengths due to the correcting tilt of the grating. Figure 4-12 shows spot diagrams of 3-D raytracing results at the exit aperture of the high resolution SNR described above. These were made of the transmitted beam at the position of the XMM telescope ~ 160 meters from the exit slit. The missing regions at 50 Angstroms shown in Figure 4-12c are due to the overillumination of the exit slit displayed in the focal plane spot diagram of Figure 4-6b.

Measurements of the 1-D spatial profiles at 15 Angstroms and 44.3 Angstroms shown in Figure 4-13 exhibit uniform intensities over the full 6 mrad meridional aperture of the grating. It should be noted that temporal variations in the intensity of the laser-plasma light source are significant in the measurement at 15 Angstroms, and thus an average of the profiles made with the aperture slit traversing in opposite directions is probably the most accurate measure of the inherent spatial non-uniformity in the beam. Similar measurements on the central 1/3 of the meridional aperture were made at the customer's facility using the stable electron beam source, and showed immeasurably small variations (< 2%) over this limited aperture of ~ 2 mrad in first spectral order. Higher spectral orders showed more significant variations, presumably due to the more pronounced variations in diffraction efficiency expected.

## *4.3 Sagittally Collimated Beam SNR Monochromator*

The most direct way of eliminating the image tilt of equation (4-6) is clearly to provide a collimated beam in the sagittal direction, for which $\Phi_y = 0$. From Figure 4-1b, this results in an equal effective spacing $d_o/\cos\Theta$ regardless of the sagittal coordinate $\ell$. This collimation can be accomplished by a mirror preceding the grating. However, to minimize the collimation uncertainty due to the finite source size, per equation (4-11), the object distance r from the source to this mirror should be maximized. Thus, such a mirror should be placed next to the grating. A source sagittal size of 0.15 mm and a mirror object distance of 750 mm was adopted, resulting in a sagittal blur of 0.2 mrad. From equation (4-6), this yields a resolving power limited to ~ 1000 at $\lambda = 5\lambda_{min}$ and to ~ 3000 at $\lambda = 2\lambda_{min}$.

Figure 4-14 is the result of raytracing such a system employing the grating discussed above and a collimating mirror with an acceptance of 5.2 mrad at a graze angle of 2.25°. The mirror was spherical and oriented at a right angle to the grating, thus aberrations in its plane of reflection are in the sagittal direction of the grating and hence contribute to the spectral aberration. The coma-type second degree aberration from the collimating mirror is found from equation (1-8):

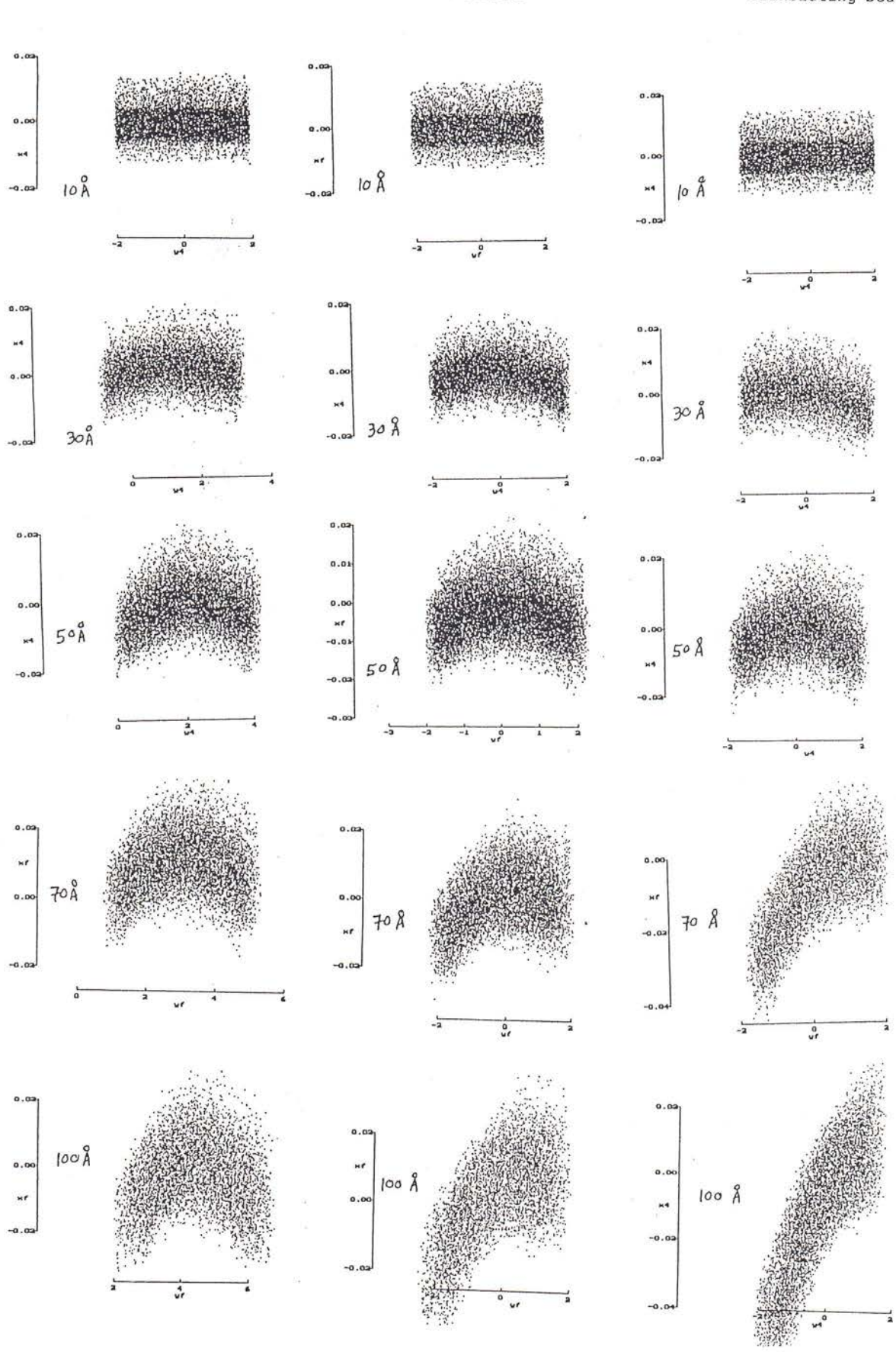


Fig. 4-14. Spot diagrams at exit slit plane of single-rotation SNR fed with a sagittally collimated beam. Entrance slit is 10 microns.

Fig. 4-15. FWHM spectral resolution of sagittally collimated SNR tracings shown in Fig. 4-14. The labels a,b and c correspond to the three cases given in the previous figure. These are a: fixed mirror and fixed source b: rotating mirror and fixed source and c: fixed mirror and translating source.

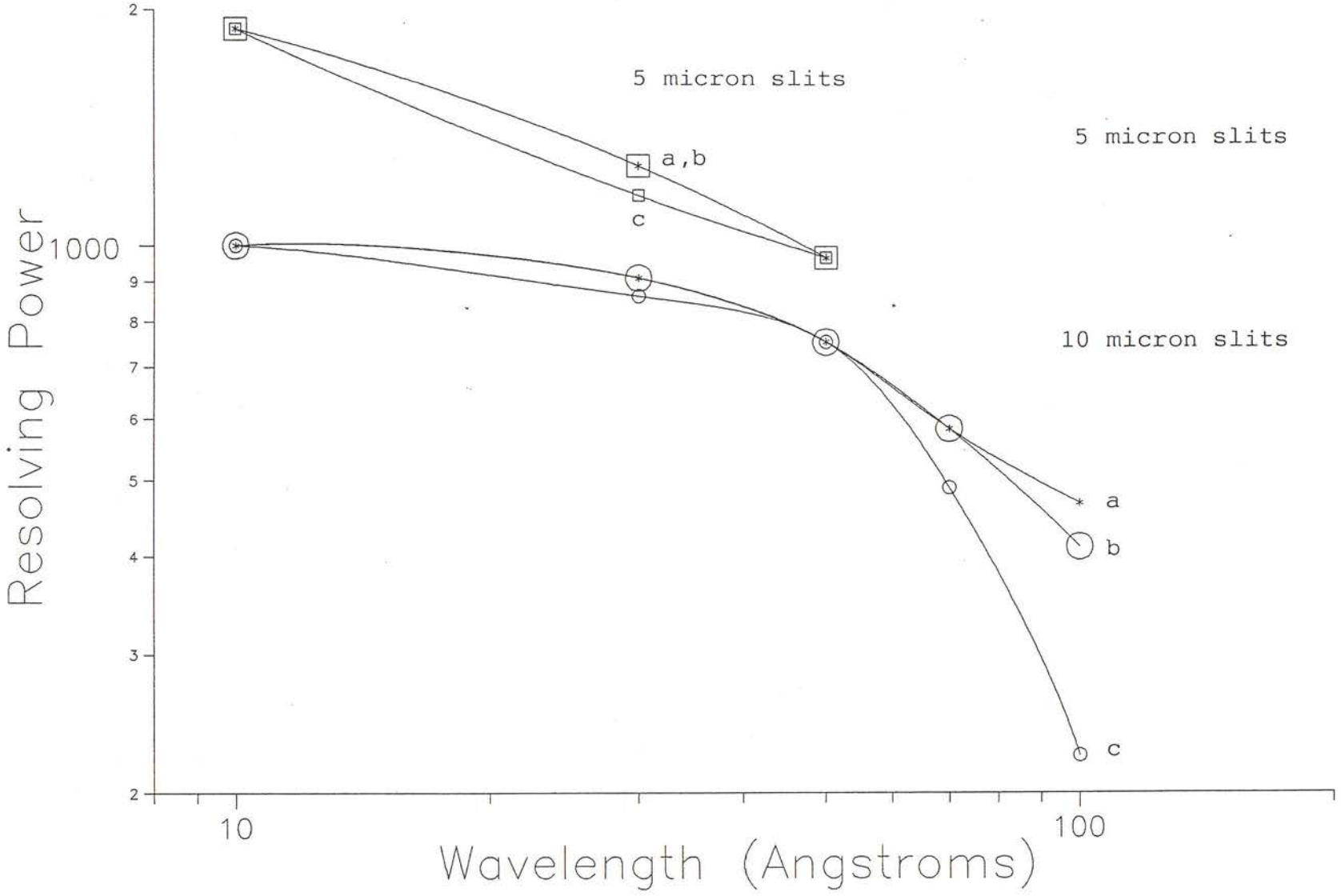

$$\Delta\Phi_y = (3/16)\,\Phi_y^2 \tan\phi \qquad (4\text{-}18)$$

where $\phi$ is the angle of incidence to the mirror, $\Phi_y$ the collection aperture of the mirror and $\Delta\Phi_y$ the aberration in the collimated beam. Given $\phi = 87.75^\circ$ and $\Phi_y = 0.0052$ radians, the aberration is calculated to be 0.13 mrad which from equation (4-6) results in a spectral aberration of 1/1500 after diffraction by the grating at a rotation angle of $78.46^\circ$ ($\lambda = 5\lambda_{min}$). This is confirmed by the ~ 0.004 Angstrom curvature seen in the 50 Angstrom spot diagrams at the exit slit plane, and also confirmed from separate raytracing of the mirror.

Figure 4-14a also confirms the numerical predictions of equation (4-5) for the image deflection in the y' direction, given the fixed source and collimating mirror. This deflection is corrected in Figure 4-14b by rotation of the collimating mirror and in Figure 4-14c by translation of the source. However, both of these remedies cause a change in the angle of incidence to the mirror, and thus result in de-collimation at all but one wavelength (50 Angstroms) for which the angle of incidence is collimated by the assumed fixed radius mirror. This de-collimation can be corrected by changing the radius of curvature of the mirror. A bent mirror, such as discussed in Sec. 2.3d can even correct for the coma aberration by introducing a gradient in the radius along the mirror length, so as to approximate a parabolic shape. This can allow a larger collection aperture in this direction, yet will result in an increased amount of non-uniformity in the beam intensity per Sec. 2.3h.

Figure 4-15 summarizes the spectral resolution as a function of wavelength for the three cases raytraced in Figure 4-14. Using 5 microns slits, the resolving power exceeds 1000 over the entire range from 10 to 50 Angstroms.

# 5. Spatial Imaging of Extended Plasmas

Magnetic fusion plasmas are confined to rather extended spatial regions (~ 0.5 meter in all directions). To study the electron temperature and density through spectral analysis of impurity ions in such plasmas requires spectroscopy as a function of two-dimensional position. The simplest way to accomplish this is by an adaptation of the classical "pinhole camera" technique. In the present case, the monochromator grating could view the extended plasma through the entrance slit. This provides a mapping of plasma position and meridional aperture. A second slit for spatial resolution in the non-dispersive direction can be crossed relative to the spectral slit, or the two slits combined as a pinhole at the entrance slit plane. In this way, the beam emerging the exit slit is a monochromatic 2-D image of the plasma. Different wavelengths are obtained by scanning the monochromator grating and thereby taking "spectral snapshots" of the plasma.

One might think that arbitrarily fine spatial resolution may be obtained in such an approach, by simply reducing the size of the pinhole. However, physical diffraction of the incident wavelength will add an uncertainty to the spatial position as illustrated in Figure 5-1a. This uncertainty (or blurring of the spatial map) is in inverse proportion to the slit width, hence as plotted in Figure 5-1b there is an optimum slit width which balances the geometrical and physical effects:

$$\Delta x_{opt} \sim ( \lambda L )^{1/2} \qquad (5\text{-}1)$$

resulting in a minimum angular resolution which is a function of the wavelength and the distance from slit to detector, L:

$$\Delta \phi_{min} \sim 1.5 ( \lambda / L )^{1/2} \qquad (5\text{-}2)$$

Figure 5-2 plots this minimum angular resolution as a function of wavelength for a 1-meter long monochromator. Clearly, the spatial resolution improves at shorter wavelengths, due to the decreased slit broadening from physical diffraction. Thus, resolutions are ~ 1 mrad in the far ultraviolet and ~ 0.1 mrad in the soft x-ray.

However, the narrow slit widths required for this optimum spatial resolution result in low throughput due to the reduced angular acceptance viewed by the source. Thus, using optics to spatially image the plasma will significantly increase the throughput due to the large aperture of an imaging mirror compared to that presented by a narrow slit. As shown in this thesis for both the plane VLS and self-focusing IFM spectrometers, such high throughput imaging is clearly advantageous in that it provides stigmatic spectra of

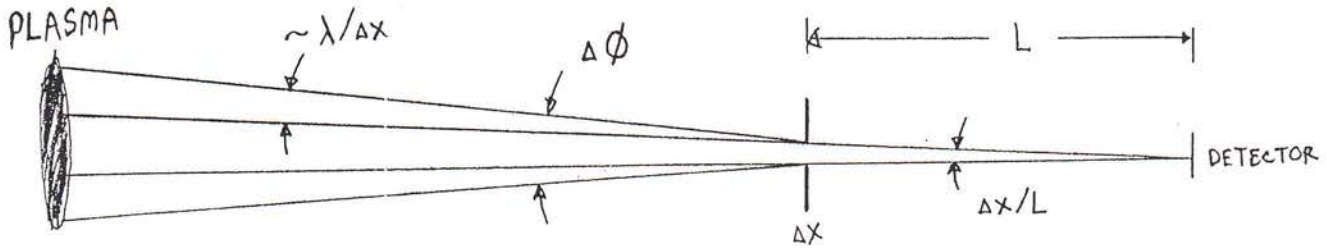


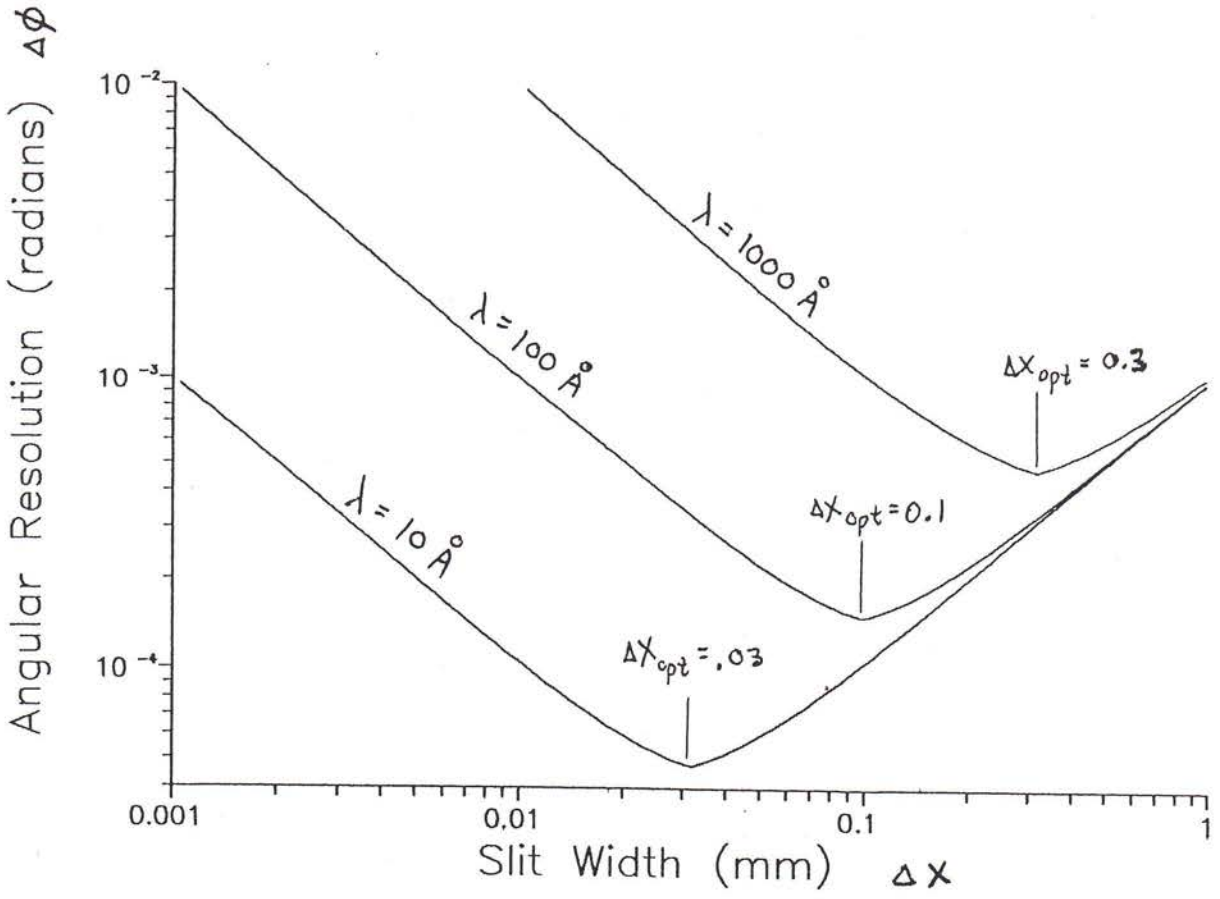


Fig. 5-1. a) Spatial resolution provided by a narrow slit is due to geometrical projection plus physical diffraction of finite wavelength. b) This results in an optimum slit width, which is a function of the the wavelength and the distance L (assumed to be 1 meter).

Fig. 5-2. Angular resolution for optimized slit width, as a function of wavelength, assuming 1 meter distance from slit to imaging detector.

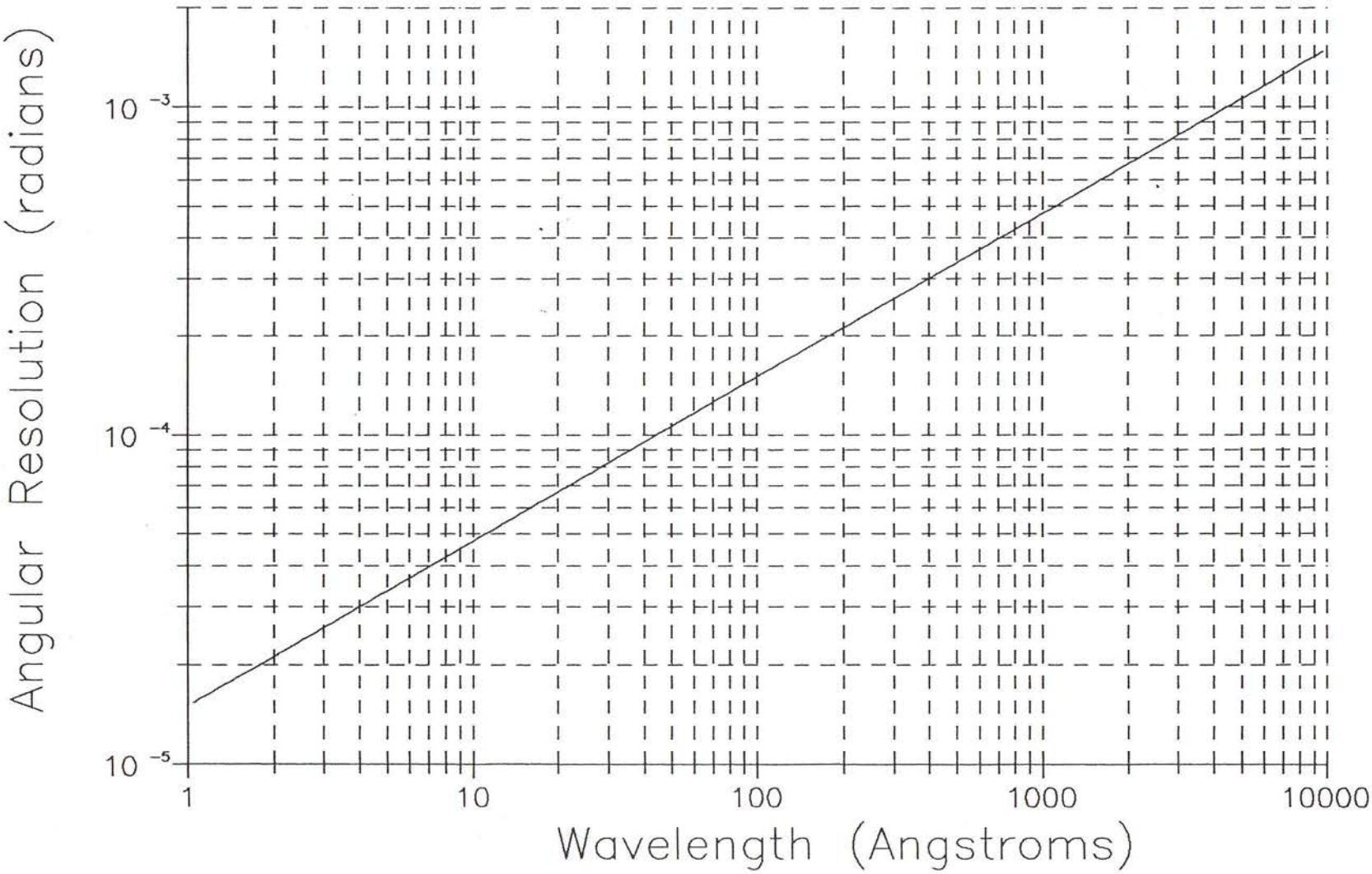

compact sources produced by pulsed-heating such as in laser-produced or z-pinched plasmas.

However, spatial imaging of extended sources requires consideration of the off-axis aberrations of the focusing optic. A (single-surface) focusing mirror at grazing incidence suffers from a large amount of defocusing away from the incident angle for which the radius of curvature was optimized. This is because the magnification varies linearly along the length of the mirror, as evident from Fig. 2-37. Simple geometry or equation (2-53) can be used to determine the field-of-view of the mirror as a function of its collection aperture ($\Phi$), graze angle ($\gamma$) and the required angular resolution ($\Delta\phi$):

$$FOV \sim (\Delta\phi/\Phi) \tan \gamma \qquad (5\text{-}3)$$

For example, a collection aperture of $\Phi = 2.5$ mrad is a 100-fold improvement over the slit method aperture optimized for 100 Angstroms (~ 0.1 mm / 4 meters). At this wavelength, Figure 1-5 indicates that a 20° graze angle provides reflectivity of ~ 40%, resulting in a net gain of a factor of ~ 25. Under these conditions, a spatial resolution of $\Delta\phi = 0.2$ mrad results in a FOV of ~ 27 mrad, and a resolution of 0.5 mrad results in a FOV of 68 mrad. The latter converts to a size of ~ 0.27 meters at a distance of 4 meters. This is sufficient to simultaneously image large sections of current and future magnetically confined plasmas.

From equation (2-62), the non-uniformity induced in the reflected beam by a focusing mirror of the required aperture (2.5 mrad) and graze angle (20°) is only ~ 1.5%. An In-Focus Monochromator similar to the stigmatic IFM system described in Sec. 3.3f having such a mirror to provide collection in the non-dispersive direction would provide the above imaging in this direction (0.5 mrad over 0.27 m size plasma) combined with spatial imaging provided by the entrance slit. A 20 micron entrance slit would provide a diffraction-limited spatial resolution of ~ 0.5 mrad in the dispersion direction at 100 Angstroms. Fermat calculations indicate that a spectral resolving power of ~ 2000 would be obtained over a meridional aperture of ~ 40 mrad for a monochromator of length ~ 1.3 meters and grating groove density 2400 g/mm. Such a monochromator could be scanned over the 100-300 Angstrom region to take 2-D imaging pictures of the plasma at many emission lines from various stages of ionization of the impurities in the plasma. These include hundreds of transitions from O III through O VIII, N IV through N VII and C IV through C VI, and thousands of transitions from higher-z (metallic) impurities. The high spectral resolution of the IFM would be necessary to separate the lines of these different ionization states and hence provide proper diagnosis of the temperature and density distribution within the plasma.

# 6. Conclusions

Three fixed slit spectrometers were invented and developed for use in the grazing incidence region ( $\lambda \sim 3$ - 1000 Angstroms). These designs employ a continuous variation of the groove spacing across the aperture of the reflection grating, or new but simple scanning motions of the grating. The light-path function and numerical raytracings were utilized to design and characterize these geometries. The performance was studied experimentally using laser-produced plasma, Garton discharge tube, z-pinch and electron beam sources.

The plane VLS spectrographs operate in converging light and deliver stigmatic spectra onto normal incidence focal surfaces, allowing use of high efficiency electronic imaging detectors such as micro-channel plates and CCDs. The laboratory High Resolution Erect Field Spectrometer (HIREFS) spectrograph/monochromator employs rotation of the grating to provide a tunable wavelength and a bendable mirror reflecting in the non-dispersive direction to provide user adjustment of the astigmatism.

The satellite-borne spectrographs provide resolving powers of several hundred, limited by the spatial resolution of the collecting telescope and the imaging detectors. This resolution was found adequate to provide the first "high resolution" spectroscopic studies of many extra-solar objects in the extreme ultraviolet and soft x-ray regions. The laboratory plane grating spectrometers achieved spectral resolutions limited by 10 micron slit widths, corresponding to resolving powers from ~ 1,500 to ~ 35,000 depending upon the length of the spectrometer. Spatial resolutions of ~ 5 arcseconds (0.025 mrad) were obtained at the center of the field-of-view in the non-dispersive direction. Absolute efficiencies of ~ 5% were obtained for the stigmatic spectrometers at the shortest wavelengths (~ Al-K) while significantly higher efficiencies result at longer wavelengths.

The In-Focus Monochromators (IFMs) provide highly corrected spectral focusing at all scanned wavelengths, using fixed slits and a single (self-focusing) optical element. The constructed soft x-ray IFMs achieved spectral resolutions limited by 5 to 10 micron slits, corresponding to resolving powers of 500 to ~ 900 for slit-to-slit distances of ~ 0.5 meter. The throughput of such devices is extremely high, due to the high collection aperture of the grating (~ 12 mrad x 30 mrad) and the nearly theoretical efficiency retrieved by the grating (up to ~ 40%). A stigmatic IFM was constructed and is being used to deliver high brightness monochromatic point-like images to surface samples residing in ultra-high vacuum.

The Surface Normal Rotation (SNR) monochromators also employ a self-focusing grating, but provide a fixed size aperture at all wavelengths, and are thus ideal for delivering monochromatic beams to fixed targets or for imaging of extended sources. The ability to use equally-spaced grating grooves allows a variety of methods for the

grating manufacture and provides high uniformity in the diffraction efficiency over the aperture. SNR monochromators have been successfully used at wavelengths from ~ 3 to ~ 200 Angstroms, providing resolving powers from ~ 200 to ~ 1,500 for slit-to-slit distances of ~ 0.7 m to ~ 1.5 m.

Spatial uniformity of the spectrometer efficiency is of particular interest in the application of such instrumentation to study the conditions of extended plasmas, such as produced by magnetic confinement. The minimization of such spatial variations for critical imaging applications is therefore a subject of future study and improvement. Spatial uniformity in grazing incidence systems depends on a number of design and fabrication parameters. The low numerical aperture of such systems generally results in a nearly constant first order diffraction efficiency within the dispersion plane of the grating. However, grazing incidence also causes varying distances from the source to the opposite edges of the optics, resulting in a variation in the intensity per unit angle in the reflected beam. As the mirrors used in the above study eliminate the astigmatism only at the center of the field-of-view, they are particularly useful in conjunction with point sources such as produced by pulsed and focused lasers.

In applying such systems to the spatial imaging of extended plasmas, one may eliminate the intensity variations and aberrations resulting from mirrors by using pinhole imaging. However, the physical diffraction from a pinhole is large at long wavelengths, limiting the spatial resolution attainable, and its collection aperture is extremely low. Therefore, higher throughput will be obtained by use of a small mirror to image in the non-dispersive direction. Such mirror has tolerable off-axis aberrations and non-uniformities in the spatial intensity distribution. An imaging IFM or other VLS grating system so configured provides high spatial and spectral resolution over the extended spatial fields required for diagnosis of magnetically confined plasmas.

# References


1. H.A. Rowland, "On Concave Gratings for Optical Purposes," Phil. Mag. vol. 16, p. 197 (1883).

2. H.G. Beutler, J. Opt. Soc. Am., vol. 35, p. 311 (1945).

3. J.A.R. Samson, "Techniques of Vacuum Ultraviolet Spectroscopy," Pied Publications (ISBN 0-918626-15-3), 1980.

4. M. Seya, "A New Mounting of Concave Grating Suitable for a Spectrometer," Sci. Light, vol. 2, p. 8 (1952).

5. P. D. Johnson, Rev. Sci. Instrum., vol. 28, p. 833 (1957).

6. R. Onaka, "Grating Mounting for Vacuum Ultraviolet Monochromator," Sci. Light., vol. 7, p. 23 (1958).

7. M. Czerny and A.F. Turner, Z. Physik, vol. 61, p. 792 (1930).

8. Haber, "The Torus Grating," J. Opt. Soc. Am. vol. 40. p. 153 (1950).

9. M.C. Hettrick and J.H. Underwood, "Stigmatic High Throughput Monochromator for Soft X-Rays," Appl. Opt. vol. 25, p. 4228 (1986).

10. M.C. Hutley, "Diffraction Gratings," Academic Press (Techniques of Physics, ISSN 0308-5392;6), 1982.

11. M.C. Hettrick,"Varied line-space gratings: past, present and future," Proc. Soc. Photo-Opt. Instrum. Eng. vol. 560, p. 96 (1985).

12. E.D. Palik (ed.), "Handbook of Optical Constants of Solids, Academic Press (ISBN 0-12-544420-6), 1985.

13. B.L. Henke, P. Lee, T.J. Tanaka, R.L. Shimabukuro and B.K. Fujikawa, "Low-energy X-Ray Interaction Coefficients: Photoabsorption, Scattering and Reflection," Atomic Data & Nuclear Data Tables vol. 27, p. 1 (1982).

14. H. Gursky and T. Zehnpfennig, "An Image-Forming Slitless Spectrometer for Soft X-Ray Astronomy," App. Opt. vol. 5, p. 875 (1966).

15. F.D. Seward et al, "Calibration and Efficiency of the Einstein Objective Grating Spectrometer," Appl. Opt. vol. 21, p. 2012 (1982).

16. W.A. Rense and T. Violett, "Method of Increasing the Speed of a Grazing Incidence Spectrograph," J. Opt. Soc. Am. vol. 49, p. 139 (1959).

17. S. Bowyer, R. Kimble, F. Paresce, M. Lampton and G. Penegor, "Continuous-Readout Extreme-Ultraviolet Airglow Spectrometer," Appl. Opt. vol. 20, p. 477 (1981).

18. P.M. McPherson, "Ultraviolet Monochromator," U.S. Patent 3,211,049, 1965.

19. G. Tondello, "Spectrograph-Monochromator of Grazing Incidence Type," U.S. Patent 4,254,335 (1981).

20. R.J. Fonck, A.T. Ramsey and R.V. Yelle, "Multichannel grazing-incidence spectrometer for plasma impurity diagnosis: SPRED," Appl. Opt. vol. 21, p. 2115 (1982).

21. H. Dietrich and C. Kunz, "A Grazing Incidence Vacuum Ultraviolet Monochromator with Fixed Exit Slit," Rev. Sci. Instrum. vol. 43, p. 434 (1972).

22. W.R. Hunter, R.T. Williams, J.C. Rife, J.P. Kirkland, and M.N. Kabler, "A Grating/Crystal Monochromator for the Spectral Range 5 eV to 5 keV," Nucl. Instrum. Meth. vol. 195, p. 141 (1982).

23. H. Petersen, "Plane-Grating Monochromator," U.S. Patent 4,553,253, 1985; Opt. Comm. vol. 40, p. 402 (1982).

24. F.C. Brown, R.Z. Bachrach and N. Lien, "The SSRL ultrahigh vacuum grazing incidence monochromator: design considerations and operating experience," Nucl. Instrum. Meth., vol. 152, p. 73 (1978).

25. T. Harada and T. Kita, "Mechanically ruled aberration-corrected gratings," Appl. Opt. vol. 19, p. 3987 (1980).

26. M.C. Hettrick, "Extreme Ultraviolet Explorer Spectrometer Option Study," MCH/EUVE/321/82, U. California, Berkeley (1982).

27. M.C. Hettrick and S. Bowyer, "Variable line-space gratings: new designs for use in grazing incidence spectrometers," Appl. Opt. vol. 22, p. 3921 (1983).

28. M.C. Hettrick, "Aberrations of varied line-space grazing incidence gratings in converging light beams," Appl. Opt. vol. 23, p. 3221 (1984).

29. M. Neviere, D. Maystre and W.R. Hunter, "On the use of classical and conical diffraction mountings for xuv gratings," J. Opt. Soc. Am. vol. 68, p. 1106 (1978).

30. M.C. Hettrick, S. Bowyer, R.F. Malina, C. Martin and S. Mrowka, "Extreme Ultraviolet Explorer spectrometer," Appl. Opt. vol. 24, p. 1737 (1985).

31. K. Schwarzschild, "Untersuchungen zur geometrischen Optik. II. Theorie der Spiegeltelescope," Abh. Akad. Wiss. Goettingen vol. 4-2, p. 1 (1905).

32. H. Wolter, "Spiegelsysteme streifenden Einfalls als abbildende Optiken fur Roentgenstrahlen," Ann. Phys. vol. 10-94, p. 286 (1952).

33. D. Maystre and R. Petit, "Quelques Recents Resultats en Theorie des Reseaux: Application a Leur Utilization dans L'Extreme Ultraviolet," Nouv. Rev. Opt. vol. 7, p. 165 (1976).

34. R.D. Hatcher and J.H. Rohrbaugh, "Theory of the Echelette Grating. I," J. Opt. Soc. Am. vol. 46, p. 104 (1956); "Theory of the Echelette Grating. II," vol. 48, p. 704 (1958).

35. R.F. Malina, C.S. Bowyer and G. Basri, "Extreme Ultraviolet Spectrophotometry of the Hot White Dwarf HZ43: Detection of HeII in the Stellar Atmosphere," Astrophys. J. vol. 262, p. 717 (1982).

36. R. Cruddace, F. Paresce, S. Bowyer and M. Lampton, "On the Opacity of the Interstellar Medium to Ultra-Soft X-Rays and Extreme Ultraviolet Radiation," Astrophys. J. vol. 187, p. 497 (1974).

37. M. Malinovsky and L. Heroux, "An Analysis of the Solar Extreme Ultraviolet Spectrum Between 50 and 300 A," Astrophys. J. vol. 181, p. 1009 (1973).

38. J. Dupuis, S. Vennes, S. Bowyer, A.K. Pradhan and P. Thejll, "Hot White Dwarfs in the Local Interstellar Medium: Hydrogen and Helium Interstellar Column Densities and Stellar Effective Temperatures from EUVE Spectroscopy," Astrophys. J. vol. 455, p. 574 (1995).

39. M.C. Hettrick and S. Kahn, "A Reflection Grating Spectrometer for the X-Ray Multi-mirror (XMM) Space Observatory: Design and Calculated Performance," SPIE vol. 597, p. 291 (1985).

40. S. Kahn and M.C. Hettrick, "The Application of Reflection Gratings to a Large Area X-Ray Spectroscopy Mission: A Discussion of Scientific Requirements and Various Design Options," Proc. ESA Workshop: *'Cosmic X-Ray Spectroscopy Mission'*, Lyngby Denmark, June 1985 (ESA SP-239, Sept. 1985).

41. M.C. Hettrick, J.H. Underwood, P. Batson and M.J. Eckart, "Resolving power of 35,000 (5 mA) in the extreme ultraviolet employing a grazing incidence spectrometer," Appl. Opt. vol. 27, p. 200 (1988).

42. M.C. Hettrick and J.H. Underwood, "Optical System for High Resolution Spectrometer/Monochromator," U.S. Patent 4,776,696 (1988).

43. M.C. Hettrick, "High Resolution Gratings for the Soft X-Ray," Nucl. Instrum. Meth. vol. A266, p. 404 (1988).

44. T.W. Barbee, S. Mrowka and M.C. Hettrick, "Molybdenum-silicon mirrors for the extreme ultraviolet," Appl. Opt. vol. 24, p. 883 (1985).

45. P. Kirkpatrick and A.V. Baez, Jr., "Formation of Optical Images in X-Rays," J. Opt. Soc. Am. vol. 38, p. 766 (1948).

46. B. Smith, J.J. Bloch and D. Roussel-Dupre, "Metal multilayer mirrors for EUV/ultrasoft x-ray wide-field telescopes," Opt. Eng. vol. 29, p. 592 (1990).

47. D.L. Windt and W.K. Waskiewicz, "Soft x-ray reflectometry of multilayer coatings using a laser-plasma source," Proc. Soc. Photo-Opt. Instrum. Eng. Conf. 1547 on *Multilayer Optics for Advanced X-Ray Applications*, San Diego, July 1991.

48. T.J. Nash et al, "Spectroscopic Diagnosis of Foam-Pinched Plasmas on SATURN," APS conf. on High Temperature Plasma Diagnostics, Monterey, May 1996, to appear in Rev. Sci. Instrum.

49. Y. Kato et al, " Development of Soft X-Ray Lasers at the Institute of Laser Engineering: Recent Results on Ge Soft X-Ray Laser," Pro. Soc. Photo-Opt. Instrum. Eng. Conference 1551 on *Ultrashort Wavelength Lasers*, San Diego, July 1991.

50. J.A. Koch et al, "Observation of Gain-Narrowing and Saturation Behavior in Se X-Ray Laser Line Profiles," Phys. Rev. Lett. vol. 68, p. 3291 (1992).

51. J.-K. Crane, M.D. Perry, S. Herman and R.W. Falcone, "High-field harmonic generation in helium," Opt. Lett. vol. 17, p. 1256 (1992); J.-K. Crane, M.D. Perry, D. strickland, S. Herman and R.W. Falcone, "Coherent and Incoherent XUV Emission in Helium and Neon, Laser-Driven Plasmas," IEEE Transactions on Plasma Science vol. 21, p. 82 (1993).

52. H. Tsunemi et al, "Application of a Newly Developed CCD for Spectral-Width Measurements of a 53 eV Germanium Laser," Appl. Phys. vol. B57, p. 331 (1993).

53. G.A. Kyrala, R.D. Fulton, J.A. Cobble, G.T. Schappert and A.J. Taylor, "Diagnostics of High-Brightness Short-Pulse Lasers and the Plasmas They Generate," SPIE conference

on Generation, Amplification and Measurement of Ultra Short Laser Pulses, Los Angeles January 22-29, 1994.

54. G. Prigozhin, M. Bautz, K. Gendreau and G. Ricker, "Calibration of X-ray CCDs with an Erect-Field Grating Spectrometer in the 0.2-1.5 keV band," Proc. Soc. Photo-Opt. Instrum. Eng., Conf. 2808, Denver, August 1996.

55. J. Zhou, J. Peatross, M.M. Murnane, H. Kapteyn and I.P. Christov, "Enhanced High-Harmonic Generation Using 25 fs Laser Pulses," Phys. Rev. Lett. vol. 76, p. 752 (1996).

56. I.P. Christov, J. Zhou, J. Peatross, A. Rundquist, M.M. Murnane and H.C. Kapteyn, "Nonadiabatic Effects in High-Harmonic Generation with Ultrashort Pulses," Phys. Rev. Lett. vol. 11, p. 1743 (1996).

57. R. Elsner et al, "Characterization of the X-ray Source System (XSS): HIREFS reflection-grating monochromator," XRCF document, Marshall Space Flight Center 1996.

58. M.C. Hettrick, "In-focus monochromator: theory and experiment of a new grazing incidence mounting," Appl. Opt. vol. 29, p. 4531 (1990).

59. M.C. Hettrick, "Varied Space Diffraction Grating and In-Focus Monochromator," U.S. Patent 4,991,934 (1991).

60. J.J. Joyce and A. J. Arko, "Resonance Photo-electron Spectroscopy Using a Laboratory Based laser Plasma Light Source," Bulletin of the American Physical Society, program of March 1996 meeting, St. Louis, vol. 41-1, p. 808 (1996).

61. M.C. Hettrick, "Surface normal rotation: a new technique for grazing incidence monochromators," Appl. Opt. vol. 31, p. 7174 (1992).

62. M.C. Hettrick, "Grating Monochromators and Spectrometers Based on Surface Normal Rotation," U.S. Patent 5,274,435 (1993).

Errata

1. On page 14, the last line of Equation (1-13):

$$cos^2\beta_1\,(cos\alpha_2 + cos\beta_2) - cos^2\beta_2\,(cos\alpha_1 + cos\beta_1)$$

should be replaced with:

$$cos^2\alpha_1\,(cos\alpha_2 + cos\beta_2) - cos^2\alpha_2\,(cos\alpha_1 + cos\beta_1)$$

2. On page 26, the left-hand side of Equation (2-4):

$$F_{15} = -3/(8\ r_o{}^4)$$

should be replaced with:

$$F_{14} = -3(\sin\beta_o - \sin\alpha_o)/(8\ r_o{}^4)$$

3. On page 28, in the first full paragraph following Equation (2-6):

[Sec. d) below]

should be replaced with:

[Sec. e) below]

4. On page 29, the section heading:

c) Off-Plane Version (Fan Grating)

should be replaced with:

b) Off-Plane Version (Fan Grating)

5. On page 32, the section heading:

d) Linear Dispersion Considerations

should be replaced with:

c) Linear Dispersion Considerations

6. On page 33, the section heading:

c) Optical System Design

should be replaced with:

d) Optical System Design

7. On page 129, in the line following Equation (4-3):

$N_{01} = (1/d_o) \cos\Theta$

should be replaced with:

$N_{01} = (1/d_o) \sin\Theta$